



SAPIENZA  
UNIVERSITÀ DI ROMA

Department of Physics ‘G. Marconi’  
PhD in Accelerator Physics

THESIS FOR THE DEGREE OF DOCTOR OF PHILOSOPHY

# Muons for high precision physics: muEDM & MEG



Thesis advisor  
**Prof. Angela Papa**

Candidate  
**Bastiano Vitali**  
**333453/1949877**

Academic Year 2023-2024 (XXXVI cycle)

# Contents

<b>List of Figures</b>	<b>v</b>
<b>List of Tables</b>	<b>xv</b>
<b>missing, started, review, corrected, done</b>	<b>1</b>
<b>1 Introduction</b>	<b>1</b>
1.1 Outline of this thesis	1
1.2 Particle physics at Paul Scherrer Institute	1
1.3 Bite-size theory	2
1.3.1 Standard Model at low energies	2
1.3.2 Beyond Standard Model at low-energy	4
1.3.3 Muon	5
1.3.4 Muon decay	6
1.3.5 Electric Dipole Moment	7
1.4 Experimental status	8
1.4.1 CLFV experiments	8
1.4.2 EDM experiments	12
1.5 The beams at PSI	17
1.5.1 High-Intensity Proton Accelerator facility	17
1.5.2 Meson production	20
1.5.3 Neutron production	23
1.5.4 High-Intensity Muon Beams	24
1.6 Proton Ionization Facility	28
<b>Bibliography for the introduction</b>	<b>29</b>
<b>I muEDM</b>	<b>34</b>
<b>2 muEDM</b>	<b>35</b>
2.1 Electric Dipole Moment	35
2.1.1 Symmetry violation	36
2.1.2 Current limits on EDM	36
2.1.3 The <i>frozen spin</i> technique	36
2.2 The muEDM experiment	37
2.3 The precursor	39
2.3.1 Beam monitor	39
2.3.2 TOF	39
2.3.3 Entrance	41
2.3.4 Superconducting injection channel	42
2.3.5 Muon tracking	43
2.3.6 Kicker	46

2.3.7	Faraday rotator . . . . .	49
2.3.8	Frozen-spin electrodes . . . . .	49
2.3.9	Positron tracking . . . . .	51
2.4	Sensitivity . . . . .	52
2.5	Systematics . . . . .	53
2.5.1	Possible sources of spin precessions . . . . .	54
2.5.2	Comparison with GEANT4 . . . . .	55
2.5.3	Constraints . . . . .	55
2.6	Schedule . . . . .	55
2.7	Conclusions . . . . .	57
<b>Bibliography on muEDM</b>	. . . . .	<b>57</b>
<b>3 Scintillators in muEDM</b>	. . . . .	<b>61</b>
3.1	Short intro to scintillators . . . . .	61
3.1.1	Plastic scintillators . . . . .	61
3.1.2	Scintillating Fibers . . . . .	62
3.1.3	Scintillation process . . . . .	63
3.2	GEANT4 simulations . . . . .	63
3.2.1	What is GEANT4? . . . . .	63
3.2.2	Entrance system . . . . .	64
3.2.3	Telescope and entrance detector . . . . .	66
3.3	Beamtime 2021 . . . . .	68
3.3.1	Description of the multiple scattering . . . . .	69
3.3.2	Data taking . . . . .	69
3.3.3	Data analysis . . . . .	72
3.3.4	Model evaluation and conclusions . . . . .	73
3.4	Beamtime 2022: Telescope and entrance detector . . . . .	73
3.4.1	Construction . . . . .	74
3.4.2	Data taking . . . . .	76
3.4.3	Data analysis . . . . .	76
3.5	Beamtime 2023: TOF and Multi readout entrance . . . . .	80
3.5.1	Data taking . . . . .	80
3.5.2	Data analysis . . . . .	87
<b>Bibliography on muEDM entrance detector</b>	. . . . .	<b>91</b>
<b>4 muEDM positron tracker</b>	. . . . .	<b>95</b>
4.1	Tracking $e^+$ in muEDM . . . . .	95
4.2	Design in the 2022 proposal . . . . .	95
4.2.1	The SciFi detector . . . . .	96
4.2.2	Scintillating fibers prototype . . . . .	97
4.2.3	Geant4 simulation and performance . . . . .	100
4.2.4	Conclusions on the 2022 proposal . . . . .	103
4.3	CHeT . . . . .	105
4.3.1	Resolutions of crossed fibers ribbons . . . . .	105
4.3.2	Angle choices for the layers . . . . .	105
4.3.3	Cylindrical geometry . . . . .	105
4.3.4	GEANT4 simulation . . . . .	106
4.3.5	From $\gamma s$ to waveforms . . . . .	107
4.3.6	Tracking . . . . .	108
4.4	A study of radial geometry . . . . .	111

4.4.1	Possible geometries . . . . .	111
4.5	Conclusions . . . . .	111
	<b>Bibliography on muEDM positron tracker . . . . .</b>	<b>111</b>
	<b>II MEG II</b>	<b>113</b>
5	<b>MEG II and the Cockcroft–Walton . . . . .</b>	<b>114</b>
5.1	MEG II . . . . .	114
5.2	The liquid XEnon Calorimeter . . . . .	115
5.2.1	Xe scintillation . . . . .	116
5.2.2	Photon detection . . . . .	116
5.2.3	Calibration . . . . .	117
5.2.4	Reconstruction and performance . . . . .	118
5.3	Spectrometer . . . . .	119
5.3.1	COBRA . . . . .	119
5.3.2	Cylindrical Drift CHamber (CDCH) . . . . .	120
5.3.3	pixelated Timing Counter (pTC) . . . . .	123
5.4	Trigger and DAQ . . . . .	123
5.4.1	WaveDAQ . . . . .	125
5.4.2	Data reduction . . . . .	125
5.4.3	Performances . . . . .	125
5.4.4	Triggers . . . . .	125
5.5	Beam and target . . . . .	126
5.5.1	$\pi E5$ . . . . .	126
5.5.2	Simulations . . . . .	128
5.5.3	MEG II target . . . . .	129
5.6	Sensitivity . . . . .	130
5.7	Cockcroft–Walton . . . . .	131
5.7.1	Description of the machine . . . . .	131
5.7.2	Usage . . . . .	134
5.7.3	CW issues and maintenance . . . . .	135
5.8	Conclusions . . . . .	138
	<b>Bibliography on MEG II . . . . .</b>	<b>138</b>
6	<b>Liquid Hydrogen target . . . . .</b>	<b>142</b>
6.1	Charge EXchange reaction . . . . .	142
6.2	BGO . . . . .	142
6.3	LH <sub>2</sub> target . . . . .	143
6.3.1	Operation and control . . . . .	144
6.4	2021 . . . . .	144
6.4.1	Data taking . . . . .	146
6.4.2	Data analysis . . . . .	146
6.5	2022 . . . . .	147
6.5.1	Upgrades . . . . .	147
6.5.2	Data taking . . . . .	149
6.6	2023 . . . . .	152
6.6.1	Upgrade . . . . .	152
6.6.2	Tests . . . . .	153
6.6.3	Data taking . . . . .	154

6.7	Conclusions . . . . .	155
	<b>Bibliography on LH<sub>2</sub> . . . . .</b>	155
<b>7</b>	<b>Search for X17 . . . . .</b>	160
7.1	ATOMKI and the X17 ‘anomaly’ . . . . .	160
7.1.1	The process . . . . .	160
7.1.2	The esults . . . . .	162
7.2	X17 in MEG II . . . . .	162
7.2.1	Magnetic field choice . . . . .	162
7.2.2	Target . . . . .	163
7.2.3	MC simulations . . . . .	164
7.2.4	Data acquisition(s) . . . . .	165
7.3	Data analysis . . . . .	166
7.3.1	Pair reconstruction . . . . .	167
7.3.2	Angular corrections . . . . .	170
7.3.3	Vertexing . . . . .	170
7.3.4	Beam spot . . . . .	170
7.3.5	Blinding strategy . . . . .	170
7.3.6	Likelihood analysis . . . . .	174
7.3.7	Asymmetry and normalization . . . . .	177
7.4	Target studies . . . . .	179
7.4.1	Al and Cu Data-taking . . . . .	181
7.5	Beam studies: Jan 2024 . . . . .	181
7.5.1	Collimator and beam studies . . . . .	185
7.6	Results and conclusions . . . . .	185
	<b>Bibliography on X17 . . . . .</b>	187
<b>A</b>	<b>Kalman filter . . . . .</b>	190
A.1	The problem . . . . .	190
A.2	The solution . . . . .	190
A.3	Implementation . . . . .	191
A.4	Example: a 2D linear fit . . . . .	192
A.4.1	Adding multiple scattering . . . . .	194
<b>B</b>	<b>BGO Calibrations . . . . .</b>	195
B.1	Calibration factors . . . . .	195
B.1.1	Sample size . . . . .	196
B.2	Stability . . . . .	198

# List of Figures

1.1	MEG experiment . . . . .	10
1.2	Mu3e experiment . . . . .	10
1.3	Mu2e experiment . . . . .	11
1.4	COMET experiment . . . . .	12
1.5	. . . . .	13
1.6	. . . . .	14
1.7	. . . . .	14
1.8	. . . . .	15
1.9	$g - 2$ ring and EDM detector . . . . .	16
1.10	$g - 2$ Traceback Wire Chamber . . . . .	17
1.11	HIPA: CW and Ring Cyclotron . . . . .	18
1.12	HIPA: layout . . . . .	18
1.13	John's N3-Law for maximum current in a cyclotron . . . . .	20
1.14	HIPA: power usage . . . . .	21
1.15	HIPA: power history . . . . .	21
1.16	HIPA: charge history . . . . .	22
1.17	UCN: source . . . . .	25
1.18	UCN: freezing behavior . . . . .	25
1.19	UCN: source statistics . . . . .	26
1.20	HIMB: H target . . . . .	26
1.21	HIMB: collection solenoids . . . . .	27
1.22	HIMB: momentum spectra . . . . .	28
2.1	. . . . .	37
2.2	Photo (a) and sketch (b) of the compact superconducting solenoid and the experimental setup for the search for the EDM of the muon. The warm bore of the solenoid has an inner diameter of 200 mm and an outer diameter of about 1000 mm. . . . .	38
2.3	Positron energy distribution as a function of the angle between the muon spin and momentum. The fractional energy $u = E/E_{\max}$ is shown on the abscissa. The maximum positron energy for Phase I is $E_{\max} = 68.9$ MeV. The color bar shows the $g - 2$ phase in units of $\pi$ radians, where 0 is spin and momentum aligned (blue) and 1 is anti-aligned (red). . . . .	38
2.4	Most probable visible deposited energy by muons and positrons in scintillators of various thicknesses, simulated in G4BEAMLINE. Muons and positrons with a momentum of 28 pass through a 2 mm-thick front scintillator before reaching a 5 mm-thick back scintillator. The green points are the decay positrons from muons stopped in the front scintillator. . . . .	40
2.5	Left: four geometries considered for the beam monitor. Right: Results of the beam centering in simulation, using the algorithm as described in the text, for the four geometries shown on the left image. Muon hits are colored differently based on which tile they hit, all positron hits are black. . . . .	40

2.6	Muon+positron (left) and muon-only (right) average asymmetries after the centering based on muon+positron counts. The asymmetries are plotted as a function of positron contribution in the beam. . . . .	40
2.7	The two versions of the beam monitor during the assembly. . . . .	41
2.8	The TOF detectors during the assembly procedure. The scintillating windows during the gluing into the light guide (top left). The MPPC boards, where four MPPCs are soldered in series to form a single channel (top middle). A detail of the light guide (Bottom-right). . . . .	41
2.9	CAD sketch of the entrance trigger. On the left, the muons exit the injection channel. The strong magnetic field immediately bends the muons onto a spiral trajectory. First, they pass through a thin ( $\leq 100 \mu\text{m}$ ) entrance scintillator. A thick second scintillator forms an active aperture, with holes at positions along the reference muon trajectory, which stops and detects muons that are outside the acceptance phase space. The trigger for the magnetic pulse, see Sec. 2.3.6, will be generated by the anticoincidence of the two. . . . .	42
2.10	(a) Experimental setup for testing of superconducting shield prototypes; Helmholtz coil pair and a HTS-prototype placed between the two coils; (b) setup submerged in LN <sub>2</sub> . . . . .	43
2.11	Measurement of the YBCO prototype. (a) Measured magnetic field versus time, <i>left</i> , and versus coil current, <i>center</i> , at 77 K with and without prototype. (b) Shielding factor of YBCO prototype. . . . .	44
2.12	Measurement of the Bi2223 prototype. (a) Measured magnetic field versus time, <i>left</i> , and versus coil current, <i>center</i> , at 77 K with and without prototype, and as simulated. (b) Comparison of experimental versus simulated shielding factor of Bi2223 prototype. . . . .	44
2.13	Average number of reconstructed hits per track in the GridPix detector, as a function of mesh voltage, normalized to the asymptotic value of a sigmoid curve fitting the data points, for three different mixtures of helium-isobutane (95:5, 90:10, and 85:15). . . . .	45
2.14	Performance of a longitudinal TPC for the reconstruction of injected muons. (a) Reconstructed momentum (assuming 28 MeV/c initial momentum). (b) True (blue) and reconstructed (red) phase space coordinates and angles (u: horizontal; v: vertical). . . . .	45
2.15	The pulse coils, (a) prototype and (b) geometry implemented in ANSYS, are responsible for kicking the remaining longitudinal momentum to permit storage in a weakly-focusing magnetic field. They will be constructed from 100 $\mu\text{m}$ copper sheets to minimize multiple scattering without significantly increasing electrical resistance for frequencies $\sim 10$ MHz. The ANSYS simulation produces field maps, shown on the central $x - y$ -plane in (c) where the dashed black line shows the stored muon orbit. The average field strength over the orbit is $8.4 \mu\text{T A}^{-1}$ , as shown by the orange line in (d), where the field strength is plotted over the orbit parametrized by the azimuthal angle $\phi$ . . . . .	47
2.16	Circuit model, developed in LTSpice, for the load attached to simplified charging-stage circuits using ideal switches. Transmission lines labeled <i>CoaxLine1-4</i> transmit from generator to the external flange of the solenoid; <i>CoaxLineB1-4</i> transmit from the flange to the center of the bore, where the coils are located. Inductive couplings between quadrants $i$ and $j$ are specified by the listed constants labeled $K_{ij}$ . Capacitive couplings between quadrants $i$ and $j$ are described by capacitors labeled $CQ_{ij}$ . The second and third quadrants are not shown for compactness. . . . .	48

2.17 Pulse current profiles simulated using the LTspice circuit model with parameters as shown in Fig. 2.16. The current plotted in (a) and (b) from $t = 0$ (entrance) to $t = 500$ ns is for the first quadrant, labeled $LQ1$ in Fig. 2.16. The dashed vertical line at 210 ns indicates the time after which the current remains below $\sim 1$ A. The voltage over the capacitor labeled $C1$ is plotted in (c), showing the recovery of the charging voltage within the desired 20 $\mu$ s duration. . . . .	49
2.18 Left: The TGG crystal holder with polarizer and analyzer. Center: Setup for characterization of the TGG crystal and verification of the performance of the magnetometer. The one loop coil serves to produce a micro-Tesla level field at 100 kHz. Right: The potassium laser used to power the probe. . . . .	50
2.19 The radial electric field corresponding to the frozen-spin field strength at the nominal orbit radius is plotted over the radial position. The dashed vertical lines indicate the radial offset due to changes in momentum $\pm 0.5\%$ . The dashed curves indicate the electric field which would satisfy the frozen-spin condition for these shifted momenta and radii. The resultant discrepancy is $\sim 1\%$ , limiting the precision necessary for the electric field strength given a momentum bite of 0.5%. . . . .	51
2.20 A segmented electrode prevents eddy current shielding of the magnetic pulse, while preserving the required electric field properties. A prototype made from aluminized Kapton (a) showed negligible shielding, while simulation studies using a wire array electrode modeled in ANSYS (b) show no significant systematic effects and sufficient uniformity of the field in the storage region. . . . .	52
2.21 Positron energy distribution $N$ , rate of change of asymmetry $\partial_\Psi A$ evaluated for spin pointing opposite and along the momentum, respectively for Phase I and II. The g-2 precession is deduced from the asymmetry ( $A_{fb}$ green) between the energy distributions, while the EDM signal is proportional to the directional asymmetry (red). The spectrum is divided into two to improve the visibility of the plot. The arrows point to the mean rate of change of asymmetry $\tilde{\alpha}$ and the fraction of the positron spectrum at the optimal threshold using the T-method. . . . .	53
2.22 The study on systematics has two main parts: (a) developing and crosschecking the results extracted analytically and (b) extracting limits on the relevant parameters. . . . .	56
2.23 Limit on the longitudinal $E$ -field, $E_z$ , when considering alternating CW/CCW injections, where the difference in mean momentum averaged over all injected muons for injections of CW and CCW beams is fixed at $\Delta p = 0.5\%$ . a) Shows the limit as a function of the initial phase difference $\Phi_0^{cw} - \Phi_0^{ccw}$ . The horizontal dashed line indicates the limit coming from $\Delta$ , keeping all other parameters equal between the two injection modes. The brown area is the constraint that results from the difference in the initial phase at $\Delta p = 0\%$ . The green area and its thick dashed line edge show the combined limits of the two effects. b) Shows the limit as a function of the difference in $E$ - or $B$ -field for CW and CCW orbits, at various times. $\Delta F = 2(F^{cw} - F^{ccw})/(F^{cw} + F^{ccw})$ , where $F \in \{B_z, \tilde{E}_\rho\}$ , while the difference in initial phases was fixed at 25 mrad. . . . .	56
2.24 ‘Short’ term muEDM schedule, with highlighted the 6 main milestones up to the <i>long shutdown</i> . Milestones: 1) off-axis injection; 2) generation of the entrance trigger; 3) generation of the pulsed B field; 4) detection of $g - 2$ ; 5) adjust $g - 2$ to zero; 6) EDM data taking. . . . .	58
2.25 ‘Long’ term muEDM schedule, with the different phases up to the end of the experiment. . . . .	58
3.1 This figure illustrates the Bethe-Bloch formula [PDG], a vital tool in particle physics, depicting how charged particles lose energy when traversing through matter. . . . .	64

3.2	Curve for the average energy deposit in a BC400® scintillator for $\mu^+$ (3.2a) and $e^+$ (3.2c) at 28 MeV/c. Clearly visible is the linearity of the energy loss for the $e^+$ with thickness. This linearity is lost for the $\mu^+$ : first, we see an exponential trend and then a plateau when $E_{dep} \approx E_k$ and the $\mu^+$ is stopped. The distribution of the energy deposit slowly transitions from a Landau to a Gaussian: (3.2b) is an example of the first type; (3.2b) is an example of the transition. . . . .	65
3.3	Detail on the lower section of the curve for the average energy deposit in a BC400® scintillator for $\mu^+$ at 28 MeV/c and 128 MeV/c. . . . .	65
3.4	asd . . . . .	66
3.5	asd . . . . .	67
3.6	. . . . .	67
3.7	Average scattering angle in different thicknesses of BC400® scintillator for $\mu^+$ at 28 MeV/c and 128 MeV/c. From these plots was found $X_0 = (54.33 \pm 0.12) \text{ g/cm}^2$ . . . . .	67
3.8	muEDM: <i>gate</i> scintillator readouts . . . . .	68
3.9	muEDM: sketch of the <i>telescope</i> . . . . .	68
3.10	Sketch of the telescope of Silicon Pixel Sensors used to study the multiple scattering in different materials. The samples are held in the position of the 'target'. In this sketch, the beam is coming from the left side. . . . .	70
3.11	Picture of the setup and one of the MuPix10 (grey-colored square) mounted on the PCBs. . . . .	70
3.12	Timing and the 2D plot for time and pulse height for 120 MeV/c particles. The three rows show what happens when inserting degraders of different thicknesses. With no degrader, the $\pi$ peak is visible at lower TOF. When increasing the thickness, the contributions of $\pi$ and $\mu$ decrease. It is important to note that the $e$ and $\mu$ distribution overlap. In gray the distribution of the previous plot to make a comparison. . . . .	71
3.13	The angular distributions show: the full distribution (black), the distribution after cuts in the distance at the sample's plane (red), the distribution after acceptance correction (blue), and the fitted function for telescope characterization (violet). . . . .	72
3.14	Results of the analysis of the different samples and confronted with predictions using the Highland formula and GEANT4. The details are not easy to read but the 'bring-home' message is that the results are somewhat in agreement and some improvement are planned on the analysis. . . . .	73
3.15	muEDM: Thin scintillators for the beamtimes. . . . .	74
3.16	muEDM 2022: entrance preparations . . . . .	75
3.17	muEDM 2022: entrance setup . . . . .	75
3.18	muEDM:2022 triggers . . . . .	76
3.19	muEDM:2022 installation . . . . .	77
3.20	muEDM:2022 gate efficiency . . . . .	78
3.21	muEDM:2022 time resolution . . . . .	79
3.22	muEDM:2022 optical crosstalk . . . . .	81
3.24	Simulation results for different nominal magnetic fields at the center of the PSC solenoid. (a) shows the relative permittivity of the injection tubes as a function of the distance along the tube, starting from the upstream position and going towards the downstream position inside the bore of the PSC magnet. (b) shows the magnetic field strength along the middle of the injection tube. Note that the two significant features are a result of a reduced wall thickness of the steel tube at these positions, for the mechanical support. . . . .	83
3.25	The support structure was developed to reduce stresses to the injection channel and the PSC magnet: (a) shows the ANSYS® studies, (b) the whole setup, (c) and (d) the detail of the US and DS detectors. . . . .	84

3.26 One of the ToF detector prototypes fabricated in 2023 with four readout channels. The detector is mounted on the downstream detector module which is attached to the injection tubes. . . . .	85
3.27 muEDM 2023: TOF momentum spread. . . . .	86
3.28 muEDM 2023: TOF detector soldering. . . . .	86
3.29 Charge integral of the 8-segmented beam monitor as extracted online in WaveDAQ GUI. Left: overlay of all the corner 2 mm thick tiles. Right: overlay of all the middle 2 mm thick tiles. The peak on the right corresponds to positrons, while the broader peak on the left corresponds to muon energy depositions. . . . .	87
3.30 The online rates in kHZ in 2 mm thick tiles of the 8-segmented beam monitor. The rates were recorded for three x-positions left and right of the nominal detector position (the center images). The top two rows show the rates for the beam monitor in "0 deg" position, while the bottom two rows show the data for the "180 deg" rotated monitor. Two rows for each detector rotation correspond to the two trigger configurations (see text), with the upper row being just the rate of a channel, and the bottom row requiring a hit in the channel and no hits in the thicker back scintillator plane. The beam is entering the image plane along the line of sight. . . . .	88
3.31 The online rates in kHZ in 2 mm thick tiles of the 4-segmented beam monitor. The rates were recorded for two x-positions left and right of the nominal detector position (the center images). The top two rows show the rates for the beam monitor in "0 deg" position, while the bottom two rows show the data for the "180 deg" rotated monitor. Two rows for each detector rotation correspond to the two trigger configurations (see text), with the upper row being just the rate of a channel, and the bottom row requiring a hit in the tile (with a signal in both channels) and no hits in the thicker back scintillator plane. The beam is entering the image plane along the line of sight. . . . .	89
3.32 The <i>short</i> and <i>long</i> configurations, used to extract the main parameters of the TOF detectors. . . . .	90
3.33 Time difference for the 100 $\mu\text{m}$ detector pair, mounted om the <i>short</i> (a) and <i>long</i> (b) configuration. In red the result of taking two fixed channels, in blue taking the first channel to be triggered in the detectors. . . . .	91
3.34 (a) Time of flight of positrons and muons measured with 50 $\mu\text{m}$ upstream and 100 $\mu\text{m}$ downstream detectors and (b) the same setup with muons at $\pm 750 \text{ mT}$ . Due to energy losses in air and the entrance trigger, the muon peak is fitted with an exponentially modified Gaussian instead. . . . .	91
3.35 In (a) the TOF means for the five detector setups are plotted against the B field settings while in (b) the change of the mean ToF versus the change of the magnetic field for consecutive measurements. A detector setup corresponds to the upstream (US) and downstream (DS) detectors for the Time of Flight measurement (#0 is the old 200 $\mu\text{m}$ detector). . . . .	93
4.1 In (a) and (b) the CAD view of the detector design while in (c) the details on the ribbon structure and the fiber <i>cladding</i> . . . . .	96
4.2 The Large Prototype . . . . .	98
4.3 Fiber tracker read-out column-wise by SiPM arrays . . . . .	98
4.4 Typical light spectrum (threshold 0.5 phe) measured by a single 250 $\mu\text{m}$ square multiclad fiber ( $\approx 50 \text{ cm}$ length) read out by a SiPM on each end (combined in logic AND) upon the passage of a MIP. . . . .	99
4.5 Timing distribution of a single fiber with a double Gaussian fit (solid line). . . . .	100

4.7	Two particles impinging 2 mm apart on the same ribbon. Using 250 $\mu\text{m}$ fibers and having no pixelation on the readout, the spatial resolution is $\sigma \approx 100 \mu\text{m}$ (p5 and p8). This value was obtained with a fit to <i>plo2+gauss+gauss</i> and with a bin width of 125 $\mu\text{m}$ (half a fiber width) . . . . .	102
4.8	In case of a particle impinging on the same position, the timing of the photon can be used to distinguish the two hits. For 20 cm fibers, the limit seems to be 3 ns to 5 ns. This value refers to the time the optical photon interacts with the SiPM. The actual distribution will be larger. . . . .	102
4.9	An example of a GEANT4 simulated event. In green the optical photons reflecting inside the fiber ribbons; in blue the trajectory of the positron. Keeping the same color scheme, the longitudinal SciFi is green while the transverse one is blue. . . . .	103
4.10	Looking at the position for the photons arriving at the readout for both SciFi layers. . . . .	104
4.11	Looking at the relationship between time and longitudinal position for the inner layer makes it possible to see if the particle is spiraling up or down. . . . .	104
4.12	The information from the joint use of transverse position and time, given by the outer layer, is more complex but essential (and a unique feature of this detector) in understanding the particle trajectory. . . . .	104
4.13	Relation between the direction of the fibers and the projection along the $\hat{x}$ ; $\hat{y}$ axes of the resolutions. The intrinsic resolutions are here assumed $\delta_x = 1 \text{ mm}$ ; $\delta_y = 10 \text{ mm}$ . In (a) Some specific orientations of two overlapping ribbons are shown and indicated in (b). . . . .	106
4.14	In a planar configuration, the angle at which the fibers run translates directly to the angle at which the ribbon is oriented. In a cylindrical geometry, a fiber running at a given angle will complete a different number of turns depending on the dimensions of the cylinder. in (b) a 3D view with two layers in opposite directions. To make it easier to read the fibers are wider than in reality. . . . .	107
4.15	The results when considering two layers in a cylindrical geometry keeping the requirement $\Delta T = 1$ : 4.15a shows the projected uncertainties; 4.15b shows the angle of the inner layer. . . . .	108
4.16	Key parameters as a function of the outer layer's angle keeping 1 turn difference between the two layers and rounding the angles to multiples of 5 deg. . . . .	109
4.17	muEDM: CHeT GEANT4 . . . . .	110
4.18	muEDM: CHeT GEANT4 and <i>ghost</i> hits . . . . .	110
5.1	Sketch of the MEG II apparatus with a $\mu^+ \rightarrow e^+\gamma$ event. . . . .	115
5.2	The PDE of the MPPCs was found to be deteriorating due to radiation damage (a). The process of annealing carried out before every physics run, allows the recovery of the PDE (b). . . . .	117
5.3	Timing (a) and energy (b) resolutions of the XEC obtained for 55 MeV $\gamma$ s generated via the CEX. The results are for the central region of the detector ( $u \in [-10, 10] \text{ cm}$ and $v \in [-30, -10] \text{ cm}$ ). . . . .	119
5.4	The specific profile of the axial magnetic field of COBRA is the result of the 5 different coils. The aim is to sweep the particles at higher $ z $ with an independent radius. . . . .	119
5.5	CDCH with all the wires mounted. The light catching the wires highlights the stereo design of the detector. . . . .	120
5.6	CDCH: Michel fit . . . . .	122
5.7	Picture of the timing counter tiles. . . . .	124
5.8	A pTC tile: $120 \times 40/50 \times 5 \text{ mm}^3$ of BC422 <sup>®</sup> read by arrays of 6 AdvanSiD $3 \times 3$ mm SiPM. . . . .	124
5.9	Hit rates map of the pTC at $R_\mu = 5 \times 10^7 \mu/\text{s}$ during the 2022 run. Each circle indicates a counter. . . . .	124

5.10	Detail sketch of the $\pi E5$ beamline at PSI . . . . .	127
5.11	Beam profile at COBRA center for a stopped muon rate of $R_\mu = 5.3 \times 10^7 \mu/\text{s}$ at $I_p = 2.2 \text{ mA}$ . . . . .	127
5.12	G4BEAMLINE simulation of few tracks (orange lines) in the $\pi E5$ beamline. It's possible to recognize the elements discussed previously and showed in Fig 5.10. . . . .	128
5.13	Comperison of the results from the G4BEAMLINE and MAD-X simulations for $\pi E5$ . While the agreement is very good for most of the beamline, there is some difference inside COBRA. This is due to the difficulty in describing the highly 'non-standard' magnet. Given MAD-X has no particle interaction, the comparison is fair only when removing all materials from the beamline in the G4BEAMLINE simulation. . . . .	129
5.14	Picture of the BC400 target. Clearly visible is the dot pattern on both the target and carbon fiber frame. Six holes, admittedly less visible, are located on the axes of the ellipse. . . . .	130
5.15	Once all the MEG II detectors are combined, the usual data-taking looks something like this. These are just examples taken from different events. . . . .	132
5.16	The sensitivity reached by MEG II has a strong dependence on the DAQ livetime, as shown in (b), and the resolution/efficiency obtained, shown in (a). . . . .	133
5.17	Sketch of the ion source of the CW. . . . .	133
5.18	The first schematic (a) is presented just for reference, given the usual depiction of a CW circuit. The second (b) shows the CW circuit and the capacitive coupling to the RF driver while the third (c) shows the internal structure of a rectifier stack ( <i>ass'y</i> ). . . . .	134
5.19	Block diagram of the driver . . . . .	135
5.20	The Q-factor is the ratio of blind to dissipated power. Via this number is possible to evaluate the energy dissipated as heat running the machine. If it is too low the machine cannot operate correctly. . . . .	136
5.21	View of the CW after the extraction from the external volume. This volume contains SF <sub>6</sub> which is used as a gaseous dielectric medium and needs to be evacuated before the extraction. . . . .	136
5.22	View of the source of the CW machine. . . . .	137
5.23	Top view of the CW after the removal of a few <i>corona rings</i> . Here we can see all the elements of a CW circuit: red - the resistors on top; metallic rings on the central tube - the capacitors; blue and metallic cups - the resistance and capacitors of the rectifiers, which run vertically. . . . .	137
5.24	Picture of the control panel for the CW machine. . . . .	138
5.25	After close inspection we found burning marks on two rectifiers' ass'y (5.25a). These were removed (5.25b) and carefully inspected (5.25c). The only salvageable part of the rectifiers were the aluminum capacitors, which we cleaned from burning residuals, while all diodes and resistors had to be exchanged. . . . .	139
5.26	The rectifiers are made of three elements: diodes; aluminum capacitors; resistors (5.26a). Only the capacitors were salvageable: we re-assembled the rectifiers with new diodes and resistors (5.26b; 5.26c). . . . .	140
6.1	Diagram of the CEX measurement, with the back-to-back photons configuration to define the XEC patch via the BGO positioning (6.1a) Picture of the BGO detector (6.1b) Picture of the BGO mover (6.1c). . . . .	143
6.2	CEX 2021: LH2 circuit. . . . .	145
6.3	Pictures of the Liquid Hydrogen target outside $\pi E5$ and after the insertion in COBRA. . . . .	146
6.4	The XEC time resolution is evaluated with the help of auxiliary detectors . . . . .	147
6.5	Timing (a) and energy (b) resolutions of the XEC obtained for 55 MeV $\gamma$ s generated via the CEX. The results are for the central region of the detector ( $u \in [-10, 10]\text{cm}$ and $v \in [-30, -10]\text{cm}$ ). . . . .	148

6.6	Position dependence of the reconstructed 55 MeV $\gamma$ from $\pi^0 \rightarrow \gamma\gamma$ . . . . .	148
6.7	A new cell was designed to be faster in the cooling/liquefaction and mountable. . . . .	150
6.8	Pictures taken while mounting the Lakeshore® sensors. . . . .	150
6.9	Picture of the improved heat shielding of the system. The multi-layer super insulation was added to the Cu rod (a) the outlet was designed to be under vacuum and with a nozzle of a transferring line for He (b) and the copper shielding of the whole target can be seen in (c). . . . .	151
6.10	To study the behaviour and stability of the system, additional Lakeshore® sensors were placed on the inlet/outlet He lines (a) and both on the CU rod and the cell (b). The additional sensor on the copper part of the cell, although not easy to place, allowed us to ensure the thermal connection. . . . .	153
6.11	The ‘compact’ version of the LH <sub>2</sub> target is shown in (a), with the Cu shield on the cooler, the new vetronite parts and the super-insulation on the different sections. An additional layer of super-insulation was placed on the cell itself (b) to reduce the heat-lode due to radiation of the vacuum pipe. . . . .	153
6.12	This plot illustrates the outcome of a successful liquefaction process. The azure line depicts the fill level of the cell. The repeated drops in the line signify that the test aimed to decrease the Helium flux while maintaining the presence of liquid Hydrogen. . . . .	154
6.13	Short Caption . . . . .	155
6.14	Dewar usage in 2022 and 2023. . . . .	156
6.15	Number of triggered events during Charge EXchange data taking in 2021 2022 and 2023. Notice the lack of events in 3 patches in 2021 due to the low dutycycle of the LH <sub>2</sub> target. For 2022 and 2023, the required statistics was collected and exceeded. . . . .	157
6.16	Measured hydrogen pressure in the target and helium pressure in the dewar used for cooling during the different CEX data takings. The beam was ON (red line) when the target was considered ‘full enough’. This value changed as a consequence of the different upgrades of the target and was evaluated by measuring the XEC trigger rate. . . . .	158
7.1	Shape of the cross-section as a function of the proton energy [X17:crossections] with two resonances. . . . .	161
7.2	Energy levels and transitions of <sup>8</sup> Be . . . . .	161
7.3	The planar geometry is the one chosen in all searches to date. In both versions, the energy is measured with plastic scintillators while the position is measured with a multi-wire proportional chamber, later upgraded to double-sided silicon strip detectors. . . . .	162
7.4	X17: Vacuum chamber and target mechanics . . . . .	163
7.5	X17:BGO LiF and LIPON . . . . .	164
7.6	X17: Auxiliarly detecotrs . . . . .	165
7.7	Position of the proton beam at 500 keV when changing the current in the dipoles (the vertical dipole V and only one of the two horizontal dipoles H). In the first row, H is changing and the beam moves diagonally. In the second row, V moves the beam on the perpendicular diagonal. . . . .	166
7.8	Focus of the proton beam at 500 keV when changing the <i>extraction voltage</i> of the CW: values in the range 6 ÷ 15 keV. Is clearly visible for extreme values the beam barely reaches the crystal. . . . .	167
7.9	Track density vs ngoodhits. Three types of tracks can be observed with increasing ngoodhits and decreasing density, tracks not exiting the chamber, tracks exiting it once and tracks exiting twice. The poorest quality tracks, in the red dashed rectangle, are rejected. . . . .	168

7.10	$E_{sum}$ distributions for the X17 data ( $E_{sum}$ sideband region, as defined in 7.3.5) before (black dots) and after (red dots) the cuts specific for removing fake pairs, described in the text. . . . .	169
7.11	Total efficiency on X17 events (trigger, acceptance, and reconstruction efficiency) as a function of the angle of the reconstructed X17 momentum direction to the beam axis. . . . .	169
7.12	X17: Angular correlations . . . . .	171
7.13	Opening angle resolution (upper plots) and invariant mass resolution (lower plots) for MC IPC18 events, fitted to a double Gaussian. On the left there is the distribution obtained without the angle correction, on the right the one with the angle correction. . . . .	172
7.14	Opening angle resolution (upper plots) and invariant mass resolution (lower plots) for MC X17 events, fitted to a double Gaussian. On the left there is the distribution obtained without the angle correction, on the right the one with the angle correction. . . . .	172
7.15	Opening angle resolution for IPC18 (upper plots) and X17 (lower plots) MC, fitted to a double Gaussian. On the left, the distribution obtained without vertexing, and on the right the one with vertexing. . . . .	173
7.16	Distribution of the reconstructed vertex position positrons (left) and electrons (right) on X17 data. . . . .	173
7.17	Y vertex distribution fitted to the MC: a 60%-40% proportion has been assumed for EPC/IPC. . . . .	173
7.18	Blinded signal region and sidebands in the $E_{sum}$ vs $\theta_{rel}$ plane. . . . .	174
7.19	The binned likelihood fit of a ToyMC sample. It uses 2-dimensional PDFs for $E_{sum}$ and $\theta_{rel}$ , presenting ToyMC data (black), the best fit (blue), and summed background PDFs (red). . . . .	176
7.20	Example of the profile likelihood ratio (a) and of the full FC construction (b) for 500 X17 events in an ideal case. In (c) the median 90% CLs and best fits expected as a function of the true X17 yield. . . . .	178
7.21	History of the CW beam current during X17 data-taking in 2023. In the second plot, the CW current is used to normalize the BGO rate, which is a way to evaluate the stability of the target itself. . . . .	179
7.22	BGO spectra at $E_p = 500$ MeV for a normal and rotated target. The two spectra are compatible. . . . .	180
7.23	BGO spectra taken at $E_p = 500$ MeV (Black), and $E_p = 1080$ MeV (Blue) on LiPON. The second spectrum should be peaked at 18.15 MeV (+500 keV) but is not. The 17.6 MeV line seems to be prevalent. . . . .	180
7.24	X17: XEC data in May 2023 . . . . .	181
7.25	SEM EDX LiPON analysis . . . . .	182
7.26	X17: Small LiPON target setup . . . . .	183
7.27	X17: Small LiPON target . . . . .	183
7.28	X17: Al and Cu support spectra . . . . .	184
7.29	X17: Cu support spectra at 500 and 1080 keV . . . . .	184
7.30	Example of the data taken in Feb. 2023 to study the CW beam. The top picture shows the dependence of the current measured with the Faraday Cup with collimator as a function of the Beam Blocker current with COBRA at 15%. The bottom plot shows the same plot with no collimator but with different magnetic fields. . . . .	186
A.1	Trajectory with variable parameters . . . . .	191
A.2	2D kalman linear filter . . . . .	192
B.1	BGO: intercalibration . . . . .	197
B.2	BGO: introducing the leak . . . . .	197

B.3	BGO: linear correction to the 17.6 MeV line	198
B.4	Time stability of the calibration factors: (a) 3 days, (b) start and finish of the data-taking.	199

# List of Tables

1.1	Limits for CLFV processes . . . . .	8
1.2	CLFV searches with muons . . . . .	9
1.3	EDM limits for neutron electron and muon . . . . .	13
1.4	Rates at the meson facilities . . . . .	22
2.2	Analysis method for the muEDM search . . . . .	54
2.3	Systematic effects for the muEDM search . . . . .	57
3.1	Efficiency for gate threshold . . . . .	77
3.2	Thermal noise rates at different thresholds for gate/exit scintillators. . . . .	77
3.3	Overview of the Time of Flight measurements ordered by date, displaying the upstream (US) and downstream (DS) detectors, the magnetic field of the solenoid, its position along the rails, the number of events and the slit settings for slits FS52 and FS54 for every measurement. . . . .	92
4.1	Detection efficiencies for m.i.p. . . . .	99
5.1	CDCH: resolutions . . . . .	122
6.1	Properties of the Material . . . . .	143
7.1	Efficiency of the different reconstructions. . . . .	169
7.2	Population sizes for different categories . . . . .	176
7.3	Summary of the measurements on the CW beam . . . . .	185
B.1	Collected datasets for the BGO calibration. . . . .	195
B.2	Calibration factors and standard deviations for different sample sizes. . . . .	196

# Chapter 1

## Introduction

Here we will provide an overview of the following chapters as well as define the theoretical and experimental background for this work. The first section will be dedicated to the outline of this thesis, to aid the readers. A somewhat shallow review of the particle physics searches at PSI will follow, with some in-depth dive into the subjects that are close to the core of this thesis. This will be complemented by the description of the different facilities at PSI, with a final section dedicated to the Proton Ionization Facility.

This whole chapter relies heavily on references [1] [2] and partially on [3].

### 1.1 Outline of this thesis

The structure of this Thesis might differ slightly from the norm. While most of my colleagues dedicated their work to a singular subject, like a particular detector or theory, my effort during the course of this Ph.D. has been spread on a quite large angle. At first glance, this work might seem the result of three separate projects, namely MEG, MuEDM, and muCool. In fact, the spirit in which this Thesis has been developed is orthogonal to the chapters themselves: the overall progress of muonic particle physics experiments. Given the nature of the different tasks I worked on, I included *a lot* of introductory material to guide the reader through the different sections.

- Introduction: theory, PSI facilities and key experiments
- muCool (?)
- muEDM: introduction, entrance detector, tracker
- MEG: introduction and CW, Liquid Hydrogen target, X17 search

### 1.2 Particle physics at Paul Scherrer Institute

Belonging to ETH domain and formed in 1988 as a national laboratory, the Paul Scherrer Institute (PSI) is the largest federal research institute in Switzerland. PSI hosts the world's most powerful proton accelerators, with an average power of 1.4 MW and a beam current of over 2 mA. On top of the proton facility, in the last 10 years, a neutron spallation target has been added for ultracold neutrons production. PSI is renowned for its extensive research across a wide range of scientific disciplines. With its world-class facilities and expertise, PSI plays a pivotal role in advancing our understanding of fundamental particles and their interactions, solidifying its position as a key player in the field of particle physics on a global scale. Everything discussed in this thesis is a

product of the fertile environment at this Institute and the active collaborations with universities and institutions, such as INFN, around the world.

### 1.3 Bite-size theory

The aim of this section is to define the framework in which (part) of particle physics research is moving. In particular, we will be focusing on the aspects which are relevant to the three experiments core of this thesis. The searches Beyond Standard Model (BSM) proceed in two main directions: *intensity frontier* is used to describe the test of contributions that are too small to be experimentally accessible observing large numbers of events; *precision frontier* is used when improving the accuracy of a specific parameter to test the agreement with the Standard Model (SM). Searches for charged lepton flavour violation (cLFV) or neutron permanent Electric Dipole Moment (EDM) are examples of the former type while precision Quantum ElectroDynamics (QED) tests with muonium are of the latter.

#### 1.3.1 Standard Model at low energies

In the low energy regime QED and Quantum ChromoDynamics (QCD) are essentially ‘frozen’, and the SM reduces to the standard Lagrangian

$$\mathcal{L}_{QED+QCD} = \sum_f \bar{f}(i\cancel{D} - m_f)f - \frac{1}{4}F_{\alpha\beta}F^{\alpha\beta} - \frac{1}{4}G_{\alpha\beta}G^{\alpha\beta} \quad (1.1)$$

where  $F$  and  $G$  are the electromagnetic and gluonic field-strength tensors. The sum here is on fermions of mass  $m_f$ , charge  $eQ_f$ , and color  $g_s t_f^a$ . For a lepton, this would mean  $Q_\ell = -1$  and  $t_\ell^a = 0$  while for a quark  $Q_q = 2/3$  or  $-1/3$  and  $t_q^a = \lambda^a/2$ , with  $\lambda$  Gell-Mann matrices. To compute the matrix element between two lepton states we find:

$$\langle \ell(p_2) | J_{em}^a | \ell(p_1) \rangle = \bar{u}(p_2, m_\ell) \left( F_1^{(\ell)}(q^2) \gamma^a + F_2^{(\ell)}(q^2) \frac{i\sigma^{\alpha\beta} q_\beta}{2m_\ell} \right) u(p_1, m_\ell) \quad (1.2)$$

Here  $u$  and  $\bar{u}$  are the spinors and the two states are with momenta  $p_1$  and  $p_2 = p_1 + q$  while  $F_1^{(\ell)}$  and  $F_2^{(\ell)}$  are related respectively to the electric charge and the anomalous magnetic moment (AMM). In particular, for the AMM we find

$$F_2^{(\ell)}(0) = a_\ell = \frac{(g-2)_\ell}{2} \quad (1.3)$$

Even when considering non point-like particles, like nucleons  $N \in \{p, n\}$  the form used in 1.2 holds and we find:

$$\langle N(p_2) | J_{em}^a | N(p_1) \rangle = \bar{u}(p_2, m_N) \left( F_1^{(N)}(Q^2) \gamma^a + F_2^{(N)}(Q^2) \frac{i\sigma^{\alpha\beta} q_\beta}{2m_N} \right) u(p_1, m_N) \quad (1.4)$$

Here  $Q^2 \equiv -q^2$  and, while 1.3 holds,  $F_2^{(N)}$  depends on strong dynamics. In the case of nucleons, it is often useful to introduce the *electric* and *magnetic form factors*

$$G_E^{(N)}(Q^2) \equiv F_1^{(N)}(Q^2) - \frac{Q^2}{4m_N^2} F_2^{(N)}(Q^2); \quad G_M^{(N)}(Q^2) \equiv F_1^{(N)}(Q^2) + F_2^{(N)}(Q^2)$$

It is of particular interest that, in the limit for small  $Q^2$ , the form factors can be understood as Fourier transform of extended classical ‘charge’ distributions  $\rho_i(r)$

$$F_i(Q^2) = \int d^3r e^{-iq \cdot r} \rho_i(r) = \int d^3r \rho_i(r) + \frac{1}{6} Q^2 \int d^3r r^2 \rho_i(r) + \dots$$

From this, we can write the general expression for the second moment of the charge distribution or EDM. This relation is used for example when determining the charge and magnetic radii of the proton.

$$r_i^2 \equiv \frac{1}{N} \int d^3r r^2 \rho_i(r) = -6 \frac{1}{N} \left. \frac{dF_i(Q^2)}{dQ^2} \right|_{Q^2=0}; \quad N = \begin{cases} 1 & \text{if } F_i(0) = 0, \\ F_i(0) & \text{else.} \end{cases} \quad (1.5)$$

When introducing the weak interaction we arrange fermions in *left-handed doublets* and *right-handed singlets*. We then define the *charged weak current*  $J_{cc}^\alpha$ , a similar *neutral weak current*  $J_{cn}^\alpha$  and we find

$$\mathcal{L}_{EW} = e A_\alpha J_{em}^\alpha + \frac{g}{\sqrt{2}} (W_\alpha^\pm J_{cc}^\alpha + h.c.) + g_Z Z_\alpha J_{nc}^\alpha; \quad J_{cc}^\alpha = \sum_\ell \bar{\nu}_\ell \gamma^\alpha P_L \ell + \sum_{ij} V_{ij} \bar{u}_i \gamma^\alpha P_L d_j \quad (1.6)$$

where  $g = e/\sin\vartheta_W$ ,  $g_Z = e/\cos\vartheta_W$  are the  $SU(2)_L$  coupling expressed through the Weinberg mixing angle  $\vartheta_W$ . Only the left-handed fermions are coupled (through  $P_L \equiv (1 - \gamma_5)/2$ ) and, in the sum over the quark, the Cabibbo–Kobayashi–Maskawa (CKM) matrix  $V_{ij}$  describes the flavor-changing effect. When dealing with masses much smaller than  $m_W$  and  $m_Z$  the result is the ‘effective’ Fermi theory current-current interaction

$$\mathcal{L}_{4F} = -\frac{4G_F}{\sqrt{2}} \left( J_{cc}^\alpha (J_{cc}^\alpha)^\dagger + J_{nc}^\alpha (J_{nc}^\alpha)^\dagger \right) \quad (1.7)$$

In this equation  $4G_F/\sqrt{2} = g^2/(2m_W^2)$  and using the definitions for  $J_{nc/cc}^\alpha$  we end up with the vector contact interactions. In this framework photons and gluons are the only gauge bosons and the gauge symmetry of the SM  $SU(3)_c \times SU(2)_L \times U(1)_Y$  is reduced to QCD and QED:  $SU(3)_c \times U(1)_{em}$ . We can write a 6-dimension vector operator which links 4 fermions in a generic form

$$[O_f^{XY}]_{ijkl} = (\bar{\psi}_i \gamma^\alpha P_X \psi_j)(\bar{\psi}_k \gamma_\alpha P_Y \psi_l) \quad (1.8)$$

where  $X, Y \in L, R$  and  $i, j, k, l$  are generation indices. There are many such operators because  $\psi$  could be leptons or quarks but the integration of the  $W$  and  $Z$  generates only a subset (i.g. we have no cLFV operator due to accidental symmetries). In a similar fashion, an operator will be a 6-dimension scalar when removing the  $\gamma$  matrices or a 5-dimension dipole operator including

photons and gluons:

$$[O_{f\gamma}^D]_{ij} = (\bar{\psi}_i \sigma_{\alpha\beta} P_R \psi_j) F^{\alpha\beta}; \quad [O_{qG}^D]_{ij} = (\bar{\psi}_i \sigma_{\alpha\beta} G^{\alpha\beta} P_R \psi_j) \quad (1.9)$$

### 1.3.2 Beyond Standard Model at low-energy

There is no shortage of BSM models and one way of (roughly) classifying them would be by the masses and coupling strengths of the particles they introduce. Light BSM particles have small couplings to SM particles, which would explain the small contribution to physical observables. Prominent examples are dark photons, axions and Axion-Like Particles (ALPs). Axions in particular were proposed as a solution to the small value of the Charge and Parity (CP) violating QCD  $\vartheta$  parameter. When discussing Heavy BSM particles we can follow the process of ‘integration’ shown for  $W$  and  $Z$  in this section, in an Effective Field Theory (EFT) approach. As long as the BSM physics respects QED and QCD gauge symmetry and involves ‘large’ mass scale  $\Lambda$  ( $m_b < \lambda < m_W$ ), it can be integrated out. This way we add higher-dimensional operators to the SM Lagrangian, obtaining a Low-energy Effective Field Theory (LEFT)

$$\mathcal{L}_{LEFT} = \mathcal{L}_{QED+QCD} + \frac{1}{\Lambda} \sum_i C_i^{(5)} O_i^{(5)} + \frac{1}{\Lambda^2} \sum_i C_i^{(6)} O_i^{(6)} + \dots \quad (1.10)$$

To parameterize low-energy observables and measuring (or constraining) associated parameters is not an easy task: a prime example would be the Michel decay (which we will discuss in the following sections), generalized in terms of scalar vector and tensor contact interactions or the similar effort for the cLFV  $\mu \rightarrow e\gamma$  and  $\mu \rightarrow eee$  with the lepton-flavor-violating contact interactions. If the BSM physics appears at a scale larger than  $m_W$ , we first have to develop a Standard Model Effective Field Theory (SMEFT). The details on how this is achieved are outside our purpose but, including all the different gauge fields, Higgs doublet, left-handed doublets, and right-handed singlet (respecting the  $SU(3)_c \times SU(2)_L \times U(1)_Y$  gauge symmetry) we find

$$\mathcal{L}_{SMEFT} = \mathcal{L}_{SM} + \frac{1}{\Lambda} (C^{(5)} O^{(5)} + \text{h.c.}) + \frac{1}{\Lambda^2} \sum_i C_i^{(6)} O_i^{(6)} + \dots \quad (1.11)$$

We can now re-evaluate the matrix in 1.2 element using 1.11 instead of 1.1. We will leave the details of the calculation under the hood but the result we get is the following

$$\begin{aligned} \langle f(p_2) | J_{em}^\alpha | f(p_1) \rangle = \bar{u}(p_2, m_f) & \left( F_1^{(f)}(q^2) \gamma^\alpha + \left( F_2^{(f)}(q^2) - i\gamma_5 F_3^{(f)}(q^2) \right) \frac{i\sigma^{\alpha\beta} q_\beta}{2m_f} + \right. \\ & \left. F_4^{(f)}(q^2) \frac{1}{m_f^2} (q^2 \gamma^\alpha - 2m_f q^\alpha) \gamma_5 \right) u(p_1, m_f) \end{aligned} \quad (1.12)$$

It is of interest that the CP-violating  $F_3$  form factor is linked to the EDM of the lepton  $d_f$

$$d_f = \frac{eF_3^{(f)}(0)}{2m_f} \quad (1.13)$$

In the SM,  $d_f$  receives contributions from quarks at 3-loops and leptons at 4-loops (induced by CP-violation in the CKM). When considering protons and neutrons there is an additional contribution from the CP violating QCD  $\vartheta$  parameter (found to be extremely low constraining the neutron EDM). For completeness sake,  $J_{cc}^\alpha$  give rise to matrix elements between different  $SU(2)$  doublets, like  $(\nu_\ell, \ell)$  or  $(p, n)$ . This leads to muon and beta decay or quasi-elastic scattering  $\ell p \rightarrow \nu_\ell n$ .

### 1.3.3 Muon

The muon is the lepton with the intermediate mass of  $m_\mu \approx 105.66$  MeV and it is unstable. The dominant process is the Michel decay  $\mu \rightarrow e\nu\bar{\nu}$  which translates to a lifetime of  $\tau \approx 2.2 \mu s$ . We already hinted at the fact that this decay is mediated by the charged current  $J_{cc}^\alpha$  through  $\langle \nu_\mu | J_{cc}^\alpha | \mu \rangle \langle e | (J_{cc})_\alpha^\dagger | \nu_e \rangle$  which in EFT corresponds to  $(\bar{\nu}_\mu \gamma^\alpha P_L \mu)(\bar{e} \gamma_\alpha P_L \nu_e)$ . The resulting EFT Lagrangian is

$$\mathcal{L}_{Fermi} = -\frac{4G_F}{\sqrt{2}}(\bar{\nu}_\mu \gamma^\alpha P_L \mu)(\bar{e} \gamma_\alpha P_L \nu_e) + \text{h.h} + \mathcal{L}_{QED+QCD} \quad (1.14)$$

When evaluating the lifetime we get an equation that contains, in  $\Delta q$ , all corrections induced by our Lagrangian: electron mass effect, higher order QED correction, and hadronic corrections.

$$\frac{1}{\tau_\mu} \equiv \Gamma_\mu = \Gamma_0(1 + \Delta q) = \frac{G_F^2 m_\mu^5}{192\pi^3}(1 + \Delta q) \quad (1.15)$$

Unfortunately, QCD corrections are non-perturbative for  $q^2 \sim m_\mu^2$  and are the leading theoretical uncertainty. These corrections are known at NNLO. Precision measurement of the muon lifetime is key for consistency checks of the SM. In fact  $G_F$  can be related to  $m_W$  and  $m_Z$

$$\frac{4G_F}{\sqrt{2}} = \frac{g^2}{2m_W^2}(1 + \Delta r) = \frac{2\pi}{\sin^2 \vartheta_W m_W^2}(\Delta r) \quad (1.16)$$

Here  $\Delta r$  are the SM corrections and  $\sin^2 \vartheta_W = 1 - m_W^2/m_Z^2$ .

On top of the Michel decay, we also have radiative and rare decays

$$\mu \rightarrow e\nu\bar{\nu}\gamma, \quad \mu \rightarrow e\nu\bar{\nu}e^+e^- \quad (1.17)$$

for which we have  $B(\mu \rightarrow e\nu\bar{\nu}\gamma) \sim 1.3 \times 10^{-2}$  (for  $E_\gamma > 10$  MeV) and  $B(\mu \rightarrow e\nu\bar{\nu}ee) \sim 3.6 \times 10^{-5}$ . At last, we arrive at the ‘golden’ channels for cLFV studies:

$$\mu \rightarrow e\gamma, \quad \mu \rightarrow eee, \quad \mu^- \stackrel{A}{Z}N \rightarrow e^- \stackrel{A}{Z}N \quad (1.18)$$

With non-vanishing neutrino masses, the branching ratios for these processes are expected to be below  $10^{-50}$ . To extract constraints on BSM physics from the branching ratios we can mostly use standard perturbative methods with the Lagrangian 1.10. For the muon conversion, additional precautions are needed due to the nuclear matrix elements  $\langle \stackrel{A}{Z}N | J | \stackrel{A}{Z}N \rangle$  as well as the study of the Decay In Orbit (DIO), electrons for which the energy spectrum was modified by the nuclear recoil.

The last two properties of interest of the muon are the AMM (eq. 1.3) and EDM (eq. 1.13). After the results of the G-2 experiment at Fermi National Accelerator Laboratory (FERMILAB),

there is some tension on the first between experimental results and theory. For the EDM the SM value is zero for practical purposes and a non-vanishing result would be a clear indication of BSM. We will further discuss the muon EDM.

### 1.3.4 Muon decay

When using a charge-changing Hamiltonian characterized by fields with define chirality [5], the general matrix element of the muon decay can be written as [7]

$$M = 4 \frac{G_F}{\sqrt{2}} \sum_{\substack{\gamma=S,V,T \\ \varepsilon,\mu=R,L}} g_{\varepsilon\mu}^{\gamma} \langle \bar{e}_{\varepsilon} | \Gamma^{\gamma} | (\nu_e)_n \rangle \langle (\bar{\nu}_{\mu})_m | \Gamma_{\gamma} | \mu_{\mu} \rangle \quad (1.19)$$

In this definition, we find:  $\gamma$  indicates a 4-scalar, 4-vector or 4-tensor;  $\Gamma$  Dirac (or Pauli) matrices;  $\varepsilon, \mu$  indicate the chirality of the spinors;  $m, n$  the chirality of the neutrinos. This means that the physical interpretation of  $g_{\varepsilon\mu}^{\gamma}$  is quite straightforward:  $n_{\gamma} |g_{\varepsilon\mu}^{\gamma}|^2$  is the probabilit of a  $\mu$ -handed muon decaying in a  $\varepsilon$ -handed electron by the interaction  $\Gamma^{\gamma}$  ( $n_{\gamma}$  are required for the correct normalization). In this picture, the SM corresponds to  $g_{LL}^V = 1$  with all other couplings to 0.

**Observables** Neglecting radiative corrections, we find the differential decay probability: with reduced energy in  $[x, x + dx]$ ; along  $\hat{x}_3$  with an angle  $[\vartheta, \vartheta + d\vartheta]$  with respect to the muon polarization  $\mathbf{P}_{\mu}$ ; spin along  $\hat{\zeta}$ .

$$\frac{\partial^2 \Gamma}{\partial x \partial \cos \vartheta} = \frac{m_{\mu}}{4\pi^3} W_{e\mu}^4 G_F^2 \sqrt{x^2 - x_0^2} \cdot \{F_{IS}(x) \pm P_{\mu} \cos \vartheta F_{AS}(x)\} \cdot \{\hat{\zeta} \cdot \mathbf{P}_e(x, \vartheta)\} \quad (1.20)$$

Here,  $W_{e\mu} = \max(E_e) = (m_{\mu}^2 + m_e^2)/2m_{\mu}$  is the maximum  $e^{\pm}$  energy and  $x = E_e/W_{e\mu}$  is the reduced energy ( $x_0 = m_e/W_{e\mu}$ ). This spectrum has both an isotropic ( $F_{IS}$ ) and anisotropic part ( $F_{AS}$ ). The electron polarization  $\mathbf{P}_e(x, \vartheta)$  can be parametrized by *Michel parameters*, which are combinations of the coupling constants  $g_{\varepsilon\mu}^{\gamma}$ . If the neutrinos' and  $x_0$  are neglected, 1.20 becomes

$$\frac{\partial^2 \Gamma}{\partial x \partial \cos \vartheta} \sim x^2 \left\{ 3(1-x) + \frac{2\rho}{3}(4x-3) + 3\eta x_0 \frac{(1-x)}{x} \pm P_{\mu} \xi \cos \vartheta \left[ 1 - x + \frac{2\delta}{3}(4x-3) \right] \right\} \quad (1.21)$$

Here  $\vartheta$  is the angle between the electron momentum and the muon spin and  $x \equiv 2E_e/m_{\mu}$ . In the SM we get the following, in which we find the total rate used in 1.15.

$$\frac{\partial^2 \Gamma}{\partial x \partial \cos \vartheta} = \frac{G_F^2 m_{\mu}^5}{192\pi^3} [3 - 2x \pm P_{\mu} \cos \vartheta (2x - 1)] x^2 \quad (1.22)$$

The way the  $g_{\varepsilon\mu}^{\gamma}$  are connected to the nine decay parameters [3, 10], or the 10 intermediate quantities we can measure [3], is outside the purpose of this short review. The bottom line is that a 20-dimensional space of the complex  $g_{\varepsilon\mu}^{\gamma}$  can be mapped to a 10-dimensional space. Unfortunately, many of these parameters are intertwined, and (generally) the precise measurement of individual parameters does not give conclusive information on the type of interaction. To avoid being too vague we will take an example from [2]. The rate  $S$  of the reaction  $\nu_{\mu} e^- \rightarrow \mu^- \nu_e$ , normalized to the rate predicted by  $V - A$  and assuming a negative helicity for  $\nu_{\mu}$ , has been found close to 1 [17].

$S$  depends on five coupling constants  $\{g_{LL}^v, g_{RL}^v, g_{LR}^s, g_{RR}^s\}$  but four of these parameters are found to be small, and in first approximation, we find [7]:

$$S = |g_{LL}^v|^2; \quad |g_{LL}^s| < 2\sqrt{1-S} \quad (1.23)$$

### 1.3.5 Electric Dipole Moment

Similarly to how the permanent Magnetic Dipole Moment (MDM)  $\mu$  represents the coupling between the spin of a quantum system and an external magnetic  $\mathbf{B}$  field, the EDM  $d$  represents the coupling between the spin of and an external electric field  $\mathbf{E}$ . The Hamiltonian describing the spin dynamics, indicating the Pauli matrices with  $\sigma$ , is then:

$$\hat{H} = -\mu\hat{\sigma} \cdot \mathbf{B} - d\hat{\sigma} \cdot \mathbf{E} \quad (1.24)$$

Given that  $\hat{\sigma} \cdot \mathbf{E}$  is odd for time reversal, the existence of a non-zero EDM would violate CP symmetry. This is an interesting topic, with many implications, and key to many searches. In a magnetic field, the dynamic of a particle at rest is described by  $ds/dt = \mu \times b = \omega_L \times s$ , where  $\mu = ge/(2m)s$  is the MDM and  $\omega_L = -2\mu B/\hbar$  the Larmor precession frequency. Similarly a hypothetical EDM  $d = \eta e/(2mc)s$  results in a precession  $\omega_d = -2dE/\hbar$  in an electric field  $\mathbf{E}$ . When considering a moving particle in both fields it is useful to introduce the polarization vector  $\Pi = s/s$  and the Thomas precession  $\Omega_0$

$$\frac{d\Pi}{dt} = \Omega_0 \times \Pi, \quad \Omega_0 = -\frac{e}{m\gamma} \left[ (1 + \gamma a)\mathbf{B} - \frac{a\gamma^2}{\gamma+1}(\boldsymbol{\beta} \cdot \mathbf{B})\boldsymbol{\beta} - \gamma \left( a + \frac{1}{\gamma+1} \right) \frac{\boldsymbol{\beta} \times \mathbf{E}}{c} \right] \quad (1.25)$$

[4][5] If there is no electrical field parallel to the momentum the acceleration is purely transverse so we get the following motion, with  $\Omega_c$  the cyclotron frequency.

$$\frac{d\boldsymbol{\beta}}{dt} = \Omega_c \times \boldsymbol{\beta}, \quad \Omega_c = -\frac{e}{m\gamma} \left( \mathbf{B} - \frac{\gamma^2}{\gamma^2-1} \frac{\boldsymbol{\beta} \times \mathbf{E}}{c} \right) \quad (1.26)$$

The relative spin precession of a muon in a storage ring will be then given by (T-BMT [**miss-59**])

$$\begin{aligned} \boldsymbol{\Omega} = \boldsymbol{\Omega}_0 - \boldsymbol{\Omega}_c &= \underbrace{\frac{q}{m} \left[ a\mathbf{B} - \frac{a\gamma}{\gamma+1} (\boldsymbol{\beta} \cdot \mathbf{B})\boldsymbol{\beta} - \left( a + \frac{1}{1-\gamma^2} \right) \frac{\boldsymbol{\beta} \times \mathbf{E}}{c} \right]}_{\text{Anomalous precession, } \omega_a = \omega_L - \omega_c} \\ &\quad + \underbrace{\frac{\eta q}{2m} \left[ \boldsymbol{\beta} \times \mathbf{B} + \frac{\mathbf{E}}{c} - \frac{\gamma c}{\gamma+1} (\boldsymbol{\beta} \cdot \mathbf{E})\boldsymbol{\beta} \right]}_{\text{Interaction of EDM and relativistic } \mathbf{E}, \omega_a} \end{aligned} \quad (1.27)$$

The second term describes the precession due to the EDM coupling to the relativistic  $\mathbf{E}$ , perpendicular to the  $\mathbf{B}$  in which the particle is moving. The simplification shown are the result of  $p$ ,  $\mathbf{B}$  and  $\mathbf{E}$  forming an orthogonal basis, hence the scalar products are null. In the case of the E821 experiment [6], the muon *magic* momentum was chosen, simplifying eq. 1.27 and making the

anomaly precession frequency independent from the electric fields needed for beam steering.

$$p_{magic} = \frac{m}{\sqrt{a}} = 3.09 \text{ GeV}/c, \quad \boldsymbol{\Omega} = \frac{q}{m} \left[ a \boldsymbol{B} + \frac{\eta}{2} \left( \boldsymbol{\beta} \times \boldsymbol{B} + \frac{\boldsymbol{E}}{c} \right) \right] \quad (1.28)$$

In the presence of a muon EDM the plane would be tilted and a vertical precession ( $\omega_e \perp \boldsymbol{B}$ ), shifted by  $\pi/2$  to the horizontal anomalous precession, would become observable.

Paul Scherrer Institute (PSI) has been for decades at the frontier in the measurements of the neutron EDM. More on this will follow in this chapter when describing the existing limits on EDMs.

[7]

## 1.4 Experimental status

To give an exhaustive recap of the experimental development, both worldwide and at PSI, is a task we will not undertake. Here we will briefly discuss the key experiments in CLFV searches (MEG, Mu3e, Mu2e, COMET) and the nEDM experiment at PSI. This choice is driven by the experiment extensively discussed in the following chapters: muEDM; MEG II.

### 1.4.1 CLFV experiments

Process	Upper limit	reference
$\mu^+ \rightarrow e^+ \gamma$	$3.1 \times 10^{-13}$	[8]
$\mu^+ \rightarrow e^+ e^+ e^-$	$1.0 \times 10^{-12}$	[9]
$\mu^- \text{Ti} \rightarrow e^- \text{Ti}$	$1.7 \times 10^{-12}$	[9]
$\mu^- \text{Au} \rightarrow e^- \text{Au}$	$7 \times 10^{-13}$	[10]
$\mu^+ e^- \rightarrow \mu^- e^+$	$8.3 \times 10^{-11}$	[11]
$\tau^\pm \rightarrow e^\pm \gamma$	$3.3 \times 10^{-8}$	[12]
$\tau^\pm \rightarrow \mu^\pm \gamma$	$4.4 \times 10^{-8}$	[12]
$\tau^- \rightarrow e^- e^- e^+$	$2.7 \times 10^{-8}$	[13]
$\tau^- \rightarrow \mu^- \mu^- \mu^+$	$2.1 \times 10^{-8}$	[13]
$\tau^- \rightarrow e^- \mu^- \mu^+$	$2.7 \times 10^{-8}$	[13]
$\tau^- \rightarrow \mu^- e^- e^+$	$1.8 \times 10^{-8}$	[13]
$\tau^- \rightarrow e^+ \mu^- \mu^-$	$1.7 \times 10^{-8}$	[13]
$\tau^- \rightarrow \mu^- e^- e^-$	$1.5 \times 10^{-8}$	[13]
$\pi^0 \rightarrow \mu e$	$3.6 \times 10^{-10}$	[14]
$K_L^0 \rightarrow \mu e$	$4.7 \times 10^{-12}$	[15]
$K^+ \rightarrow \pi^+ \mu^+ e^-$	$1.3 \times 10^{-11}$	[16]
$K_L^0 \rightarrow \pi^0 \mu^+ e^-$	$4.4 \times 10^{-10}$	[14]
$Z^0 \rightarrow \mu e$	$7.5 \times 10^{-7}$	[17]
$Z^0 \rightarrow \tau e$	$9.8 \times 10^{-6}$	[18]
$Z^0 \rightarrow \tau \mu$	$1.2 \times 10^{-6}$	[18]

**Tab. 1.1:** Experimental upper limits for a variety of CLFV processes.

	$\mu^+ \rightarrow e^+ \gamma$	$\mu^+ \rightarrow e^+ e^- e^+$	$\mu^- N \rightarrow e^- N$
Background	Accidental	Radiative muon decay	Decay in orbit
Beam	Continuous	Continuous	Pulsed
Current limit	$3.1 \times 10^{-13} (*)$ MEG II [8]	$1 \times 10^{-12}$ SINDRUM [9]	$7 \times 10^{-13}$ SINDRUM II [19]
Planned/running	MEG II [20][21][22]	Mu3e [23][24][22]	Mu2e [25] [26][27] COMET [28][29][30][31]
Planned sensitivity	$\sim 6 \times 10^{-16}$	$\sim 10^{-16}$	$\sim \text{few} \times 10^{-17}$

**Tab. 1.2:** Overview of muon CLFV experiments.(∗) The current limit recently surpassed the one set by MEG,  $4.2 \times 10^{-13}$  [32].

## MEG

The MEG experiment [32] is designed based on two key concepts: the utilization of a liquid xenon detector (LXe) for photon detection, and the implementation of an anti-bottle magnetic field for positron tracking. Muons are stopped within a polyethylene target located at the magnet's center. The momentum of positrons is measured using a combination of drift chambers (DCH) and plastic scintillator timing counters (TC). Photon energy and direction, on the other hand, are determined in a liquid xenon volume containing over 800 photo-multiplier tubes. The measured quantities include electron and photon energies ( $E_e$  and  $E_\gamma$ ), as well as relative positions (angles  $\vartheta_{e\gamma}$ ,  $\varphi_{e\gamma}$ ) and time  $t_{e\gamma}$ . Achieving resolutions that effectively separate background signals, such as radiative muon decays, necessitates an energy resolution of  $\lesssim 1\%$  for both particles.

MEG's magnetic field is not uniform to avoid the accumulation of positrons emitted at low-pitch angles within the tracker. Instead, the magnetic field diminishes symmetrically from the center towards the periphery, pushing the particles away from the center. The specific field shape is chosen so that the track radius is proportional to the *absolute* momentum rather than the transverse momentum. This allows low-energy positrons to be discarded by positioning the detector at a sufficient distance from the magnet axis. The magnetic system of MEG, known as "COnstant Bending RAdius" (COBRA) magnets, possesses this distinctive feature.

The DCH spectrometer comprises 16 trapezoidal drift chambers filled with He-C<sub>2</sub>H<sub>6</sub>, arranged radially. The radial coordinate is determined using the timing data collected by the DCH and TC, while the z position is inferred from the induced charge on the zig-zag-shaped pads on the drift chamber sides. The momentum resolution for positrons is approximately 330 keV.

The choice of employing a liquid xenon scintillating detector for photon reconstruction is motivated by the aim to minimize passive material within the detector and achieve excellent time resolution. This choice provides a higher light yield and shorter decay time compared to other options, such as NaI crystals. The timing resolution for photon interaction time is below 100 ps.

MEG successfully gathered  $7.5 \times 10^{14}$  stopped muons between 2008 and 2013 and, as previously mentioned, established the previous world's best limit on the branching ratio of  $\mu^+ \rightarrow e^+ \gamma$  at 90% confidence level, with  $\text{BR}(\mu^+ \rightarrow e^+ \gamma) < 4.2 \times 10^{-13}$  [32].

**MEG II** The upgraded MEG II experiment was proposed to reduce the contamination due to the accidental background that could not be further reduced in MEG [20] [21]. MEG II is currently running and a whole part (Part II) of this thesis will be dedicated to this experiment.

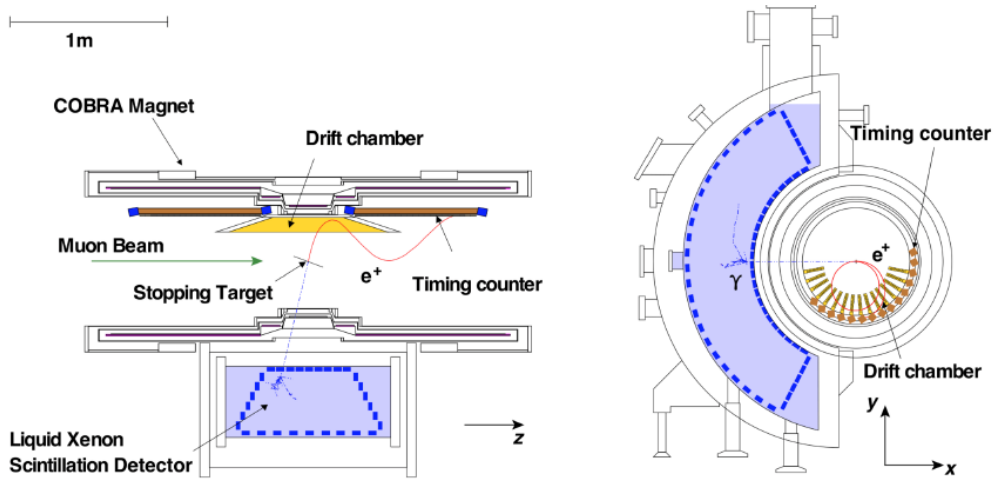


**Fig. 1.1:** Pictorial view of the MEG experiment [33][32].

### Mu3e

The goal of the Mu3e experiment is to achieve a single-event sensitivity on the  $\mu^+ \rightarrow e^+e^+e^-$  decay at the order of  $10^{-16}$  [24]. This experiment will utilize the same muon beam as MEG II and employ a thin hollow double-cone Mylar target to stop muons. The detector will be a 2 m cylinder situated within a 1.5 T magnetic field and divided into 5 sections (Fig. ??). The central station will consist of two double layers of pixel detectors and a scintillating fiber tracker, while the other four stations will consist of two layers of pixel sensors and a scintillator hodoscope. A visual representation of the Mu3e apparatus can be seen in Fig. 1.2. To mitigate the impact of multiple Coulomb scattering, which poses limitations on precise track reconstruction, the tracker will utilize High Voltage Monolithic Active Pixel (HV-MAPS) technology, designed to partially cancel out the scattering effect within half of a turn. The estimated resolutions for time and vertex are  $\sigma_t \approx 100$  ps and  $\sigma_{xy} \approx 200 \mu\text{m}$ , respectively, while the momentum resolution ranges from 100 to 400 keV for particles with momenta between 10 and 53 MeV/c [1].

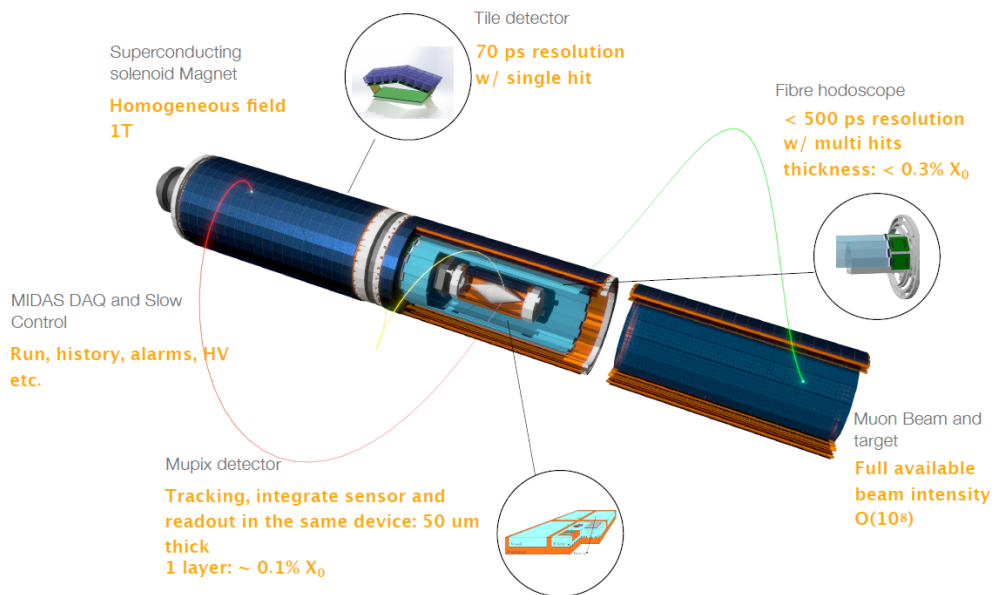


**Fig. 1.2:** Pictorial view of the Mu3e apparatus [22].

## Mu2e

Mu2e employs an 8 GeV, 25 kW pulsed proton beam with 100 ns wide bunches separated by 1.7  $\mu\text{s}$ . Figure 1.3 illustrates the experimental setup, which consists of three sections: the Production Solenoid, Transport Solenoid, and Detector Solenoid. The magnetic field layout around the production target is graded to guide the particles into the transport section. Within this section, the gradient directs the particles toward the stopping target, while the S shape reduces the background from neutral particles and enables charge sign selection using collimators. Generally, only negative muons with momenta below 100 MeV/c reach the stopping target. Downstream of the aluminum target, the straw tube tracker and crystal electromagnetic calorimeter are located. Both detectors feature a hollow-cylinder geometry, with the tracker consisting of crossed straw tubes grouped in 20 stations and the calorimeter composed of two identical disks made of CsI crystals read by SiPMs. With three years of data taking, Mu2e aims to achieve an expected sensitivity of  $R_{\mu e} < 3 \times 10^{-17}$  [26].

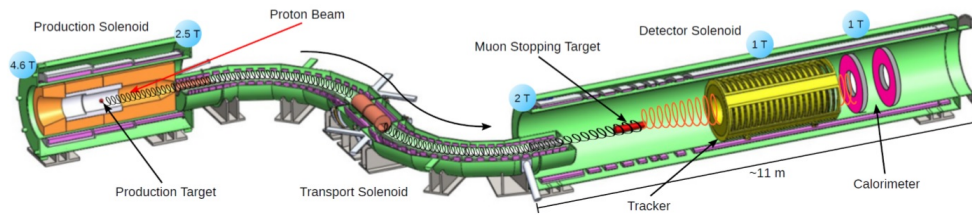


**Fig. 1.3:** Pictorial view of the muon beam-line of the Mu2e experiment [26].

The Mu2e Collaboration is also conducting preliminary investigations for the upgraded Mu2e II [34]. The proton beam intensity will be enhanced through the PIP-II upgrade [35], resulting in a higher rate of stopped muons on target, increasing from  $10^{10} \mu^-/\text{s}$  (Mu2e) to  $10^{11} \mu^-/\text{s}$ . For the upgraded Mu2e II, new detector technologies are being explored. Simulation studies indicate that with three years of data acquisition, Mu2e II is expected to achieve a sensitivity of  $R_{\mu e} < \times 10^{-18}$ .

## COMET

The COherent Muon-to-Electron Transition (COMET) experiment is currently being constructed at the Japanese Proton Accelerator Research Center (J-PARC) [31]. While sharing similarities with Mu2e, such as the use of an 8 GeV, 56 kW pulsed proton beam with a bunch separation of 1.17  $\mu\text{s}$ , COMET differs in two main aspects, as illustrated in Fig. 1.4:

- The presence of a C-shaped transport solenoid, instead of an S-shaped one, enables a tighter selection of muon momentum, at the cost of reduced beam intensity (approximately 70 %)
- An additional curved solenoid after the stopping target eliminates most of the non-interesting electrons before they reach the tracker.

The development of COMET will occur in two phases: Phase-I and Phase-II (Fig. 1.4).

**COMET Phase-I** This initial phase aims to establish the experimental techniques, study background effects, and achieve an intermediate measurement at  $R_{\mu e} \approx 7 \times 10^{-15}$ . The proton power will be limited to 3.2 kW, and a single 90° bend will be employed. The main challenge lies in the short distance between the various elements, with a cylindrical drift chamber serving as the

electron tracker. Scintillating hodoscopes will surround the tracker for triggering and timing purposes. The Technical Design Report (TDR) for COMET Phase I can be found in [31].

**COMET Phase-II** To accommodate the increased particle rate, COMET Phase-II will introduce a straw tube tracker and a crystal electromagnetic calorimeter utilizing LYSO crystals. The entire magnetic system will be expanded and refined. The two-step approach is driven by uncertainties in the understanding of the underlying physics processes. Firstly, the backward production by 8 GeV protons remains poorly known, despite results from the HARP experiment [36]. Additionally, data on muon nuclear capture in aluminum is still limited, although efforts from the Mu2e and COMET collaborations have led to the development of the AlCap experiment at PSI [37][38][39]. The AlCap collaboration aims to measure the rate and spectra of particles emitted during muon capture in aluminum to improve the physics models employed in Monte Carlo simulations.

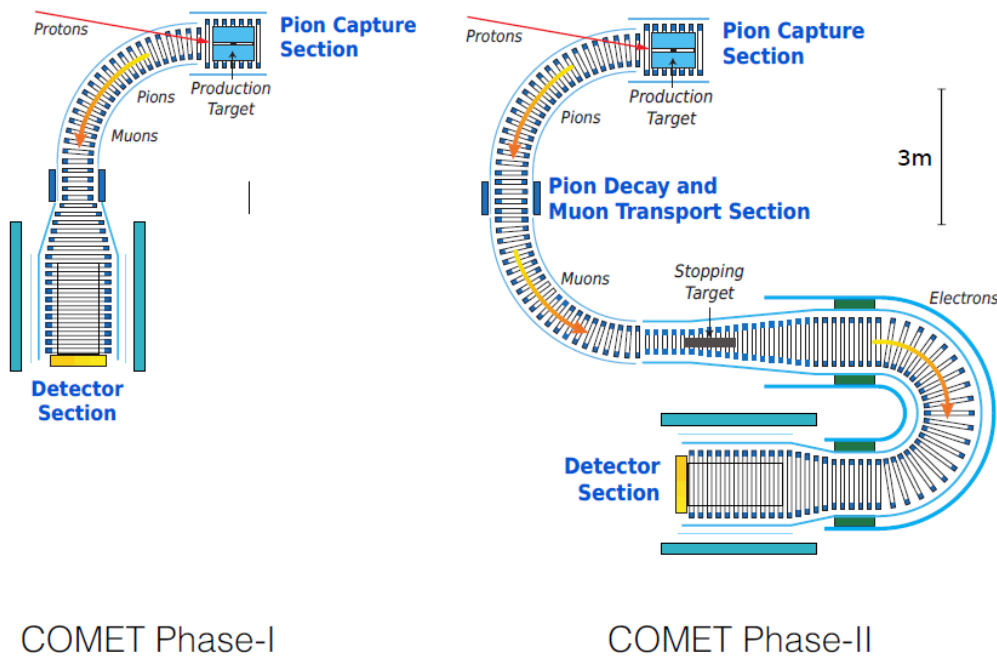


Fig. 1.4: Pictorial view of the COMET apparatus [31].

### 1.4.2 EDM experiments

In the last decades, the interest towards EDM measurements and limits played an important part in testing old and new theories. A summary of (some of) the current limits is in Tab. 1.3. This subsection is a rundown of the experiments setting these limits.

#### Neutron: nEDM

The current upper limit on the neutron EDM comes from the apparatus built by the RAL/Sussex/ILL collaboration [40] using the PSI UCN source (see 1.5.3): the measured result of  $d_n = (0 \pm 1.1_{\text{stat}} \pm 0.2_{\text{sys}}) \times 10^{-26}$  ecm translates to an upper limit of  $|d_n| < 1.8 \times 10^{-26}$  ecm (90% CL). The method used was to determine the change in Larmor precession frequency of neutrons ( $f_n =$

Experiment	Particle	EDM limit in ecm
nEDM [40]	n	$0.18 \times 10^{-25}$
ACME [41]	e	$1.1 \times 10^{-29}$
Indirect [42]	$\mu$	$0.19 \times 10^{-19}^*$
g-2 [43]	$\mu$	$1.8 \times 10^{-19}$

**Tab. 1.3:** Sumary of the current limits on the EDM for neutron electron and muon.

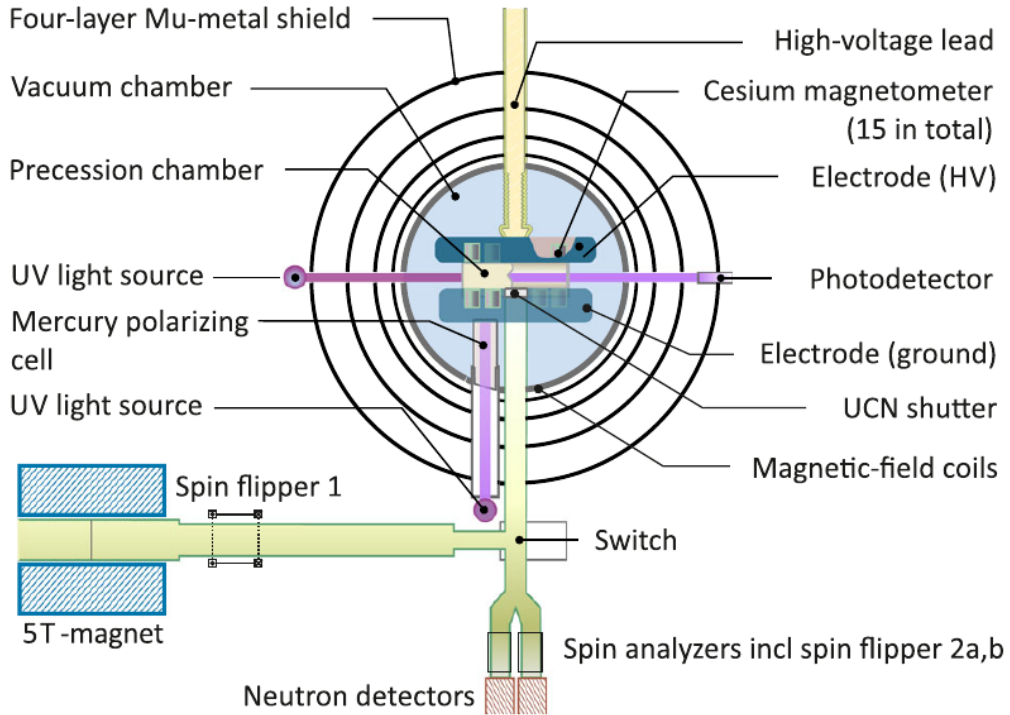


**Fig. 1.5**

$\frac{1}{\pi\hbar} |\mu_n \mathbf{B}_0 + d_n \mathbf{E}|$ ) using the spectrometer sketched in Fig. 1.5. This frequency is correlated to the change in polarity of the electric field. Each cycle of measurement consisted in:

- Polarizing UCNs with a 5 T solenoid, selecting the initial state with a spin flipper
- Confining them in the precession chamber to the equilibrium density of  $\sim 2 \text{ UCN/cm}^3$
- A small quantity of polarized  $^{199}\text{Hg}$  vapor was injected as comagnetometer
- Different low-frequency pulses were used to tip Hg or UCNs spins by  $\pi/2$
- The detection system counts both spin-up ( $\uparrow$ ) and down ( $\downarrow$ ) states
- For each cycle i, the asymmetry is evaluated:  $A = (N_\uparrow - N_\downarrow)/(N_\uparrow + N_\downarrow)$ .

An interesting detail is that, to compensate for residual magnetic-field fluctuations and drifts, the frequency ratio  $R = f_n/f_{\text{Hg}}$  was used.

**n2EDM** Any significant improvement on the limit requires a completely new setup. With this aim the n2EDM was developed [44]. This measurement will (again) rely on the estimation of the precession frequency  $f_n$  of polarized ultracold neutrons in weak B and strong E fields:

$$d_n = \frac{\pi\hbar}{2|E|} (f_{n,\uparrow\downarrow} - f_{n,\uparrow\uparrow})$$

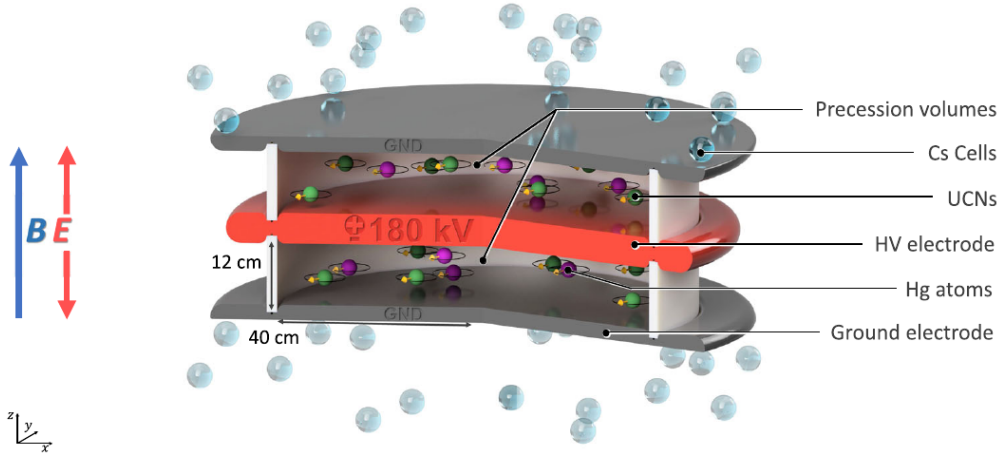


Fig. 1.6

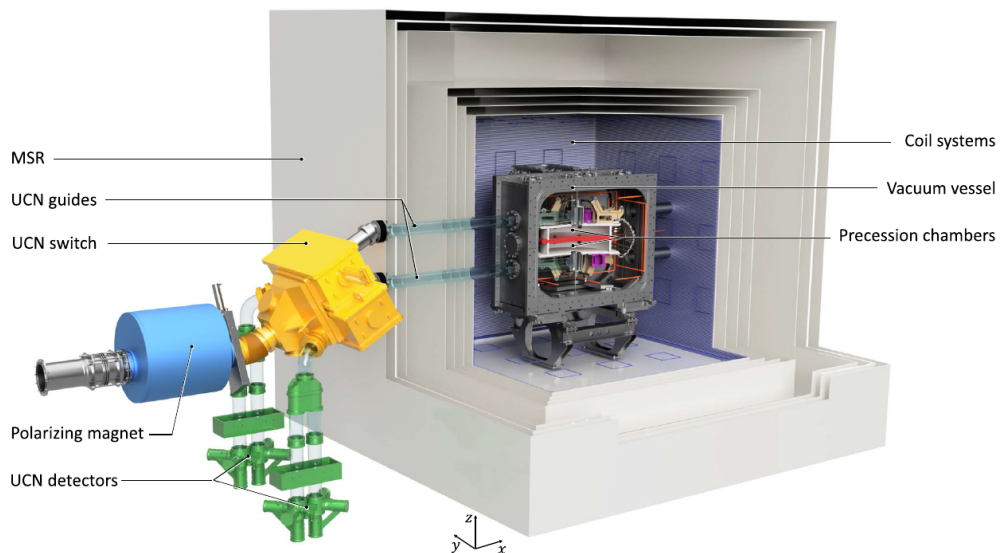


Fig. 1.7

Key aspects are the size and quality of the cylindrical storage chambers and the precision of the magnetometry, which will rely on mercury and cesium. A sketch of the concept design is in Fig. 1.6 and the whole design in Fig. 1.7. Other sizable improvements, here not discussed, will be the further optimization of the production and transport of the UCN from the source as well as the improved magnetic shielding.

## Electron

The conventional way to measure EDM is the separated oscillatory fields method: when a particle is subjected to an electric field parallel to a weak magnetic field the EDM interaction changes the Larmor frequency [45]. An alternative approach is to use solid-state techniques: in the presence of a strong magnetic field the EDM of valence electrons in a paramagnetic insulator would generate a small magnetization. Even though the effect is negligible for singular electrons, the cumulative effect can be detected using sensitive magnetometry. Using this method the limit  $d_e < 6.05 \times 10^{-25} \text{ e} \cdot \text{cm}$  was obtained in  $\text{Eu}_{0.5}\text{Ba}_{0.5}\text{TiO}_3$  [46]. Not long after, a different limit was

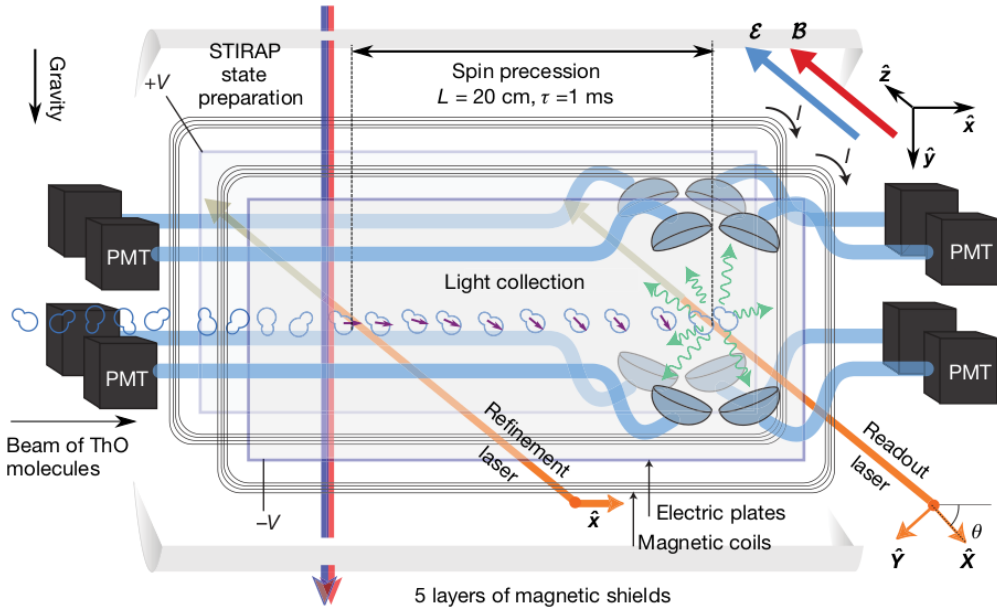


Fig. 1.8

set with the same technique in Gadolinium Gallium Garnet (GGG,  $\text{Gd}_3\text{Ga}_5\text{O}_{12}$ ):  $d_e = -5.57 \pm 7.89 \pm 0.12 \times 10^{-25} \text{ e} \cdot \text{cm}$  [47]. The choice of material is driven by:

- A strong magnetic response, generated by the high density of  $\text{Gd}^{3+}$  ions ( $\sim 10^{-22} \text{ cm}^{-3}$ ), each with 7 unpaired electrons in  $4f$  shell
- High dielectric strength ( $10 \text{ MV/cm}$ ) and electrical resistivity

**ACME** The current limit on eEDM was actually set by the ACME collaboration [41] using a different method: measuring the spin precession in a superposition of quantum states. As illustrated in Fig. 1.8, the measuring principle is the following:

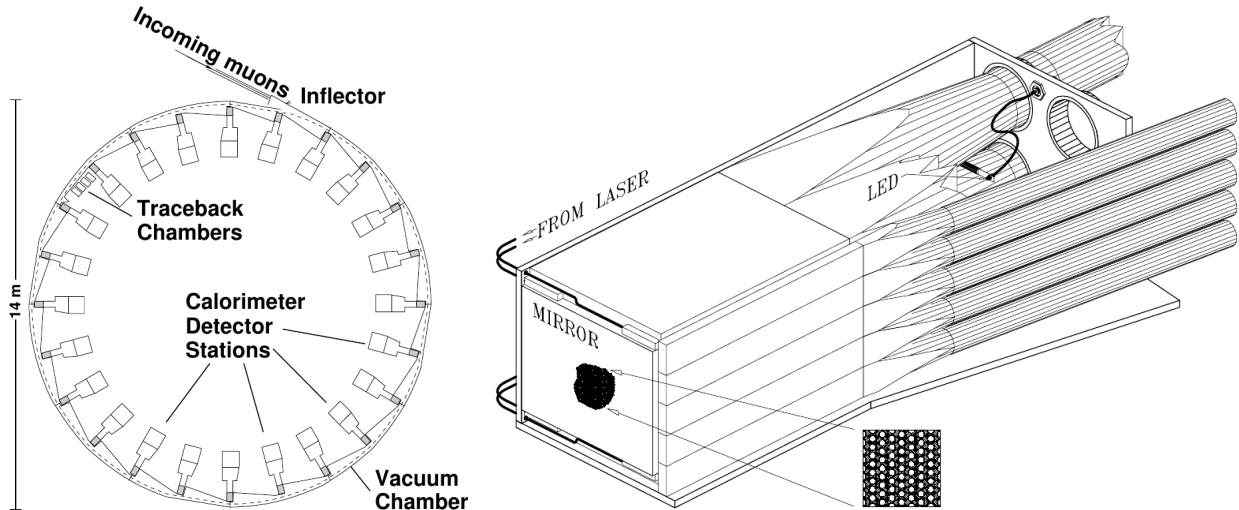
- A collimated beam of ThO enters a  $E, B$  fields region
- A combination of lasers creates a spin state aligned with  $\hat{x}$
- The spin precesses in the  $E, B$  fields
- The final spin alignment is readout by a laser: the resulting fluorescence depends on the angle between the laser linear polarization and the spin direction

The key aspect is that the precession frequency is linked to the states of the system and is modified by the presence of  $d_e$ . The results obtained is  $d_e = (4.3 \pm 3.1 \pm 2.6) \times 10^{-30} \text{ e} \cdot \text{cm}$ . Applying the Feldman–Cousins prescription this value translates to the limit  $|d_e| < 1.1 \times 10^{-29} \text{ e} \cdot \text{cm}$ .

## Muon

We now come to the muon, to which most of this thesis is dedicated. The  $d_\mu$  search at PSI is going to be discussed in detail in the following chapters but we will here review the current limits. These are the references for the direct [43] and indirect [42] limits, where all the missing details can be found.

**Muon g-2** In 2018 the  $g-2$  collaboration performed three independent searches for  $d_\mu$ . All results were compatible with a null value and a combined upper limit was set:  $|d_\mu| < 1.9 \times 10^{-19} \text{ e} \cdot \text{cm}$



(a) Layout of the g-2 storage ring with the de-infector, Traceback Chambers, Calorimeter Detector Stations, and Vacuum Chamber. (b) Sketch of the Front Scintillation Detectors (FSD). The Position-Sensitive Detector (PSD) is not shown but is set in front of the FSD.

**Fig. 1.9:** Sketches of the g-2 storage ring and the detector used to measure the muon EDM.

[43]. We will here skip the details but we will outline the methods used and the results (all 95% CL). Three additional detectors were added to the BNL experiment to measure the EDM measuring the positrons coming from the muon decay. In Fig. 1.9a a sketch of the g-2 ring and the different detectors.

- Front Scintillator Detectors (FSD): stacks of five horizontal scintillators to measure oscillation of the average vertical position. A sketch of such a detector is in Fig. 1.9b. The analysis of the data collected in 2000 yielded:  $|d_{\mu^+}| < 2.9 \times 10^{-19}$  ecm
- Position-Sensitive Detectors (PSD): a version of FSD that is segmented both horizontally and vertically.  $|d_{\mu^-}| < 1.5 \times 10^{-19}$  ecm
- Traceback Wire Chamber (TWC): series of eight, three-layer drift tube planes in front of one of the calorimeters (a sketch is shown in Fig. 1.10). These are used to track the positrons back to the storage volume. The analysis conducted on the 1999-2000 data with this detector yielded:  $|d_{\mu^+}| < 3.2 \times 10^{-19}$  ecm

**Indirect limit** Given the rise in interest for EDM measurements an effort was undertaken to assess the indirect constraints imposed on  $d_\mu$  by the EDM measurements performed with heavy atoms and molecules [42]. This was done by evaluating the  $d_\mu$ -induced *Shiff moment*<sup>1</sup> of the  $^{199}\text{Hg}$  nucleus, and a specific CP-odd operator for ThO. The results,  $d_\mu(^{199}\text{Hg}) < 6.4 \times 10^{-20} \text{ e} \cdot \text{cm}$  and  $d_\mu(\text{ThO}) < 1.9 \times 10^{-20} \text{ e} \cdot \text{cm}$ , are more stringent than the current measured limit but are *indirect*. This means that an assumption on lepton universality is done when considering this limit.

<sup>1</sup>As pointed out in [48], this is the operator inducing the atomic EDM.

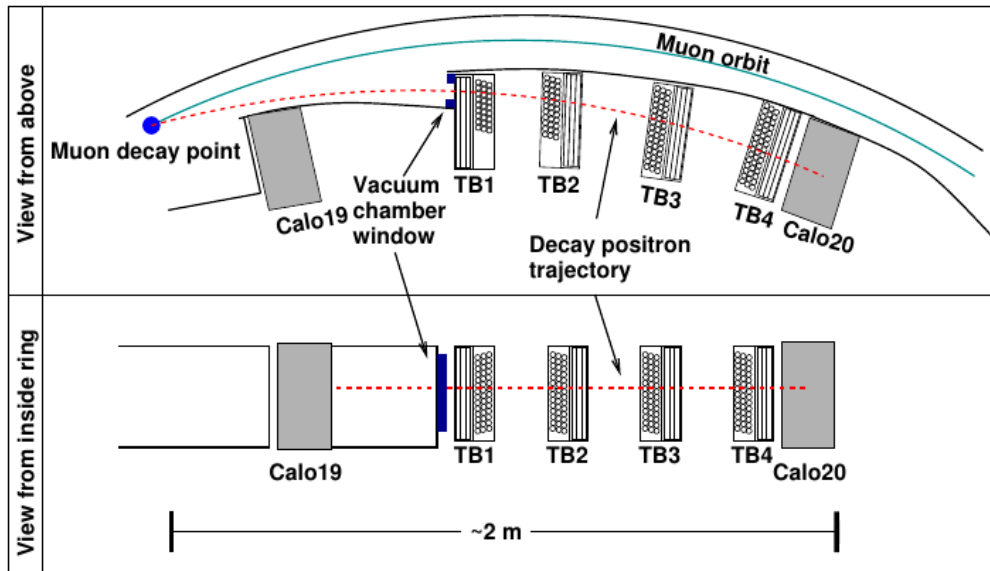


**Fig. 1.10:** The Traceback Wire Chamber is the most complex detector added for the EDM measurement. It consists of eight three-layer drift tube planes to propagate the positron track back to the decay point.

## 1.5 The beams at PSI

### 1.5.1 High-Intensity Proton Accelerator facility

The proposal for the accelerator facility at PSI was completed in 1963. The objective was to develop a proton beam of tens of microAmpere and energy above 450 MeV to produce  $\pi/\mu$ . The main accelerator is a cyclotron designed to accelerate the beam from 72 MeV to 590 MeV. The first pre-accelerator, Injector I cyclotron, was developed to accelerate protons and light ions up to 72 MeV and 180  $\mu\text{A}$ . The performances steadily improved up to 180  $\mu\text{A}$  but the beam losses at the extraction from the Injector I were the bottleneck. The Ring cyclotron was deemed to have the potential to surpass 2 mA. For this reason, in 1978, the proposal of using two pre-accelerators was approved: a 860 keV Cockcroft-Walton (CW) followed by a new Injector II cyclotron.

Since 2010 the chain is the following:

- Protons are produced by an electron cyclotron resonance source with a 60 kV extraction
- Two solenoids focus the protons onto a collimator: here  $^2\text{H}^+$  and  $^3\text{H}^+$  ions are stopped
- Protons are then accelerated in three stages
  - From 60 keV to 870 keV by the CW DC linear accelerator, shown in Fig. 1.11a  
The beamline connecting the CW to the Injector II is equipped with a bunching system to match the acceptance of Injector II
  - Injector II accelerates the pre-bunched beam up to 72 MeV. An electrostatic beam splitter can redirect a fraction of the beam extracted beam (up to 100  $\mu\text{A}$ ) to produce radioisotopes
  - The beam is sent to the Ring cyclotron, shown in Fig. 1.11b. Eight magnets keep the particles on the spiral path and four cavities accelerate the beam up to 590 MeV
- After the acceleration the beam is extracted and sent to the meson production targets
- The surviving  $\sim 65\%$  of the beam is sent to the spallation source SINQ (or to a beam dump)



(a) CW feeding the Injector II

(b) Picture of the Ring cyclotron.

**Fig. 1.11:** Picture of two of the stages of the HIPA facility: the Cockcroft-Walton bringing the proton up to 870 keV and the Ring Cyclotron accelerating them up to 590 MeV.

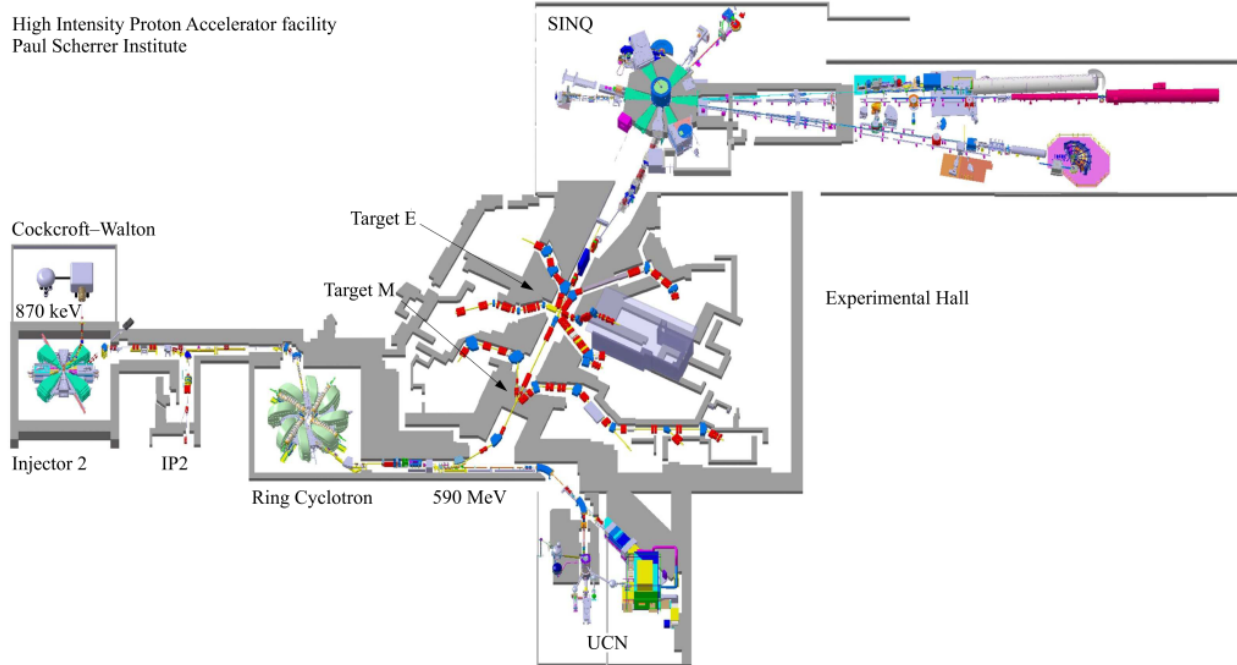


**Fig. 1.12:** High Intensity Proton Accelerator (HIPA) facility at PSI

**Injector II** The Injector II cyclotron is designed for high-current operation (1 mA and above) with minimal extraction losses. It achieves high extraction efficiency through a combination of factors: high accelerating voltage, large radius, large gap magnets, and low energy spread. To counter space charge forces, a high vertical betatron tune<sup>2</sup> is employed. Injector II is a low-field separate sector machine with four wedge sectors, accommodating two high-voltage double-gap resonators and two single-gap flat-top resonators. Its 870 keV injection energy allows for beam collimation and halo cleanup, being below the Coulomb threshold. The "vortex motion" is an interesting phenomenon caused by space charge in isochronous cyclotrons [49]. For long initial bunches, self-sustaining round sub-bunches are generated, while for short and compact bunches, the vortex effect stabilizes the bunch [50] [51]. The PSI operation crew discovered the usefulness of self-focusing, achieving high extracted currents with low losses by operating in an accelerating mode without the need for the flat-top system. In an ongoing upgrade program, Injector II will replace the flat-top resonators with two 50MHz high-voltage resonators. This upgrade aims to reduce extraction losses and enable higher beam currents. Notably, Injector II is the only known production cyclotron worldwide that harnesses the vortex effect.

**Ring cyclotron** Over time, the Ring cyclotron's performance was improved, particularly its extraction efficiency. Initially, a well-centered beam was required to pass the Walkinshaw resonance<sup>3</sup> without significant loss. However, by December 1976, an extraction efficiency of 99.9% was achieved with a peak intensity of 112  $\mu$ A. Ten years later, Injector II alone achieved a beam current of 1mA, and in combination with the Ring cyclotron, reached 310  $\mu$ A. To increase the intensity, the Ring underwent an RF system upgrade, while a bunching system was implemented in the injection line. The upgrades allowed for a reduction in Ring turns, resulting in a production current of 2.2 mA and a beam power of 1.3 MW, in line with Joho's  $N^3$ -Law (see Fig. 1.13). Further upgrades, including the replacement of the 150MHz flattop cavity, are expected to enable a beam current of 3 mA and power of SI1.8MW for both Injector II and the Ring cyclotron.

## Performances

HIPA operates at a beam power of up to 1.42 MW. The maximum beam power (1.42 MW) is limited by the activation and damage of the accelerator components while the maximum beam current authorized is 2.4 mA. The increase of the beam power in the period between 1974 to 2020 is shown in Fig. 1.15. The history of the delivered charge to the meson production targets and SINQ is shown in Fig. 1.16. A major limiting factor is the scattering of halo particles in the extraction septum. There are two key elements for low-loss beam extraction: the generation of beam tails must be suppressed as best as possible and the turn separation at the extraction septum must be maximized. In this way, the density of halo particles at the position of the extraction septum is minimized. The beam is operated 24/7 around 200 days a year. Every three weeks of operation two days of maintenance are scheduled. The details of the different particle production are discussed in the following subsections.

<sup>2</sup>Refers to the number of vertical or horizontal oscillations that a particle undergoes per turn in a cyclotron, indicating the level of vertical or horizontal focusing.

<sup>3</sup>The Walkinshaw resonance is a phenomenon in cyclotrons where beams experience a resonance with the machine's magnetic field modulation. Proper alignment and adjustments are necessary to prevent significant beam loss.

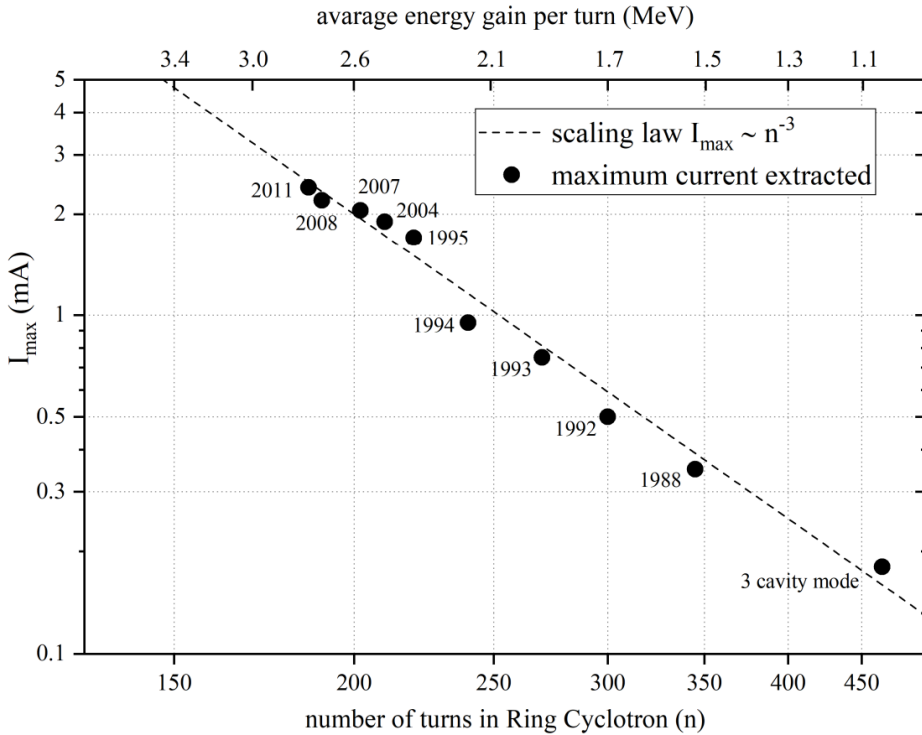


**Fig. 1.13:** In 1981, Werner Joho introduced Joho's N3-Law, an analysis of high-intensity issues in cyclotrons [52]. This law states that the current limit dominated by losses scales inversely with the third power of the number of turns in the cyclotron:  $I_{\max} \propto N^{-3}$ . Remarkably, this formula accurately predicted the performance of the PSI Ring cyclotron for the subsequent two decades.

**Power** The experiments at HIPA require high-intensity particle beams for precise measurements, which consume significant electrical power. Upgrades aim to achieve higher particle flux and brightness, necessitating even greater power. Considering the global energy consumption challenges, improving HIPA's energy efficiency is crucial. Fig. 1.14 displays the power consumption breakdown of the proton facility. During routine operation at a beam current of 2.2 mA, 1.3 MW, the overall power consumption is approximately 12.5 MW leading to an efficiency of 11%. For the bare accelerator, the figure is 18%. The RF-to-beam power conversion accounts for the majority of this consumption, around 5.4 MW. It scales linearly with beam power, while the power consumption of magnets and auxiliary systems remains independent of the beam power. It can be shown that the efficiency can increase with higher current and the aim is >20% with 3 mA

### 1.5.2 Meson production

As we saw in 1.5.1, High Intensity Proton Accelerator (HIPA) delivers a continuous 2.4 mA 590 MeV proton beam. To have a high pion/muon yield a low Z material is the best choice for the Meson Production Targets: graphite has been used since 1990's. The whole system (target, collimators, beam dumps, ...) has to be cooled and, due to nuclear reactions, is highly radioactive. Pions are produced by the interaction with nucleons in the target (threshold at 280 MeV in the center-of-mass frame) and muons are then produced by pion decay. When  $\pi$  are stopped at  $\sim 1$  mm from the surface of the target,  $\mu^+$  can escape and are called *surface muons*. These muons have energies below 4.1 MeV ( $p = 29.8$  MeV) and are  $\approx 100\%$  polarized. Muons created by in-flight decay have higher energies and are cooled *cloud muons*. Both positive and negative muons are

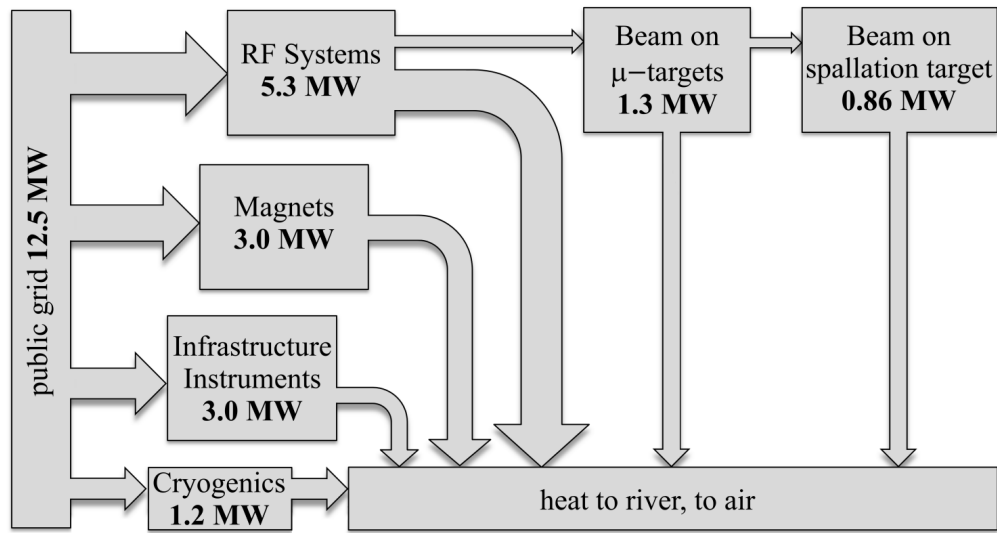


Fig. 1.14: Detail of the power usage of the HIPA facility.

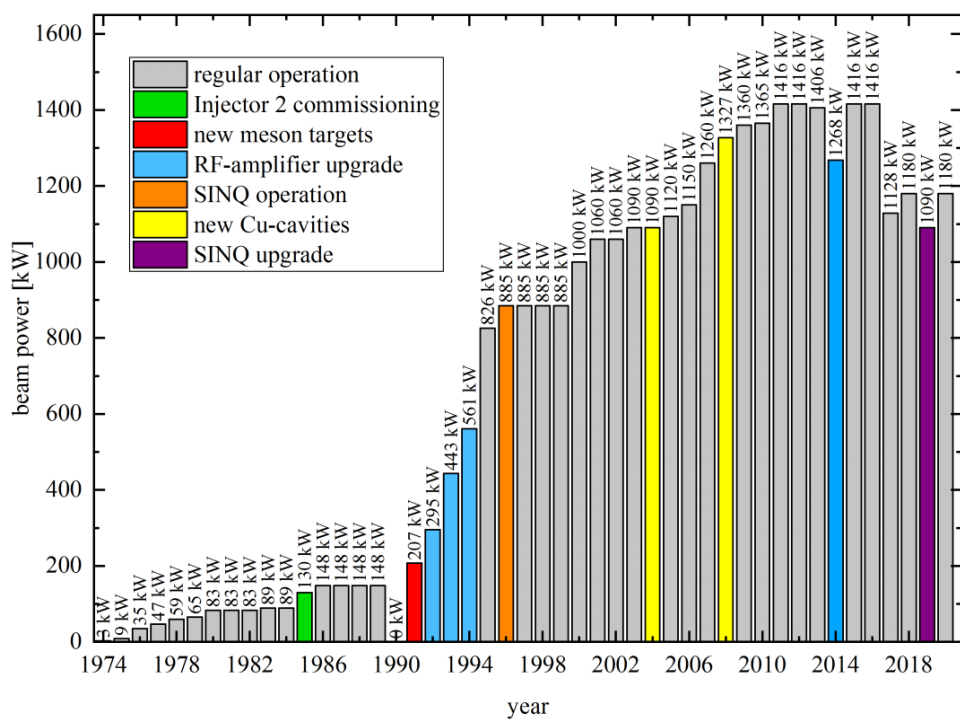
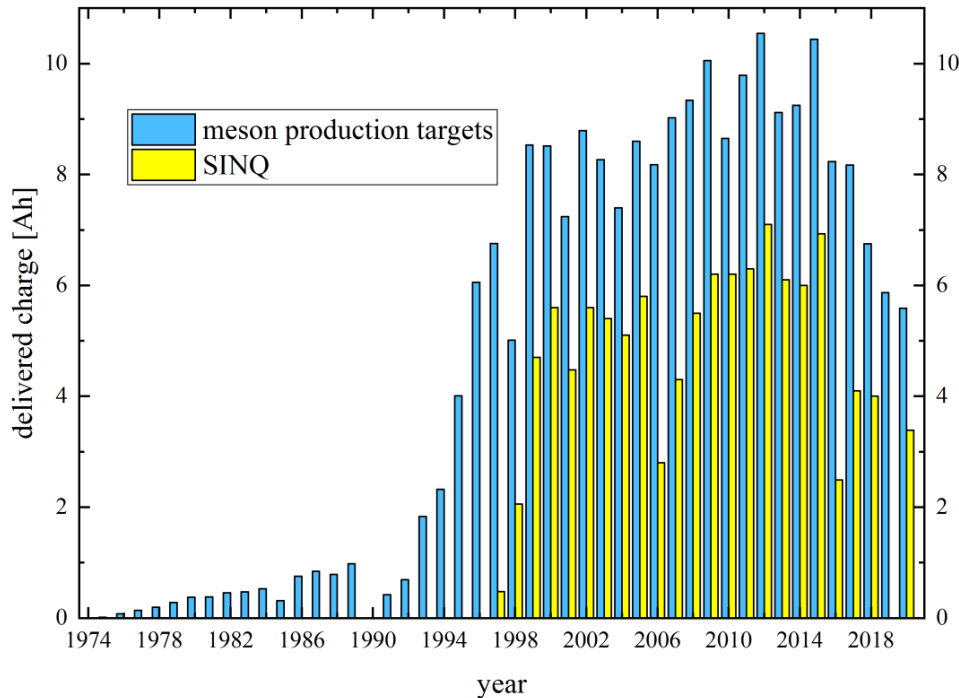


Fig. 1.15: History of the power of the HIPA proton beam.



**Fig. 1.16:** History of the charge delivered by the HIPA beam on the meson production targets and SINQ.

Target	User facility	Particles	Momenta (MeV/c)	Rate ( $s^{-1}mA^{-1}$ )
M (5 mm)	$\pi M1$ $\pi M3.1-3$	$e/\pi/\mu/p$ $\mu/$	10-450 10-40	$2 \times 10^8$ $3 \times 10^6$
E (4/6 cm)	$\pi E1$ $\pi E3$ $\pi E5$ $\pi E1$ $\pi E4$	$\pi/\mu/p$ $\mu$ $\pi/\mu$ $\mu$ $\mu$	10-450 10-40 10-120 60-120 10-40	$1 \times 10^9$ $3 \times 10^7$ $5 \times 10^8$ $6 \times 10^7$ $4 \times 10^8$

**Tab. 1.4:** Particle types available at the meson facilities. The rate in particles per second per 1 mA of proton

possible but the negative charge is suppressed by a factor  $\sim 3$ . There are two targets: M feeds two beamlines (PiM1 and PiM3; E feeds 5 beamlines (PiE1, MuE1, MuE4, PiE3, PiE5). The detail of the facilities are summarized in Tab. 1.4. The targets are graphite wheels which rotate to distribute the heat due to the impinging beam. The material is polycrystalline graphite made of small crystallites of  $\sim 20 \mu\text{m}$  irregularly arranged.

**E Target** The target is inserted vertically into the beamline and held by a horizontal rotating shaft. The graphite and the hub are connected by six spokes. While operated at 2 mA, the temperature of this 40 mm/60 mm target is  $\sim 1700$  K. Water-cooled copper shields are mounted on the rear of the target. To reduce the deformations the graphite rim is made of 12 segments. Variations of the beam positions are crucial and to improve the sensitivity the graphite wheel was modified: small grooves were applied on both sides. This modulates the beam transmission. At the end of 2019 a new target wheel was tested, having a small angle for the impinging beam. This *slanted target* keeps the effective thickness creating a larger active surface and two different spots for IN-/OUT of the beam. The net effect is an increase  $\sim 50\%$  in the surface muons. As the bearings

degrade from heat and radiation they have to be replaced after a few months of operation. The procedure for the maintenance of the target here will not be discussed.

**M Target** This target is smaller in thickness and the bearings are far from the beam thus the demands are less challenging. The rim of the target is 2 cm wide and 2 mm thick. With an impinging angle of 30 deg the effective thickness is 5.2 mm inducing a beam loss of 1.6%. The target operates at 1100 K and is cooled by conduction. For the upcoming High Intensity Muon Beam (HIMB) the aim is to increase the muon rate by a factor up to 100. For this purpose studies for an upgrade of the M target station, with a slanted target design, are ongoing. A similar slanted target was already tested in the E target station, yielding a  $\sim 50\%$  increase in surface muon rate.

**Collimators and Beam dump** Just like target E, Collimators and beam dump are inserted vertically and shielded. Both are made of oxygen-free copper: improve thermal conductivity; avoid hydrogen embrittlement<sup>4</sup>; for brazing of the steel tubes onto the copper body. To avoid any significant change in the material, the copper is kept below 400 K using water-cooling. The collimator system as well as the beam dump have to stand more than 100 kW per component. The water flows in stainless steel pipes are wound outside and brazed on the cylindrical body. This is done to avoid direct contact of the proton beam with the water, which would create corrosion-inducing ions. The main body is made of six slices brazed together. The shape and manufacture of these sections were optimized using computational fluid dynamics in order to reduce the energy deposit and thermal stress. An aperture, made of 4 slits of 100  $\mu\text{m}$  Nikel foils, is mounted in front of the devices. Here free electrons from ionization are collected and used for beam position and size monitoring. Aside from a water leak problem, likely due to thermal stress, no visible signs of radiation damage are observed since installation.

### 1.5.3 Neutron production

#### SINQ

The first spallation neutron source built at PSI was SINQ, which has dedicated neutron scattering instruments and was used as a polarized cold-neutron beam line for fundamental neutron physics. After passing through the meson production target the proton energy is degraded to 570/565 MeV. The beam is bent downwards and then up vertically onto the spallation target. The thermal neutron flux scales with the beam current and is  $\sim 1.5 \times 10^{14} \text{ cm}^{-2}\text{s}^{-1}$  near the target. This beamline was used for many measurements conducted in preparation for the UCN source and many parameters of UCN production (and loss) were here determined.

#### UltraCold Neutrons

Neutrons below 4 mK are called UltraCold. This corresponds to energy below 300 neV, which is comparable with the gravitational potential of a neutron at a few meters height and also the neutron optical potential: material bottles can hence contain UCNs. The design of the UCN source, shown in Fig. 1.17, was presented in 2000 to push the sensitivity of the nEDM search.

<sup>4</sup>Hydrogen can be produced by the spallation reaction of the protons with copper. This hydrogen can bond with oxygen creating water molecules that can produce cracks in the copper.

**Source setup** The HIPA 590 MeV proton beam is deflected by a magnetic kicker and sent in the spallation source. Each spallation reaction with the lead atoms leads to an average of 8 neutrons, which are then thermalized in heavy water. The main moderator is made of solid deuterium at 5 K. The UCN produced exit the moderator's vessel through a thin aluminum lid in a vertical guide and their energy is lost to gravity. From here the UCN are delivered via long neutron guides: two at the bottom and one at the top of the vessel. The 30 liters of solid D<sub>2</sub> is the core of the whole system and takes several days to achieve a good ice quality. UCN intensity reflects the quality of the achieved solid deuterium, as shown in Fig. 1.18 exemplifying a typical UCN intensity behavior during such a slow freezing process.

**Performance** A key parameter in the performance of a UCN source is the number of particles delivered. The exponential decay measured at the lower ports reflects the emptying time of the central storage vessel. Measuring in the higher port a faster exponential is found, demonstrating that the UCNs with energies high enough to reach that port are quickly drained. Several studies to understand all aspects of the UCN source have been conducted since its inauguration, as well as the UCN transport from production in the solid deuterium to a beam port. A slow decrease in performance was discovered and a temperature-cycling "conditioning" was developed to regain maximum UCN intensity. The UCN source has been reliably operating since 2011 (see Fig. 1.19).

**Results** The resulting nEDM limit  $d_n = (0.0 \pm 1.1_{stat} \pm 0.2_{sys}) \times 10^{-26}$  ecm (see 1.4.2) was published in 2020 [40] but other results were also obtained thanks to this facility:

- A measurement of the mercury-to-neutron magnetic moment ratio
- Spin-echo spectroscopy with ultracold neutrons
- Measurement of gravitational depolarization of ultracold neutrons
- limit for oscillating electric dipole moments
- limit for spin-dependent forces mediated by axion-like particles

#### 1.5.4 High-Intensity Muon Beams

Currently, PSI delivers the most intense continuous muon beam in the world with up to a few  $10^8 \mu^+/\text{s}$ . The High-Intensity Muon Beams (HiMB) project at PSI focuses on the development of a new target station and muon beamlines to deliver up to  $10^{10} \mu^+/\text{s}$  [53][54]. The aim is to boost the production, collection, and transport of surface muons. HiMB is part of the Isotope and Muon Production using Advanced Cyclotron and Target Technologies project (IMPACT)[[impact](#)].

##### Production and collection

To increase the surface muon yield, the M target discussed in 1.5.2 will be substituted with target H, having a more slanted geometry. This new target, shown in Fig. 1.20, will be 20 mm thick in the proton direction, with a 10 deg slanting angle: surface muon yields comparable to a 40 mm thick non-slanted target. The protons will impinge below the rotation shaft (Fig. 1.20b), from the back of the target, in a copper water-cooled shielding (Fig. 1.20a). The target will fit in the remote-controlled exchange flask of target E for easier handling and maintenance.

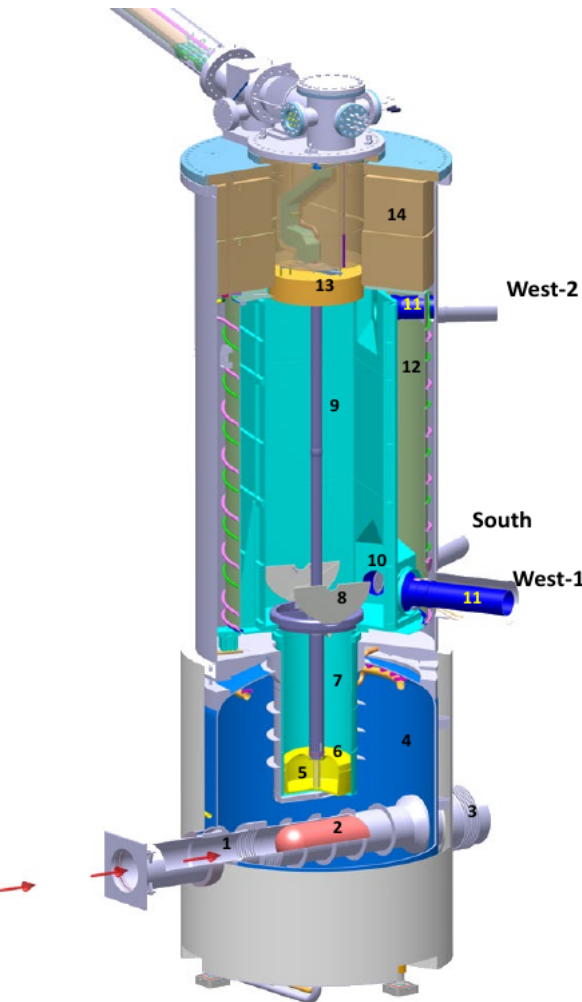


**Fig. 1.17:** CAD for the UCN source taken from [2]. Some of the key aspects are: 2 - lead spallation source, 4 - heavy water moderator, 5 - D<sub>2</sub> moderator, 9 - storage vessel, 10 - 11 UCN guide and guide shutter.

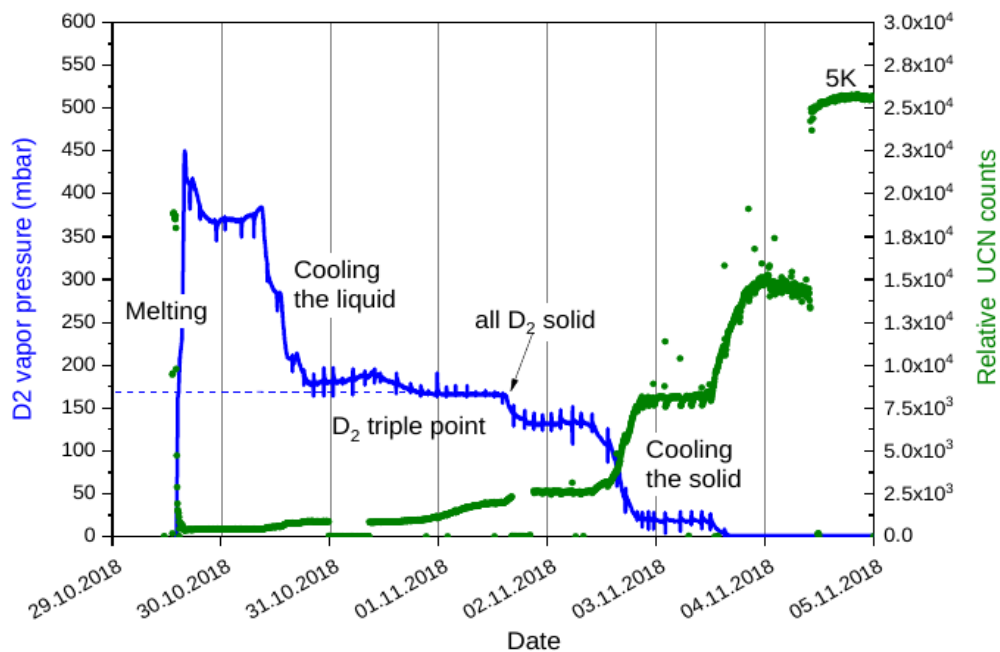


**Fig. 1.18:** The observed behavior during the slow freezing of the deuterium. The large increase in UCN output demonstrates the strong reduction in UCN losses within the D<sub>2</sub>. Figure taken from [2]

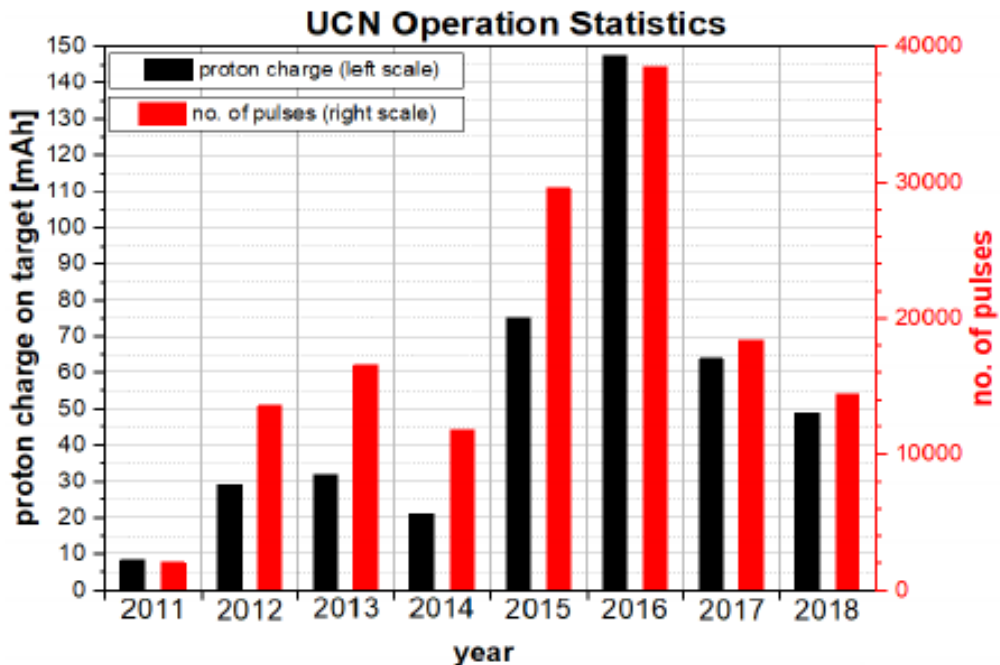


**Fig. 1.19:** Annual statistics of the UCN source showing total accumulated beam current on target (black bars) and number of beam pulses (red bars) on the UCN spallation target. Figure taken from [2]

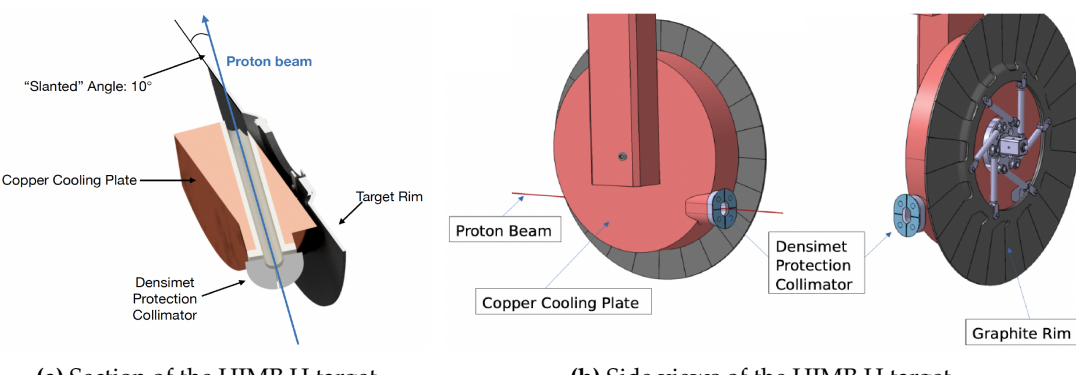


**Fig. 1.20:** Depiction of the target H for the HIMB project. The slanted target improves the production of surface muons. **a)** The proton beam impinges from the back side passing through a copper water-cooled shielding. **b)** The beam travels lower to avoid the rotating shaft.

When using solenoids to capture particles, the target is often completely enclosed in the solenoid aperture. This solution is not viable for HIMB because the proton beam is not stopped in the H target. The proposed solution, shown in Fig. 1.21, is to have two different NC solenoids ( $\sim 0.45$  T) sideways to the target.

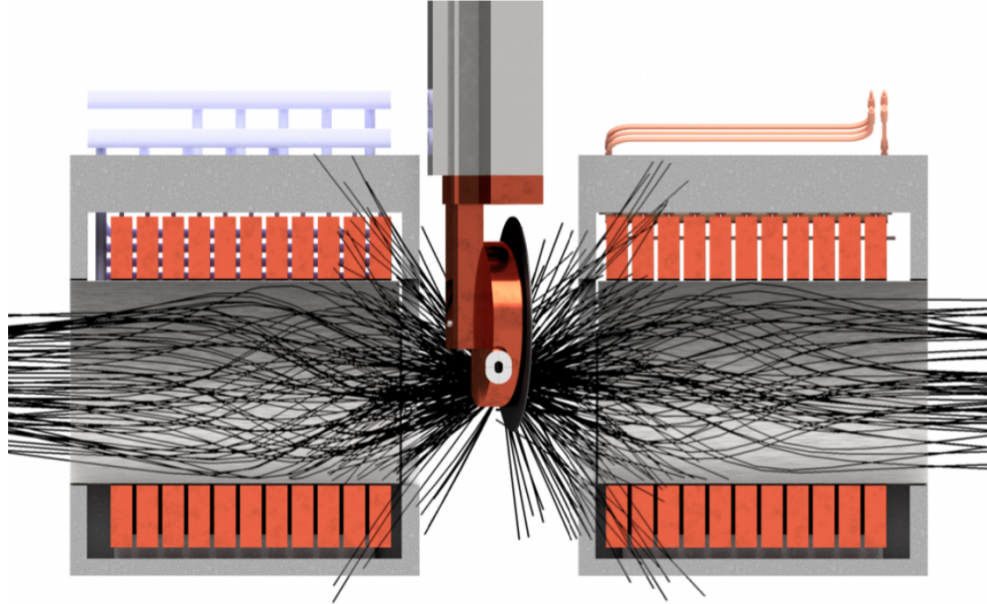


**Fig. 1.21:** HIMB will have two different NC solenoids sideways to the target. These are required to collect the produced muons and let the surviving proton beam continue toward the spallation SINQ setup.

The particles produced by the impact of the 590 MeV proton beam are: electrons, muons and pions. The momentum spectrum of the generated particle is shown in Fig. 1.22: the peak in the  $\mu^+$  spectrum is caused by surface muon production while, at higher energies, the muons come from pion decay in flight. This peak is not present for  $\mu^-$  because stopped  $\pi^-$  undergoes nuclear capture and no muons are produced. In a similar fashion, the peak in positron around Michel edge is produced by stopped  $\mu^+$ . The HIMB project focuses on surface muons but the optimization are done to accept and transport momenta up to 80 MeV/c, while keeping the focus on 28 MeV/c.

## Beamlines

HIMB will introduce two beamlines: MUH2 and MUH3. The peculiarity of these lines is the extensive use of solenoids. Solenoids achieve focus on both axes (wrt. quadrupoles) but usually, their usage is limited by the required magnetic fields. For the momentum of the surface muons  $\sim 0.45$  T are sufficient and achievable with NC solenoids.

The MUH2 beamline is designed to deliver beams to fixed target experiments (e.g. Mu3e). It will be located at the left-hand side of the target station and its most important figure of merit for MUH2 is transmission. Two 40 deg bends are included in the beam trajectory with dipoles to avoid a direct line of sight to the target.

The model reported in the Conceptual Design Report (CDR) published in January 2022 [10] is able to deliver  $1.22 \times 10^{10} \mu^+/\text{s}$  at a proton current of 2.4 mA at the entrance of the experimental area at the surface muon momentum. The beam spot size and the average polarization at the end of the channel are  $\sigma_x = 40$  mm,  $\sigma_y = 42$  mm, and  $\varepsilon = 0.88$ . Interesting to note that a double Wien

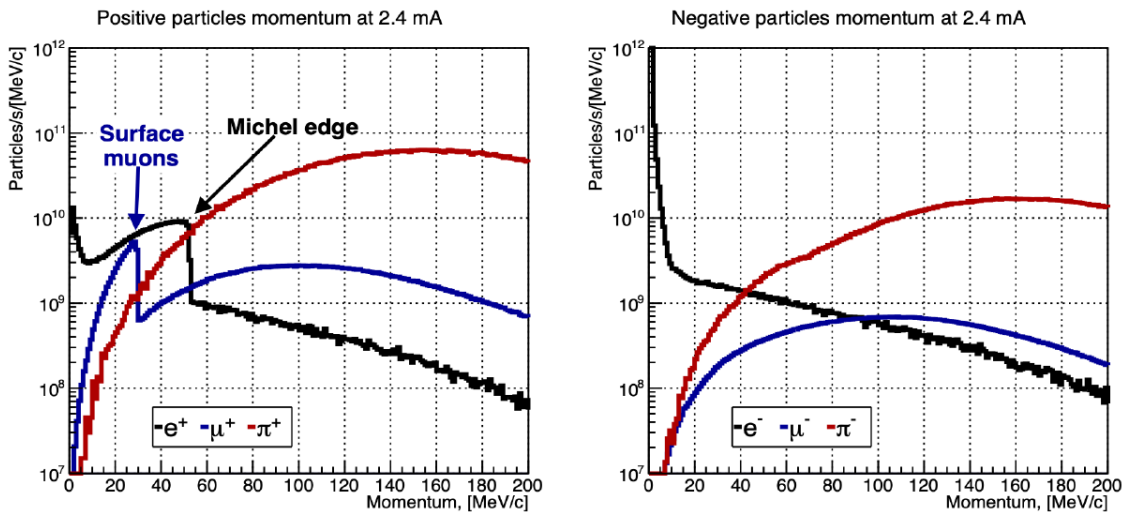


**Fig. 1.22:** Momentum spectrum for positive and negative  $e$ ,  $\mu$ ,  $\pi$  produced at the HIMB H target for a proton current of 2.4 mA.

filter scheme is currently under study to keep the positron contamination under control.

The MUH3 beamline, on the right-hand side of the target station, aims at delivering muon beams for muon spin rotation spectroscopy ( $\mu$ SR). For these applications,  $10^{10} \mu/\text{s}$  is not required and part of the beamline follows a more standard approach with quadrupoles. From simulations, while the solenoid section delivers more than  $10^{10} \mu/\text{s}$ , the rate drops to  $3 \times 10^8 \mu/\text{s}$  at 15 MeV and  $6 \times 10^6 \mu/\text{s}$  at 10 MeV when reaching the two experimental area. The expected beam spots and polarization are  $\sigma_x = 40 \text{ mm}$ ,  $\sigma_y = 42 \text{ mm}$ , and  $\epsilon \gtrsim 0.95$ .

## 1.6 Proton Ionization Facility

Another interesting facility at PSI is the Proton Ionization Facility (PIF) [55][56]. This was designed, in conjunction with the European Space Agency, to be a user-friendly testing ground for spacecraft components. The deteriorating effect that high-energy protons can have on semiconductors is a key aspect of the correct functioning of spacecraft in the space environment. Depending on the orbit and the duration of the flight the exposure to this hazard can vary and having reproducible test grounds is cardinal during the design phase. The original goals of this facility:

- Radiation hardness of the new electronic products
- Single Event Upsets (SEU) and Latch-ups (SEL) of electronic components
- Properties of radiation monitors for space and laboratory applications
- Basic mechanics of radiation effects in semiconductors
- Space radiation environment by on-earth simulations

Given the broad range of energy and intensities of the facility, alongside ESA many other users apply for beamtime at PIF within the accelerator communities, such as CERN, but also external laboratories, industries, and universities. During the daytime, the beam is usually reserved for biomedical applications and these irradiation studies are done parasitically during the night and on weekends. Although only for a short period, I joined PIF and I had the opportunity to be a shifter. It was quite an interesting experience, allowing me to become acquainted with a different setup and to see a different aspect of the research in particle physics. The usual shift would consist

in tuning the beam to be suited to the user's needs and supporting during the data taking.

# Bibliography for the introduction

- [1] Lorenzo Calibbi and Giovanni Signorelli. "Charged Lepton Flavour Violation: An Experimental and Theoretical Introduction". In: *Riv. Nuovo Cim.* 41.2 (2018), pp. 71–174. DOI: 10.1393/ncr/i2018-10144-0. arXiv: 1709.00294 [hep-ph].
- [2] Adrian Signer, Klaus Kirch, and Cyrus Hoffman. "Review of Particle Physics at PSI". In: *SciPost Physics Proceedings* (Sept. 2021). DOI: 10.21468/SciPostPhysProc.5.
- [3] Bastiano Vitali. "In situ monitoring of the stopped muon flux at Mu2e". MA thesis. Pisa U., 2020. DOI: 10.2172/1764143.
- [4] M. Raidal et al. "Flavour physics of leptons and dipole moments". In: *Eur. Phys. J. C* 57 (2008). Ed. by R. Fleischer, T. Hurth, and M. L. Mangano, pp. 13–182. DOI: 10.1140/epjc/s10052-008-0715-2. arXiv: 0801.1826 [hep-ph].
- [5] F. J. M. Farley et al. "A New method of measuring electric dipole moments in storage rings". In: *Phys. Rev. Lett.* 93 (2004), p. 052001. DOI: 10.1103/PhysRevLett.93.052001. arXiv: hep-ex/0307006.
- [6] G. W. Bennett et al. "Final report of the E821 muon anomalous magnetic moment measurement at BNL". In: *Physical Review D* 73.7 (Apr. 2006). ISSN: 1550-2368. DOI: 10.1103/physrevd.73.072003. URL: <http://dx.doi.org/10.1103/PhysRevD.73.072003>.
- [7] Maxim Pospelov and Adam Ritz. "Electric dipole moments as probes of new physics". In: *Annals of Physics* 318.1 (2005). Special Issue, pp. 119–169. ISSN: 0003-4916. DOI: <https://doi.org/10.1016/j.aop.2005.04.002>. URL: <https://www.sciencedirect.com/science/article/pii/S0003491605000539>.
- [8] MEG II collaboration et al. *A search for  $\mu^+ \rightarrow e^+ \gamma$  with the first dataset of the MEG II experiment.* 2024. arXiv: 2310.12614 [hep-ex].
- [9] Wilhelm H. Bertl et al. "Search for the Decay  $\mu^+ \rightarrow e^+ e^+ e^-$ ". In: *Nucl. Phys. B* 260 (1985), pp. 1–31. DOI: 10.1016/0550-3213(85)90308-6.
- [10] Wilhelm H. Bertl et al. "A Search for muon to electron conversion in muonic gold". In: *Eur. Phys. J. C* 47 (2006), pp. 337–346. DOI: 10.1140/epjc/s2006-02582-x.
- [11] L. Willmann et al. "New bounds from searching for muonium to anti-muonium conversion". In: *Phys. Rev. Lett.* 82 (1999), pp. 49–52. DOI: 10.1103/PhysRevLett.82.49. arXiv: hep-ex/9807011.

- [12] B. Aubert, Y. Karyotakis, et al. "Searches for Lepton Flavor Violation in the Decays  $\tau^\pm \rightarrow e \pm \gamma$  and  $\tau^\pm \rightarrow \mu^\pm \gamma$ ". In: *Phys. Rev. Lett.* 104 (2 Jan. 2010), p. 021802. DOI: 10.1103/PhysRevLett.104.021802. URL: <https://link.aps.org/doi/10.1103/PhysRevLett.104.021802>.
- [13] K. Hayasaka et al. "Search for Lepton Flavor Violating Tau Decays into Three Leptons with 719 Million Produced Tau+Tau- Pairs". In: *Phys. Lett. B* 687 (2010), pp. 139–143. DOI: 10.1016/j.physletb.2010.03.037. arXiv: 1001.3221 [hep-ex].
- [14] E. Abouzaid et al. "Search for lepton flavor violating decays of the neutral kaon". In: *Phys. Rev. Lett.* 100 (2008), p. 131803. DOI: 10.1103/PhysRevLett.100.131803. arXiv: 0711.3472 [hep-ex].
- [15] D. Ambrose et al. "New limit on muon and electron lepton number violation from  $K0(L) \rightarrow \mu\mu- e\bar{e}$  decay". In: *Phys. Rev. Lett.* 81 (1998), pp. 5734–5737. DOI: 10.1103/PhysRevLett.81.5734. arXiv: hep-ex/9811038.
- [16] Aleksey Sher et al. "An Improved upper limit on the decay  $K^+ \rightarrow \pi^+ \mu^+ e^-$ ". In: *Phys. Rev. D* 72 (2005), p. 012005. DOI: 10.1103/PhysRevD.72.012005. arXiv: hep-ex/0502020.
- [17] Georges Aad et al. "Search for the lepton flavor violating decay  $Z \rightarrow e\mu$  in pp collisions at  $\sqrt{s}$  TeV with the ATLAS detector". In: *Phys. Rev. D* 90.7 (2014), p. 072010. DOI: 10.1103/PhysRevD.90.072010. arXiv: 1408.5774 [hep-ex].
- [18] R. Akers et al. "A Search for lepton flavor violating  $Z^0$  decays". In: *Z. Phys. C* 67 (1995) () .
- [19] Wilhelm H. Bertl et al. "A Search for muon to electron conversion in muonic gold". In: *Eur. Phys. J. C* 47 (2006), pp. 337–346. DOI: 10.1140/epjc/s2006-02582-x.
- [20] A.M. Baldini et al. "MEG Upgrade Proposal". In: (Jan. 2013). arXiv: 1301.7225 [physics.ins-det].
- [21] A.M. Baldini et al. "The design of the MEG II experiment". In: *Eur. Phys. J. C* 78.5 (2018), p. 380. DOI: 10.1140/epjc/s10052-018-5845-6. arXiv: 1801.04688 [physics.ins-det].
- [22] Angela Papa. "Towards a new generation of Charged Lepton Flavour Violation searches at the Paul Scherrer Institut: The MEG upgrade and the Mu3e experiment". In: *EPJ Web Conf.* 234 (2020). Ed. by G. D'Ambrosio et al., p. 01011. DOI: 10.1051/epjconf/202023401011.
- [23] Niklaus Berger. "The Mu3e Experiment". In: *Nucl. Phys. B Proc. Suppl.* 248-250 (2014). Ed. by Francesco Grancagnolo and Marco Panareo, pp. 35–40. DOI: 10.1016/j.nuclphysbps.2014.02.007.
- [24] Ann-Kathrin Perrevoort. "Status of the Mu3e Experiment at PSI". In: *EPJ Web Conf.* 118 (2016). Ed. by G. D'Ambrosio et al., p. 01028. DOI: 10.1051/epjconf/201611801028. arXiv: 1605.02906 [physics.ins-det].
- [25] R.M. Carey et al. "Proposal to search for  $\mu^- N \rightarrow e^- N$  with a single event sensitivity below  $10^{-16}$ ". In: (Oct. 2008). DOI: 10.2172/952028.
- [26] L. Bartoszek et al. "Mu2e Technical Design Report". In: (Oct. 2014). DOI: 10.2172/1172555. arXiv: 1501.05241 [physics.ins-det].
- [27] F. Abdi et al. "Mu2e Run I Sensitivity Projections for the Neutrinoless  $\mu^- \rightarrow e^-$  Conversion Search in Aluminum". In: *Universe* 9.1 (2023), p. 54. DOI: 10.3390/universe9010054. arXiv: 2210.11380 [hep-ex].

- [28] Y.G. Cui et al. "Conceptual design report for experimental search for lepton flavor violating mu- - e- conversion at sensitivity of 10\*\*(-16) with a slow-extracted bunched proton beam (COMET)". In: (June 2009).
- [29] R. Akhmetshin et al. "Letter of Intent for Phase-I of the COMET Experiment at J-PARC". In: (). URL: [http://192.153.106.200/researcher/Hadron/en/pac\\_1203/pdf/COMET-PhaseI-LoI.pdf](http://192.153.106.200/researcher/Hadron/en/pac_1203/pdf/COMET-PhaseI-LoI.pdf).
- [30] R. Akhmetshin et al. "Experimental Proposal for Phase-I of the COMET Experiment at J-PARC." In: (). URL: [https://j-parc.jp/researcher/Hadron/en/pac\\_1207/pdf/E21\\_2012-10.pdf](https://j-parc.jp/researcher/Hadron/en/pac_1207/pdf/E21_2012-10.pdf).
- [31] R. Abramishvili et al. "COMET Phase-I Technical Design Report". In: *PTEP* 2020.3 (2020), p. 033C01. DOI: 10.1093/ptep/ptz125. arXiv: 1812.09018 [physics.ins-det].
- [32] A.M. Baldini et al. "Search for the lepton flavour violating decay  $\mu^+ \rightarrow e^+ \gamma$  with the full dataset of the MEG experiment". In: *Eur. Phys. J. C* 76.8 (2016), p. 434. DOI: 10.1140/epjc/s10052-016-4271-x. arXiv: 1605.05081 [hep-ex].
- [33] Marco Chiappini. "The construction and commissioning of the ultra low mass MEG II drift chamber for the search of the  $\mu^+ \rightarrow e^+ \gamma$  decay at branching ratios below  $10^{-13}$ ". PhD thesis. Pisa U., 2019.
- [34] F. Abusalma et al. "Expression of Interest for Evolution of the Mu2e Experiment". In: (Feb. 2018). arXiv: 1802.02599 [physics.ins-det].
- [35] David Neuffer. "Mu2e-II Injection from PIP-II". In: (Apr. 2018). DOI: 10.2172/1437287.
- [36] M.G. Catanesi et al. "Large-angle production of charged pions with 3-12.9-GeV/c incident protons on nuclear targets". In: *Phys. Rev. C* 77 (2008), p. 055207. DOI: 10.1103/PhysRevC.77.055207. arXiv: 0805.2871 [hep-ex].
- [37] Andrew Williams John Edmonds. "An Estimate of the Hadron Production Uncertainty and a Measurement of the Rate of Proton Emission after Nuclear Muon Capture for the COMET Experiment". PhD thesis. U. Coll. London, 2015.
- [38] Benjamin Edward Krikler. "Update on the AlCap Experiment". In: *17th International Workshop on Neutrino Factories and Future Neutrino Facilities*. 2015, pp. 408–417.
- [39] Andrew Edmonds. "Latest Updates from the AlCap Experiment". In: *13th Conference on the Intersections of Particle and Nuclear Physics*. Sept. 2018. arXiv: 1809.10122 [physics.ins-det].
- [40] C. Abel et al. "Measurement of the Permanent Electric Dipole Moment of the Neutron". In: *Phys. Rev. Lett.* 124 (8 Feb. 2020), p. 081803. DOI: 10.1103/PhysRevLett.124.081803. URL: <https://link.aps.org/doi/10.1103/PhysRevLett.124.081803>.
- [41] V. Andreev et al. "Improved limit on the electric dipole moment of the electron". In: *Nature* 562.7727 (2018), pp. 355–360. DOI: 10.1038/s41586-018-0599-8.
- [42] Yohei Ema, Ting Gao, and Maxim Pospelov. "Improved Indirect Limits on Muon Electric Dipole Moment". In: *Phys. Rev. Lett.* 128.13 (2022), p. 131803. DOI: 10.1103/PhysRevLett.128.131803. arXiv: 2108.05398 [hep-ph].
- [43] G. W. Bennett et al. "An Improved Limit on the Muon Electric Dipole Moment". In: *Phys. Rev. D* 80 (2009), p. 052008. DOI: 10.1103/PhysRevD.80.052008. arXiv: 0811.1207 [hep-ex].

- [44] N. J. Ayres et al. "The design of the n2EDM experiment". In: *The European Physical Journal C* 81.6 (June 2021). DOI: 10.1140/epjc/s10052-021-09298-z. URL: <https://doi.org/10.1140/epjc/s10052-021-09298-z>.
- [45] Norman F. Ramsey. "A Molecular Beam Resonance Method with Separated Oscillating Fields". In: *Phys. Rev.* 78 (6 June 1950), pp. 695–699. DOI: 10.1103/PhysRev.78.695. URL: <https://link.aps.org/doi/10.1103/PhysRev.78.695>.
- [46] S. Eckel, A. O. Sushkov, and S. K. Lamoreaux. "Limit on the Electron Electric Dipole Moment Using Paramagnetic Ferroelectric  $\text{Eu}_{0.5}\text{Ba}_{0.5}\text{TiO}_3$ ". In: *Phys. Rev. Lett.* 109 (19 Nov. 2012), p. 193003. DOI: 10.1103/PhysRevLett.109.193003. URL: <https://link.aps.org/doi/10.1103/PhysRevLett.109.193003>.
- [47] Y. J. Kim et al. "New Experimental Limit on the Electric Dipole Moment of the Electron in a Paramagnetic Insulator". In: *Phys. Rev. D* 91.10 (2015), p. 102004. DOI: 10.1103/PhysRevD.91.102004. arXiv: 1104.4391 [nucl-ex].
- [48] V. V. Flambaum, I. B. Khriplovich, and O. P. Sushkov. "On the Possibility to Study  $P$  Odd and  $T$  Odd Nuclear Forces in Atomic and Molecular Experiments". In: *Sov. Phys. JETP* 60 (1984), p. 873.
- [49] M. M. Gordon. "The longitudinal space charge effect and energy resolution". In: *Conf. Proc. C* 690917 (1969), pp. 305–317.
- [50] E. Pozdeyev et al. "Longitudinal beam dynamics studies with space charge in small isochronous ring". In: *Phys. Rev. ST Accel. Beams* 12 (2009), p. 054202. DOI: 10.1103/PhysRevSTAB.12.054202.
- [51] C. Baumgarten. "Transverse-Longitudinal Coupling by Space Charge in Cyclotrons". In: *Phys. Rev. ST Accel. Beams* 14 (2011), p. 114201. DOI: 10.1103/PhysRevSTAB.14.114201. arXiv: 1109.1996 [physics.acc-ph].
- [52] W. Joho. "High Intensity Problems in Cyclotrons". In: *9th International Conference on Cyclotrons and their Applications*. 1982, EI03.
- [53] M. Aiba et al. "Science Case for the new High-Intensity Muon Beams HIMB at PSI". In: (Nov. 2021). arXiv: 2111.05788 [hep-ex].
- [54] Giovanni Dal Maso et al. "Future facilities at PSI, the High-Intensity Muon Beams (HIMB) project". In: *EPJ Web Conf.* 282 (2023), p. 01012. DOI: 10.1051/epjconf/202328201012.
- [55] Wojtek Hajdas et al. "The Proton Irradiation Facility at the Paul Scherrer Institute". In: *Nuclear Instruments and Methods in Physics Research Section B: Beam Interactions with Materials and Atoms* 113.1 (1996). Accelerators in Applied Research and Technology, pp. 54–58. ISSN: 0168-583X. DOI: [https://doi.org/10.1016/0168-583X\(95\)01327-X](https://doi.org/10.1016/0168-583X(95)01327-X). URL: <https://www.sciencedirect.com/science/article/pii/0168583X9501327X>.
- [56] Wojtek Hajdas et al. "Proton Irradiation Facility and Space Radiation Monitoring at the Paul Scherrer Institute". In: *Physica medica : PM : an international journal devoted to the applications of physics to medicine and biology : official journal of the Italian Association of Biomedical Physics (AIFB)* 17 Suppl 1 (Feb. 2001), pp. 119–23.

# **Part I**

# **muEDM**

## Chapter 2

# muEDM

This chapter is an introduction to the muEDM experiment. After describing in some detail the spin dynamics, a reminder on the EDM searches for the different particles will follow. We will then outline the measuring principle of the experiment, the frozen spin technique, and a deep dive into the current status of the experiment. The study of systematic uncertainties and the upcoming schedule will close this chapter. As always, the early stage of the experiment means the rate of changes and improvement is outstanding. This is my attempt at an up-to-date description, which relies on the “muEDM Status Report 2023” submitted to PSI, but some details might be already outdated.

[1] [2] [3] [4] [5] [6] [7]

### 2.1 Electric Dipole Moment

As introduced in 1.3.5, the Hamiltonian describing the spin dynamics is:

$$\hat{H} = -\mu \hat{\sigma} \cdot \mathbf{B} - d \hat{\sigma} \cdot \mathbf{E}$$

We then saw that, when considering a combination of magnetic and electric fields and a moving particle it is useful to introduce the polarization vector  $\Pi = \mathbf{s}/s$  and the Thomas precession  $\Omega_0$ :

$$\frac{d\Pi}{dt} = \Omega_0 \times \Pi, \quad \Omega_0 = -\frac{e}{m\gamma} \left[ (1 + \gamma a) \mathbf{B} - \frac{a\gamma^2}{\gamma+1} (\beta \cdot \mathbf{B}) \beta - \gamma \left( a + \frac{1}{\gamma+1} \right) \frac{\beta \times \mathbf{E}}{c} \right]$$

With no electrical field parallel to the momentum and with  $\Omega_c$  the cyclotron frequency, the relative spin precession of a muon in a storage ring is described by (T-BMT [**miss-59**]):

$$\begin{aligned} \Omega = \Omega_0 - \Omega_c &= \underbrace{\frac{q}{m} \left[ a \mathbf{B} - \frac{a\gamma}{\gamma+1} (\beta \cdot \mathbf{B}) \beta - \left( a + \frac{1}{1-\gamma^2} \right) \frac{\beta \times \mathbf{E}}{c} \right]}_{\text{Anomalous precession, } \omega_a = \omega_L - \omega_c} \\ &\quad + \underbrace{\frac{\eta q}{2m} \left[ \beta \times \mathbf{B} + \frac{\mathbf{E}}{c} - \frac{\gamma c}{\gamma+1} (\beta \cdot \mathbf{E}) \beta \right]}_{\text{Interaction of EDM and relativistic } \mathbf{E}, \omega_a} \end{aligned} \tag{2.1}$$

The second term describes the precession due to the EDM coupling to the relativistic  $\mathbf{E}$ , perpendicular to the  $\mathbf{B}$  in which the particle is moving. In the presence of a muon EDM the plane would

be tilted and a vertical precession ( $\omega_e \perp \mathbf{B}$ ), shifted by  $\pi/2$  to the horizontal anomalous precession, would become observable.

### 2.1.1 Symmetry violation

In physics, there are three cardinal discrete symmetries: Charge (C), Parity (P), and Time (T). P and T are related to the invariance under spatial and temporal reversal while C is the invariance for particle  $\leftrightarrow$  antiparticle exchange. While the magnetic field and the spin are *pseudo-vectors* under P and vectors under T, the electric field behaves in the opposite way. The implication of this difference is that EDM and MDM behave differently under C, P, and T:

$$MDM : \begin{cases} \mathbf{P}(-\mu\hat{\sigma} \cdot \mathbf{B}) = -\mu\mathbf{P}(\hat{\sigma}) \cdot \mathbf{P}(\mathbf{B}) = -\mu(+\hat{\sigma}) \cdot (+\mathbf{B}) = -\mu\hat{\sigma} \cdot \mathbf{B} \\ \mathbf{T}(-\mu\hat{\sigma} \cdot \mathbf{B}) = -\mu\mathbf{T}(\hat{\sigma}) \cdot \mathbf{T}(\mathbf{B}) = -\mu(-\hat{\sigma}) \cdot (-\mathbf{B}) = -\mu\hat{\sigma} \cdot \mathbf{B} \end{cases} \quad (2.2)$$

$$EDM : \begin{cases} \mathbf{P}(-d\hat{\sigma} \cdot \mathbf{E}) = -d\mathbf{P}(\hat{\sigma}) \cdot \mathbf{P}(\mathbf{E}) = -d(+\hat{\sigma}) \cdot (-\mathbf{E}) = +d\hat{\sigma} \cdot \mathbf{E} \\ \mathbf{T}(-d\hat{\sigma} \cdot \mathbf{E}) = -d\mathbf{T}(\hat{\sigma}) \cdot \mathbf{T}(\mathbf{E}) = -d(-\hat{\sigma}) \cdot (+\mathbf{E}) = +d\hat{\sigma} \cdot \mathbf{E} \end{cases} \quad (2.3)$$

In light of the CPT theorem, the breaking of the T symmetry implies the breaking of CP.

### 2.1.2 Current limits on EDM

As discussed in 1.4.2, the last decades saw a continuous effort to measure the EDM of different particles. There the experiments setting the current limits were discussed but we report in Tab. 2.1 the results to aid the reader. It is important to note there are two limits for  $\mu$ : one obtained by rescaling the limit on  $d_e$ , obtaining an *indirect limit*; one, less stringent, is a *direct limit* (\*).

Experiment	Particle	EDM limit in ecm
nEDM [8]	n	$0.18 \times 10^{-25}$
ACME [9]	e	$1.1 \times 10^{-29}$
Indirect [10]	$\mu$	$0.19 \times 10^{-19} *$
g-2 [11]	$\mu$	$1.8 \times 10^{-19}$

**Tab. 2.1:** Sumary of the current limits on the EDM for neutron electron and muon.

### 2.1.3 The *frozen spin* technique

As illustrated in [1, 9], with the appropriate choice of electric field and having  $\mathbf{p}$ ,  $\mathbf{B}$  and  $\mathbf{E}$  forming an orthogonal basis, the anomalous precession term in eq. 2.1 can be set to zero.

$$a\mathbf{B} = \left( a - \frac{1}{\gamma^2 - 1} \right) \frac{\beta \times \mathbf{E}}{c} \quad (2.4)$$

In this situation the relative angle between  $\mathbf{p}$  and spin remains unchanged if  $\eta = 0$ , hence 'frozen'. In the presence of an EDM the change in polarization would then follow

$$\frac{d\Pi}{dt} = \omega_e \times \Pi, \quad \omega_e = \frac{\eta q}{2m} \left( \beta \times \mathbf{B} + \frac{\mathbf{E}_f}{c} \right) = \frac{2d_\mu}{\hbar} (\beta c \times \mathbf{B} + \mathbf{E}_f) \quad (2.5)$$

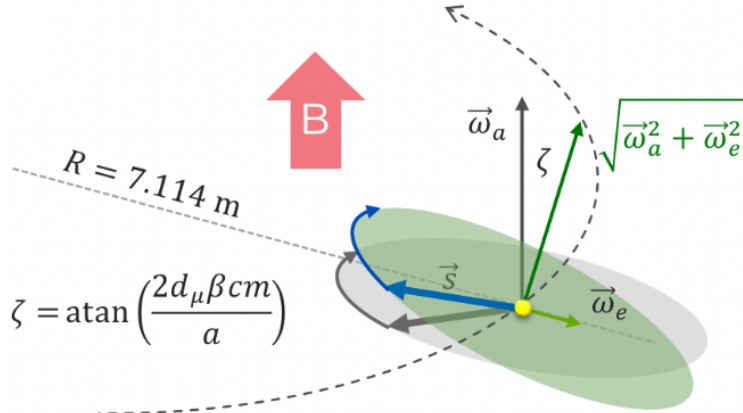


Fig. 2.1

The net result of the EDM is then a vertical build-up of the polarization given by Eq. 2.6 and illustrated by the sketch in Fig. 2.1.

$$|\Pi(t)| = P(t) = P_0 \sin(\omega_e t) \approx P_0 \omega_e t \approx 2P_0 \frac{d_\mu}{\hbar} \frac{E_f}{a\gamma^2} t \quad (2.6)$$

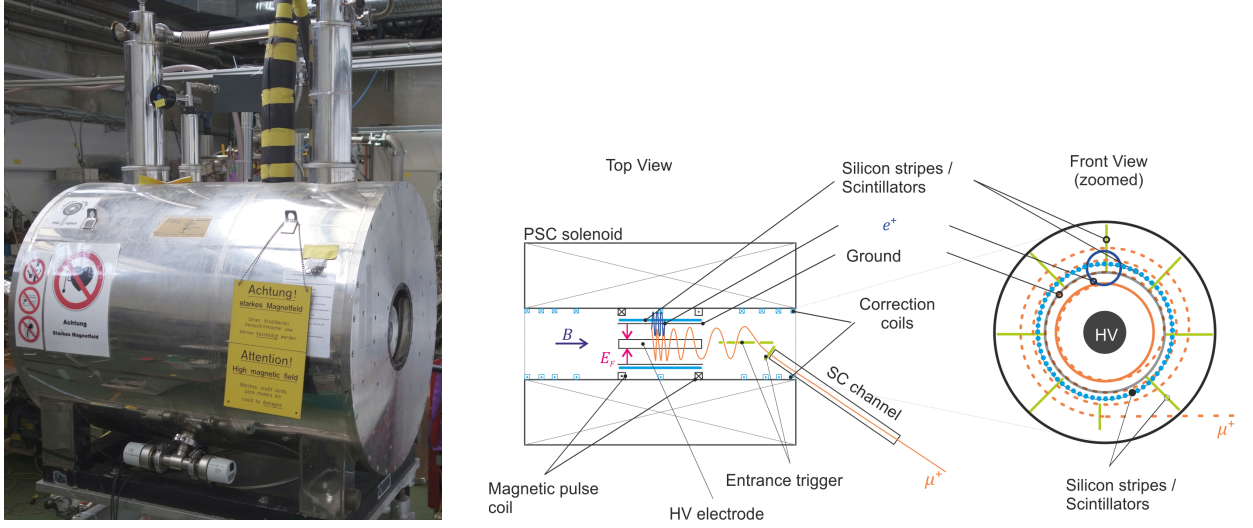
The evaluation of the sensitivity will follow a brief introduction to the muEDM experiment, to better familiarize the reader with the system.

## 2.2 The muEDM experiment

In the upcoming years, we plan to search for a muon Electric Dipole Moment (EDM) using an existing solenoid, as shown in Fig. 2.2a. The experiment will be connected to a surface muon beam line at PSI, delivering approximately  $4 \times 10^6 \mu/\text{s}$  of  $p = 28 \text{ MeV}/c$ . The muons are confined in a transverse phase space of  $\epsilon_{xx'} = 192 \pi \text{ mm rad}$  and  $\epsilon_{yy'} = 171 \pi \text{ mm rad}$ . To enhance precision, a long copper tube within a superconducting shield is employed for collimation, reducing the number of muons inside the solenoid to about  $1.2 \times 10^5 \mu/\text{s}$ . A precisely timed magnetic pulse is then used to capture and store the selected muons within the weakly focusing magnetic field.

A trigger is generated from the anticoincidence between two scintillators at the collimation channel exit. This setup allows us to store only one muon at a time, with an expected rate of about  $800 \mu/\text{s}$  meeting the required conditions. During storage, muons circulate with a radius of  $r = 31 \text{ mm}$ , and a scintillating fiber tracker is employed to track the direction of the positron resulting from muon decay. The precession frequency,  $\Omega$ , is extracted by measuring the oscillation of the positron energy distribution as a function of decay time. The frozen-spin condition is determined when  $\Omega(E) = 0$ , allowing for the measurement of a non-zero EDM.

In the presence of an EDM, the muon spin precesses out of the orbit plane, influencing the decay positron's trajectory. By detecting the decay asymmetry, we can identify the EDM. The project is to divide the task into phases. During Phase I, the highest sensitivity is achieved for positron momenta above  $40 \text{ MeV}/c$ , resulting in a mean asymmetry of about  $A = 0.35$ . With an expected sensitivity of  $\sigma(d_\mu) < 2.8 \times 10^{-16} \text{ ecm}$  per muon, we anticipate achieving  $\sigma(d_\mu) < 3 \times 10^{-21} \text{ ecm}$  in a year of data taking with a detection rate of  $N = 300 \text{ s}^{-1}$  positrons.



(a) Picture of the muEDM superconducting solenoid.

**Fig. 2.2:** Photo (a) and sketch (b) of the compact superconducting solenoid and the experimental setup for the search for the EDM of the muon. The warm bore of the solenoid has an inner diameter of 200 mm and an outer diameter of about 1000 mm.

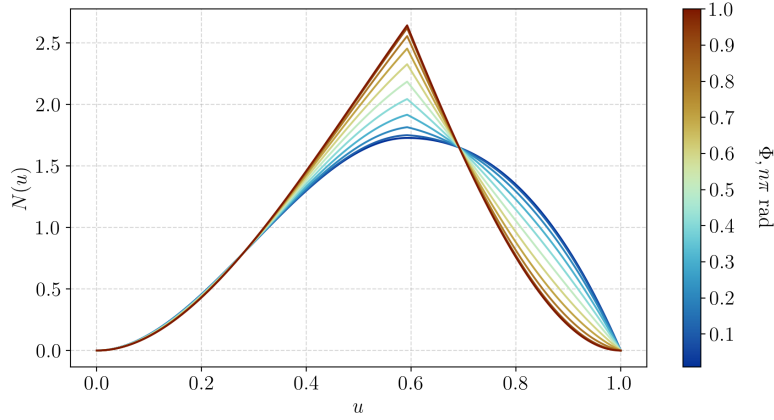


**Fig. 2.3:** Positron energy distribution as a function of the angle between the muon spin and momentum. The fractional energy  $u = E/E_{\max}$  is shown on the abscissa. The maximum positron energy for Phase I is  $E_{\max} = 68.9$  MeV. The color bar shows the  $g - 2$  phase in units of  $\pi$  radians, where 0 is spin and momentum aligned (blue) and 1 is anti-aligned (red).

## 2.3 The precursor

The task at hand is quite complex and for this reason, the aim is to first have a working prototype to demonstrate the measuring principles, the achieved control on the different sources of uncertainties, and the correct working of the different subdetectors. A review of the design and status of the different parts will be now given, in order of appearance during an event:

Muon injection: beam monitor → TOF → Injection → Injection channel → muon tracker

Storing and decay: kicker → Faraday rotator → Frozen-spin electrodes → positron tracker

### 2.3.1 Beam monitor

For precise muon beam focusing in the muonEDM experiment, a detector with front and back scintillator planes was designed. The beam passes through the central hole of the detector, corresponding to the injection tube size. The scintillator tiles, optically coupled to SiPMs, register the muon rates and these are used to center the beam by adjusting the count imbalances. To discriminate muons from positrons, the front scintillator layer fully absorbs surface muons, while the thicker back layer detects positrons. Simulation using G4BEAMLINE determined that a 2 mm-thick scintillator for the front layer and a 5 mm-thick one for the back provide optimal separation. Two detector geometries, with four diagonally-segmented tiles and eight rectangular tiles, were tested during the 2023 beam time. Sketch and simulation are shown in Fig. 2.5 while the picture of the detectors tested is in Fig. 2.7.

A preliminary centering algorithm based on hit counting in individual tiles was implemented. It adjusted the beam position iteratively until asymmetries were reduced. The simulation results showed that muon-positron discrimination becomes crucial for positron contamination above 10% (see Fig. 2.6), emphasizing the importance of proper centering for the muon component. Eljen Technology plastic scintillator (EJ-212) and BC-404 are used for the front and back layers, respectively. Hamamatsu SiPMs S13360-1325PE and S13360-3025PE are coupled to the scintillator tiles. The SiPMs are coupled to the tiles using optical cement, and the detectors are wrapped in Tedlar foil for light-tightness. Ongoing optimizations of the centering algorithm will benefit from data obtained during the beam time to enhance future measurements.

### 2.3.2 TOF

The accurate measurement of the muon Electric Dipole Moment (EDM) relies heavily on systematic effects control, which will be discussed in Sec. 2.5. The primary concern is the alignment of the electric field in the frozen-spin technique relative to the magnetic field defining the storage orbit. To address this, a strategy involves alternating measurements with both clockwise (CW) and counter-clockwise (CCW) injected muons. Switching from CW to CCW involves inverting the magnetic field and shifting the entire experiment by about 90 mm, changing the magnetically shielded injection channel.

The optimal cancellation of systematic effects requires identical initial conditions for the muon beam, like the spin phase and mean momentum. Time of Flight (TOF) measurements for individual muons during injection enable the selection of CW and CCW datasets with nearly identical momentum distributions. In 2023, prototype detectors were produced and TOF was measured in

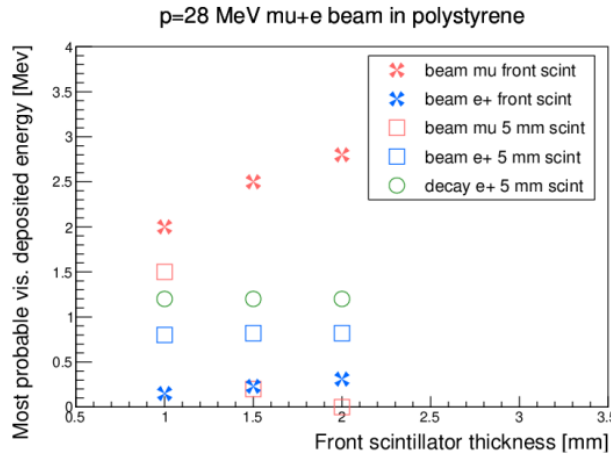


**Fig. 2.4:** Most probable visible deposited energy by muons and positrons in scintillators of various thicknesses, simulated in G4BEAMLINE. Muons and positrons with a momentum of 28 pass through a 2-mm-thick front scintillator before reaching a 5 mm-thick back scintillator. The green points are the decay positrons from muons stopped in the front scintillator.

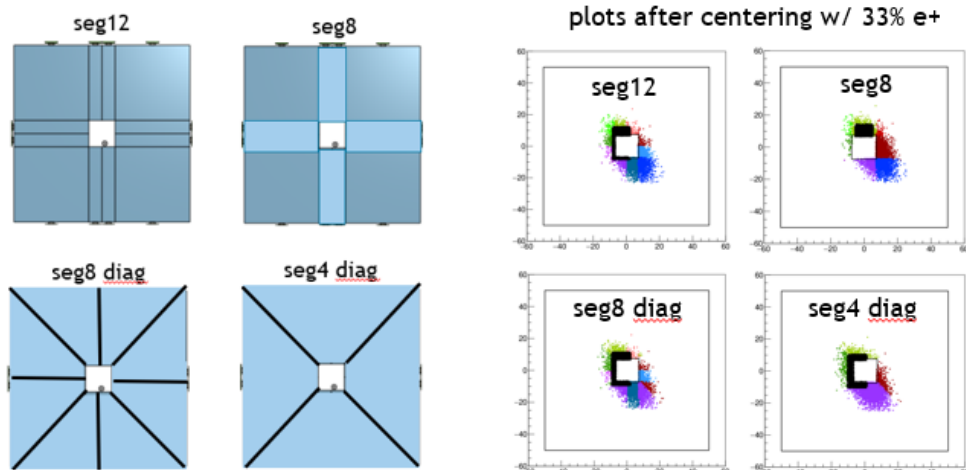


**Fig. 2.5:** Left: four geometries considered for the beam monitor. Right: Results of the beam centering in simulation, using the algorithm as described in the text, for the four geometries shown on the left image. Muon hits are colored differently based on which tile they hit, all positron hits are black.

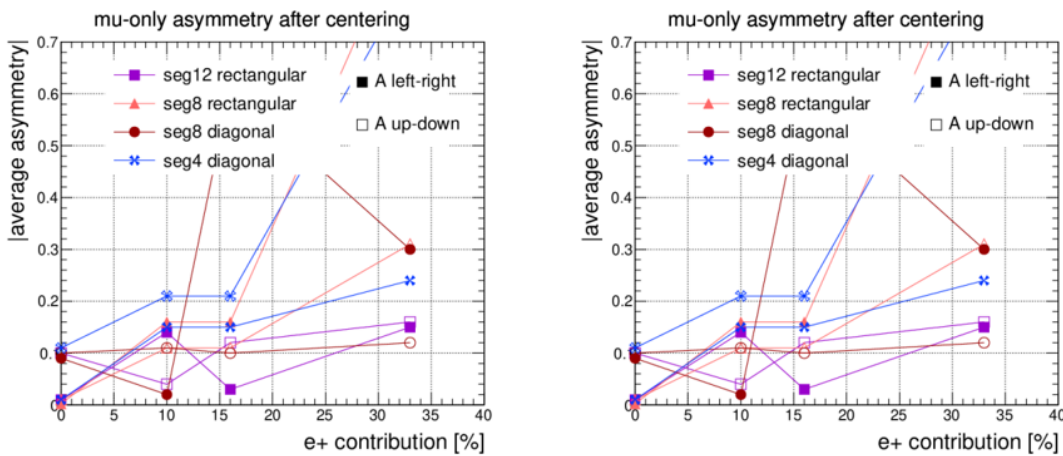


**Fig. 2.6:** Muon+positron (left) and muon-only (right) average asymmetries after the centering based on muon+positron counts. The asymmetries are plotted as a function of positron contribution in the beam.

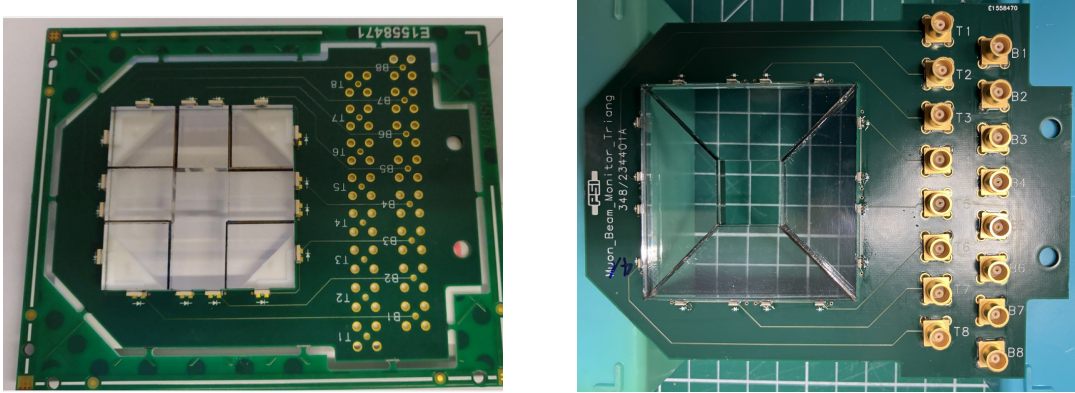


**Fig. 2.7:** The two versions of the beam monitor during the assembly.

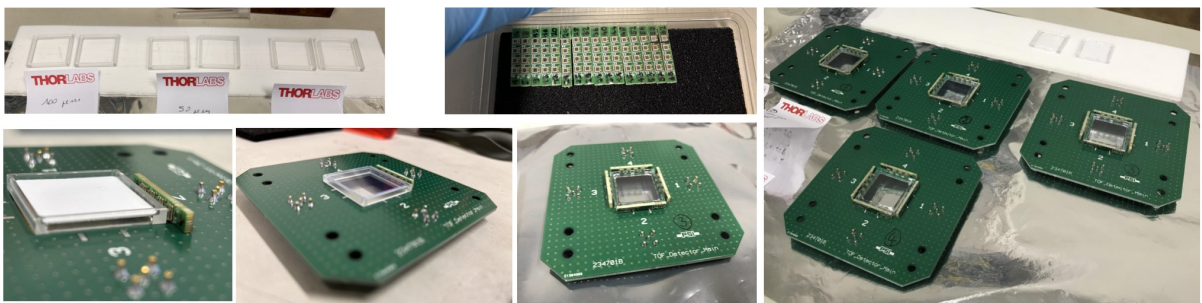


**Fig. 2.8:** The TOF detectors during the assembly procedure. The scintillating windows during the gluing into the light guide (top left). The MPPC boards, where four MPPCs are soldered in series to form a single channel (top middle). A detail of the light guide (Bottom-right).

a test setup for alternating magnetic fields. In 2024, the plan is to characterize the relative change in the initial muon spin after CW and CCW injection.

The TOF detectors consist of thin Eljen Technology EJ-212 plastic scintillators coupled to Hamamatsu silicon photomultipliers. Each detector has four channels, and their assembly details are shown in Fig. 2.8. The detectors aim for high detection efficiency (>95%) and timing resolution (<1 ns). Challenges include addressing the low number of collected scintillating photons due to the thin scintillator and handling a relatively high rate of thermal noise photon-electrons (~kHz). The flexible detector design, with four independent channels, allows for optimal threshold triggering to achieve high detection efficiency and timing resolution. Additionally, a GEANT4-based Monte Carlo simulation aids in optimizing the detector design and complements data analysis.

### 2.3.3 Entrance

To store muons at the center of the solenoid, a magnetic kick must be triggered at the right moment when the muon passes the weakly focusing field region. An entrance detector, crucial for generating the trigger signal, consists of two thin scintillator tiles for CW and CCW injection and a thicker scintillator with openings around the nominal reference trajectory of the muon. The trigger is initiated by the thin scintillator in anticoincidence with the thick one, reducing the required pulse rate of the kicker power supply from 120 kHz to 500 Hz. Phase I entrance detector designs are under investigation GEANT4-based simulation tools, namely MUSR SIM and G4BEAMLINE. The CAD design of the entrance detector is shown in Fig. 2.9.

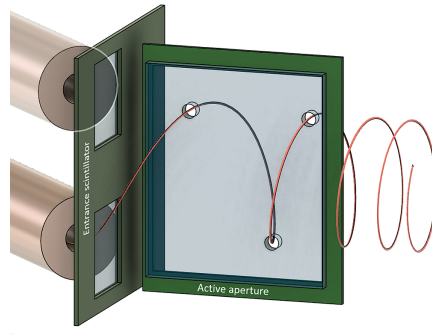


**Fig. 2.9:** CAD sketch of the entrance trigger. On the left, the muons exit the injection channel. The strong magnetic field immediately bends the muons onto a spiral trajectory. First, they pass through a thin ( $\leq 100 \mu\text{m}$ ) entrance scintillator. A thick second scintillator forms an active aperture, with holes at positions along the reference muon trajectory, which stops and detects muons that are outside the acceptance phase space. The trigger for the magnetic pulse, see Sec. 2.3.6, will be generated by the anticoincidence of the two.

A fast electronic circuit is essential for the timely activation of the magnetic pulse, with simulation studies emphasizing the critical need for pulse latency within the 120 ns to 150 ns window. Minimizing time delays throughout the system is crucial to meet these specifications.

In 2023, data analysis from a test beam at PSI in late 2022 was conducted. Two prototypes, featuring a thin entrance scintillator followed by a channel of four thick scintillators, all read out by SiPMs, were tested. The measured results, particularly in terms of collected light, showed good agreement with simulations. The results of the simulations and the dedicated beamtimes will be discussed in Ch. 3. Additionally, in Dec. 2023 new data, with a different readout scheme, were taken. The preliminary analysis (and promising results) of these data will be also discussed. Based on these findings, ongoing work focuses on finalizing the design of the entrance detector for its intended functionality.

Dallo status report 2023 ho tagliato "Power supply for muon trigger electronics", "Pre-amplifier and splitter", "Discriminator". Forse vale la pena di aggiungere? Plus, Injection o Entrance?

### 2.3.4 Superconducting injection channel

To allow the incoming muons to enter the magnet without being reflected or deviated by fringing fields an injection channel is needed. For reasons that will be discussed in the section dedicated to the systematics (see Sec. 2.5), we will actually require two symmetrical injections. The idea is to use a superconducting pipe: the fields around the pipe will generate Eddy currents which will, in turn, generate an opposite field inside the pipe, canceling the first. Clearly, the development of such a system is not trivial, and a precise study of the different shapes and materials is required. The hope would be to find a suitable *high-temperature* superconductor.

**Prototypes** Three different concepts for SC-prototype shields are currently being investigated and tested. The first concept employs high-temperature superconducting (HTS) tape<sup>1</sup> made of Yttrium barium copper oxide (YBCO), with a high  $T_c$  of 93 K, wound helically around a copper tube. The second prototype consists of Nb-Ti/Nb/Cu SC-sheets [12], with a  $T_c$  of 9.2 K, clamped

<sup>1</sup>2G HTS wire, S-Innovations, 2011-2020

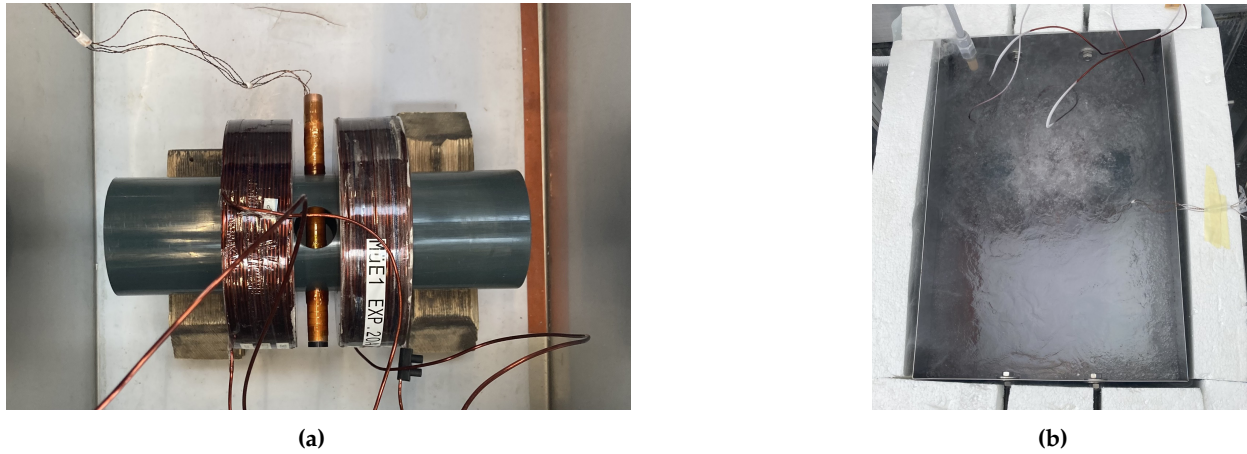


**Fig. 2.10:** (a) Experimental setup for testing of superconducting shield prototypes; Helmholtz coil pair and a HTS-prototype placed between the two coils; (b) setup submerged in  $\text{LN}_2$ .

around a hollow copper tube. Lastly, the third prototype will be a combination of a commercial SC-tube Bi-2223<sup>2</sup>, with an inner diameter of 15 mm, and a  $T_c$  between 105 K to 110 K, and a stack of discs made of rare-earth barium copper oxide (REBCO). This approach benefits from isotropically induced currents in the Bi-2223 tube, as well as persistent currents along the circular paths in the disks. Once the SC-prototypes are assembled, we will test them and compare the shielding factor to results from numerical models using the finite element method (COMSOL) to identify the most efficient configuration with the highest shielding factor.

**First tests** We are using a test setup made of a Helmholtz coil pair with a magnetic field strength of 100 mT and a liquid nitrogen ( $\text{LN}_2$ ) bath maintained at 77 K to evaluate the superconducting prototypes. The SC prototype, under study, will be placed between the two coils and the whole system will be submerged in the cryogenic bath, as shown in Figure 2.10.

Initial measurements were performed on a prototype with a YBCO-tape, helically wound around a copper tube with an inner diameter of 15 mm and a Bi-2223 sintered tube. Measurements of the magnetic field inside the prototypes were conducted using four Hall sensors<sup>3</sup>, distributed along a 3D-printed support inside the tube on four positions with a separation of 24 mm between each of them. This setup enabled the measurement of the magnetic field as a function of position. The measurements were taken at 77 K, with and without superconducting shielding, as illustrated in Figures 2.11 and 2.12.

### 2.3.5 Muon tracking

Although during physics runs it is important to minimize the number of interactions of the muon along the path, it is a cardinal step to prove the muons are following the correct path and are properly stored. On top of this, the momentum difference between the CW and CCW injection needs to be below 0.5%. For this reason, a removable muon-tracking device is under development. The proposed solution is a Time Projection Chamber (TPC) operated with an extremely light gas mixture based on helium, separated from the vacuum in the magnet bore by an extremely thin and

<sup>2</sup>CAN-superconductors, 2023

<sup>3</sup>THS119 Hall Sensors, TOSHIBA Electronic Devices & Storage Corporation, 2023

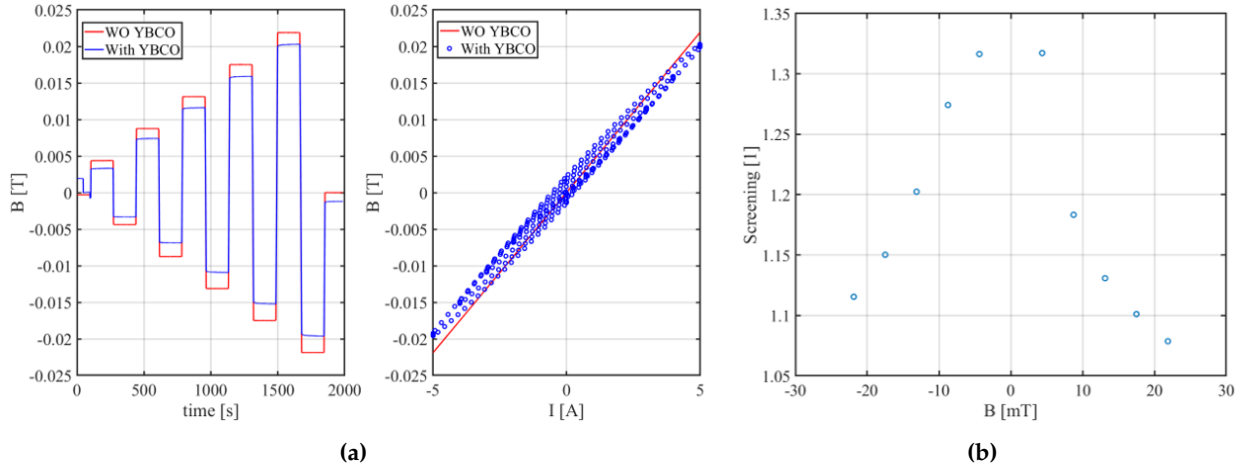


**Fig. 2.11:** Measurement of the YBCO prototype. (a) Measured magnetic field versus time, *left*, and versus coil current, *center*, at 77 K with and without prototype. (b) Shielding factor of YBCO prototype.

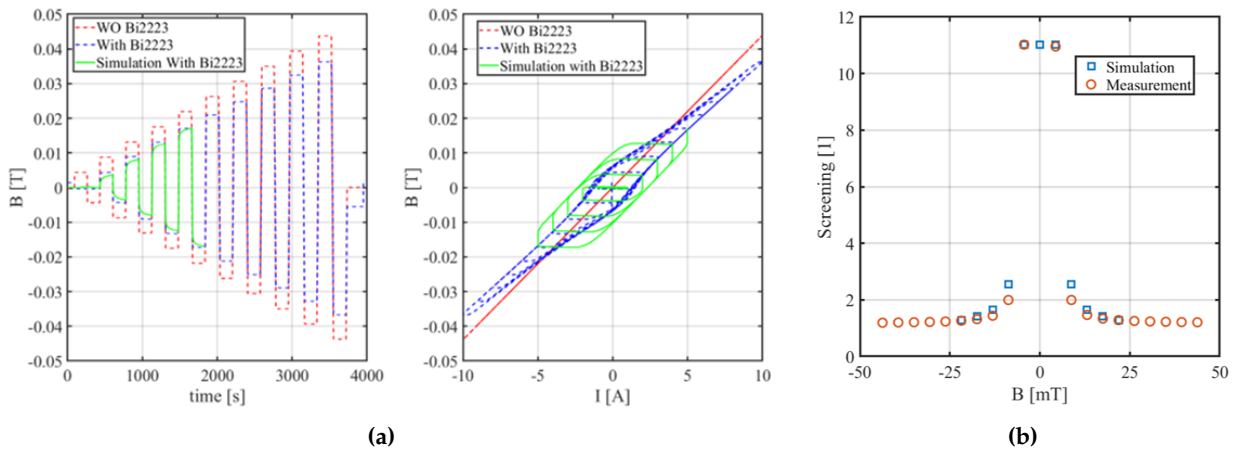


**Fig. 2.12:** Measurement of the Bi2223 prototype. (a) Measured magnetic field versus time, *left*, and versus coil current, *center*, at 77 K with and without prototype, and as simulated. (b) Comparison of experimental versus simulated shielding factor of Bi2223 prototype.

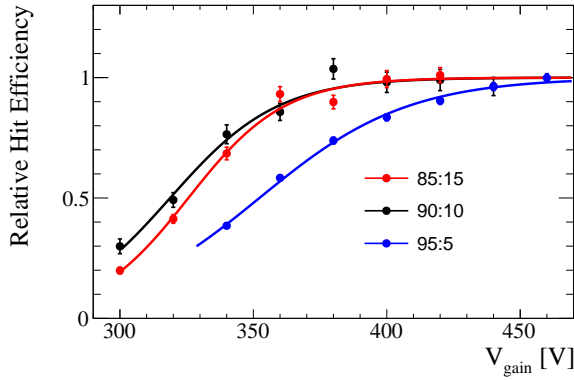


**Fig. 2.13:** Average number of reconstructed hits per track in the GridPix detector, as a function of mesh voltage, normalized to the asymptotic value of a sigmoid curve fitting the data points, for three different mixtures of helium-isobutane (95:5, 90:10, and 85:15).

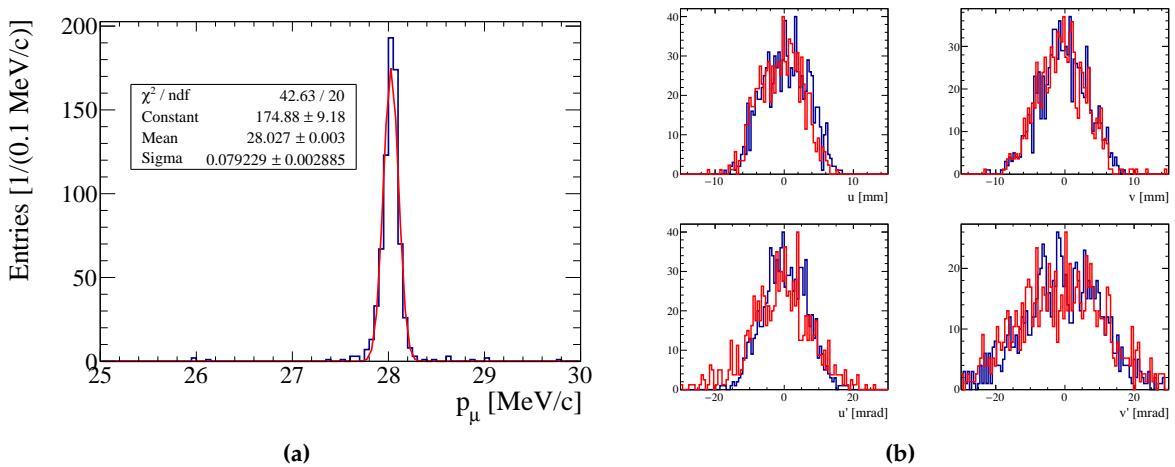


**Fig. 2.14:** Performance of a longitudinal TPC for the reconstruction of injected muons. (a) Reconstructed momentum (assuming 28 MeV/c initial momentum). (b) True (blue) and reconstructed (red) phase space coordinates and angles (u: horizontal; v: vertical).

vacuum-tight window (300 nm Silicon Nitride). As a readout structure for this TPC, the GRIDPIX detector is considered. GRIDPIX is a gaseous detector made of a conductive mesh implanted 50  $\mu\text{m}$  above a Timepix chip [13]. A voltage difference between the mesh and the chip produces an avalanche when drift electrons reach the mesh so that the GRIDPIX behaves like a sort of microscopic Micromegas.

**Beamtime** A prototype of this detector was developed with a single GridPix and flushed with helium-isobutane gas mixtures. It was tested in 2022, and the results have been published and can be found in [14]. The setup was quite simple: the beam was centered through the TPC and scintillators were used as an external trigger. During this testing, the detector was tested at different pressures and voltages, and with different mixtures of gas. In Fig. 2.13 the trend of the detection efficiency of GridPix as a function of the mesh voltage is shown, demonstrating that the detector can be used with these kinds of mixtures with a wide efficiency plateau. In Fig. 2.14 the reconstructed momentum and phase space.

Following a successful beam test, simulation studies were conducted to evaluate the tracking capabilities of a Time Projection Chamber (TPC) designed for tracking 28 MeV/c muons within the Phase I magnet. Two geometries were explored: a conventional longitudinal setup, where electrons drift along the  $z$  axis parallel to the magnetic field, and an unconventional radial configuration, with electron drift in the  $(x, y)$  plane. Typically, TPC track resolution is highest in the direction orthogonal to the drift, favoring the longitudinal option for optimal momentum resolution, while the radial geometry excels in measuring muon entrance angles. Despite assuming a detector pressure of 400 mbar in the simulations, the prevalence of multiple scattering effects diminishes the characteristic differences between the two geometries, making the resolution advantages less distinct. Achieving a momentum resolution surpassing 0.3 % appears feasible, and the phase space resolutions seem adequate for alignment purposes. In early 2024, a decision will be made regarding the TPC configuration, and the detector engineering will be finalized by year-end. This encompasses the development of mechanical mockups for installing silicon nitride entrance windows with a thickness of 300 nm. On the detector front, tests are scheduled to experimentally validate the proposal to operate the detector at sub-atmospheric pressure, considering the anticipated very high ionization rates in the Phase I experiment. The design process will be complemented by thorough simulation studies aimed at optimizing the final configuration.

### 2.3.6 Kicker

The prerequisite for the *frozen spin* is to first store the muon around the design orbit. This is achieved by applying a longitudinal kick, canceling the momentum component parallel to the magnetic field. The development of this element is non-trivial because of the stringent requirements on the strength, time scale, and residual effects of the kick. A weakly focusing static field, produced by a circular coil, ensures confinement. To compensate for muon acceleration upon entering the weakly focusing field, the pulsed field must be optimized to reduce longitudinal oscillations. The trigger signal for the magnet pulse, generated by the entrance detector previously discussed, selects muons within the storage phase space. Considering processing delays, the *on-demand* pulse generator must have an internal latency <60 ns.

The Institute for Pulsed Power and Microwave Technology at KIT developed high-voltage switching technology [15], meeting current pulse specifications. The generator, designed with a 20  $\mu$ s recovery time, can deliver up to 2000 pulses per second. Pulse amplitude and shape are defined passively by load circuit impedance characteristics. Lower inductance, achieved by splitting pulse coils into quadrants supplied in parallel, allows operation at 12 kV, supporting the required pulse width and reducing voltage ratings of components and cables.

**Prototype** A 100  $\mu$ m copper sheet prototype for the quadrant pulse coil configuration (Fig. 2.15(a)) was constructed, minimizing positron multiple scattering compared to 500  $\mu$ m thick plastic scintillating fibers. The measured inductance per loop was  $(76 \pm 3)$  nH, in line with the ANSYS model prediction of 79 nH.

ANSYS-generated field maps (Fig. 2.15(c) and(d)) simulated the kick and characterized field strength and inductance. The quadrant model's geometry (Fig. 2.15(b)) with overlapping longitudinal sections led to partial cancellation due to opposite polarities. The DC magnetic field map

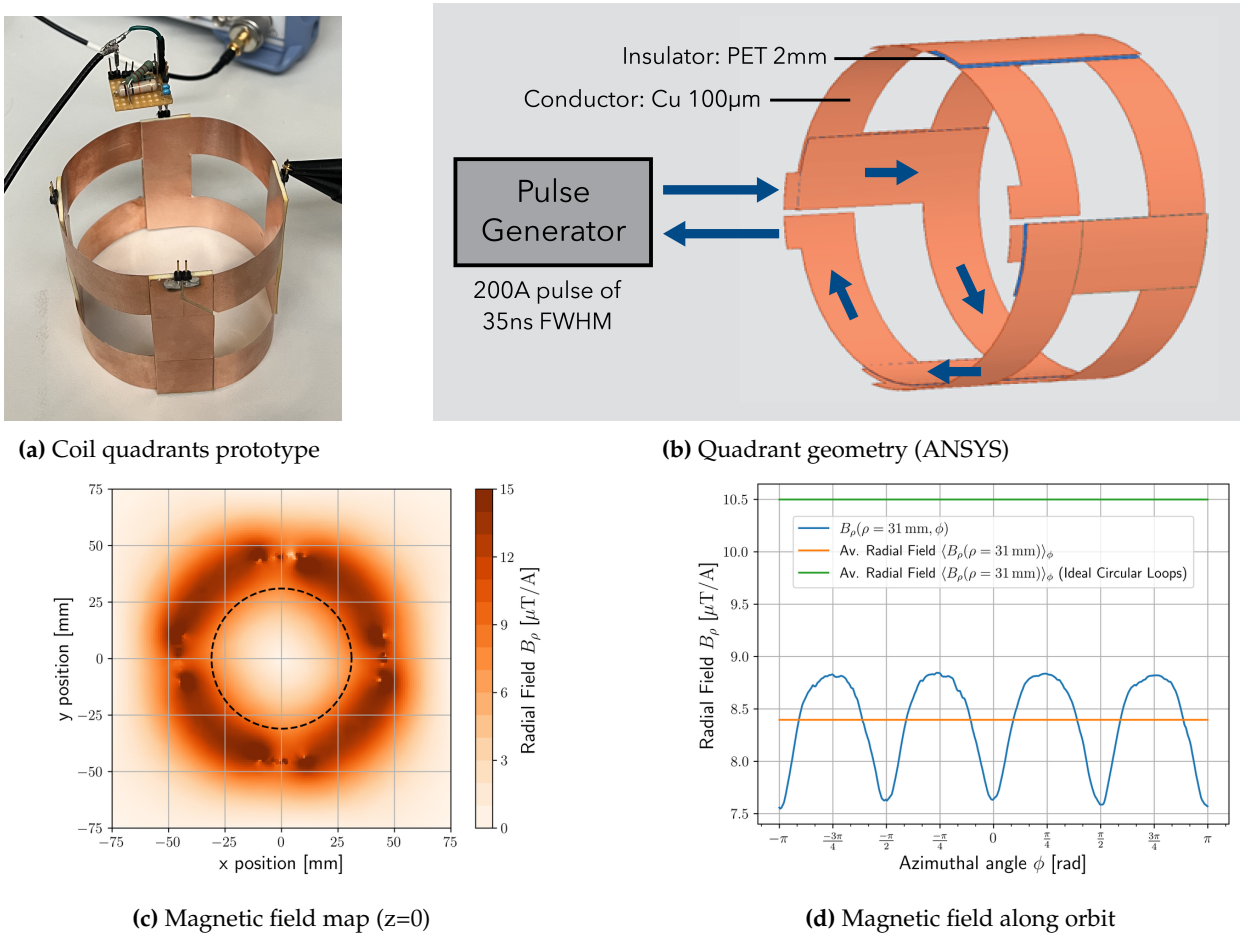


**Fig. 2.15:** The pulse coils, (a) prototype and (b) geometry implemented in ANSYS, are responsible for kicking the remaining longitudinal momentum to permit storage in a weakly-focusing magnetic field. They will be constructed from 100  $\mu\text{m}$  copper sheets to minimize multiple scattering without significantly increasing electrical resistance for frequencies  $\sim 10$  MHz. The ANSYS simulation produces field maps, shown on the central  $x - y$ -plane in (c) where the dashed black line shows the stored muon orbit. The average field strength over the orbit is  $8.4 \mu\text{T A}^{-1}$ , as shown by the orange line in (d), where the field strength is plotted over the orbit parametrized by the azimuthal angle  $\phi$ .

in the central ( $z = 0$ )  $x - y$ -plane is shown in(c), and plot (d) displays the field along the orbit, parameterized by azimuthal angle  $\phi$ .

The orange line at  $8.4 \mu\text{T A}^{-1}$  in plot (d) represents the average field strength over the orbit, falling 20% below the expected strength for ideal circular loops. Despite requiring a higher current for a given field strength, the quadrant model's advantage lies in the shorter pulse width allowed by low-inductance parallel circuits. The compact design minimizes stray capacitance and inductance. Supplying upstream and downstream segments in series within each quadrant ensures better longitudinal symmetry of the field, with equal current flow in both segments.

**Generator** The pulse generator design, developed in collaboration with the KIT team, adheres to constraints from injection simulations and systematic effects studies. Operating at 12 kV, it delivers 200 A to each coil quadrant. Load characteristics, shaping the pulse, are defined based on prototype measurements and ANSYS simulations. Inductive couplings between parallel circuits are determined from induced voltage measurements on the prototype.

The current design, shown in Fig. 2.16 includes resistance-capacitive (RC) damping elements

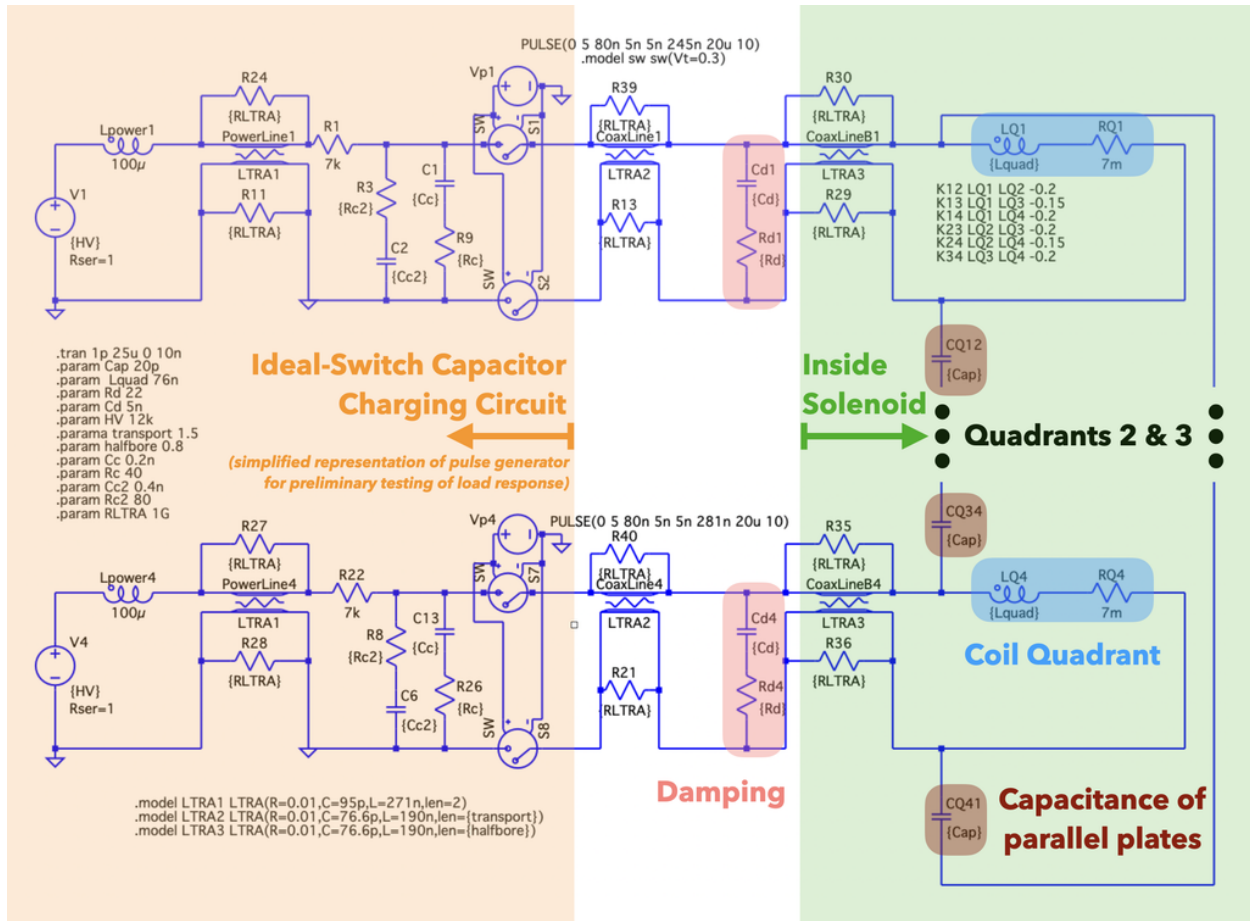


**Fig. 2.16:** Circuit model, developed in LTSpice, for the load attached to simplified charging-stage circuits using ideal switches. Transmission lines labeled *CoaxLine1-4* transmit from generator to the external flange of the solenoid; *CoaxLineB1-4* transmit from the flange to the center of the bore, where the coils are located. Inductive couplings between quadrants *i* and *j* are specified by the listed constants labeled *Kij*. Capacitive couplings between quadrants *i* and *j* are described by capacitors labeled *CQij*. The second and third quadrants are not shown for compactness.

on the coaxial cable, tuned to critically damp the primary pulse and suppress after-pulse oscillations. This avoids perturbing the muon orbit or inducing time-dependent spin precession signals. The pulse shape, influencing the applied momentum kick, is adjustable to maximize storage efficiency. Simulated current profiles, shown in Fig. 2.17, illustrate optimized damping for maximizing peak current and reducing after-pulse oscillations. The voltage over the charging capacitor *C1* demonstrates recovery within 1% of the nominal operating voltage after a 20  $\mu$ s delay, meeting the desired interval between muon triggers. We plan to commission and test the pulse generator in mid-2024 for the upcoming beam test. The circuit parameters are being finalized, while a full load circuit characterization, utilizing a network analyzer, is ongoing to refine the ANSYS model of the quadrant configuration.

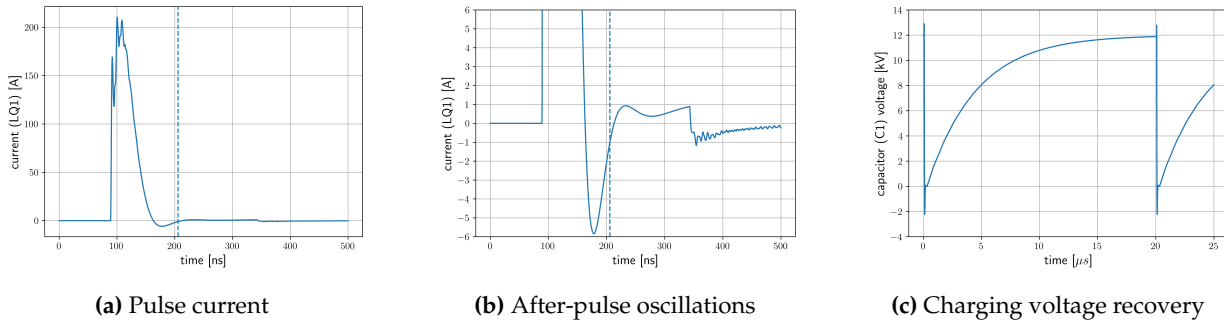


**Fig. 2.17:** Pulse current profiles simulated using the LTspice circuit model with parameters as shown in Fig. 2.16. The current plotted in (a) and (b) from  $t = 0$  (entrance) to  $t = 500\text{ ns}$  is for the first quadrant, labeled  $LQ1$  in Fig. 2.16. The dashed vertical line at  $210\text{ ns}$  indicates the time after which the current remains below  $\sim 1\text{ A}$ . The voltage over the capacitor labeled  $C1$  is plotted in (c), showing the recovery of the charging voltage within the desired  $20\text{ }\mu\text{s}$  duration.

### 2.3.7 Faraday rotator

To measure the field strength and time dependence of short high-intensity magnetic-field pulses, a compact sensor was designed. The sensor, based on Faraday rotation<sup>4</sup>, aims for a sensitivity of a few microtesla up to 200 MHz. Powered by a Toptica potassium laser, it employs a probe with a polarizer, a  $1\text{ cm}^3$  TGG crystal with a high Verdet<sup>5</sup> constant, a right-angle mirror, and an analyzer. The laser beam passes twice through the crystal, enhancing sensitivity. In Fig. 2.18 a picture of it. The angular shift in the polarization plane is measured by a ThorLabs photodiode.

The sensor's performance was tested by applying a small AC magnetic field at 100 kHz to the TGG crystal using a custom copper coil. The setup, shown in Fig. 2.18, achieved microtesla sensitivity, crucial for the 100 kHz to 10 MHz range. The experimental results demonstrate efficient measurement of microtesla magnetic fields, enhanced by strong laser power and noise cancellation using a differential photodiode. The compact design enables measurements in confined spaces, crucial for the muonEDM experimental setup.

### 2.3.8 Frozen-spin electrodes

After the muon has been successfully stored around the design orbit the next step is to apply a radial electric field. The strength of this field is going to modify the frequency of the g-2 precession, eventually *freezing* the spin (eq. 2.5) along the momentum direction. The radial electric field will be induced by concentric cylindrical electrodes at  $r = 40\text{ mm}$  (grounded) and  $r = 20\text{ mm}$  (high voltage), requiring  $\sim 6\text{ kV}$  to achieve a frozen-spin field strength of  $\approx 3\text{ kV/cm}$  at the nominal orbit radius ( $\rho = 31\text{ mm}$ ). A momentum bite of 0.5% leads to a limit of approximately 1% for matching the frozen-spin field strength over the momentum distribution, requiring a voltage precision better than 0.5%. To control systematic effects from a longitudinal electric field, the applied voltage stability must be constrained to  $\sim 10^{-4}$ . The 20HVA24-BP1-F high voltage amplifier by *Advanced Energy*<sup>6</sup> meets these requirements with limited voltage ripple and a bipolar supply,

<sup>4</sup>The Faraday effect causes a polarization rotation which is proportional to the projection of the magnetic field along the direction of the light propagation.

<sup>5</sup>The Verdet constant describes the strength of the Faraday effect in a material.

<sup>6</sup>[www.advancedenergy.com/en-us/products/dc-dc-conversion-products/high-voltage-boost-\(u-v\)/high-voltage-amplifiers/hva-series/](http://www.advancedenergy.com/en-us/products/dc-dc-conversion-products/high-voltage-boost-(u-v)/high-voltage-amplifiers/hva-series/)

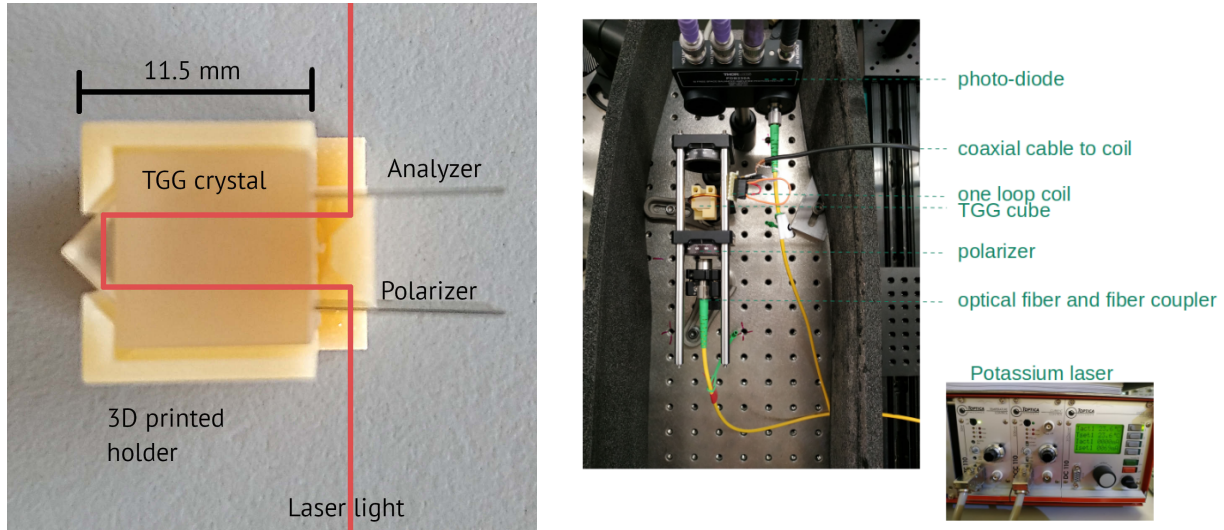


**Fig. 2.18:** Left: The TGG crystal holder with polarizer and analyzer. Center: Setup for characterization of the TGG crystal and verification of the performance of the magnetometer. The one loop coil serves to produce a micro-Tesla level field at 100 kHz. Right: The potassium laser used to power the probe.

enabling calibration of the frozen-spin field strength. This calibration involves observing spin precession due to the anomalous magnetic moment when the electric field is offset from  $E_f$ . The device will be tested with existing electrode prototypes to verify stability under applied high voltage in a vacuum, facilitating electric field measurements and geometric alignment. This progress informs the final electrode system design for integration in 2024, with further development leading to incorporation into anticipated beam tests in 2025.

**Prototype** Prototype electrodes, made from aluminized Kapton films, were designed to study eddy currents induced by the magnetic field pulse. To minimize eddy currents, material with higher resistivity or optimized geometry is crucial. Measurement of the radial component at the muon orbit is necessary for shielding determination and design optimization. Using a 5 mm radius pickup coil, voltages induced by a 10 MHz sinusoidal current in the pulse coils were compared for various electrode configurations. A ground electrode made from homogeneously aluminized Kapton exhibited a maximum shielding factor of 1.9(1), increasing to 3.0(2) with the HV electrode installed. However, azimuthal asymmetry along the muon orbit was observed due to the discontinuity at the gluing seam.

A new prototype with aluminum distributed in 2 mm stripes (2.2 mm pitch) was prepared (see Fig. 2.20(a)). Measurements with this segmented electrode showed shielding factors  $< 1.1$  (90% C.L.), indicating effective restriction of radial eddy-current flow across length scales comparable to the coils. This allows near-complete transmission of the radial field at frequencies relevant to the magnetic field pulse, with no measurable shielding or azimuthal asymmetry. Noting that a segmented electrode introduces periodic field non-uniformity along the orbit, investigations were conducted to explore possible systematic effects arising from the accumulation of a geometric phase. For instance, separating the electrodes into 100 longitudinal strands would induce  $E$ -field oscillations of approximately 40 GHz. Implemented in ANSYS with 60 wires of 1 mm diameter for the high voltage electrode and 120 for the ground (Fig. 2.20(b)), the transverse cross-section of the electric field shows negligible high-frequency oscillations for a displaced orbit (6 mm). The study

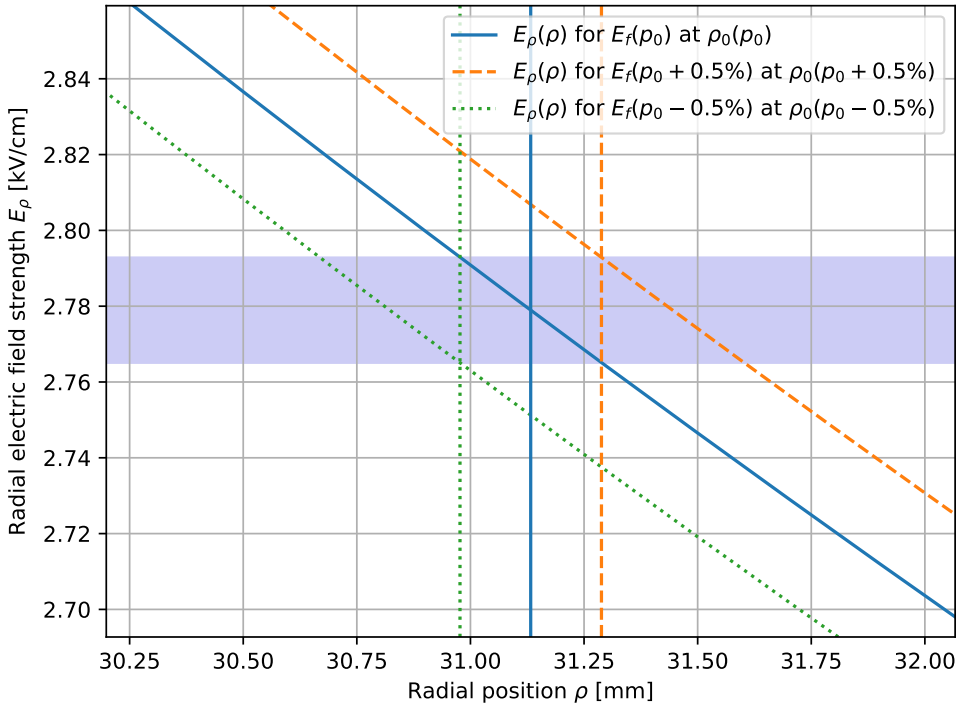


**Fig. 2.19:** The radial electric field corresponding to the frozen-spin field strength at the nominal orbit radius is plotted over the radial position. The dashed vertical lines indicate the radial offset due to changes in momentum  $\pm 0.5\%$ . The dashed curves indicate the electric field which would satisfy the frozen-spin condition for these shifted momenta and radii. The resultant discrepancy is  $\sim 1\%$ , limiting the precision necessary for the electric field strength given a momentum bite of  $0.5\%$ .

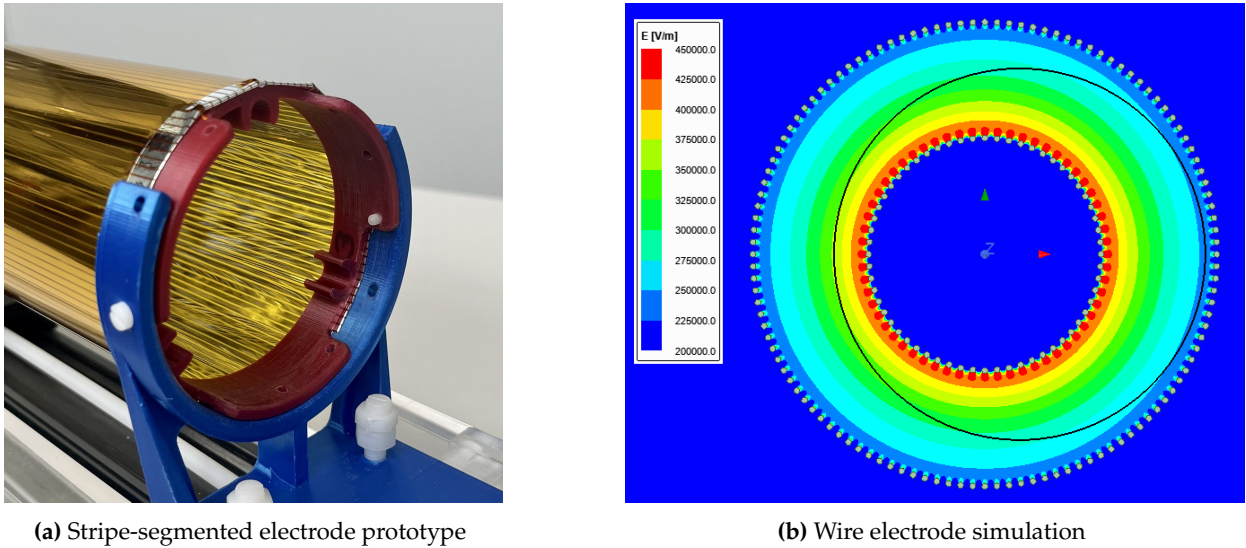
demonstrates that a segmented electrode will not introduce additional systematic effects.

### 2.3.9 Positron tracking

The development of the positron tracker has been a big part of my work in the collaboration. For this reason, an in-depth description will follow in a dedicated chapter (see Ch. 4) while here we will just outline the basic idea. The project started with a ‘two subsystems’ approach:

- A silicon pixel external tracker will be used to track precisely the transverse position of the positron. This sub-detector aims to measure the g-2 precession to fine-tune the radial electric field to achieve the frozen-spin condition. A straw-tube-based alternative design for this sub-detector has also been studied but later discarded.
- An internal scintillating fiber detector (with comparable resolution on the transverse position) will complement the silicon pixel with additional hits. The requirement is to have a better resolution on the longitudinal position of the hits to measure the EDM by looking at the pitch of the outgoing helical track. I dedicated most of my effort to this sub-detector.

Unfortunately, the development of the Pixel detector met some complications and we will rely exclusively on the scintillating fibers during Phase I, prompting a review of the whole detector design.



(a) Stripe-segmented electrode prototype

(b) Wire electrode simulation

**Fig. 2.20:** A segmented electrode prevents eddy current shielding of the magnetic pulse, while preserving the required electric field properties. A prototype made from aluminized Kapton (a) showed negligible shielding, while simulation studies using a wire array electrode modeled in ANSYS (b) show no significant systematic effects and sufficient uniformity of the field in the storage region.

## 2.4 Sensitivity

If the muon spin has a component parallel to the main magnetic field, the difference in probability  $p$  for positron emission along ( $p_\uparrow$ ) or opposite ( $p_\downarrow$ ) the magnetic field will generate an asymmetry

$$A = \frac{p_\uparrow - p_\downarrow}{p_\uparrow + p_\downarrow} \quad (2.7)$$

For an EDM-induced spin precession, the observable is the time derivative of  $A$ . The variables  $p_\uparrow$  and  $p_\downarrow$  are the result of the angular distribution of Michel decay positrons

$$W(x, y) dx dy = x^2 ((3 - 2x) + (2x - 1)y) dx dy, \quad (2.8)$$

where  $x = E/E_{\max}$ , and  $y = |\vec{p}_\mu \cdot \vec{p}_e|$  is the angle between the momenta of the muon and decay positron. We can express the non-boosted variables in terms of the boosted ones, such as

$$u = \frac{E'}{E'_{\max}} = x \frac{\sqrt{\gamma^2(y + \beta)^2 + 1 - y^2}}{\gamma(1 + \beta)}, \quad v = \cos \left( \arctan \frac{E'_x}{E'_z} \right) = \frac{1}{\sqrt{(E'_x/E'_z)^2 + 1}}. \quad (2.9)$$

Expressing non-boosted variables with these, and with some manipulation, we obtain the boosted energy spectrum  $N(u)$ , the asymmetry  $A(u, v)$ , and its rate of change  $\partial_\Psi A$  with respect to the polar angle  $\Psi$  of the spin. For details, see [16]. These variables are shown in Fig. 2.21 for phases I and II. The aim is then to optimize the sensitivity by applying a selection of positron energies and emission angles at the cost of statistics. Therefore, we optimize the sensitivity to  $d_\mu$ :  $\sigma(d_\mu) \sim 1/(\alpha\sqrt{N})$  and define the figure of merit, where  $N_{e^+}$  is the number of detected decay positrons,  $N_{\mu^+}$  is the total number of muons stored, and  $\tilde{\alpha}$  is the weighted average of the rate of change of

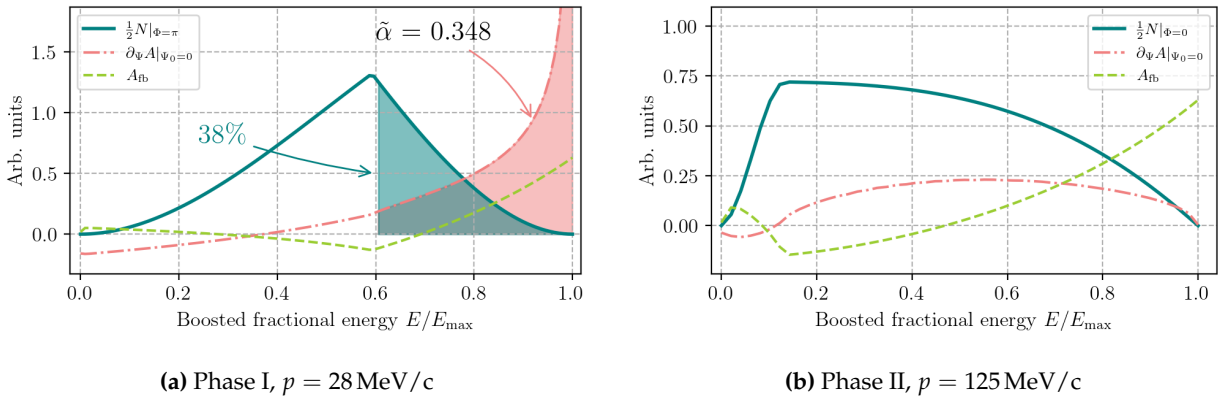


**Fig. 2.21:** Positron energy distribution  $N$ , rate of change of asymmetry  $\partial_\Psi A$  evaluated for spin pointing opposite and along the momentum, respectively for Phase I and II. The g-2 precession is deduced from the asymmetry ( $A_{fb}$  green) between the energy distributions, while the EDM signal is proportional to the directional asymmetry (red). The spectrum is divided into two to improve the visibility of the plot. The arrows point to the mean rate of change of asymmetry  $\tilde{\alpha}$  and the fraction of the positron spectrum at the optimal threshold using the T-method.

the parity-violating decay asymmetry.

$$F = \tilde{\alpha} \sqrt{\frac{N_{e^+}}{N_{\mu^+}}}; \quad \tilde{\alpha} = \frac{1}{N_{\mu^+}} \int \partial_\Psi A(u) N(u) du, \quad (2.10)$$

At this point, we have a few options:

- A The first option is to count all positrons, independently of the emission variables. This leads to  $F = \tilde{\alpha} \approx 0.166$  for both phases I and II
- T The second option is to count only positrons above a given fractional energy  $u_0$ . For the two phases, maximizing the figure of merit results in 0.22 for  $u_0 \approx 0.60$  and 0.17 for  $u_0 = 0.18$
- W Last option is to define emission angle and/or fractional energy bins. For each bin  $(u, \theta, \phi)$  we can define a figure of merit  $W_{ijk} = \alpha_{ijk} \sqrt{N_{ijk}}$ , with  $N_{ijk}$  as integral of  $N(u, \theta, \phi)$  on the  $ijk$  bin, and  $\alpha_{ijk}$  the integral of  $\partial_\Psi A(u, \theta, \phi) N(u, \theta, \phi) / N_{ijk}$ . The resulting figure of merit is then  $\mathcal{W} = \sqrt{\sum_{ijk} W_{ijk}^2}$  and its maximum is  $\approx 0.29$ . On a practical level, it depends on the reconstruction in the different bins and is evaluated as:

$$W_{ijk}^2 = \frac{(N_{\uparrow} - N_{\downarrow})^2}{N_{\uparrow} + N_{\downarrow}}, \quad \text{and} \quad \dot{A}_{ijk} = \frac{d}{dt} \left( \frac{N_{\uparrow} - N_{\downarrow}}{N_{\uparrow} + N_{\downarrow}} \right)$$

All these values are illustrated in Tab. 2.2. The key aspects are clearly shown in Fig. 2.21 and here summarized. In Phase I, the impact of positrons with energy below 27.6 MeV on measurement asymmetry is negligible. Optimal sensitivity is achieved when considering positrons within an opening angle range of  $30^\circ$  to  $90^\circ$ , provided their energy exceeds 41 MeV. For Phase II, valuable asymmetry information is present in emission angles up to  $135^\circ$  and energies surpassing 21 MeV.

## 2.5 Systematics

Like for the majority of the experiment at the edge of our current understanding, the systematic effects play a key role. Most of the studies on this topic were performed by Chavdar Dustov, Post

Method	Phase I				Phase II			
	Threshold $\times 68.9 \text{ MeV}$	$\tilde{\alpha}$	$N_{e^+} / N_{\mu^+}$	FoM	Threshold $\times 140.2 \text{ MeV}$	$\tilde{\alpha}$	$N_{e^+} / N_{\mu^+}$	FoM
Simple	None	0.166	1.0	0.166	None	0.166	1.0	0.166
T-method	0.596	0.348	0.384	0.216	0.183	0.195	0.835	0.178
W-method (20 energy bins)	None	0.251	1.0	0.251	None	0.183	1.0	0.183
W-method (20 energy bins)	0.4	0.280	0.800	0.250	0.15	0.194	0.876	0.183
W-method (20x20x20 bins)	None	0.292	1.0	0.292	None	0.280	1.0	0.280
W-method (20x20x20 bins)	0.4	0.326	0.800	0.291	0.15	0.299	0.876	0.280

**Tab. 2.2:** Summary of analysis methods. The ratio  $N_{e^+} / N_{\mu^+}$  is the fraction of detected positrons with respect to the total number of injected muons and  $\tilde{\alpha}$  is the mean asymmetry above a threshold. The presented values are the theoretical maximum and do not include the effects of multiple scattering of positrons or limited detector acceptance.

Doc at PSI. The key aspects have been compiled in a recent publication [16], on which this section relies. For the precursor and final experiment, the expected angular velocity of the spin induced by the EDM is here evaluated. These values give us a benchmark for the systematic effects.

$$\dot{\Pi} = \begin{cases} 21.15 \mu\text{rad}/\mu\text{s}; & \text{for } \beta = 0.26 \text{ and } d_\mu = 3 \times 10^{-21} \text{ ecm} \\ 1.26 \mu\text{rad}/\mu\text{s}; & \text{for } \beta = 0.77 \text{ and } d_\mu = 6 \times 10^{-23} \text{ ecm} \end{cases}$$

### 2.5.1 Possible sources of spin precessions

We will now outline different sources of possible spin precession. From each of these sources, a limit on a specific aspect of the experiment was extracted.

**Radial** If the particle stays at a constant radius, the coupling of the MDM with the radial component of the weakly focusing field generates a precession. A similar effect arises from the non-zero longitudinal electric field. This component, seen from the muon reference frame, corresponds to a radial magnetic field and also leads to a radial precession.

**Azimuthal** When stored in the equilibrium orbit the muons oscillate. Because of this oscillation, the momentum is not perfectly perpendicular to the longitudinal magnetic field. This produces a non-zero projection of the magnetic field along the trajectory. On top of this, if the radial electric field is not *exactly* set to the value required to freeze the spin, it will interact with the longitudinal momentum of the particle.

**E imperfections** Another source of precession can be the change of the electric field along the orbit. This can be the case if the axes of the magnetic field and electric fields are displaced or at an angle. The effect of such imperfections can be mitigated by developing two injection channels

and inverting the  $B$  field, obtaining ‘specular’ trajectories (CW and CCW). Just like for the other sources, we will omit the calculations, which can be found in the reference [16]. In these effects, it is important to consider the cylindrical symmetry of the problem and evaluate the effects averaged over the circular orbit. In the next order, the deviations from circular to distorted orbits are also an interesting exercise, although the approximation holds quite well.

**Apparent spin precession** As already discussed, a longitudinal component of the spin produces an asymmetry. This asymmetry changes in time because of the coupling of the spin with the EM fields. What is measured is this rate of change of the asymmetry. The number of observed particles in a direction will be  $N_{\uparrow} = \Omega_{\uparrow}\varepsilon_{\uparrow}p_{\uparrow}N_{\mu^+} = \kappa_{\uparrow}p_{\uparrow}N_{\mu^+}$ , where  $\kappa$  takes into account the acceptance and efficiency of the detector, while  $p$  is the probability and  $N_{\mu^+}$  the number of stopped muons.

$$A_m = \frac{1}{N_{\mu^+}} \left( \frac{n_{\uparrow}}{\kappa_{\uparrow}} - \frac{n_{\downarrow}}{\kappa_{\downarrow}} \right) \quad (2.11)$$

This equation highlights why a requirement on the temporal stability of the detectors is necessary to avoid detecting apparent asymmetry.

### 2.5.2 Comparison with GEANT4

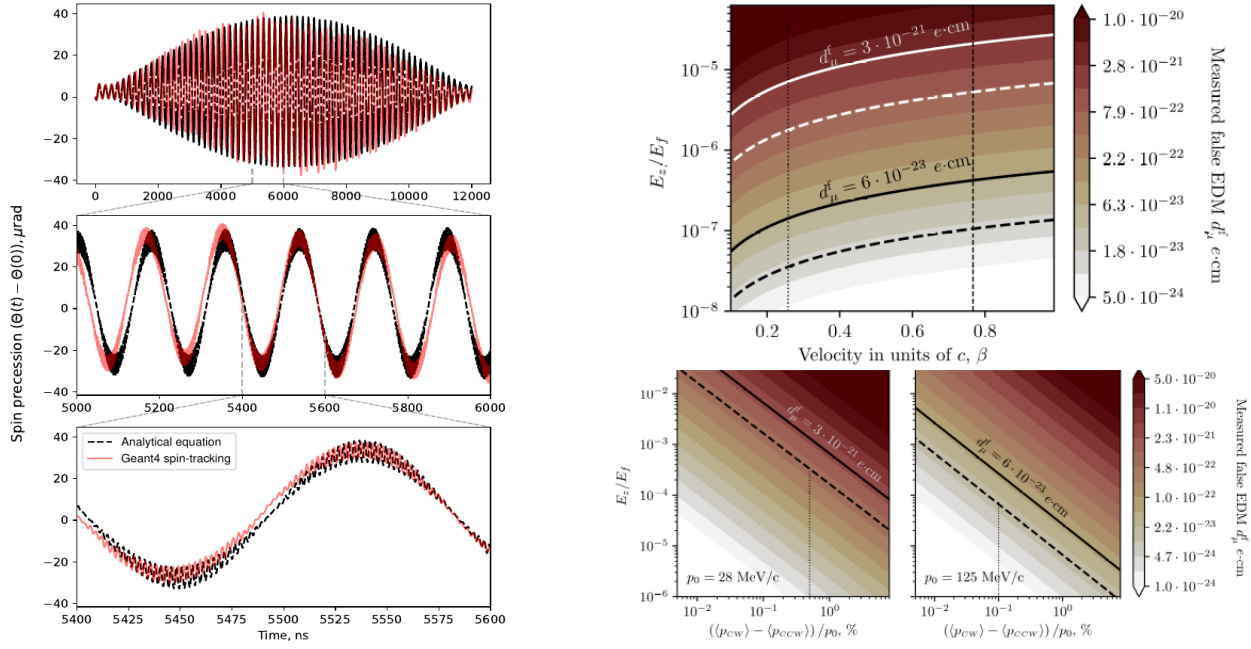
The analytical part of this study has two types of parameters: 8 stochastic, defining the initial condition of every stored particle, and 10 constant/slowly changing parameters of the experimental setup. To verify the results of the analytical mode, a GEANT4 simulation was developed. In this simulation, the EM fields can be calculated or interpolated from ANSYS field maps. The simulation tracks the spin orientation in the muon and in the laboratory reference frame, which can be then compared with the analytic results. The example in Fig. 2.22 shows very good agreement.

### 2.5.3 Constraints

To extract from each aspect a constraint on the variables at play in the experiment is not an easy task. Although we highlighted some key sources of real/apparent spin precession, we will not delve into the evaluation of the actual constraints and the way they can be extracted, which is partially described in [16]. An example of the plot showing this type of study is in Fig. 2.22, in which the measured ‘false’ EDM is shown as a function of the longitudinal E field and  $\beta$  of the muons. The introduction of the CW and CCW injection brings us to the plot in Fig. 2.23. The summary of the current understanding of the systematics is shown in Tab. 2.3. For each entry of this table plots similar to Fig. 2.22 or Fig. 2.23 have been used, but we will not include them. For the detail see [16].

## 2.6 Schedule

As we just saw, although the development of the precursor is moving at a very nice speed, the tasks are very challenging. To put in perspective the current understanding of the different challenges and time constraints, we add here the schedule that was included in the proposal of the



**(a)** Comparison between the spin precession analytical description and the GEANT4 tracking.

**(b)** Constraints to avoid asymmetry rising from the electric fields. The vertical lines refer to the two Phases I and II.

**Fig. 2.22:** The study on systematics has two main parts: (a) developing and crosschecking the results extracted analytically and (b) extracting limits on the relevant parameters.

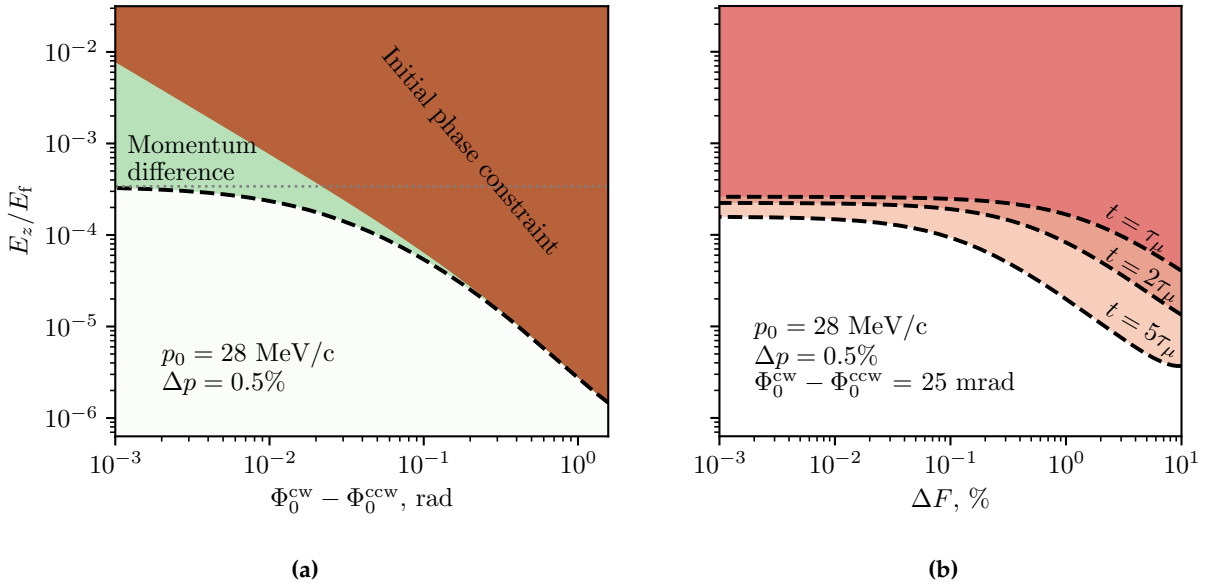


**Fig. 2.23:** Limit on the longitudinal  $E$ -field,  $E_z$ , when considering alternating CW/CCW injections, where the difference in mean momentum averaged over all injected muons for injections of CW and CCW beams is fixed at  $\Delta p = 0.5\%$ . a) Shows the limit as a function of the initial phase difference  $\Phi_0^{CW} - \Phi_0^{CCW}$ . The horizontal dashed line indicates the limit coming from  $\Delta$ , keeping all other parameters equal between the two injection modes. The brown area is the constraint that results from the difference in the initial phase at  $\Delta p = 0\%$ . The green area and its thick dashed line edge show the combined limits of the two effects. b) Shows the limit as a function of the difference in  $E$ - or  $B$ -field for CW and CCW orbits, at various times.  $\Delta F = 2(F^{CW} - F^{CCW})/(F^{CW} + F^{CCW})$ , where  $F \in \{B_z, \tilde{E}_\rho\}$ , while the difference in initial phases was fixed at 25 mrad.

Systematic effect	Constraints	Phase I		Phase II	
		Expected value	Syst. ( $\times 10^{-21} e\cdot\text{cm}$ )	Expected value	Syst. ( $\times 10^{-23} e\cdot\text{cm}$ )
Cone shaped electrodes (longitudinal E-field)	Up-down asymmetry in the electrode shape	$\Delta_R < 30 \mu\text{m}$	0.75	$\Delta_R < 7 \mu\text{m}$	1.5
Electrode local smoothness (longitudinal E-field)	Local longitudinal electrode smoothness	$\delta_R < 3 \mu\text{m}$	0.75	$\delta_R < 0.7 \mu\text{m}$	1.5
Residual B-field from kick	Decay time of kicker field	$< 50 \text{ ns}$	$< 10^{-2}$	$< 50 \text{ ns}$	0.5
Net current flowing muon orbit area	Wiring of electronics inside the orbit	$< 10 \text{ mA}$	$< 10^{-2}$	$< 10 \text{ mA}$	0.3
Early-to-late detection efficiency change	Shielding and cooling of detectors	–	–	–	–
Resonant geometrical phase accumulation	Misalignment of central axes	Pitch $< 1 \text{ mrad}$ Offset $< 2 \text{ mm}$	$2 \times 10^{-2}$	Pitch $< 1 \text{ mrad}$ Offset $< 2 \text{ mm}$	0.15
TOTAL			1.1		2.2

**Tab. 2.3:** Summary of systematic effects for both phases of the experiment. The determination of the effects related to early-to-late detection efficiency changes is currently under evaluation.

experiment in 2022. Fig. 2.24 is a schedule on the short period up to the long shut-down, in which 6 main milestones are highlighted:

- 1 Demonstration of off-axis injection
- 2 Muon selection and generation of trigger
- 3 Generation of the pulsed magnetic field and measurement of eddy-currents
- 4 Stopping of muons and detection of  $(g - 2)$  precession
- 5 Adjusting the electric field by tuning  $(g - 2)$  precession to zero
- 6 Data-taking in muon EDM mode

Fig. 2.25 goes beyond the long shut-down and covers the full life of the experiment, up to 2033.

## 2.7 Conclusions

After reviewing the concept of EDM, the current limits, and the frozen spin technique, we described the MuEDM experiment. A description of the different subsystem and their current status was given, leaving the muon detection and the positron tracking for the Ch. 3 and Ch. 4. A status on the study of the systematics and a brief section on the upcoming schedule end the chapter. The experiment is still in an early phase but a lot of progress has been made during the last 2/3 years.

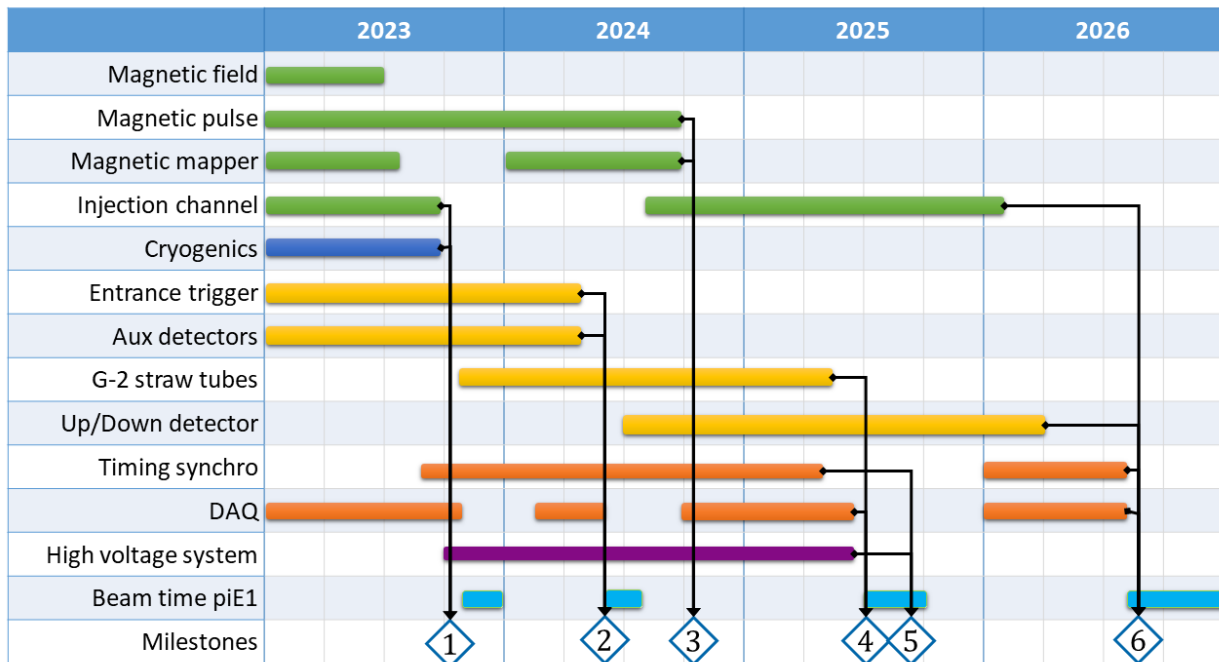


**Fig. 2.24:** ‘Short’ term muEDM schedule, with highlighted the 6 main milestones up to the *long shutdown*. Milestones: 1) off-axis injection; 2) generation of the entrance trigger; 3) generation of the pulsed B field; 4) detection of  $g - 2$ ; 5) adjust  $g - 2$  to zero; 6) EDM data taking.

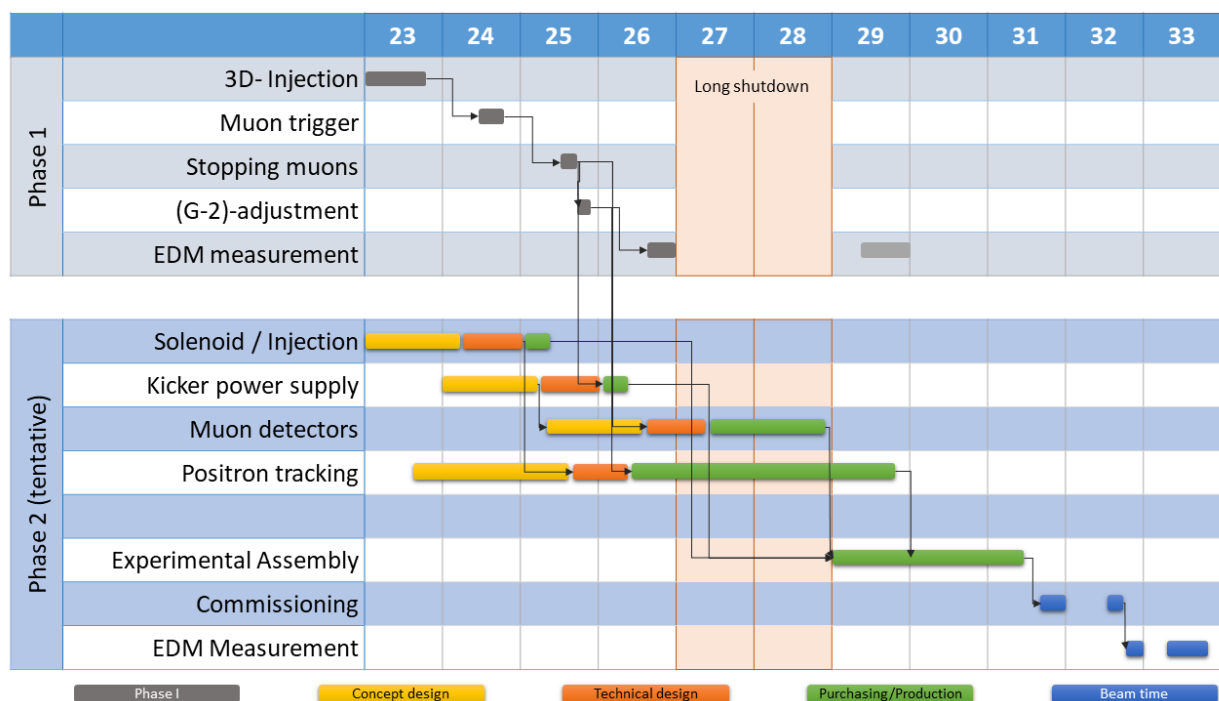


**Fig. 2.25:** ‘Long’ term muEDM schedule, with the different phases up to the end of the experiment.

# Bibliography on muEDM

- [1] Yannis K. Semertzidis et al. "A sensitive search for a muon electric dipole moment". In: *AIP Conf. Proc.* 564.1 (2001). Ed. by G. Cantatore, pp. 263–268. DOI: 10.1063/1.1374993.
- [2] A. Adelmann et al. "Compact storage ring to search for the muon electric dipole moment". In: *J. Phys. G* 37 (2010), p. 085001. DOI: 10.1088/0954-3899/37/8/085001.
- [3] Hiromi Iinuma. "New approach to the muon g-2 and EDM experiment at J-PARC". In: *J. Phys. Conf. Ser.* 295 (2011). Ed. by Hans Stroher and Frank Rathmann, p. 012032. DOI: 10.1088/1742-6596/295/1/012032.
- [4] Hiromi Iinuma et al. "Three-dimensional spiral injection scheme for the g-2/EDM experiment at J-PARC". In: *Nucl. Instrum. Meth. A* 832 (2016), pp. 51–62. DOI: 10.1016/j.nima.2016.05.126.
- [5] A. Adelmann et al. "Search for a muon EDM using the frozen-spin technique". In: (Feb. 2021). arXiv: 2102.08838 [hep-ex].
- [6] Mikio Sakurai et al. "muEDM: Towards a search for the muon electric dipole moment at PSI using the frozen-spin technique". In: *24th International Symposium on Spin Physics*. Jan. 2022. arXiv: 2201.06561 [hep-ex].
- [7] Kim Siang Khaw et al. "Search for the muon electric dipole moment using frozen-spin technique at PSI". In: *PoS NuFact2021* (2022), p. 136. DOI: 10.22323/1.402.0136. arXiv: 2201.08729 [hep-ex].
- [8] C. Abel et al. "Measurement of the Permanent Electric Dipole Moment of the Neutron". In: *Phys. Rev. Lett.* 124 (8 Feb. 2020), p. 081803. DOI: 10.1103/PhysRevLett.124.081803. URL: <https://link.aps.org/doi/10.1103/PhysRevLett.124.081803>.
- [9] V. Andreev et al. "Improved limit on the electric dipole moment of the electron". In: *Nature* 562.7727 (2018), pp. 355–360. DOI: 10.1038/s41586-018-0599-8.
- [10] Yohei Ema, Ting Gao, and Maxim Pospelov. "Improved Indirect Limits on Muon Electric Dipole Moment". In: *Phys. Rev. Lett.* 128.13 (2022), p. 131803. DOI: 10.1103/PhysRevLett.128.131803. arXiv: 2108.05398 [hep-ph].
- [11] G. W. Bennett et al. "An Improved Limit on the Muon Electric Dipole Moment". In: *Phys. Rev. D* 80 (2009), p. 052008. DOI: 10.1103/PhysRevD.80.052008. arXiv: 0811.1207 [hep-ex].
- [12] D. Barna et al. "NbTi/Nb/Cu multilayer shield for the superconducting shield (SuShi) septum". In: *IEEE Trans. Appl. Supercond.* 29.1 (2018), p. 4900108. DOI: 10.1109/TASC.2018.2872860. arXiv: 1809.04330 [physics.acc-ph].

- [13] X. Llopart et al. "Timepix, a 65k programmable pixel readout chip for arrival time, energy and/or photon counting measurements". In: *Nucl. Instr. Meth. Phys. Res. A* 581.1-2 (Oct. 2007), pp. 485–494.
- [14] G. Cavoto et al. "Operating the GridPix detector with helium-isobutane gas mixtures for a high-precision, low-mass Time Projection Chamber". In: *JINST* 18 (May 2023), P10035. DOI: 10.1088/1748-0221/18/10/P10035. arXiv: 2305.03599 [physics.ins-det].
- [15] M. Sack et al. "Fast SiC-MOSFET Switch with Gate Boosting Technology". In: *PCIM Europe digital days 2021; International Exhibition and Conference for Power Electronics, Intelligent Motion, Renewable Energy and Energy Management*. 2021.
- [16] Chavdar Dutsov, Timothy Hume, and Philipp Schmidt-Wellenburg. "Systematic effects in the search for the muon electric dipole moment using the frozen-spin technique". In: *EPJ Web of Conferences* 282 (Apr. 2023). DOI: 10.1051/epjconf/202328201013.

# Chapter 3

## Scintillators in muEDM

In the previous chapter, the muEDM experiment was introduced and the current status was described. In this, we will describe the simulations and beamtimes connected to few items of this experiment: entrance detector, the TOF measurement and the beam monitor. We will start with the GEANT4 simulations of thin and thick scintillators, moving then to the entrance detector and the ‘telescope’ used in the beamtime of 2022. After that the TOF detector. We will then move through the beamtimes.

### 3.1 Short intro to scintillators

A scintillator is any material that emits light when exposed to ionizing radiation, like high-energy photons or charged particles. The main distinction is between organic and inorganic scintillators:

- Organic scintillators are typically composed of carbon, hydrogen, and other organic (carbon-based) compounds. These materials often include fluorescent dyes or organic molecules that emit light when excited by ionizing radiation. They are often used for neutron detection and can also be used for other types of radiation, such as alpha and beta particles. They are versatile and find applications in various fields, including nuclear and particle physics
- Inorganic scintillators are composed of inorganic materials that do not primarily contain carbon-hydrogen (C-H) bonds. These materials can include compounds like sodium iodide ( $\text{NaI}(\text{Tl})$ ), cesium iodide ( $\text{CsI}(\text{Tl})$ ), bismuth germanate ( $\text{Bi}_4\text{Ge}_3\text{O}_{12}$  often “BGO”), and lanthanum halides ( $\text{LaBr}_3$  and  $\text{LaCl}_3$ ). These are commonly used in applications requiring high energy resolution and efficiency, like in gamma-ray spectroscopy, high-energy physics experiments, or medical imaging.

Organic scintillators typically have relatively fast response times and are less expensive, while inorganic scintillators tend to have better energy resolution. Organic scintillators dived in: liquid, crystalline and plastic. We will discuss plastic scintillators. An example of a liquid scintillator, based on Xenon, will be presented when describing the MEG II apparatus (see Ch.5).

#### 3.1.1 Plastic scintillators

Plastic scintillators are by far the most widely used and their densities range from  $1.03$  to  $1.2 \text{ g/cm}^3$ , with a light yield of  $1 \div 100 \gamma/\text{eV}$  of energy deposit [1]. The number of photons emitted is not linear with the energy deposit: in very dense ionization the light yield is lower than expected. This

effect is described with the Birks's formula (Eq. 3.1) for the luminescence  $\mathcal{L}$ .

$$\frac{d\mathcal{L}}{dx} = \mathcal{L}_0 \frac{\frac{dE}{dx}}{1 + k \frac{dE}{dx}} \quad (3.1)$$

Where  $\frac{d\mathcal{L}}{dx}$  is the Light output,  $\frac{dE}{dx}$  the energy loss per unit length by ionizing radiation and  $k$  Birks' constant (also known as the stopping power ratio).

Plastic scintillators are widely used in particle detectors due to their high light yield and fast response time, enabling sub-nanosecond timing resolution. They offer the advantage of pulse shape discrimination, allowing for particle identification based on emitted light during the decay "tail". These are also popular due to their ease of fabrication into various shapes and cost-effectiveness. Scintillating fibers made from plastic scintillators are commonly used in tracking and calorimetry applications.

### 3.1.2 Scintillating Fibers

This is also a good moment to introduce The concept of *scintillating fibers*. We will not use them in this chapter but will be key in Ch. 4, dedicated to the  $e^+$  tracking.

A fiber is generally a thin plastic scintillator that undergoes a process named *cladding*. This process consists of covering the thin structure with multiple layers of lower refractive index, which helps to trap the scintillation light in the *core* of the fiber. Scintillating fibers (SciFi) have become quite common due to their speed, density, radiation resistance, and resolution. At the same time, SciFi trackers can handle high rates and radiation. The downside of this technology is the requirement for sensitive photodetectors, due to low photon yield at the fiber's end.

Another interesting aspect is that it is possible to control the sensitive region by pairing scintillating and non-scintillating fibers. This results in a loss in the collected light but allows the extraction of the light produced in specific regions without creating unwanted hits. On this point is important to remember that the particles will still interact with the non-scintillating fiber, losing energy and undergoing multiple scattering. A careful balance is required.

**Typical Fibers** The typical material for the core is a polystyrene-based scintillator or Wave-Length Shifter (refractive index  $n \approx 1.59$ ) while the cladding is often of PMMA<sup>1</sup> ( $n \approx 1.49$ ), sometimes followed by an additional fluorinated PMMA cladding ( $n \approx 1.42$ ) for enhanced light capture. The resulting diameter is of the order of few 0.1 mm. The fraction of the light transported is around 6% for single-clad fibers and 10% for double-clad fibers. Considering concrete numbers: a minimum-ionizing particle in 1 mm diameter fiber would generate a few thousand photons. The number of these reaching the ends of the fiber depends on the length and the *attenuation length* but goes from a few hundred to a few photons. The attenuation length, the distance over which the signal diminishes to 1/e of its original value, is influenced by factors such as re-absorption of emitted photons, polymer base crystallinity, photodetector sensitivity, and internal surface quality. High-quality fibers can achieve attenuation lengths of several meters. In case the quality of the fiber is not enough for the task at hand, the addition of a very thin layer (few atoms) of a reflective material, like aluminum, can further improve the light collection.

<sup>1</sup>Poly(methyl methacrylate) is a synthetic polymer which goes by many names: acrylic glass, plexiglas, lucite, ...

### 3.1.3 Scintillation process

Charged particles passing through matter create excited molecules, some of which release a small amount of their energy as optical photons through a process known as scintillation. This phenomenon is prominent in organic substances containing aromatic rings like polystyrene (PS) and polyvinyltoluene (PVT), as well as in liquids such as toluene, xylene, and pseudocumene.

In fluorescence, molecules are initially excited by absorbing a photon and then deexcite by emitting a longer wavelength photon. To shift scintillation light to a more convenient wavelength, fluorescent materials are used as "wave-shifters". However, complex molecules in fluorescence can exhibit self-absorption, which shortens the attenuation length. The greater the difference between absorption and emission wavelengths (Stokes' shift), the less self-absorption occurs, making a larger shift desirable.

In high-energy physics, plastic scintillators are typically composed of selected fluors dissolved in a plastic base containing aromatic rings. Most plastic scintillators use either PVT or PS as their base, with PVT-based scintillators being often brighter. Adding a fluor in high concentration (1% by weight) into the base helps improve the attenuation length, as it efficiently re-radiates absorbed energy at wavelengths where the base is more transparent. The primary fluor also plays a crucial role in shortening the scintillator's decay time, increasing the total light yield. The strong coupling between the base and fluor, known as Foerster resonance energy transfer, occurs at short distances, enhancing the speed and light yield of plastic scintillators. In some cases, a "secondary" fluor may be added in fractional percent levels, and occasionally even a third. External wavelength shifters are employed to aid light collection in complex geometries. They consist of a lightpipe with a wave-shifting fluor dissolved in a non-scintillating base. Typically, an acrylic base is used for its optical qualities, along with a single fluor to shift the emitted light to the blue-green range. These shifters also contain additives to absorb ultraviolet light and reduce sensitivity to Cherenkov radiation. For specialized applications, scintillators with increased radiation resistance or unique properties like neutron/gamma discrimination can be created by significantly increasing fluor concentrations.

## 3.2 GEANT4 simulations

### 3.2.1 What is GEANT4?

GEANT4 (GEometry ANd Tracking) is a powerful open-source simulation toolkit used in various scientific fields, primarily for studying the interactions of particles with matter, and is widely employed in particle, nuclear, and medical physics. At its core, GEANT4 works by representing the physical world as a set of geometric shapes and materials. After defining the properties of particles, their energy, and the materials they interact with, GEANT4 simulates their behavior. This toolkit utilizes a range of physics models and algorithms to accurately model particle interactions, including electromagnetic, hadronic, and optical processes. It can simulate particles of various energies, from subatomic to cosmic ray levels. The simulation is *step* based: at every interaction, the physical properties of the particle are updated and, if needed, secondary particles are generated. Steps are forced to end when crossing the boundary between two materials/volumes to ensure

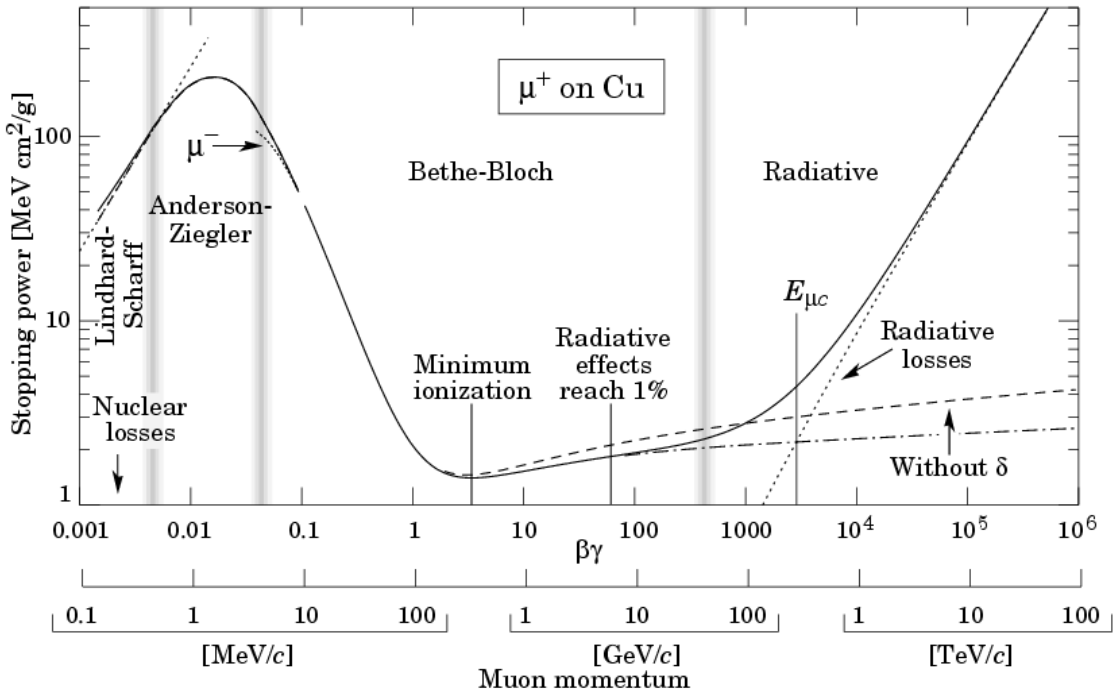


**Fig. 3.1:** This figure illustrates the Bethe-Bloch formula [1], a vital tool in particle physics, depicting how charged particles lose energy when traversing through matter.

proper care is taken in the transition. This is of particular importance for optical simulations, such as the propagation of OpticalPhotons produced by scintillation.

### 3.2.2 Entrance system

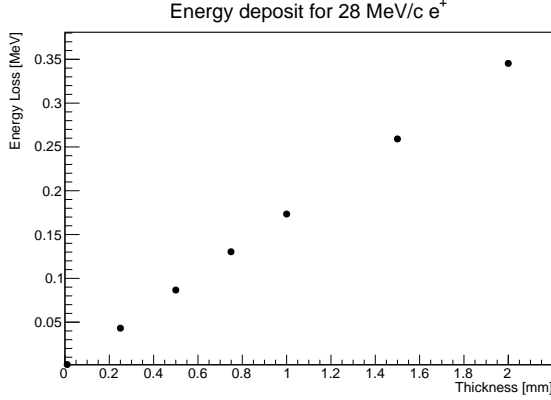
To study the feasibility of the entrance thin scintillator, a GEANT4 simulation was developed. The first step, after achieving a running simulation of scintillation, was to study the range of muons of the interesting momenta, as well as the energy deposit. These first results are shown in Fig. 3.2. Here we can see the energy deposit for  $e^+$  and  $\mu^+$  in scintillators of different thicknesses, reflecting the well-known Bethe-Bloch plot shown in Fig. 3.1. Interesting features are:

- The energy deposit is linear with the thickness for the  $e^+$
- The linearity is lost for the  $\mu^+$ . First, we have an exponential trend and then a plateau, when  $E_{dep} \approx E_k$  and the  $\mu^+$  is stopped
- The shape of the deposit slowly changes from Landau to Gaussian

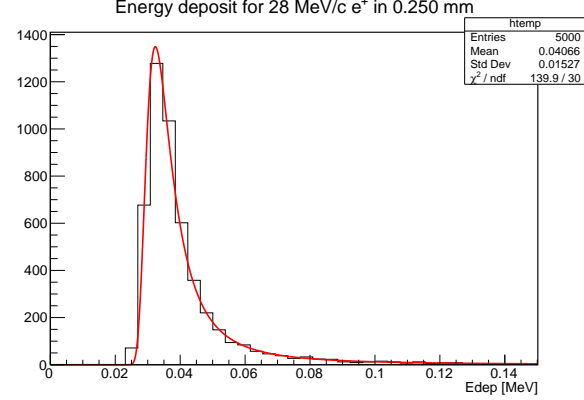
In Fig. 3.3 we recover the linear (and then exponential) trend when sampling the energy deposit for  $\mu^+$  for lower thicknesses at both 28 MeV/c and 128 MeV/c.

### Multiple scattering

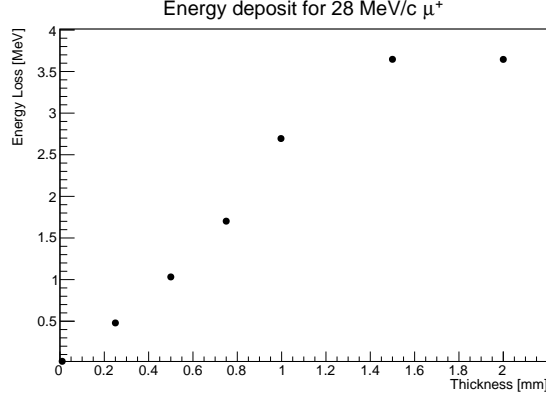
An important sanity check was also to study the multiple scattering in the scintillator. More details on the functional description and the GEANT4 implementation of the multiple scattering will follow, in 3.3. This was done with a fit to the Highland formula (Eq. 3.2) the average value of the scattering angle as a function of the thickness. These fits are shown in Fig. 3.7 and the results,  $X_{0,28MeV} = (54.36 \pm 0.17) \text{ gm/cm}^2$  and  $X_{0,128MeV} = (54.30 \pm 0.14) \text{ gm/cm}^2$ , are consistent with the value for BC400® of  $X_0 \sim 50$ .



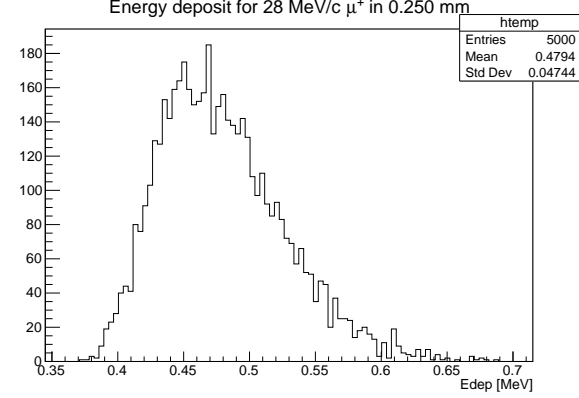
(a) A 28 MeV / c  $e^+$  has  $E_k \approx 27.5$  MeV.



(b) Landau energy deposit for the positrons.

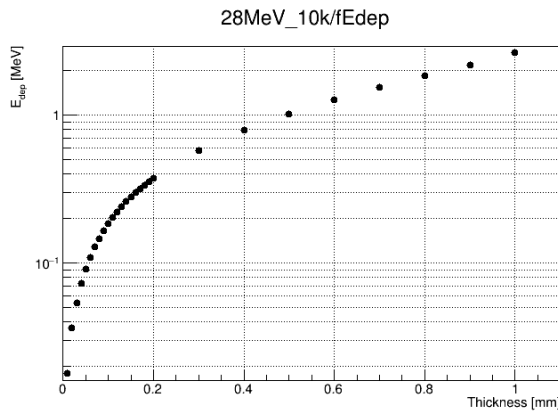


(c) A 28 MeV/c  $\mu^+$  has  $E_k \approx 3.6$  MeV.

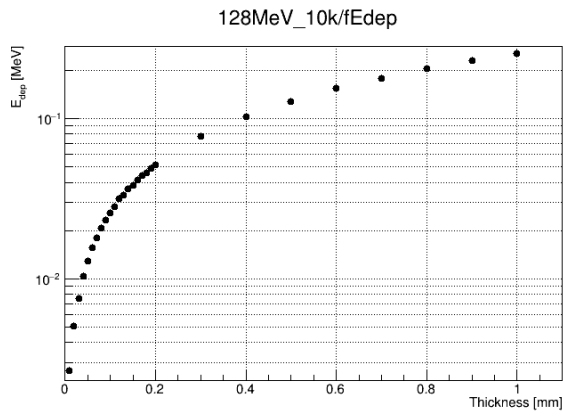


(d) The energy deposit slowly moves from Landau to a gaussian distribution.

**Fig. 3.2:** Curve for the average energy deposit in a BC400® scintillator for  $\mu^+$  (3.2a) and  $e^+$  (3.2c) at 28 MeV/c. Clearly visible is the linearity of the energy loss for the  $e^+$  with thickness. This linearity is lost for the  $\mu^+$ : first, we see an exponential trend and then a plateau when  $E_{dep} \approx E_k$  and the  $\mu^+$  is stopped. The distribution of the energy deposit slowly transitions from a Landau to a Gaussian: (3.2b) is an example of the first type; (3.2b) is an example of the transition.

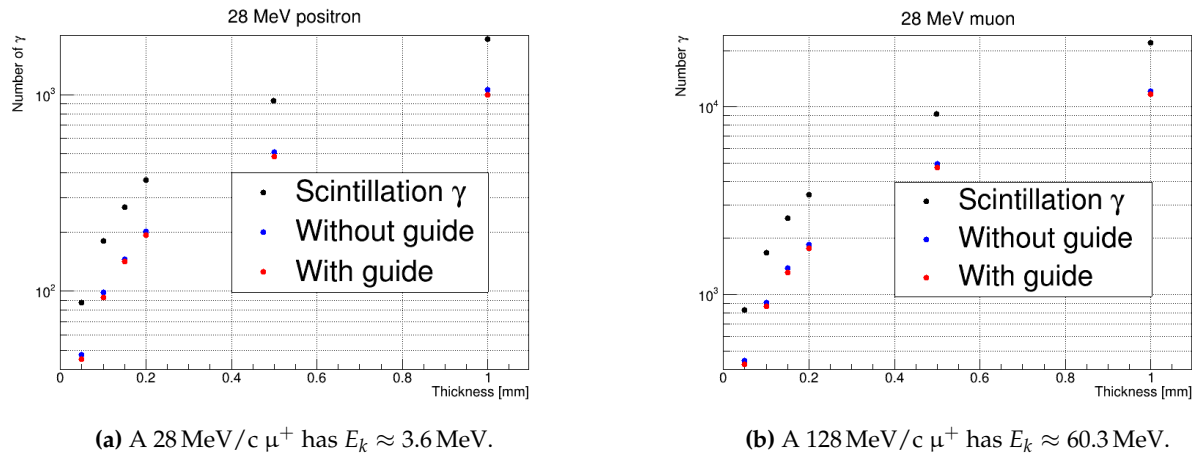


(a) A 28 MeV/c  $\mu^+$  has  $E_k \approx 3.6$  MeV.



(b) A 128 MeV/c  $\mu^+$  has  $E_k \approx 60.3$  MeV.

**Fig. 3.3:** Detail on the lower section of the curve for the average energy deposit in a BC400® scintillator for  $\mu^+$  at 28 MeV/c and 128 MeV/c.

**Fig. 3.4: asd**

### Thickness and number of photons

The amount of energy deposited by the incoming particle is reflected by the number of photons generated by scintillation. These photons scatter inside the scintillator until they arrive on the external surface. Not all photons produced will be detected. This is affected by the position, number, size, and PDE<sup>2</sup> of the SiPMs. To simulate the SiPM readout we can use a silicon volume coupled to the scintillator via an additional volume of optical grease<sup>3</sup>. The first iteration was performed in a perfect scenario, with a floating scintillator glued to the sensors. The second iteration matches reality more, and a light guide is used to hold the scintillator and give enough surface for the SiPM gluing. In Fig. 3.4 the total number of produced optical photons is compared to the number of photons collected with/without an optical guide. A few points are worth underlying:

- There is a drop in the number of photons arriving at the sensors, as expected
- The number of photoelectrons is further reduced by the PDE ( $20\% \div 40\%$ ) of the SiPM
- Number and size of the SiPM active region plays a big role (here 16 SiPMs were used)
- The position of the SiPM on the edges is less influential than what naively might be expected.

The photon distribution is quite uniform once the scintillator size is  $\sim$ cm

Looking at Fig. 3.4b, the number of expected photoelectrons per SiPM for interesting thicknesses is around  $(50 \mu\text{m}, \sim 10 \gamma) \div (200 \mu\text{m}, \sim 30 \gamma)$ . At the same time, the dark rate count limits how low the thresholds can be set in a real setup. Multiple readouts would allow us to lower the threshold and improve the dark noise rejection. Calling the sides  $s_i$ , options could be  $(s_1 \wedge s_3) \vee (s_2 \wedge s_4)$ ,  $(s_1 \wedge s_3) \wedge (s_2 \wedge s_4)$ , or simply  $(s_1 \wedge s_3)$ . We studied these different readouts schemes in the beamtime of Dec. 2023 (see Sec. 3.5)

### 3.2.3 Telescope and entrance detector

To study the entrance detector, a prototype was envisioned with a thin *gate* scintillator read by multiple sides, a channel of 4 long scintillators creating a *telescope*, and an additional scintillator as *exit*. The development of such a system stems from the idea of having a way of vetoing the muons

<sup>2</sup>Photon detection efficiency describes the effectiveness of a photon detector in registering incoming photons. It quantifies the probability that a photon incident on the detector will be detected and converted into an electrical signal

<sup>3</sup>Also known as optical coupling grease or index-matching grease, is a specialized type of grease used in optics and photonics applications. It is designed to improve the optical coupling between optical components.



Fig. 3.5: asd

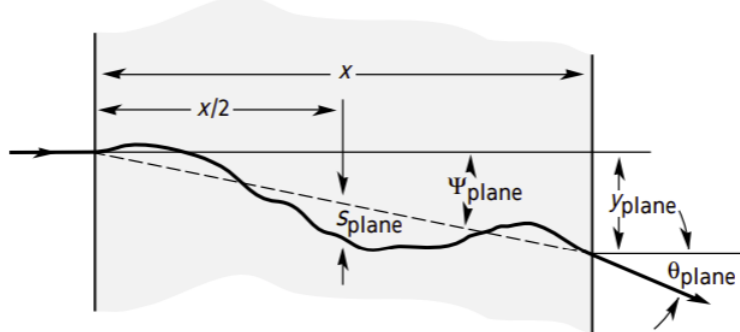


Fig. 3.6

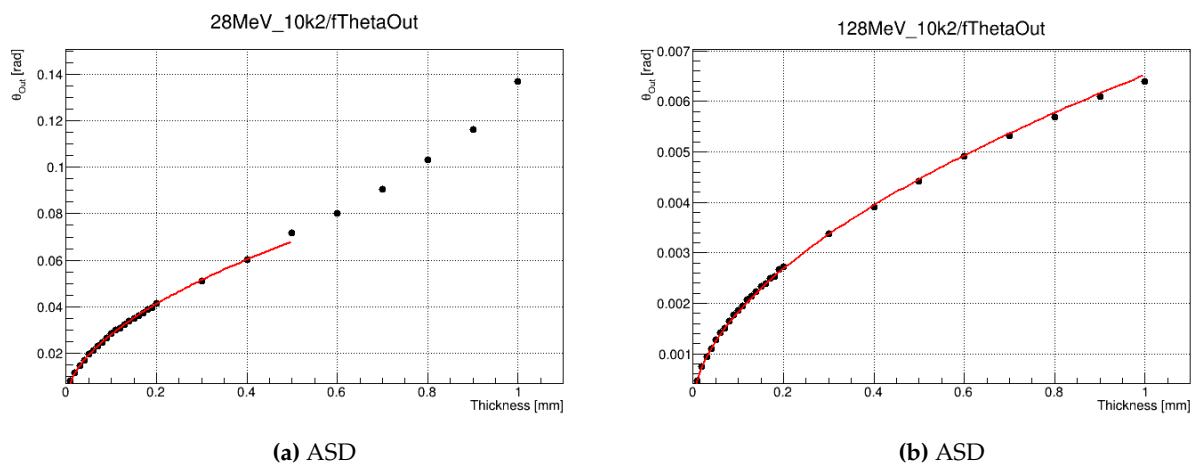
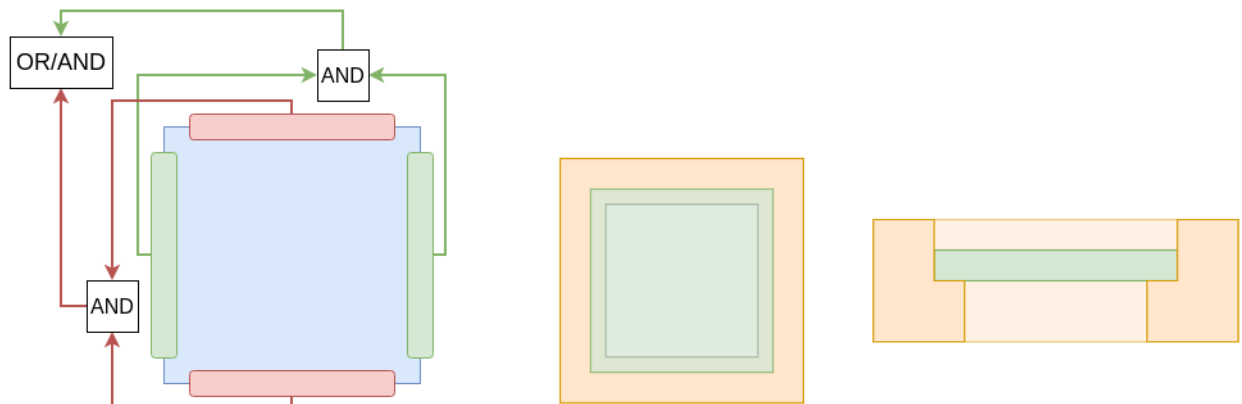


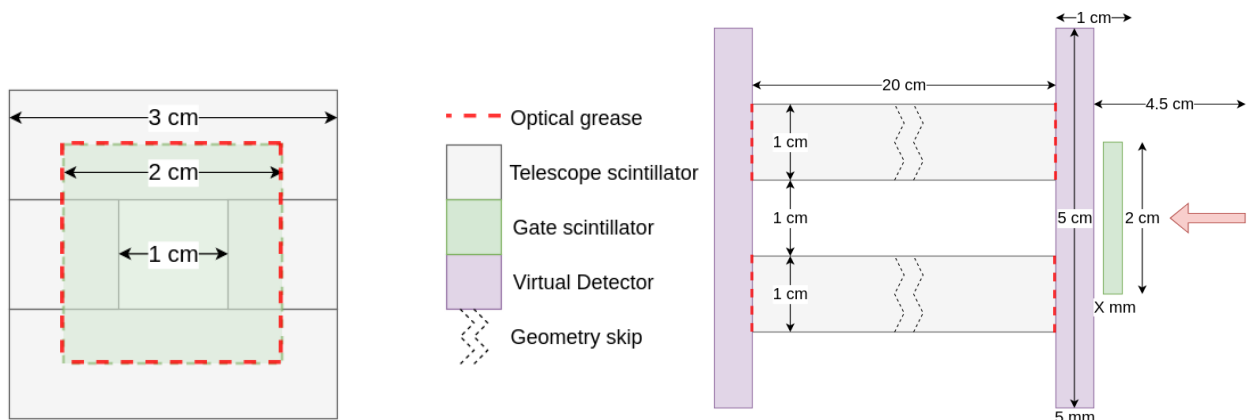
Fig. 3.7: Average scattering angle in different thicknesses of BC400<sup>®</sup> scintillator for  $\mu^+$  at  $28 \text{ MeV}/c$  and  $128 \text{ MeV}/c$ . From these plots was found  $X_0 = (54.33 \pm 0.12) \text{ g/cm}^2$ .



**(a)** Possible readouts include all combinations of the different sides, like asking at least N sides, or  $(s_1 \wedge s_3) \vee (s_2 \wedge s_4)$ .

**(b)** Mounting a thin scintillator in a light guide can improve the photon collection. A ‘frame’ shape prevents the incoming particle from interacting with additional material.

**Fig. 3.8:** Two strategies to lower the threshold and improve the dark noise rejection: multiple readouts of a thin scintillator (a) and/or a light guide to improve the photon collection (b).



**(a)** Front view of the detector system.  
The *gate* is big enough to cover the aperture of the *telescope*.

**(b)** Side view of the system. Additional VD used in the simulation for debugging are also shown.

**Fig. 3.9:** Sketch of the first geometry for the *gate* and *telescope* detector for the 2022 muEDM beamtime. The aim was to test the thin *gate* scintillator and the effect it has on the beam.

scattering at bigger angles while traversing the gate without requiring multiple detectors on the muon path. I started this simulation in GEANT4 and it was later passed to the Shanghai colleagues, who further optimized and developed it using MUSRSIM. The last step was to validate it with the data taken during the beamtime of 2022, discussed in Sec. 3.4. Although quite an interesting system, the collaboration decided not to implement it in the muEDM injection, deciding instead to rely on a Time Of Flight (TOF) measurement, which was tested in 2023 and discussed in Sec. 3.5.

### 3.3 Beamtime 2021

This was the first muEDM beamtime I participated in. I took an active part in the setup and measurement and I followed the analysis of the data collected. This section relies on the Master Thesis of Tim Hume, part of the muEDM collaboration. This beamtime was designed to study the positron multiple scattering in different thin foils of the material expected to be viable solutions for

the different parts of the experiment. On top of the material details, the aim was also to validate the scattering model used in the GEANT4 simulations for further reference. The setup was quite simple: a telescope of five silicon pixel sensors, three upstream and two downstream.

### 3.3.1 Description of the multiple scattering

**Highland** The Highland formula for multiple scattering is a parameterization for the width of the multiple scattering distribution. For a particle of charge  $z$ , momentum  $p$  traversing a thickness of  $x$  of a material with radiation length  $X_0$ , the RMS of the gaussian distribution is estimated as:

$$\theta_0 = \frac{13.6 \text{ MeV}}{\beta p c} z \sqrt{\frac{x}{X_0}} \left( 1 + 0.038 \ln\left(\frac{xz^2}{X_0 \beta^2}\right) \right) \quad (3.2)$$

Often, in the context of high particle physics, the projection on the directions orthogonal to the momentum are considered:

$$P(\theta_{x,y}) = \frac{1}{\theta_0 \sqrt{2\pi}} \exp\left(-\frac{\theta_{x,y}^2}{2\theta_0^2}\right) \quad (3.3)$$

**GEANT4** The default parameterization of the multiple scattering in GEANT4 is the Urbán. This is based on a different description of the process, required because the evaluation is done at each step of the simulation, meaning *within* the volume. This model describes the angular distribution of multiple scattering and samples it every interaction. The probability density of the angular distribution is usually indicated with  $g(u)$  where  $u = \cos \theta$  and the form is the following:

$$g(u) = \alpha + \begin{cases} \beta \exp(\gamma u) & \text{for } u_0 \leq u \leq 1 \\ \delta(1-u)^\epsilon & \text{for } -1 \leq u < u_0 \end{cases} \quad (3.4)$$

The parameter  $u_0$  is the one used to transition between the central Gaussian-like distribution and the Rutherford-like tails at larger angles.

For the Highland formula, the PDG reports an accuracy of  $\sim 10\%$  in the range  $10^{-3} < x/X_0 < 10^2$  [1], meaning it is less reliable for thin targets for which  $x/X_0 \sim \mathcal{O}(10^{-4})$ . On the other hand, while GEANT4 results have been widely tested against experimental measurements, there is a lack of data to compare in the ranges we are interested in.

### 3.3.2 Data taking

The idea behind the data taking is quite simple: a study on the multiple scattering can be performed using a beam telescope, such as the one sketched in Fig 3.17, in which the two sides of the telescope are used to track the in/out-coming particles. The delicate point is to carefully take into account the scattering of the particles in the telescope itself. It is then needed to collect data without the sample to apply a deconvolution of the telescope response. The downstream part of the detector is not symmetrical to the upstream because only five sensors had the necessary performance. This made the tracking task more challenging, leading to wider distributions. The beamline used is the  $\pi E1$ , which provides  $\pi^\pm, \mu^\pm, e^\pm$  in a momentum range  $100 \text{ MeV} \div 500 \text{ MeV}$ .

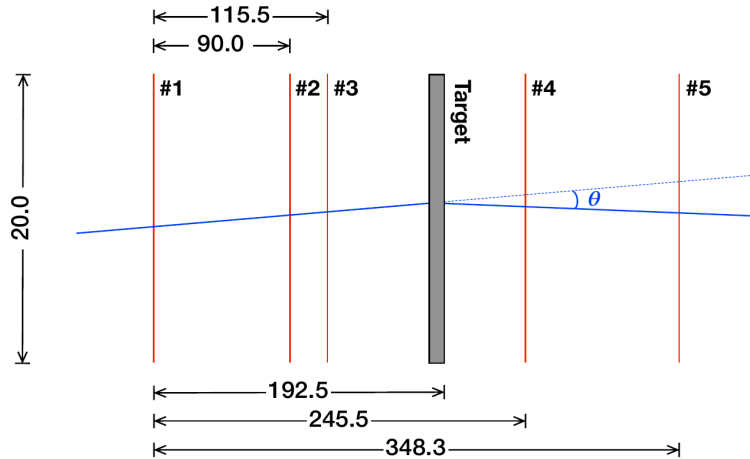


**Fig. 3.10:** Sketch of the telescope of Silicon Pixel Sensors used to study the multiple scattering in different materials. The samples are held in the position of the 'target'. In this sketch, the beam is coming from the left side.



(a) Picture of the setup for the beamtime of 2021. On the right, the scintillator was used as an external trigger, on the left, beam exit window.

(b) Picture of one of the MuPix10 mounted on the two PCBs.

**Fig. 3.11:** Picture of the setup and one of the MuPix10 (grey-colored square) mounted on the PCBs.

Clearly, a good understanding of the beam is key in both data-taking and analysis. An example is the study of the beam changing the degrader's thickness, shown in Fig. 3.12. For brevity, the description of the electronics and DAQ system will be skipped.

**Silicon Pixel Sensors** The sensors used are the last iteration of the sensors of the *mu3e* experiment, the MuPix10. These are High Voltage Monolithic Active Pixel Sensors (HV-MAPS) with  $250 \times 256$  pixels of dimensions  $80 \mu\text{m} \times 80 \mu\text{m}$ . The sensor itself is on a PCB used for delivering the required voltages. A second, larger, PCB is set below the first and is responsible for reading and transmitting the data to FPGA. These sensors have been developed to achieve excellent position and time resolutions ( $100 \mu\text{m}$  and  $20 \text{ ns}$ ) with efficiency of  $\epsilon \approx 0.99$ . The thickness of these sensors is  $50 \mu\text{m}$  but this was the case for just the detector positioned after the samples. The others were  $100 \mu\text{m}$ , important to be considered during the analysis. The whole apparatus is shown in Fig. 3.11a while a singular MuPix10 is shown in Fig. 3.11b.

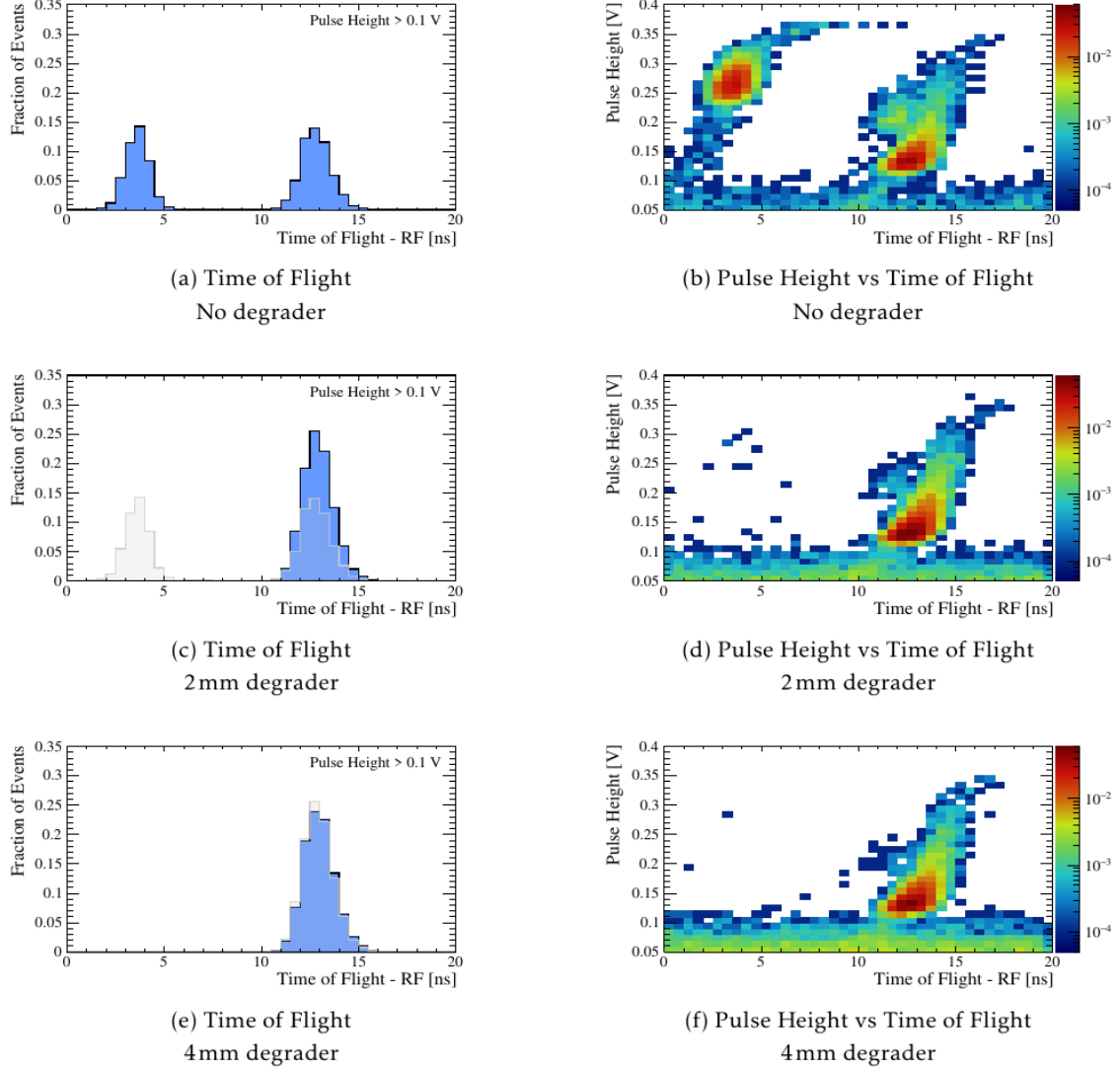


**Fig. 3.12:** Timing and the 2D plot for time and pulse height for 120 MeV/c particles. The three rows show what happens when inserting degraders of different thicknesses. With no degrader, the  $\pi$  peak is visible at lower TOF. When increasing the thickness, the contributions of  $\pi$  and  $\mu$  decrease. It is important to note that the  $e$  and  $\mu$  distribution overlap. In gray the distribution of the previous plot to make a comparison.

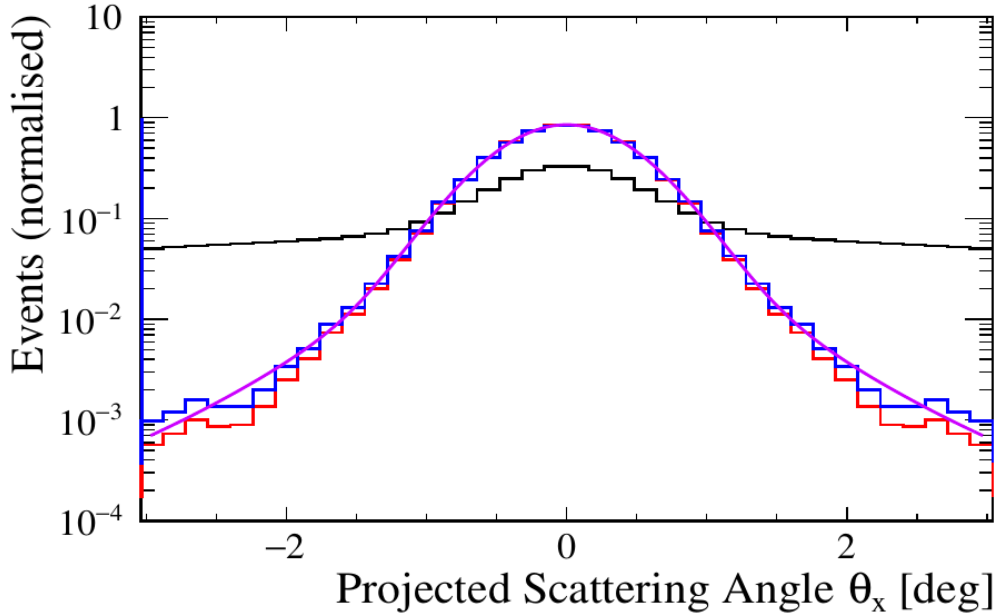
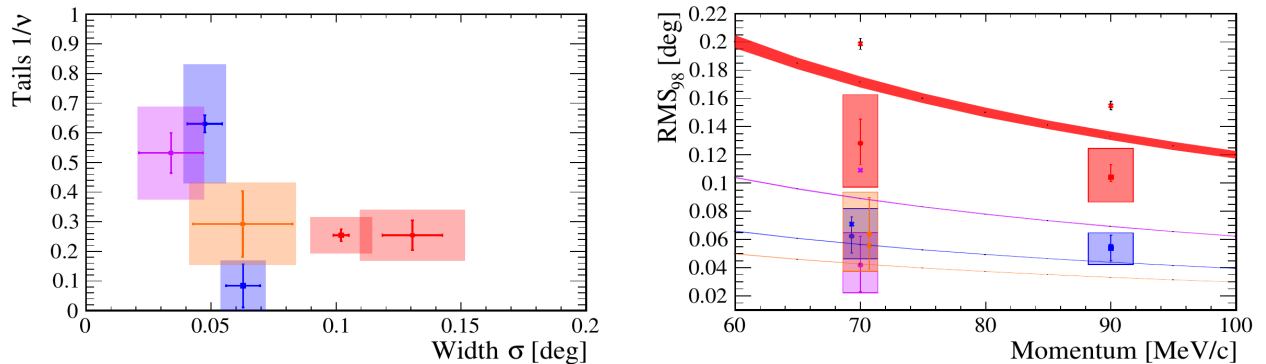


**Fig. 3.13:** The angular distributions show: the full distribution (black), the distribution after cuts in the distance at the sample’s plane (red), the distribution after acceptance correction (blue), and the fitted function for telescope characterization (violet).

### 3.3.3 Data analysis

**Track selection** Initial angular distributions obtained were broad due to noise in downstream sensors, making it difficult to distinguish noise from true hits. To address this, a filtering process was developed to select the track candidate with the least spatial separation between the intersections of upstream and downstream tracks on the plane of the sample. The expected angular distribution for particles passing through a material at normal incidence should be spatially symmetric and independent of chosen projection axes. Any deviation from this symmetry could indicate experimental, data processing, or analysis errors. To mitigate the effects the idea was to combine distributions from multiple axes. In the initial distributions, the broad background can be attributed to false tracks generated by noise, poor fits, and some contribution of events with large angles of scattering in the telescope itself. This background was suppressed by enforcing a distance of 1 mm between the points at which the upstream and downstream tracks intersect the plane of the sample. Distributions before and after applying this filter are shown in black and red in Fig. 3.13. This distribution was then corrected for the geometric acceptance of the telescope.

**Acceptance** The correction for the geometrical acceptance of the telescope was essential to accurately determine the tails of the angular distribution. To estimate the acceptance, for each upstream track identified, scattering angles were randomly assigned and added to a histogram, distinguishing instances within the acceptance of the most downstream sensor. The ratio of histograms yielded the average acceptance as a function of projected scattering angles. The acceptance correction was applied on a per-event basis, adjusting the scattering angles based on the acceptance value. An example of such correction is shown in blue in Fig. 3.13



**(a)** Pokalon (orange), 17  $\mu\text{m}$  Graphite (blue), 50  $\mu\text{m}$  Graphite (violet), Silicon (red); circular markers for data at 70 MeV, squared at 90 MeV; error bars are the statistical and the shaded the total uncertainties.

**(b)** Same color/shape coding as Fig. 3.14a and the predictions of the Highland formula are shown by lines of width representing the uncertainty in thickness.

**Fig. 3.14:** Results of the analysis of the different samples and confronted with predictions using the Highland formula and GEANT4. The details are not easy to read but the ‘bring-home’ message is that the results are somewhat in agreement and some improvement are planned on the analysis.

**Deconvolution** The method of track selection and acceptance correction was applied to both runs with and without the sample. The distributions from these runs were then fitted. The process involved:

- Characterizing the telescope’s response without the sample using a weighted sum of a Gaussian distribution and a Student’s t distribution
- Convoluting the response function with the sample’s angular distribution, assumed to follow a single Student’s t distribution
- using the negative log-likelihood to determine the best-fit parameters for describing the measured distribution with the sample

### 3.3.4 Model evaluation and conclusions

This first beamtime aimed at testing the agreement between the Highland formula and the GEANT4 Urbán model for the multiple scattering in thin materials. The analysis of the data collected is still not finalized, but a rough agreement between data and models can be seen in Fig. 3.14. Some improvements could be added to the analysis and/or to the simulation of the experimental setup, so updated results are expected in the following months.

## 3.4 Beamtime 2022: Telescope and entrance detector

This second beamtime<sup>4</sup> happened in November 2022. The aims were:

- Test of entrance scintillator with the additional ‘telescope’
- parasitic measurements for the TPC + GRIDPIX

This time I, together with Prof. Angela Papa and David Stäger (a master student from ETH) participated actively in the development of the setup. In particular, we took care of the entrance scintillator, auxiliary detectors, the electronic, vacuum system, and one version of the telescope.

<sup>4</sup>Not counting the one for the TPC + GRIDPIX of Sec. 2.3.5.

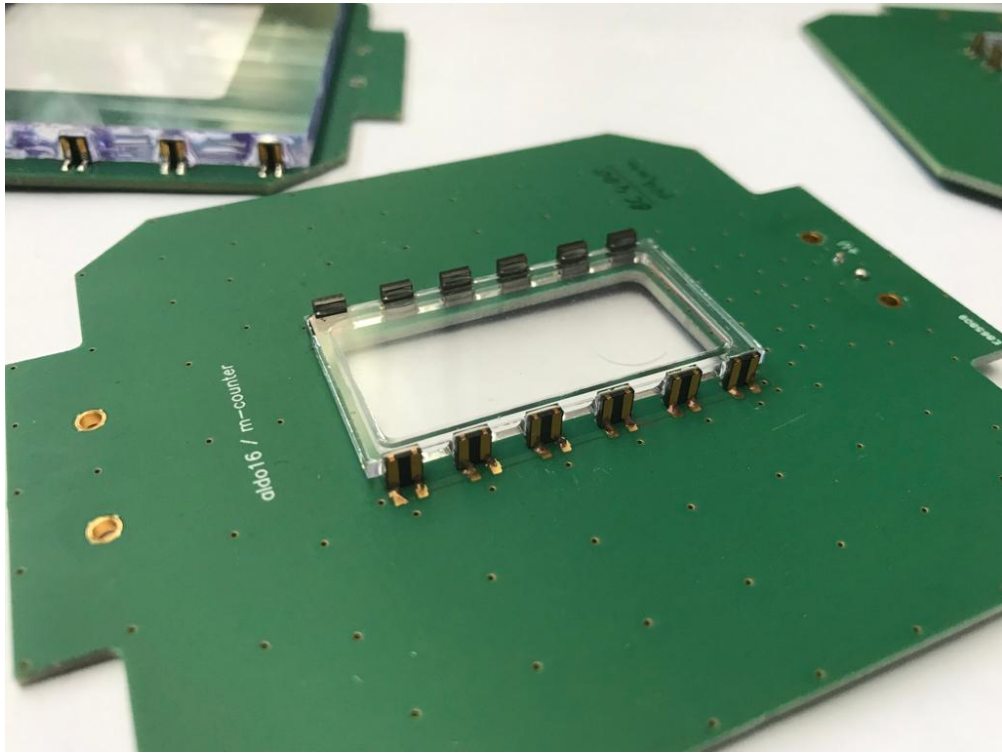


**Fig. 3.15:** Picture of different scintillators mounted on PCBs and read by multiple SiPMs. The signals of the SiPMs are summed and different thicknesses were already available at the time of the 2021 beam time.

To test different reading options a second telescope was developed by the Shanghai part of the collaboration and they also helped develop the mechanical structure.

### 3.4.1 Construction

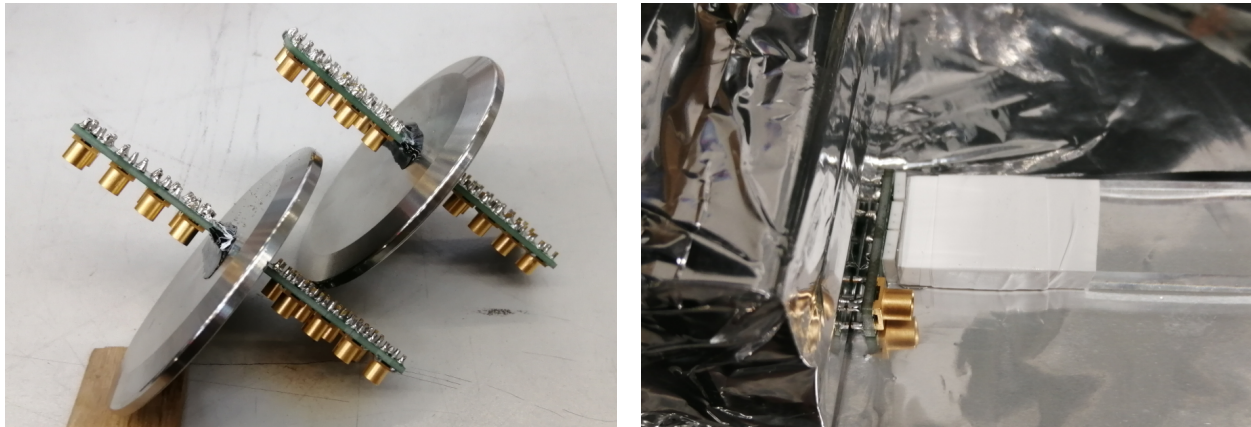
**Scintillators** The thin scintillators used during this beamtime had already been tested for previous purposes. We had  $100\text{ }\mu\text{m}$  and  $200\text{ }\mu\text{m}$  to be used as entrance and exit from the telescope. These were already mounted on PCB boards with multiple SiPMs as readouts. The SiPMs were read all together so the sum of the signals was the only information available. An example of this setup is shown in Fig. 3.15. On the other side, the long scintillators which compose the telescope were not already available. Two versions were built in parallel.

- The "Shanghai's version" was made of  $200 \times 20 \times 10\text{ mm}$  scintillators read on one side.
- The "Pisa's version" was made of  $200 \times 25 \times 5\text{ mm}$  scintillators read on both sides.

Two versions were built to study how much the longitudinal information of the hits on the telescope would benefit the study of the overall system. I worked on the soldering of the SiPMs on the PCB boards for the readout (3 per side). Then I glued the scintillators using *optical cement*. The gluing to the PCB is shown in Fig. 3.16b. Gluing the scintillators this way, we knew small gaps between them after mounting the telescope were unavoidable. This was actually to confront it with the Shanghai telescope<sup>5</sup>, for which the cross-talk between different crystals was expected.

**Electronics** The First challenge was to bring the necessary power to the detectors and bring the readout out of the vacuum chamber. The choice was to use a WaveDream board as a DAQ unit

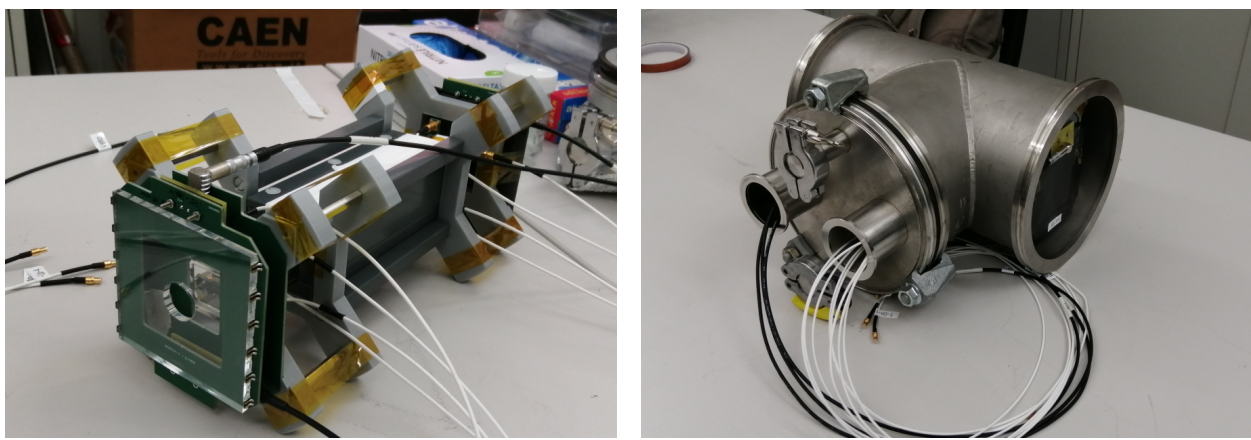
<sup>5</sup>Being my first gluing I used too much optical cement, which further increased the gap between crystals.



(a) Custom feed-throughs: PCB board, with soldered connectors, sealed with Styrofoam in a blind flange.

(b) A small PCB board with 3 SiPMs and one connector attached with optical cement to one of the scintillators.

**Fig. 3.16:** Part of the preparation needed for the beamtime was to develop the detectors, as well as the vacuum in which the measurement would have taken place.



(a) Assembly of the *telescope* with *entrance* and *veto*.

(b) "T" beampipe piece used as vacuum chamber.

**Fig. 3.17:** The *entrance* scintillator, the *telescope*, and the *veto* were assembled in a rigid structure. A "T" beampipe piece was used to put the detector in the beamline. The lateral flange was adapted for the feedthroughs while, on the back, a Mylar® widow was mounted to allow further measurements of the beam.

for this beamtime. We custom-made the necessary feed-throughs, gluing with STYCAST® PCB boards through two blind flanges. The connectors were then soldered to the PCB, creating the feed-throughs shown in Fig. 3.16a.

**Final setup** Combining the thin scintillators as *gate* and *exit* with the telescope and the needed feed-throughs we get the complete setup shown in Fig. 3.17a. The last additions were a *veto* scintillator ( $100 \times 100 \times 5$  mm with a circular 10 mm hole) to optimize the particle selection and a tube to contain the whole thing. For this last item, to allow the feed-throughs to be on the side of the setup, we used a "T" beampipe piece, shown in Fig. 3.17b.

**Additional items** After the system just described, two more items were added:

- SIMON/PIL: Beam monitors were used to characterize the beam.
- TPC + GRIDPIX: Used parasitically to gather some missing details, which were merged to the data from 2021 beam-time in the publication already mentioned (see Sec. 2.3.5) [2].

		Trigger Patterns																	
Chn	Pol	P00	P01	P02	P03	P04	P05	P06	P07	P08	P09	P10	P11	P12	P13	P14	P15	P16	P17
CH0	-	•		X	X	X	X	X	X	X	X	X	X	X	X	X	•		
CH1	-		•	•	•	•	•	•	•	•	•	•	•	•	•	•	X		
CH2	-			X		X	•	•								•	•		
CH3	-			X		X	•	•											
CH4	-			X		X			•	•									
CH5	-			X		X			•	•									
CH6	-			X		X					•	•							
CH7	-			X		X					•	•							
CH8	-			X		X							•	•					
CH9	-			X		X							•	•					
CH10	-		•	•					•		•		•		•		•		
CH11	-																		
CH12	-																		
CH13	-																		
CH14	-																		
CH15	-																		
EXT	-																		

**Fig. 3.18:** WaveDREAM interface to set the triggers. A dot is a required channel while a cross is used as veto. Some examples are: P00 - veto only; P01 - gate only; P03 - !veto & gate & exit.

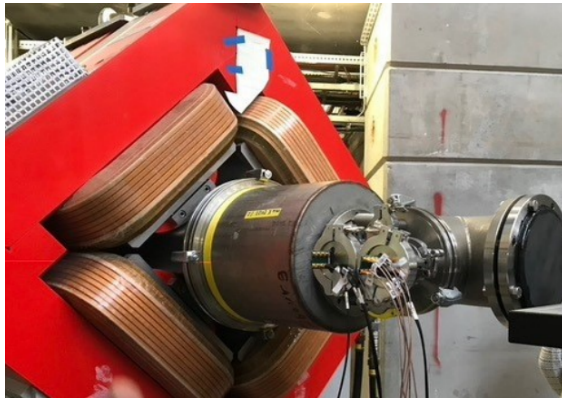
### 3.4.2 Data taking

The whole beamtime was roughly two weeks. The first days were dedicated to the beam tuning and measurements. Two settings were defined to have the beam focused on the gate or the exit scintillator. These two setups allowed us to study different aspects of the prototype, which will be discussed in the following section. For each channel, supply and threshold were decided by measuring the rate of triggers with/without a Sr<sub>90</sub> source. A picture of the end of the beamline and the setup is in Fig. 3.19a while in Fig. 3.19b the end Mylar window before being covered with Teflon to make it light tight. The DAQ of choice was a standalone WaveDREAM. Different trigger configurations were used to study the different aspects of the setup. A ‘typical’ trigger window of the DAQ system is shown in Fig. 3.18. In this, a dot means that channel is required while a cross means it is used as a veto<sup>6</sup>. The system has 16 channels and 18 triggers.

### 3.4.3 Data analysis

The data collected were analyzed in parallel to study the behavior of the gate and the telescope. The first will be part of the muEDM experiment, the second was developed to test such a system.

<sup>6</sup>We later found out this feature was bugged and we had to manually set up a veto system using NIM modules.



(a) The setup mounted at the end of the beamline.



(b) The view of the detectors from the Mylar window before making it light-tight.

**Fig. 3.19:** Pictures of the system after the installation along the beamline.

### Gate

The main aim is to evaluate the current efficiency of the gate and evaluate if/how to improve it, to have a reliable trigger for the magnetic kicker. For this measurement, the events were triggered with the exit scintillator, ensuring the muon had to pass through the gate. Changing offline the charge requirement on the gate, the efficiency vs threshold can be evaluated. Taking into consideration also the time difference between the gate and exit we can construct a ‘side-band’ to correct for accidental coincidences. The plot resulting is in Fig. 3.20 and the results are summarized in table Tab. 3.1. From these is clear a low threshold is required to achieve high efficiency in detecting 28 MeV/c. Looking at the values obtained for the thermal noise for this detector (see Tab. 3.2), unfortunately, the readout implemented does not allow to reduction of the threshold without hitting the thermal noise. This was somewhat expected, and for this reason, the beamtime of 2023 (see Sec. 3.5) was planned to test a 4-way readout to require coincidences between channels.

Thr. [mV]	10 ns			5 ns		
	$N_{coin}$	$N_{coin}^{acc}$	$\epsilon$ [%]	$N_{coin}$	$N_{coin}^{acc}$	$\epsilon$ [%]
-50	3798	130	91.7	3549	65	87.1
-100	3385	116	81.8	3169	58	77.8
-150	2067	64	50.1	1934	32	47.6
-200	820	30	19.8	768	15	18.8
-250	266	8	6.5	253	4	6.2

**Tab. 3.1:** Number of coincidences, accidentals, and efficiency as a function of the gate threshold.

Thr. [mV]	100 $\mu$ m gate noise [kHz]	200 $\mu$ m exit noise [kHz]
-20	$1435 \pm 5$	$16,750 \pm 50$
-30	$643 \pm 2$	$8800 \pm 50$
-40	$287 \pm 1$	$4350 \pm 50$
-50	$150 \pm 1$	$2350 \pm 50$
-60	$78 \pm 0.5$	$1330 \pm 20$
-70	$42 \pm 0.5$	$745 \pm 5$
-80	$23.7 \pm 0.2$	$435 \pm 5$
-90	$13.3 \pm 0.3$	$250 \pm 3$
-100	$7.2 \pm 0.1$	$141 \pm 2$
-150	$0.6 \pm 0.02$	$11.5 \pm 0.5$
-200	$0.04 \pm 0.01$	$1.2 \pm 0.05$
-250	$\approx 0.005$	$0.13 \pm 0.02$
-275	$\approx 0.001$	$0.04 \pm 0.01$
-375	$\approx 0$	$\approx 0.001$

**Tab. 3.2:** Thermal noise rates at different thresholds for gate/exit scintillators.

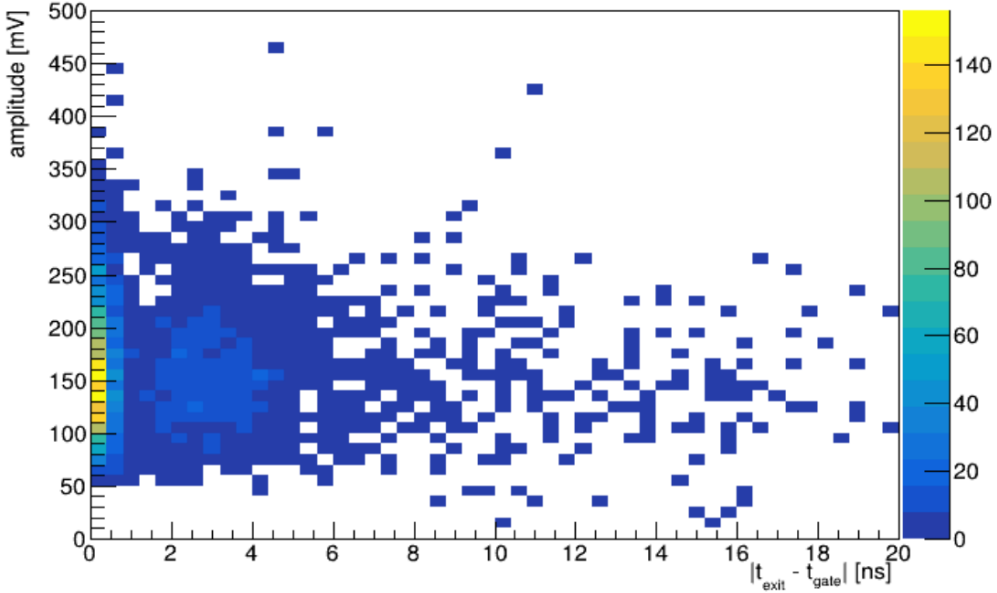


**Fig. 3.20:** Correlation plot for the amplitude of the signal in the gate and the TOF measured. If this plot is produced while triggering only on the exit, it can be used to evaluate the gate efficiency.

Another key aspect of the gate scintillator we wanted to study was the time resolution, a key parameter for the triggering of the magnetic pulser, and a TOF detector for the CW/CCW analysis discussed in the section on systematics (Sec. 2.5). Evaluating the time difference between gate and exit we can evaluate the time of flight of the particles. The spread of this measurement is the convolution of the momentum spread and the intrinsic resolution of the system made of the two scintillators:  $\sigma_{TOF} = \sigma_p \oplus \sigma_{scint}$ . Given gate and exit have different thicknesses, their contribution will be only approximated by  $\sigma_{scint} \approx \sqrt{2}\sigma_{gate/exit}$ . The result of the Gaussian fit on the TOF measurement is in Fig. 3.21 and the resulting resolution is  $\sigma_{TOF} \approx 241$  ps. Assuming a 3% momentum spread, the resulting resolution of the detector is  $\sigma_{scint} \approx 241 \ominus 78$  ps  $\approx 228$  ps. From this we can make a rough estimate of  $\sigma_{gate} \approx 228$  ps /  $\sqrt{2} \approx 160$  ps. These results are completely satisfying.

## Telescope

Naively one might expect that either the muon undergoes a small scatter in the gate and gets to the exit scintillator, or is scattered at a bigger angle and is stopped in one of the scintillators creating the telescope. In reality, the position of the beam focus and the trigger used changes the topology of the events. The first distinction is if the focus is set on the gate or the exit. In the former, if the trigger is performed only on the gate, we expect the divergence of the beam to increase the probability of the muon hitting the telescope. Once we require the exit to be also triggered, the fractions of accepted and rejected events swap. This is exemplified looking at the difference between top and bottom plots in Fig. 3.22. Studying the exit-focused beam we expect a similar fraction of events when triggering on both scintillators, while triggering only on the gate should increase the fraction of accepted events. The reason is that the convergence of the beam should reduce the probability of the muon hitting the telescope. This behavior is seen comparing left and right plots in Fig. 3.22. An interesting feature is the presence of events in which the muons produce hits in the gate, telescope, and exit. This fraction depends on the trigger but, for example,

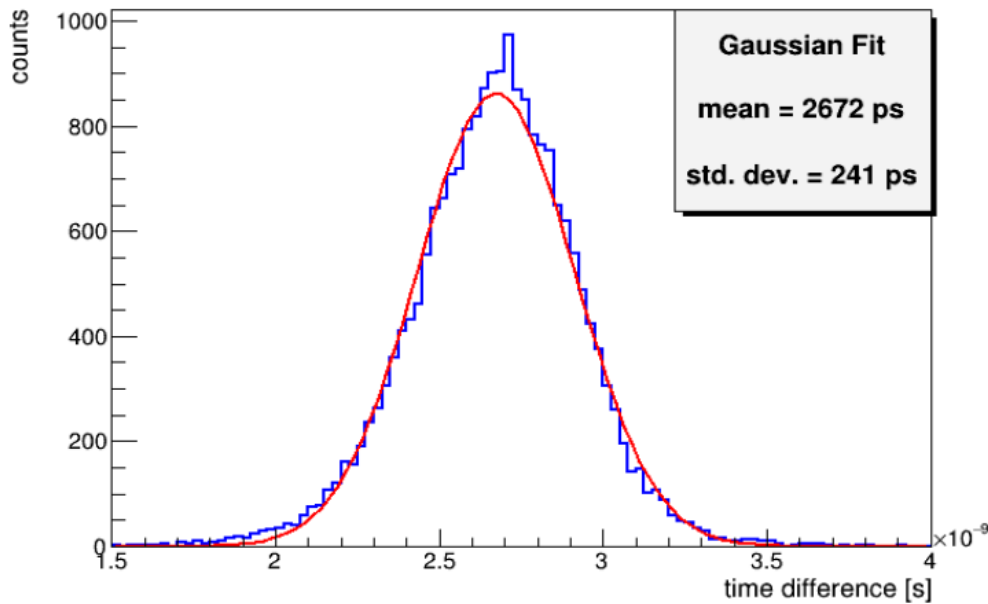


**Fig. 3.21:** Measuring the TOF resolution, and assuming a momentum spread of 3%, we can extract a combined resolution of gate and exit of  $\sigma_{scint} \approx 241 \oplus 78 \text{ ps} \approx 228 \text{ ps}$ . This result meets the requirements.

when triggering on gate&exit, this constitutes  $> 15\%$  of the events.

Let's now consider a particle interacting in one of the four scintillators of the telescope. If the photons produced by scintillation can bleed into the neighbor scintillators, secondary hits could be measured in these. So a small fraction of light will be seen by the next scintillators and very little by the one opposite (looking at Fig. 3.23a, an example could be hitting A, small fraction in D and B, and even smaller in C). If we now look at the charge correlation between the different scintillators, we find some interesting pattern.

Looking at the correlation in a neighbor channel (A and B), we find a 4-dot pattern, the central graph of Fig. 3.23a. A hit in:

- A will deposit charge in A and some in B - yellow
- B will deposit charge in B and some in A - green
- C will deposit some in B and little in A - blue
- D will deposit some in A and little in B - gray

If we now look at the correlation with the opposite scintillator (C), we find a different pattern, the right graph of Fig. 3.23a. A hit in:

- A will deposit charge in A and little in C - yellow
- C will deposit charge in C and little in A - blue

B/D will deposit some in A and some in C - green

These structures are the result of the optical crosstalk between scintillators so we expect these to be present in the Shanghai version of the telescope, but not in the Pisa one, having small gaps due to the gluing. The expectations are in line with the data, as shown in Fig. 3.23b and Fig. 3.23c.

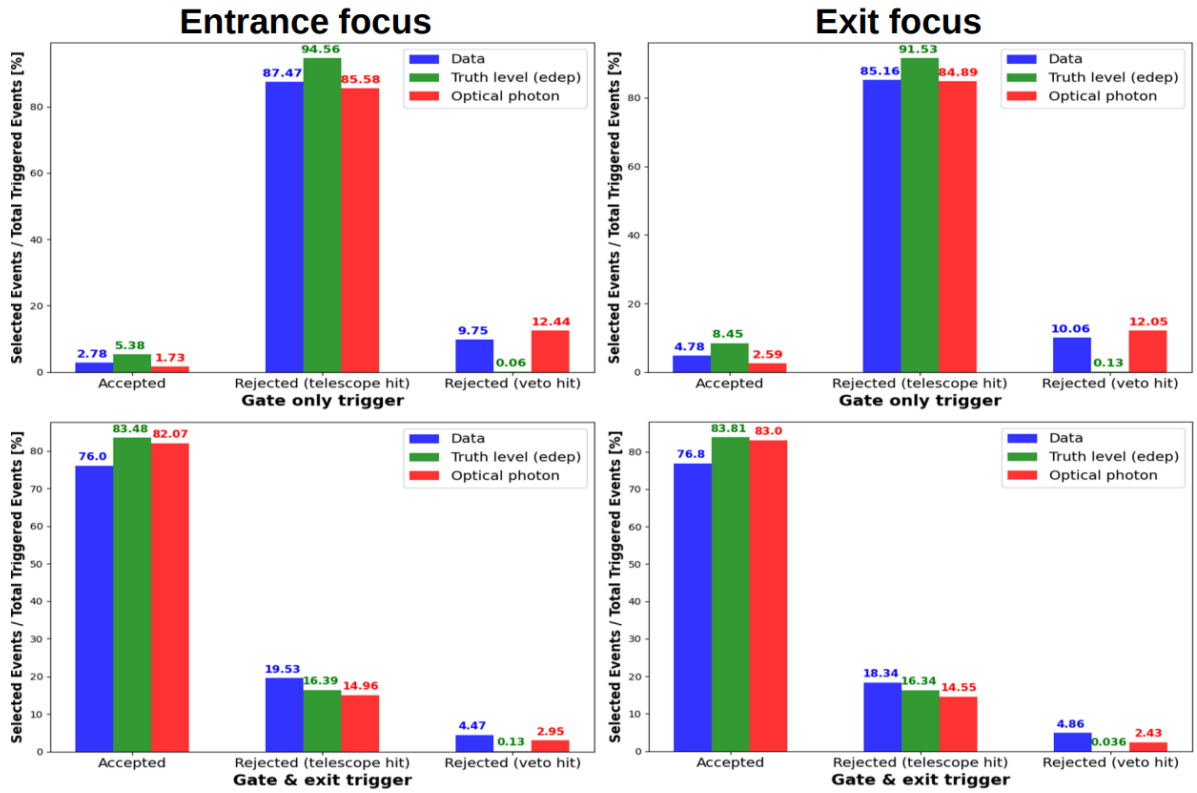


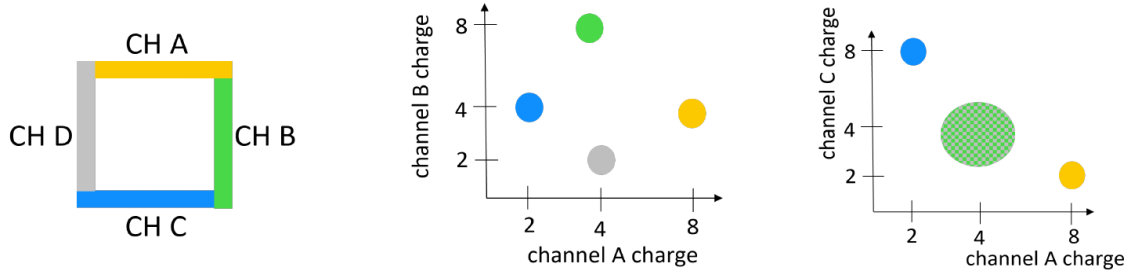
**Fig. 3.22:** Summary of the different events for the two beam focuses and the prediction from the G4BEAMLINE prediction. See the main text for the details.

## 3.5 Beamtime 2023: TOF and Multi readout entrance

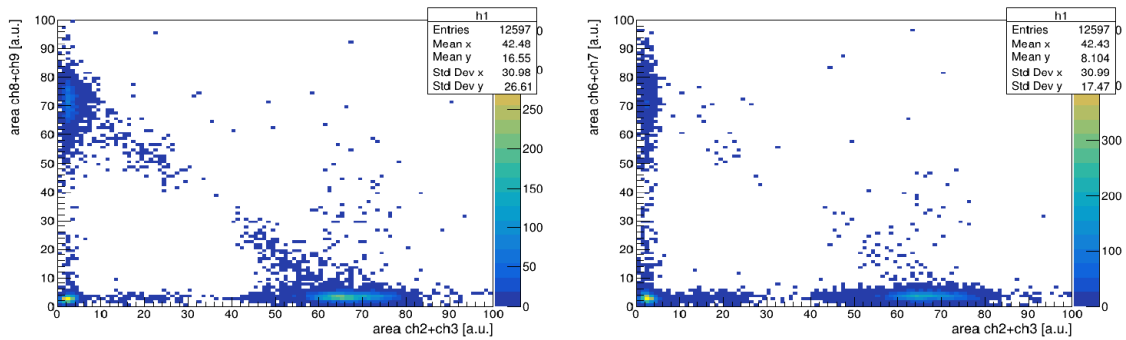
In this section, we present the experimental setup along with the first preliminary results of the test beam measurement in  $\pi E1$  in December 2023. The main goal of this test beam was to study the systematic effect of a change in the momentum of injected muons for magnetic fields with different polarities and magnitudes. For this purpose, we focused on the measurement of the time of flight (ToF) of muons as they pass through the vacuum of an injection channel that acts as a magnetic shield permitting a low magnetic-field path into the bore of the solenoid. At the same time, different detectors were tested, such as the beam monitor and ToF detector prototypes of varying scintillator thicknesses, between 25  $\mu\text{m}$  to 200  $\mu\text{m}$ .

### 3.5.1 Data taking

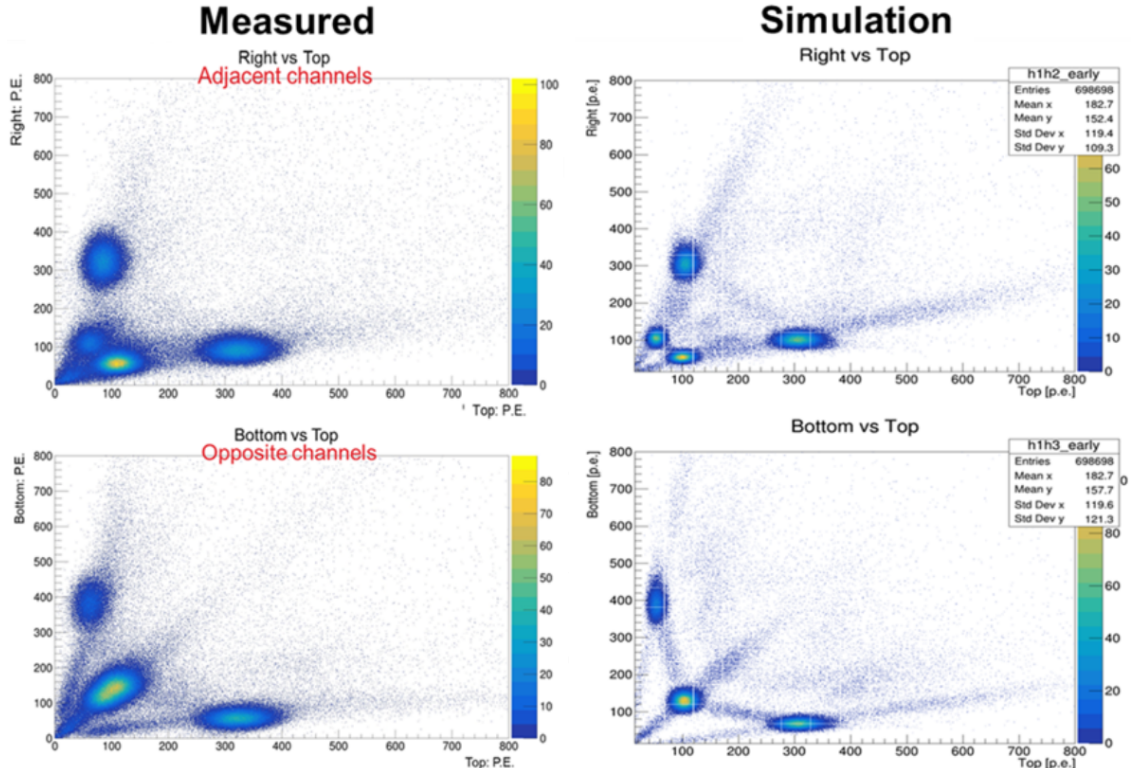
Let's start by describing the setup used during this beam time. The idea was to have two injection channels: inject the beam on the top line, then invert the magnetic field and shift the whole apparatus vertically to inject from the bottom line. Due to the delay of the height-adjustable magnet support, we could only use one channel. Additionally, given the studies on SC injections (Sec. 2.3.4) were still ongoing, we opted for magnetic steel, which would shield up to 0.8 T. For this reason, we limited the magnet field to  $-750 < B < 750$  mT, so that the fringing fields could not behave as magnetic mirrors, rejecting the incoming muon, or deflecting them too much from the trajectory. Figure 3.24a shows a simulation of the relative permittivity of the injection tube for three different nominal magnetic-field values in the center of the solenoid bore. With a field of



(a) Sketch to explain the correlation patterns between the charges of the different scintillators in the telescope in case of crosstalk. The scintillators are color-coded to aid understanding the patterns.



(b) In the case of the telescope from Pisa, the double readout and modular style created small gaps between the scintillators. The result is that no optical crosstalk is expected nor found.



(c) In the Shanghai telescope, the scintillators are in contact. The result is the appearance of the correlation structures. These are in agreement with the expectations and nicely reproduced by the simulations.

**Fig. 3.23:** In case optical crosstalk is present, the correlation of the charges measured by the different scintillators show interesting patterns. These are expected and found in the Shanghai telescope, and not in the Pisa version, due to small gaps in the system.

750 mT the relative permittivity of the tubes remains above 10 indicating no or only low saturation along the tube. Moreover, as seen in Figure 3.24b, with a field of 750 mT the magnetic field strength in the middle of the tube is below 100 mT for  $\sim 98\%$  of the length of the injection tube. By setting the PSC magnet to produce a magnetic field of 750 mT inside its bore, a shielding factor of almost two along the center axis of the injection tube is expected. The expected stress for these injection channels is significant and for this reason, a proper holding structure was developed and we opted for *dummy*-injection tubes to mitigate the stress generated on the magnet. The ANSYS<sup>®</sup> structural simulation, the CAD design of the holder, and the overall setup are shown in Fig. 3.25. The injection channel was vacuumed and sealed with 35  $\mu\text{m}$  Mylar<sup>®</sup> foils. At both ends of the injection channels detector modules were connected: three upstream (Veto, BeamMonitor, TOF in) and one downstream (TOF out), all described in the following paragraphs. The DAQ system was the WaveDAQ standalone board, able to digitize the waveforms of each channel up to 5 GSample/s. The WaveDAQ provides also the power for the MPPC, up to  $\approx 220\text{ V}$  per channel. The trigger configurations were also set using the GUI interface of WaveDAQ.

**Beam and Beam Monitor** The first thing was to measure the lateral phase space to later match the simulations. This can be calculated from measurements of the beam profile taken over a scan of the current in the last two quadrupoles. The profiles were measured using a  $2 \times 2\text{ mm}^2$  pill counter moved by an  $xy$ -scanner for each implemented beam configuration. After removing the pill, the first item in the setup was the Beam Monitor, a squared detector made of scintillators arranged to have a squared hole. The aim of this detector, as outlined in Ch. 2, where the details of the working principles were previously discussed, is to center the beam. Two monitors with different segmentation and scintillator tile shapes were tested. One consisted of eight rectangular tiles, while the other consisted of four triangular tiles per layer. Additionally, two orientations at a rotation of  $0^\circ$  and  $180^\circ$  around the beam axis were compared to check the performance of individual tiles. Finally, the measurements were performed at different magnetic fields generated by the PSC magnet to map the deflection of the beam spot at the entrance of the injection channel.

**Time Of Flight (TOF)** Following the beam monitor, two scintillators are used to evaluate the time of flight. The idea is to use thin scintillators to reduce the multiple scattering. From the previous beamtime, we know we can use  $100\text{ }\mu\text{m} \div 200\text{ }\mu\text{m}$  achieving an intrinsic time resolution of  $\sigma_{int} \approx 300\text{ }\mu\text{s}$ . The aim here is to evaluate the momentum spread of the beam by measuring the TOF. The difference in momentum translates into the difference in time of the scintillator signals  $\Delta t$ . The distribution of  $\Delta t$  is the convolution of the momentum distribution and the intrinsic time resolution of the system. Assuming a Gaussian distribution for the beam momentum, centered around 28 MeV/c and having spread 1%, 3%, and 5%, we can evaluate the  $\Delta t_{measured}$  for different distances. In Fig 3.27 the expected distributions for 1% spread and  $\sigma_{int} \approx 300\text{ }\mu\text{s}$ , while the *std. dev.* of the obtained distributions is shown as a function of distance for 3% and 5%. From these estimations we can conclude a 1% momentum spread, with the given  $\sigma_{int}$  and reasonable distances, cannot be appreciated. The situation seems different for 3% and 5%. Figure 3.26 shows one of the ToF prototypes fabricated in 2023, while it was being mounted to the injection tubes.

The coincidence of different channels per detector was studied, to decrease the threshold, increase

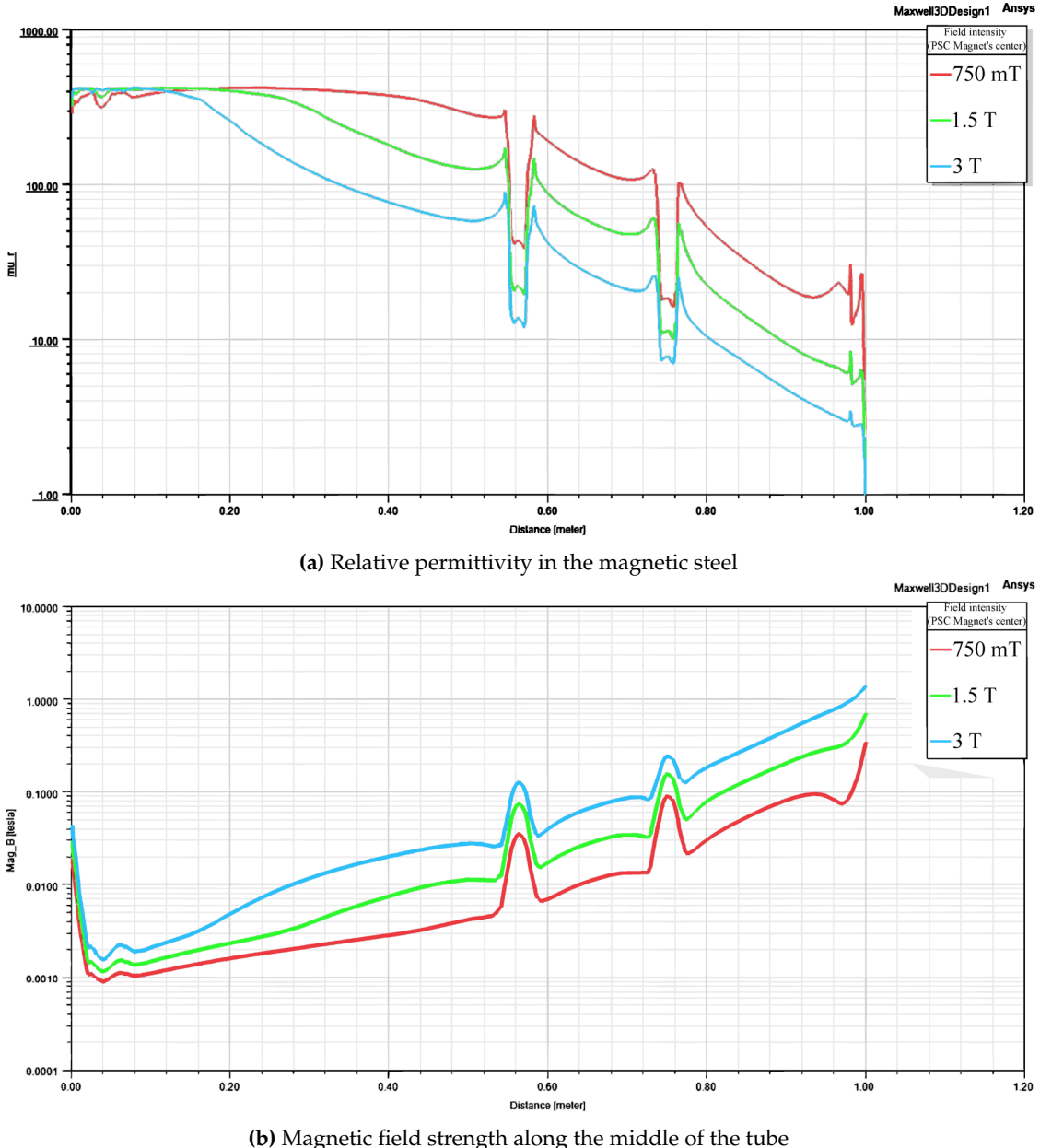
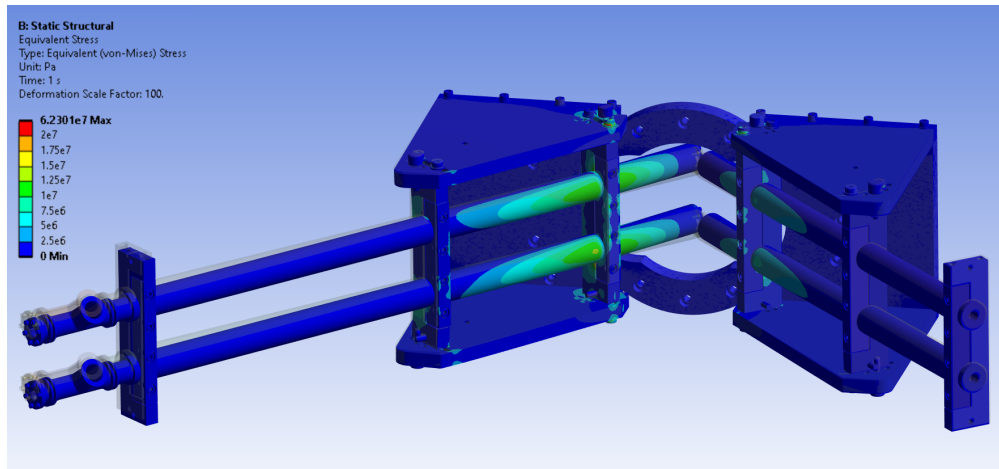
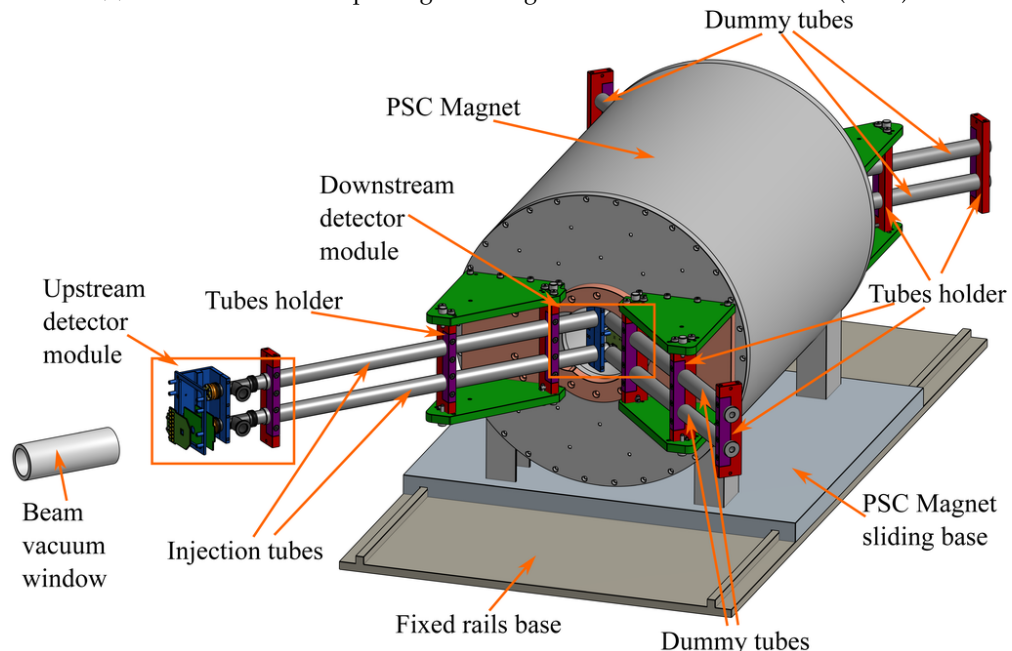


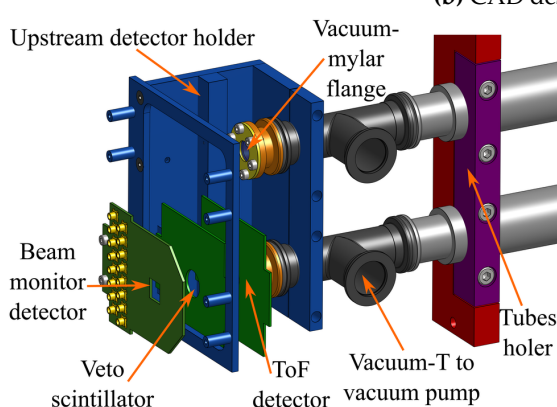
**Fig. 3.24:** Simulation results for different nominal magnetic fields at the center of the PSC solenoid. (a) shows the relative permittivity of the injection tubes as a function of the distance along the tube, starting from the upstream position and going towards the downstream position inside the bore of the PSC magnet. (b) shows the magnetic field strength along the middle of the injection tube. Note that the two significant features are a result of a reduced wall thickness of the steel tube at these positions, for the mechanical support.



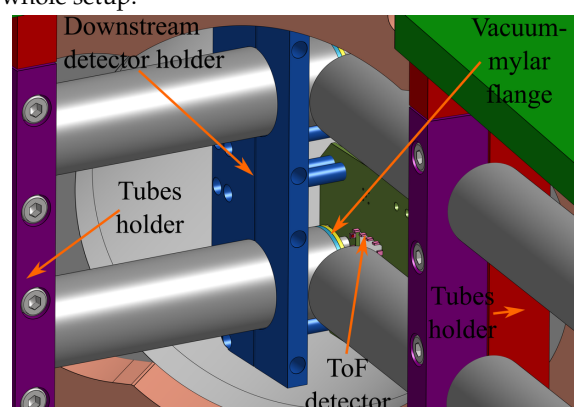
(a) The stress of the setup and ghost image of the deformation caused ( $\times 100$ ).



(b) CAD design of the whole setup.



(c) CAD detail of the US detectors.



(d) CAD detail of the DS detectors.

**Fig. 3.25:** The support structure was developed to reduce stresses to the injection channel and the PSC magnet: (a) shows the ANSYS® studies, (b) the whole setup, (c) and (d) the detail of the US and DS detectors.



**Fig. 3.26:** One of the ToF detector prototypes fabricated in 2023 with four readout channels. The detector is mounted on the downstream detector module which is attached to the injection tubes.

the sensitivity of each detector, and reach the maximum efficiency by comparing combinations of different prototypes under test beam conditions. As the beam characteristics and the momentum of the muons were essentially constant, it was possible to test the effects of the magnetic field “handedness”, CW vs. CCW storage of the muons inside the storage magnet, on the momentum and muon trajectory along the injection channel by measuring the ToF between upstream (US) and downstream (DS) detector. Measurements with different magnetic field strengths and polarities were performed. The changes in the magnetic field were performed by sweeping between the maximum magnetic-field magnitudes of  $\pm 750$  mT, in such a way as to also be sensitive to possible hysteresis effects.

**Multi-readout gate** A cardinal point was the implementation of four independent readout channels for the new thin scintillators. This was discussed earlier (Sec 3.4) and is linked to the necessity of lowering the threshold while keeping a low dark rate. A picture during the soldering and the CAD design are shown in Fig. 3.28. We took data with mixed (old 1ch and new 4ch) and matched (new 4ch and new 4ch) setups. This allowed us to benchmark the new detectors.

**Efficiency and calibration** Along the  $\pi E1$  beamline, a separator akin to a Wien filter is employed to discriminate between muons and pions by adjusting the relative strengths of magnetic and electric fields. When both fields are set to zero, particles with the desired momentum (in our case, 28 MeVc/) pass through the separator and reach the experiment. We utilized this functionality to calibrate the Time of Flight (ToF) setup by measuring the ToF of positrons traveling near the

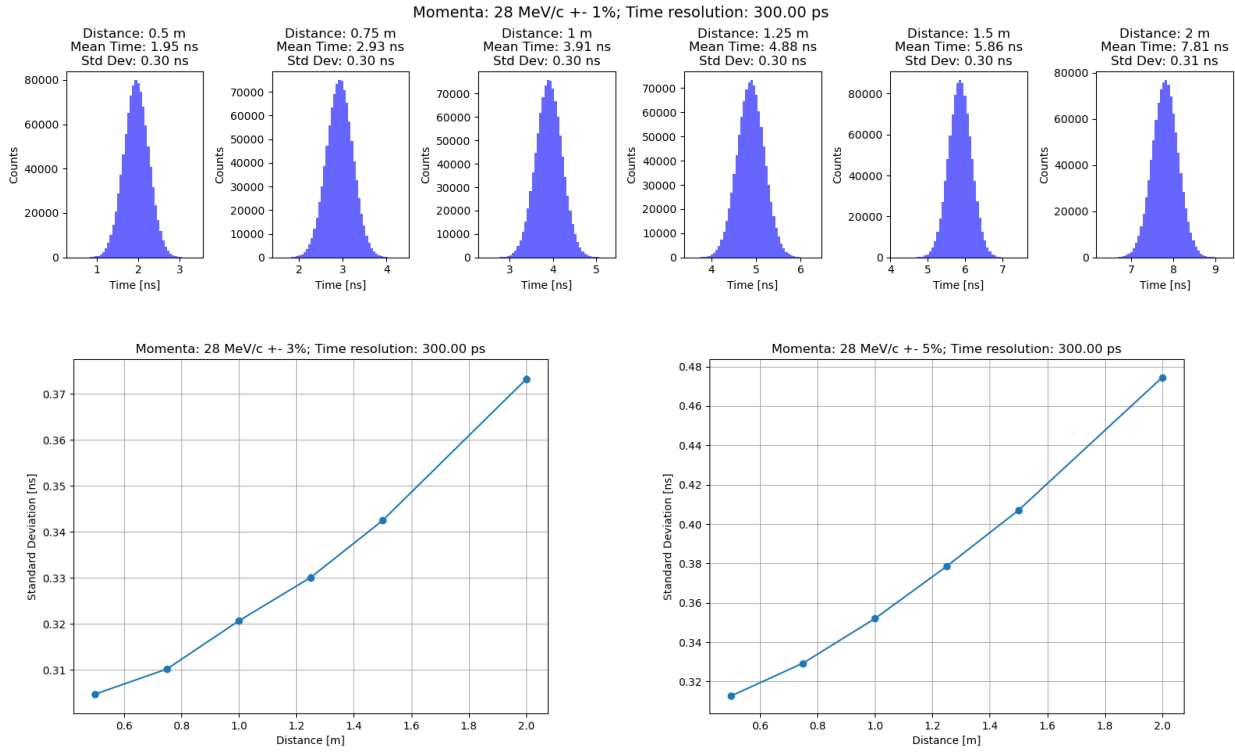


**Fig. 3.27:** A simple Python simulation to evaluate the resolution for the TOF for different distances, momentum spread, and time intrinsic resolution of the couple of scintillators used. For  $\sigma_{int} = 300$  ps we do not appreciate a 1% spread in momentum while we have the sensitivity for 3% and 5%.

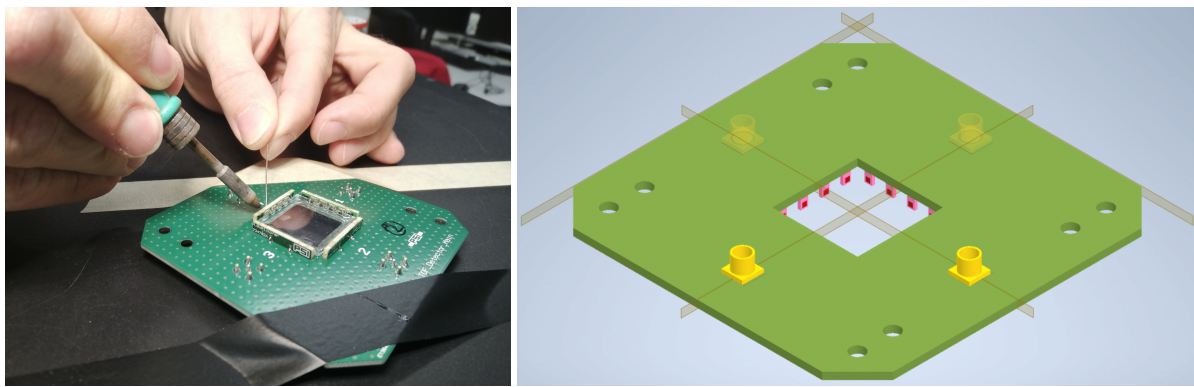


**Fig. 3.28:** A picture of the TOF detectors used during the 2023 December beam-time. Thin scintillators (50 and 100  $\mu\text{m}$ ) read on four sides by four SiPMs.

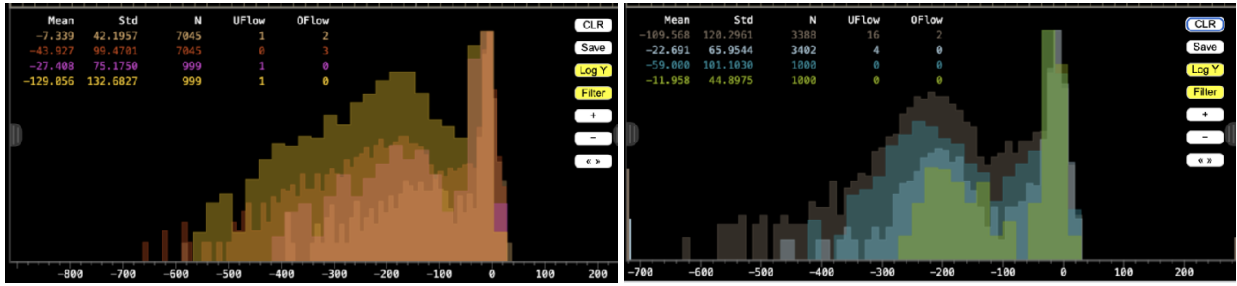


**Fig. 3.29:** Charge integral of the 8-segmented beam monitor as extracted online in WaveDAQ GUI. Left: overlay of all the corner 2 mm thick tiles. Right: overlay of all the middle 2 mm thick tiles. The peak on the right corresponds to positrons, while the broader peak on the left corresponds to muon energy depositions.

speed of light. Another setup was dedicated to evaluating the relative efficiency and intrinsic time resolution of the detectors. Two detectors were positioned back-to-back with minimal spacing (a few millimeters), and this configuration was repeated for all possible detector pairs.

### 3.5.2 Data analysis

**Beam Monitor** The two tested versions were the 4 and 8-segmented variants. Using the WaveDREAM board, the 16 different channels had a threshold adjusted so to keep the dark noise manageable. Ideally, with the beam on, the front 2 mm scintillators would distinguish the particle ID creating two peaks but this was not the case for all channels (Fig. 3.29). Optical coupling and soldering of these channels are under test. At this point, the threshold of the front layer was changed to select muons. Two triggers were used during data-taking: requiring a hit in the channel of interest, regardless of all other 15 channels, and requiring a hit in the tile of interest, while vetoing a hit in all the 5 mm channels. The beam monitor position and B field scan were repeated by flipping the detector by 180 deg. Examples of the measurements taken for the two versions are in Fig. 3.30 and Fig. 3.31. Overall the 8-segmented version behaved as expected while the other presented a ‘hot’-channel. The analysis is still ongoing but the positioning of the beam seems to be sub-optimal. For example, the 4-segmented version misplaced the beam center by 6.3 mm.

**TOF scintillators** Two TOF detectors per scintillating foil thickness (100  $\mu\text{m}$  and 50  $\mu\text{m}$ ) have been tested, for a total of four detectors, in different combinations. The beamtime aimed to measure the detection efficiency of each detector and its intrinsic timing resolution, as well as the time-of-flight resolution for all the possible combinations of the available detectors. The threshold of each channel was set to have a dark count rate of a few 100 Hz (apart from a couple of noisy channels up to 1 kHz) with the Beam Blocker closed. As a reference, with the settings of our beamline, we had a typical rate of  $\approx 50$  KHz on the US detector.

Two experimental setups have been used to extract the detector characteristics as listed above:

- the *short* configuration, with the two detectors separated by less than 1 cm, along the beam-line direction. The first detector is the detector under test (DUT), while the second is the reference (REF). This configuration can be used to extract the efficiency of the DUT, by triggering on the REF, and the intrinsic timing resolution for the detector pair under study, due to the relatively short distance between the two detectors.

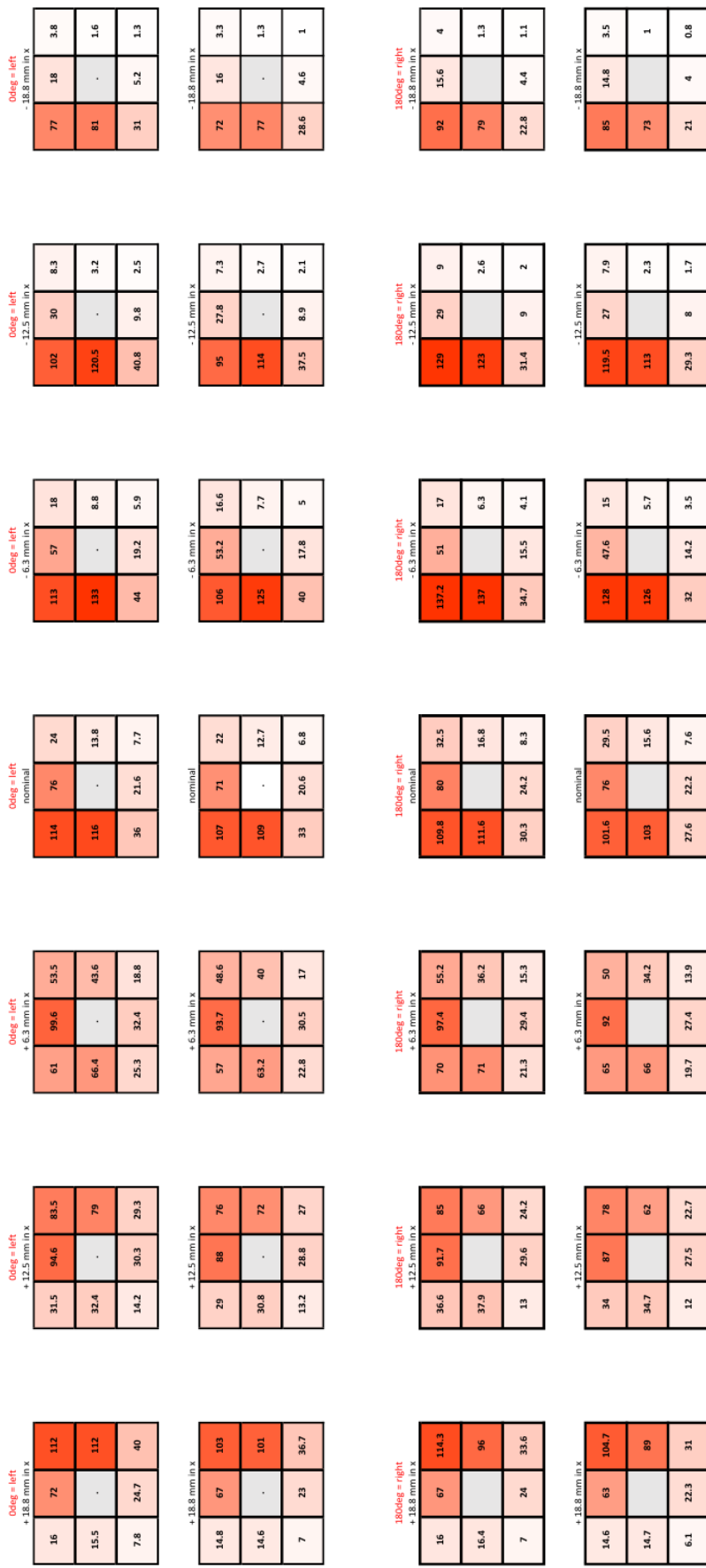


**Fig. 3.30:** The online rates in kHz in 2 mm thick tiles of the 8-segmented beam monitor. The rates were recorded for three x-positions left and right of the nominal detector position (the center images). The top two rows show the rates for the beam monitor in "0 deg" position, while the bottom two rows show the data for the "180 deg" rotated monitor. Two rows for each detector rotation correspond to the two trigger configurations (see text), with the upper row being just the rate of a channel, and the bottom row requiring a hit in the channel and no hits in the thicker back scintillator plane. The beam is entering the image plane along the line of sight.

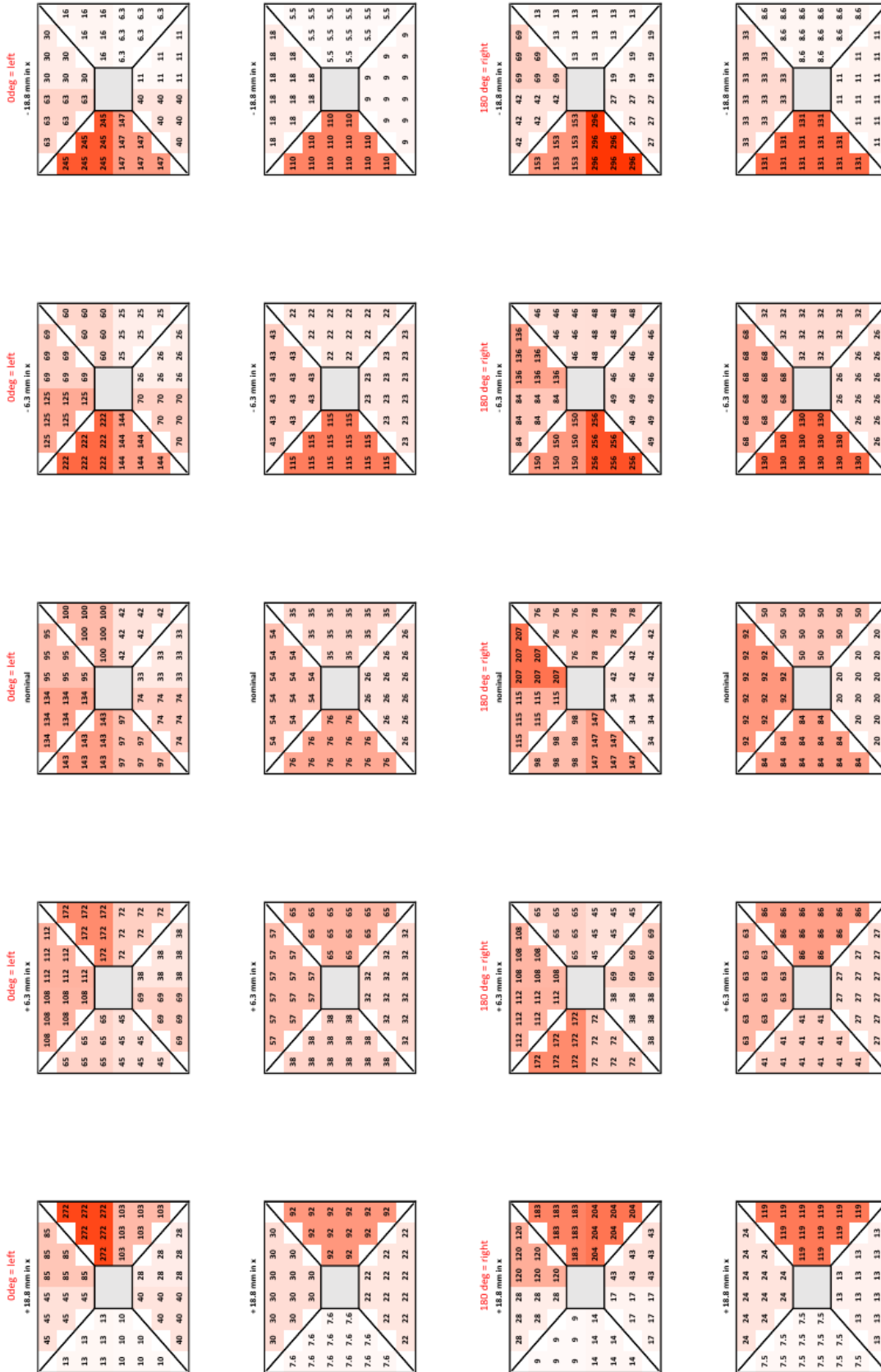


**Fig. 3.31:** The online rates in kHz of the 4-mm thick tiles of the 4-segmented beam monitor. The rates were recorded for two x-positions left and right of the nominal detector position (the center images). The top two rows show the rates for the beam monitor in "0 deg" position, while the bottom two rows show the data for the "180 deg" rotated monitor. Two rows for each detector rotation correspond to the two trigger configurations (see text), with the upper row being just the rate of a channel, and the bottom row requiring a hit in the tile (with a signal in both channels) and no hits in the thicker back scintillator plane. The beam is entering the image plane along the line of sight.



**Fig. 3.32:** The *short* and *long* configurations, used to extract the main parameters of the TOF detectors.

- the *long* configuration, with the two detectors mounted at the entrance and exit of the injection line. This configuration is the one used to measure the TOF.

Fig. 3.32 shows the pictures of the mounted detectors in short (left) and long (right) configurations.

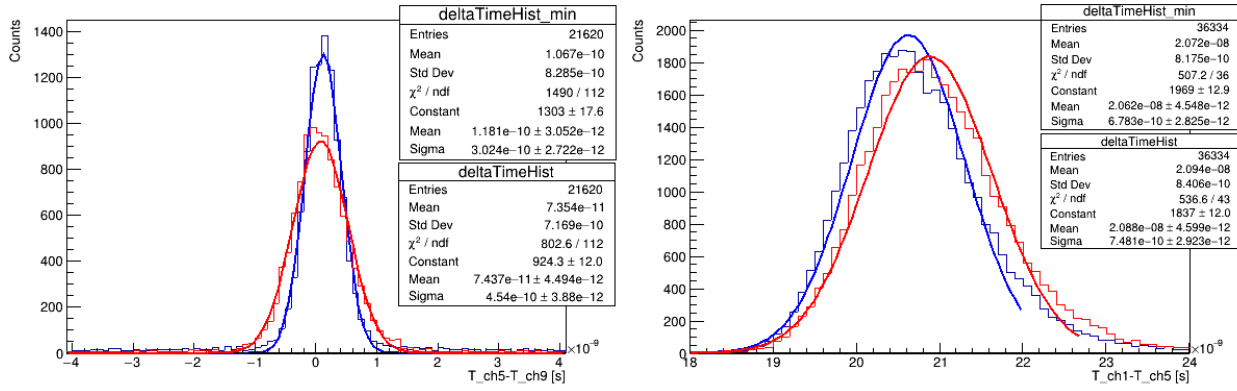
Detectors of the same thickness showed similar efficiency. The numbers reported here refer to the mean of the two. They are still preliminary and conservative but provide a reasonable overview.

- 100  $\mu\text{m}$ : A full detection efficiency ( $> 99\%$ ) is measured requiring *at least one fired channel*. It decreases if at least *two, three, or four* fired channels is requested ( $>98\%$ ,  $>96\%$ ,  $>95\%$ ).
- 50  $\mu\text{m}$ : With similar requirements the efficiency measured is  $>87\%$ ,  $>64\%$ ,  $>45\%$ , and  $>40\%$ .

Fig. 3.33a shows the intrinsic time resolution for the 100  $\mu\text{m}$  detector pair, using a constant fraction method to extract the time of each channel. A timing resolution of 450 ps is measured if the time difference of two fixed channels is plotted (red line). The timing algorithm can be easily optimized by taking advantage of the segmented detector, made of four independent channels. For each event, the fastest channel on each side can be used to plot the time difference. This is shown as the blue line, with a timing resolution down to 300 ps. The same analysis can be repeated with the two detectors mounted in the long configuration, with the results shown in Fig. 3.33b with the mean of the distribution being the TOF of the impinging particles and its resolution being the convolution of several terms, including the intrinsic timing resolution of the detector pair and the momentum spread of the particles. Although these results are very preliminary, the expected detector performances are nicely addressed and satisfy the experiment requirements.

**TOF** TOF measurements were taken for different detector setups and at different magnetic fields in the range of  $-750$  mT to  $750$  mT. The mounted detectors have scintillating foil thicknesses of 200  $\mu\text{m}$  (Detector #0), 100  $\mu\text{m}$  (Detector #1 and #2) and 50  $\mu\text{m}$  (Detector #3 and #4) and were used in five different configurations: US#0-DS#1, US#2-DS#1, US#3-DS#1, US#4-DS#3 and US#4-DS#1. Table 3.3 shows an overview of the TOF measurements taken. For the preliminary Time of Flight study, only measurements with changing B fields have been considered.

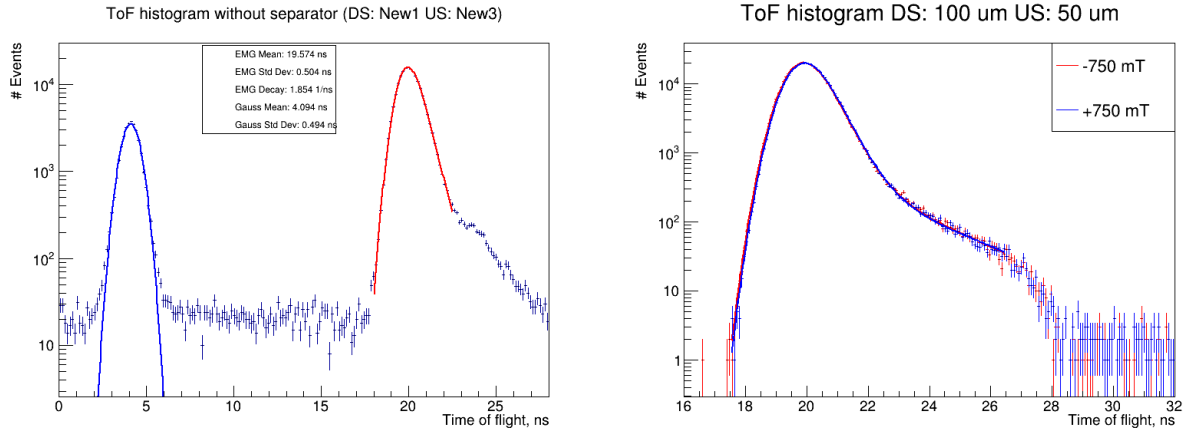
To extract the time when a particle passes a detector, the signals of all four channels of a detector are summed and a constant fraction discrimination (CFD) method is applied. This is akin to taking the first channel per detector. The CFD delays the original signal by five data points, corresponding to a delay of about 1 ns, and half of the original signal is subtracted from the delayed pulse.



(a) Short configuration with 100 μm detector pair.

(b) Long configuration with 100 μm detector pair.

**Fig. 3.33:** Time difference for the 100 μm detector pair, mounted on the *short* (a) and *long* (b) configuration. In red the result of taking two fixed channels, in blue taking the first channel to be triggered in the detectors.



(a) Time of flight of positrons (blue) and muons (red). The (b) ToF histograms with the same detector setup at positive widths of the two are in agreement, indicating good per-and negative 750 mT magnetic field. The means of the two ToF spectra differ by only 0.16%.

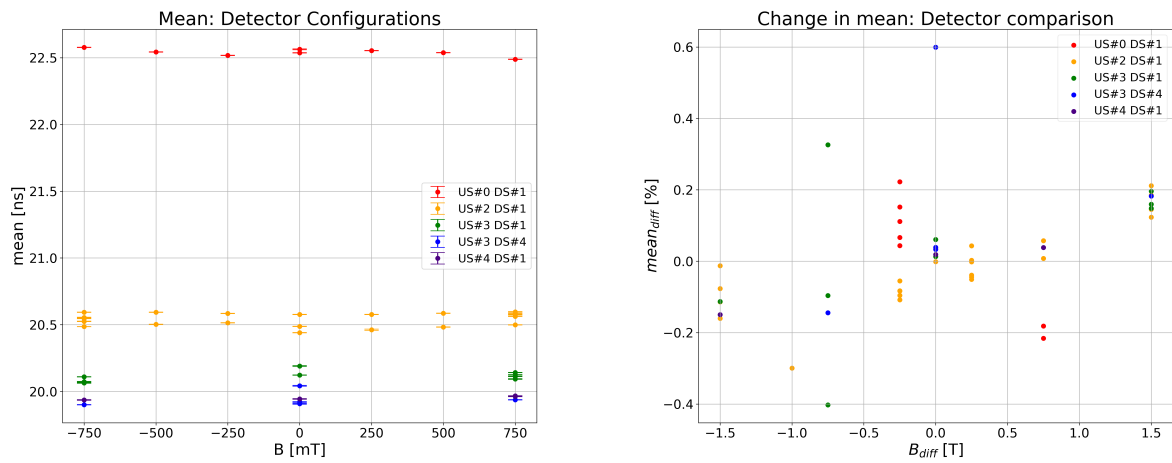
**Fig. 3.34:** (a) Time of flight of positrons and muons measured with 50 μm upstream and 100 μm downstream detectors and (b) the same setup with muons at  $\pm 750$  mT. Due to energy losses in air and the entrance trigger, the muon peak is fitted with an exponentially modified Gaussian instead.

This results in a histogram for the ToF, see as an example Fig. 3.34. The mean of the distribution is calculated without taking into account the long tail<sup>7</sup> on the right side of the distribution and Fig. 3.35a shows a comparison of the preliminary means for the five detector setups. Fig. 3.35b displays the change of the mean plotted against the change in the magnetic field for consecutive measurements in the same detector configuration. Some significant trends are present and currently under study.

<sup>7</sup>This will be later fixed by fitting to an exponentially modified Gaussian.

Detector US	Detector DS	B Field, mT	Position	Events	FS52, mm	FS54LR0U, mm
Old0 200um	New1 100um	0 [0]	0 mm	100k	50	50,50,50,50
Old0 200um	New1 100um	250 [0]	0 mm	500k	50	50,50,50,50
Old0 200um	New1 100um	500 [250]	0 mm	500k	50	50,50,50,50
Old0 200um	New1 100um	750 [500]	0 mm	500k	50	50,50,50,50
Old0 200um	New1 100um	0 [750]	0 mm	500k	50	50,50,50,50
Old0 200um	New1 100um	-750 [0]	0 mm	500k	50	50,50,50,50
Old0 200um	New1 100um	-500 [-750]	0 mm	500k	50	50,50,50,50
Old0 200um	New1 100um	-250 [-500]	0 mm	500k	50	50,50,50,50
Old0 200um	New1 100um	-250 [-250]	0 mm	250k	50	50,50,50,50
Old0 200um	New1 100um	-250 [-250]	0 mm	250k	50	50,50,50,50
New2 100um	New1 100um	0 [-250]	0 mm	550k	50	50,50,50,50
New2 100um	New1 100um	250 [0]	0 mm	500k	50	50,50,50,50
New2 100um	New1 100um	500 [250]	0 mm	500k	50	50,50,50,50
New2 100um	New1 100um	750 [500]	0 mm	500k	50	50,50,50,50
New2 100um	New1 100um	0 [750]	0 mm	500k	50	50,50,50,50
New2 100um	New1 100um	-750 [0]	0 mm	500k	50	50,50,50,50
New2 100um	New1 100um	-500 [-750]	0 mm	500k	50	50,50,50,50
New2 100um	New1 100um	-250 [-500]	0 mm	500k	50	50,50,50,50
New2 100um	New1 100um	750 [-250]	0 mm	500k	50	50,50,50,50
New2 100um	New1 100um	500 [+750]	0 mm	500k	50	50,50,50,50
New2 100um	New1 100um	250 [+500]	0 mm	500k	50	50,50,50,50
New2 100um	New1 100um	0 [+250]	0 mm	500k	50	50,50,50,50
New2 100um	New1 100um	-250 [0]	0 mm	500k	50	50,50,50,50
New2 100um	New1 100um	-500 [-250]	0 mm	500k	50	50,50,50,50
New2 100um	New1 100um	-750 [-500]	0 mm	500k	50	50,50,50,50
New2 100um	New1 100um	0 [-750]	0 mm	100k	8.55-8.60	50,50,50,50
New2 100um	New1 100um	0 [-750]	0 mm	100k	8.6	50,50,50,50
New2 100um	New1 100um	0 [-750]	0 mm	100k	15	50,50,50,50
New2 100um	New1 100um	0 [-750]	0 mm	400 k	30	50,50,50,50
New2 100um	New1 100um	0 [-750]	0 mm	400 k	50	50,50,50,50
New2 100um	New1 100um	750 [0]	0 mm	500k	50	50,50,50,50
New2 100um	New1 100um	-750 [+750]	0 mm	500k	50	50,50,50,50
New2 100um	New1 100um	750 [-750]	0 mm	200K	50	50,50,50,50
New2 100um	New1 100um	-750 [+750]	0 mm	200K	50	50,50,50,50
New2 100um	New1 100um	750 [-750]	0 mm	200K	50	50,50,50,50
New3 50um	New1 100um	0 [-750]	0 mm	500k	50	50,50,50,50
New3 50um	New1 100um	0 [-750]	0 mm	500k	50	50,50,50,50
New3 50um	New1 100um	0 [-750]	0 mm	500k	50	50,50,50,50
New3 50um	New1 100um	0 [-750]	0 mm	500k	50	50,50,50,50
New3 50um	New1 100um	0 [-750]	0 mm	500k	50	50,50,50,50
New3 50um	New1 100um	0 [-750]	0 mm	500k	50	50,50,50,50
New3 50um	New1 100um	0 [-750]	0 mm	400k	50	20,20,15,15
New3 50um	New4 50um	0 [-750]	0 mm	400k	50	20,20,15,15
New3 50um	New4 50um	0 [-750]	0 mm	500k	50	20,20,15,15
New3 50um	New4 50um	0 [-750]	0 mm	50k	50	20,20,15,15
New3 50um	New4 50um	0 [-750]	0 mm	100k	50	20,20,15,15
New3 50um	New4 50um	750 [-750]	0 mm	500k	50	20,20,15,15
New3 50um	New4 50um	750 [-750]	0 mm	500k	50	20,20,15,15
New3 50um	New4 50um	750 [-750]	0 mm	500k	50	20,20,15,15
New3 50um	New4 50um	750 [-750]	0 mm	500k	50	20,20,15,15
New3 50um	New4 50um	750 [-750]	0 mm	500k	50	20,20,15,15
New3 50um	New1 100um	0 [-750]	27.8 mm	50	50,50,50,50	
New3 50um	New1 100um	0 [-750]	-27.8 mm	50	50,50,50,50	
New3 50um	New1 100um	0 [-750]	-18.5 mm	50	50,50,50,50	
New3 50um	New1 100um	0 [-750]	-9.3 mm	50	50,50,50,50	
New3 50um	New1 100um	0 [-750]	9.3 mm	50	50,50,50,50	
New3 50um	New1 100um	0 [-750]	18.5 mm	50	50,50,50,50	
New4 50um	New1 100um	0 [-750]	0 mm	500k	50	50,50,50,50
New4 50um	New1 100um	-750 [0]	0 mm	250k	50	50,50,50,50
New4 50um	New1 100um	750 [-750]	0 mm	250k	50	50,50,50,50
New4 50um	New1 100um	750 [-750]	0 mm	250k	50	50,50,50,50
New4 50um	New1 100um	0 [750]	27.8 mm	100 k	50	50,50,50,50
New4 50um	New1 100um	0 [750]	18.5 mm	10 k	50	50,50,50,50
New4 50um	New1 100um	0 [750]	18.5 mm	20 k	50	50,50,50,50
New4 50um	New1 100um	0 [750]	9.3 mm	30 k	50	50,50,50,50
New4 50um	New1 100um	0 [750]	-9.3 mm	30 k	50	50,50,50,50
New4 50um	New1 100um	0 [750]	-18.5 mm	30 k	50	50,50,50,50
New4 50um	New1 100um	0 [750]	-27.8 mm	30 k	50	50,50,50,50
New2 100um	New1 100um	-750 [+750]	0 mm	250k	50	50,50,50,50
New2 100um	New1 100um	750 [-750]	0 mm	250k	50	50,50,50,50
New2 100um	New1 100um	750 [-750]	0 mm	250k	50	50,50,50,50
New2 100um	New1 100um	-750 [+750]	0 mm	250k	50	50,50,50,50

**Tab. 3.3:** Overview of the Time of Flight measurements ordered by date, displaying the upstream (US) and downstream (DS) detectors, the magnetic field of the solenoid, its position along the rails, the number of events and the slit settings for slits FS52 and FS54 for every measurement.



**(a)** TOF means vs PSC magnetic field. Differences can be explained with the energy loss in the upstream detector.

**(b)** TOF mean change vs change in field between consecutive measurements.

**Fig. 3.35:** In **(a)** the TOF means for the five detector setups are plotted against the B field settings while in **(b)** the change of the mean ToF versus the change of the magnetic field for consecutive measurements. A detector setup corresponds to the upstream (US) and downstream (DS) detectors for the Time of Flight measurement (#0 is the old 200  $\mu\text{m}$  detector).

# Bibliography on muEDM entrance detector

- [1] R. L. Workman et al. "Review of Particle Physics". In: *PTEP* 2022 (2022), p. 083C01. DOI: [10.1093/ptep/ptac097](https://doi.org/10.1093/ptep/ptac097).
- [2] G. Cavoto et al. "Operating the GridPix detector with helium-isobutane gas mixtures for a high-precision, low-mass Time Projection Chamber". In: *JINST* 18 (May 2023), P10035. DOI: [10.1088/1748-0221/18/10/P10035](https://doi.org/10.1088/1748-0221/18/10/P10035). arXiv: [2305.03599 \[physics.ins-det\]](https://arxiv.org/abs/2305.03599).

## Chapter 4

# muEDM positron tracker

*This chapter is an in-depth study on the development of the scintillating fiber part of the muEDM positron tracker. We will skip some preliminary studies and we will start with the description of the positron tracker which was included in the proposal of the experiment submitted to PSI at the end of 2022. We will move to the simulations done after that and the current design of this detector.*

### 4.1 Tracking $e^+$ in muEDM

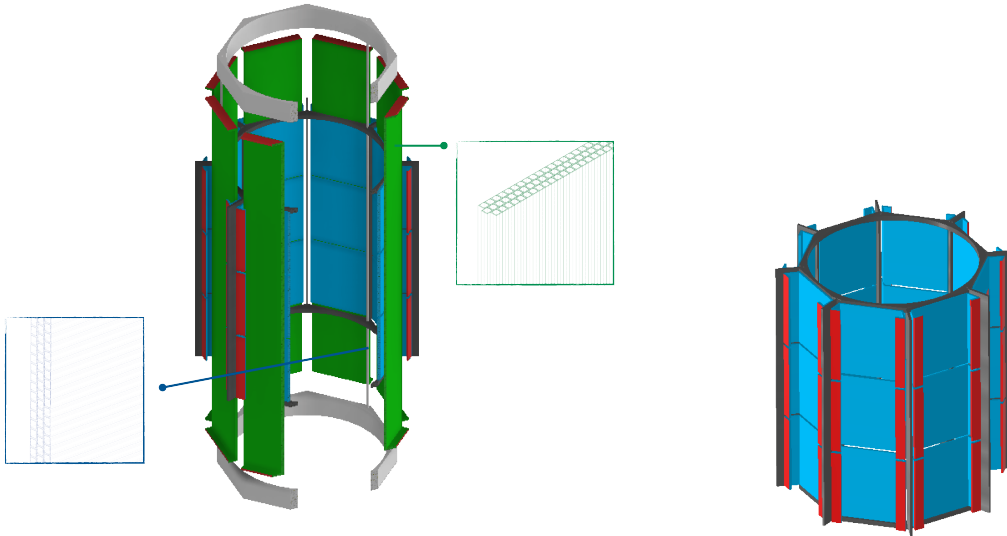
As already introduced in Ch. 2, the muEDM experiment is based on the *frozen spin* technique. For this purpose, it is cardinal to stop the muon in the right orbit. After the muon has been stored, the careful calibration of the radial electric field will then change the  $(g - 2)$  precession, bringing it eventually to 0. At this point, the direction of the positron emission will be the relevant variable for the EDM search. These three steps require a way to track the outgoing  $e^+$ . Developing such a tracker in the muEDM environment is the challenge to which this chapter is dedicated.

We will start by presenting the detector included in the proposal of 2022 and then the version obtained in 2023 refining the original design. The original detector design was developed to be complemented with silicon devices. By the end of 2023, the requirement for this detector changed, with the delay of the Pixel sub-detector. Some studies on a radial solution will close the chapter.

### 4.2 Design in the 2022 proposal

The kinematics of the  $e^+$  coming from the decay is described in a Sec. 2.4. From preliminary results, the resolutions required for the different studies are the following:

- Momentum resolution: around a few MeV/c. This is necessary for selection cuts on positrons with the desired asymmetry, which is momentum dependent, as discussed in Section 2.4.
- Position resolution: around 1 mm. This seems to be the necessary resolution for track fitting with the required uncertainties on the emission direction. This result was achieved by geometric means, assuming that reliable timing information is not available.
- Timing resolution: less than 1 ns. The 28 MeV/c positron travels at  $c$ , meaning that in the expected magnetic field a complete rotation takes  $\gtrsim 0.6$  ns imposing this limit.



(a) Sketch of the SciFi conceptual design. The outer part is made of eight ribbons, with the fibers oriented longitudinally.

(b) The inner part is made up of three barrels of scintillating fiber ribbons. Each barrel constitutes eight ribbons, with the fibers oriented transversely.

**Fig. 4.1:** In (a) and (b) the CAD view of the detector design while in (c) the details on the ribbon structure and the fiber *cladding*.

To accomplish these requirements, the idea was to implement a two sub-system tracker: a positron tracker based on scintillating fibers of  $250 \div 1000 \mu\text{m}$  size coupled to silicon photomultipliers (SiPM) plus a tracker based on the silicon Pixel technology, developed by the UK part of the collaboration. The scintillating fiber part of the detector allows for a fast, versatile, modular, and low-cost detector technology that is operational in magnetic fields and vacuum, the environment in which the muEDM measurement takes place.

#### 4.2.1 The SciFi detector

The SciFi detector is designed to provide excellent tracking capacities for minimum-ionizing particles with a detector thickness below 0.4 %, a timing resolution better than 1 ns, and a spatial resolution of 1 mm, or better. Fig. 4.1 shows the first conceptual design of the detector. The tracker would be a compact detector made of several *ribbons* of  $250 \mu\text{m}$  scintillating fibers arranged in an inner (transverse) and an outer (longitudinal) detector. The inner detector would be made of a minimum of three barrels, extendable to five, of scintillating fiber ribbons. Each barrel made of eight ribbons, with the fibers oriented transversely. This is the SciFi transverse detector, as shown in Fig. 4.1b, providing the necessary longitudinal resolution (up/down) to measure the EDM signal.

In this detector, the fiber ribbons are polygonally shaped as shown by the blue elements in the figure. The red elements represent the photosensors. The optional outer detector is made of eight ribbons, with the fibers oriented longitudinally. Here, the ribbons have a parallelepipedal shape (green elements) with photosensors at both ends (red elements), as shown in Fig. 4.1a. This is the SciFi longitudinal detector, which could complement the silicon strip detector discussed in the previous sections. Both detectors are arranged to cover a cylindrical surface, with the radius of the inner detector currently equal to 50 mm (AAA ???).

Each ribbon has three layers of fibers, and these three layers are glued together in a staggered way, as sketched in Fig. 4.1c. Each layer is made up of 128 250  $\mu\text{m}$  square or round multiclads fibers. One layer has a width of approximately 32 mm and a thickness of approximately 200 mm. Each ribbon is read out at both ends by silicon photomultiplier (SiPM) arrays. Double-readout of each ribbon is essential for matching the experiment requirements. The amount of energy deposited in such a thin fiber by a MIP is small ( $\mathcal{O}(35 \text{ keV})$ ) and, given the size of the detector, the relative light reaching the photosensor turns out to be equal to a few photons/fiber. To successfully collect these few photons with maximum efficiency and high dark noise rejection factor, a double readout scheme is foreseen, as well as extreme care in the coupling of the fibers to the photosensors.

### 4.2.2 Scintillating fibers prototype

A prototype to mimic the behavior of a fiber ribbon was built and tested. It consists of 32 squared, 250  $\mu\text{m}$  thin multiclads BCF-12 fibers manufactured by Saint-Gobain<sup>1</sup> and it is shown in Fig. 4.2. The fibers were assembled to make four fiber layers; the first one was used as a trigger, and the others, staggered by half a fiber, were used to mimic the detector. Each fiber was coated by physical vapor deposition with  $\sim 100 \text{ nm}$  of aluminum along its whole length, with the aluminum acting as an optical insulator. The fiber ends were fixed on two plexiglass end plates, which were polished with a diamond cutting blade and fixed to an aluminum support structure. Each fiber end was coupled with BC630 optical grease to a Hamamatsu 13360-1350CS SiPM (active area  $1.3 \times 1.3 \text{ mm}^2$ , pixel size 50  $\mu\text{m}$ , PDE 40 %<sup>2</sup> [1]), resulting in 64 channels. All SiPMs were biased at the same bias voltage ( $\approx 55 \text{ V}$ ). The signal was passed through a minicircuit amplifier, working with a typical gain of 40 dB, and finally digitized with DRS V5 evaluation boards [2, 3] at a sampling speed of 5 GSPS. To emulate the situation in which the fiber tracker is read out column-wise by SiPM arrays (see Fig. 4.3a), rather than reading out every fiber individually, the information from fibers of three consecutive layers was combined at the software level, as shown in Fig. 4.3b.

The prototype was studied in both the laboratory with a  ${}^{90}\text{Sr}$  source (electrons with endpoint energy 2.28 MeV) and at PSI's  $\pi\text{M1}$  beam line. Unless otherwise stated, the following results refer to measurements at the  $\pi\text{M1}$  beamline when selecting minimum ionizing positrons and irradiating the fibers at approximately half the fiber length, perpendicularly to their central axes. The  $\pi\text{M1}$  beam was tuned to positive polarity and to a momentum of 115 MeV/c.

<sup>1</sup><https://www.crystals.saint-gobain.com/radiation-detection-scintillators/fibers>

<sup>2</sup>[www.hamamatsu.com/us/en/product/category/3100/4004/4113/S12571-100C/index.html](http://www.hamamatsu.com/us/en/product/category/3100/4004/4113/S12571-100C/index.html)

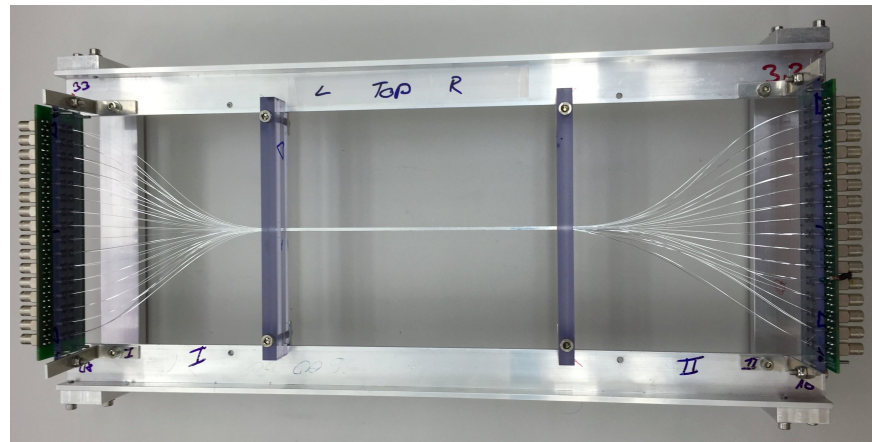


**Fig. 4.2:** The fibers prototype, made of 32 squared, multiclaid BCF-12 fibers of 250  $\mu\text{m}$  thickness. Each individual fiber is coated with  $\sim 100 \text{ nm}$  of aluminum and read out by a SiPM at each end.

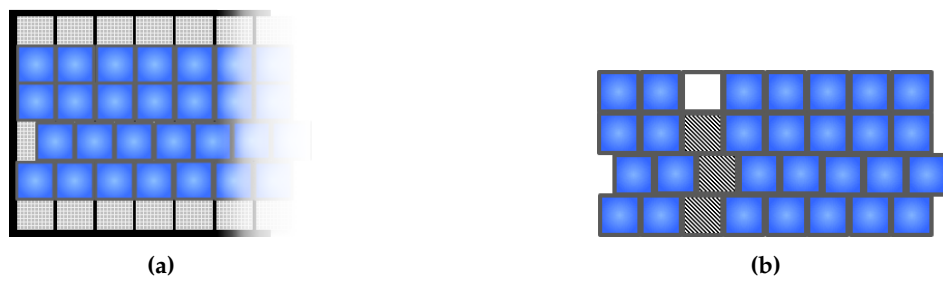


**Fig. 4.3:** Illustration of a column-wise readout of fiber tracker using SiPM arrays, rather than reading out every fiber individually. Fiber tracker (blue) coupled to a SiPM array (gray/b). Emulation of the column-wise read-out by SiPM arrays, combining offline the SiPM read out (b).

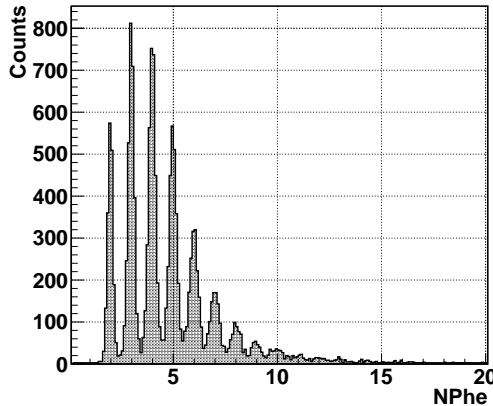


**Fig. 4.4:** Typical light spectrum (threshold 0.5 phe) measured by a single 250  $\mu\text{m}$  square multiclad fiber ( $\approx 50 \text{ cm}$  length) read out by a SiPM on each end (combined in logic AND) upon the passage of a MIP.

	Single layer	Double layer	Triple layer	Array
$\varepsilon_{AND}$ [%] (1.5 phe)	$34 \pm 1$	$52 \pm 1$	$67 \pm 1$	$88.0 \pm 0.3$
$\varepsilon_{OR}$ [%] (1.5 phe)	$79 \pm 1$	$93 \pm 1$	$97 \pm 1$	$97.5 \pm 0.2$
$\varepsilon_{AND}$ [%] (0.5 phe)	$72 \pm 1$	$89 \pm 1$	$95 \pm 2$	$95.8 \pm 0.2$
$\varepsilon_{OR}$ [%] (0.5 phe)	$96 \pm 1$	$99 \pm 1$	$98 \pm 1$	$98.3 \pm 0.2$

**Tab. 4.1:** MIP detection efficiencies  $\varepsilon_{AND}$  and  $\varepsilon_{OR}$  when triggering at the indicated threshold (0.5 or 1.5 phe) on the respective SiPMs in the AND and OR logic. The errors are statistical.

## Results

The Large Prototype showed a uniform response (variations between fibers  $\lesssim 10\%$ , variations in time and different trigger conditions  $\leq 5\%$ ) with the average number of photoelectrons (phe) being  $4.6 \pm 0.3$  (stat) for the AND and  $3.7 \pm 0.3$  (stat) for the OR configuration at a threshold of 0.5 phe, consistent with the expectations. A typical light spectrum is shown in Fig. 4.4.

The detection efficiency for both individual and multiple fibers combined was evaluated by using the first fiber layer (and, where appropriate, also preceding / successive fibers) as a trigger. The measured MIP detection efficiency for the different logic configurations, thresholds, and layer numbers are summarized in Table 4.1. The time resolution on the mean time for a single fiber was determined considering the distribution  $T_{single} = (t_1 - t_2)/2$ , where  $t_1$  and  $t_2$  denote the time extracted from the SiPM at the left and right ends of the fiber, respectively. A typical distribution measured for a single fiber is shown in Fig. 4.5.

When a particle hits more than just one fiber, the mean times of the individual fibers can be combined to obtain more precise timing information. Table 4.2 summarizes the measured timing resolutions for different combinations of fibers, which correspond to potentially different thick ribbons, and thresholds. The quoted sigma was obtained with a single Gaussian fit. A better resolution can be quoted using a double Gaussian fit but is beyond the scope of this report. As shown by the measurements, with a ribbon made of three layers of fibers, a timing resolution of 500 ps can be achieved with a detection efficiency  $\geq 90\%$ .

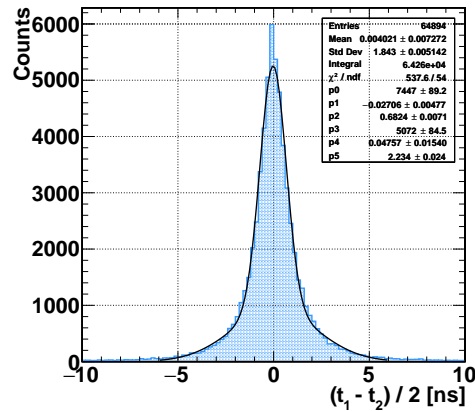


**Fig. 4.5:** Timing distribution of a single fiber with a double Gaussian fit (solid line).

		Single	Double	Triple
$\sigma_t$ [ps]	(0.5 NpHe)	$1160 \pm 50$	$830 \pm 3$	$681 \pm 4$
$\sigma_t$ [ps]	(1.5 NpHe)	$803 \pm 5$	$600 \pm 5$	$504 \pm 6$

**Tab. 4.2:** Timing resolutions measured by the Large Prototype when triggering at the indicated threshold on the respective SiPMs in the AND logic. The numbers are extracted from single Gaussian fits to the timing spectra. The errors are statistical.

Finally, Fig. 4.6 shows the tracking capability of the detector with real data. Positrons are impinging at different angles meaning the fired fibers reproduce the particle path. To push the detector performance in this direction, each fiber was coated with a layer of 100 nm aluminum before assembling the prototype, reducing optical crosstalk between fibers from around 30% with naked fibers to  $\leq 1\%$  with coated aluminum fibers.

#### 4.2.3 Geant4 simulation and performance

For current simulations, fiber implementation is based on double-clad BCF20 Saint-Gobain scintillating fiber parameters<sup>3</sup> LINK BROKEN. The sketches of the fiber section and the ribbon are shown in Fig. 4.3b. Currently, we are performing simulations that include the interaction between radiation and matter using GEANT4 physics processes. Complete photosensor readout and electronics will be implemented once all details of the detector are finalized. At this point, we implemented an ideal readout scenario in which all photons that reach the ends of the fibers

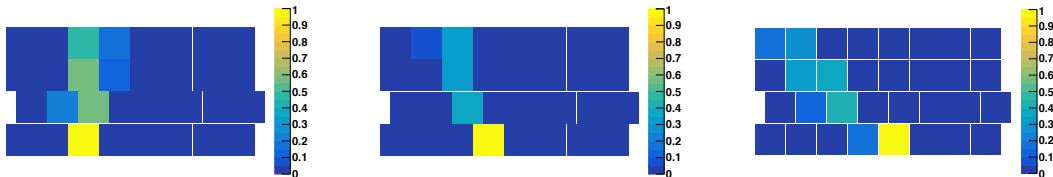


**Fig. 4.6:** Particle tracks observed in the Large Prototype as a function of the inclination angle  $\phi$ . From left to right, the impinging angle is  $\phi = 0^\circ$ ,  $\phi = 22^\circ$ , and  $\phi = 60^\circ$ . The color scale indicates the number of events involving the corresponding fiber relative to the number of triggered events.

<sup>3</sup><https://www.crystals.saint-gobain.com/radiation-detection-scintillators/fibershttps://inldigitallibrary.inl.gov/sites/sti/sti/5532301.pdf>

are detected and the exact position and timing of each photon are recorded. The idea is to add PDE and smearing offline, simulating different resolutions and efficiencies. Additionally, we implemented both a readout scheme 1:1, mimicking a single fiber readout, and a SiPM array system.

As we saw in Sec. 4.2.2, we are considering merging multiple fibers into a single photosensor to reduce the number of channels required for the Data Acquisition System (DAQ) of the experiment. However, the performance of the resulting system may be compromised by the balance between the desired resolution and the number of available DAQ channels, as well as by the pixelation of the SiPMs. Despite this, the initial results of tests with a prototype ribbon using a fiber merging readout scheme under realistic conditions (including photosensor response, front-end electronics, and noise) show promising potential to meet muon EDM requirements.

**Fibers and read-out** Aside from the specific geometry, the cardinal point is how to describe the fibers and their readout. The fiber itself is simulated as a three-layer volume: a scintillating core and two claddings of PMMA. The optical property of the surface between the different layers is specified with a G4OpticalSurface<sup>4</sup>. The readout is a somewhat simplified simulation of a SiPM (the same one used also for the different scintillators discussed in the previous chapter):

- Optical grease: to simulate the optical coupling of the SiPM to the fibers/scintillators
- SiPM window: SiPMs have a Silicon resin window covering the active region
- SiPM: The bulk of the SiPM is simulated as a simple block of silicon

The idea of this readout is not to simulate the actual physical processes leading to an electric signal, but just to record the position and time of optical photons entering the system.

### Single ribbon

The first step is to study the characteristics and performance of a single ribbon. Having two impinging particles at the same time at a given distance, we can estimate the spatial resolution of this system. Fig. 4.7 shows an event with two particles separated by 2 mm. Looking at the position of the generated photons, we can clearly distinguish the two hits, and the resolution is of the order of 0.1 mm. In Fig. 4.8, the arrival time of the scintillating photons at the photosensor, generated by two consecutive particles, is shown. The position of the impinging particles is the same, but a different  $\Delta t$  was set between them. Although the time resolution for a single particle is given by the rising edge of the distribution, much sharper than required  $\sim 1$  ns, the distribution itself is quite broad. This means that a particle that crosses at the same position within  $\lesssim 3$  ns will induce a pile-up event. Note that here we neglect the shaping of the waveform, for which a bigger width is expected. Although with a short time difference, the hits might not be recognizable, the resulting distribution would still be quite different from that of a single impinging particle, and this feature could be somewhat mitigated. On top of this, the probability of having no deflection due to multiple scattering on a full rotation is quite low: the spatial resolution will further mitigate this pile-up effect.

---

<sup>4</sup>The documentation can be found here: [G4OpticalSurface](#)

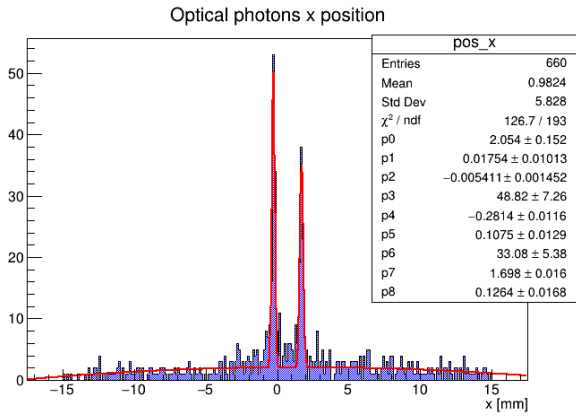


**Fig. 4.7:** Two particles impinging 2 mm apart on the same ribbon. Using 250  $\mu\text{m}$  fibers and having no pixelation on the readout, the spatial resolution is  $\sigma \approx 100 \mu\text{m}$  (p5 and p8). This value was obtained with a fit to *plo2+gauss+gauss* and with a bin width of 125  $\mu\text{m}$  (half a fiber width).

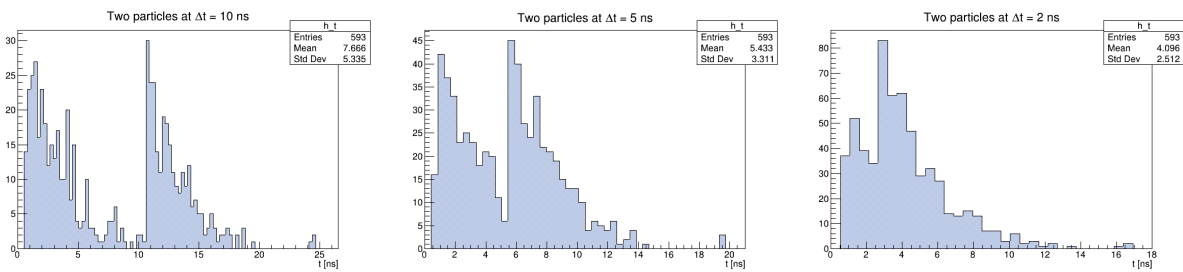


**Fig. 4.8:** In case of a particle impinging on the same position, the timing of the photon can be used to distinguish the two hits. For 20 cm fibers, the limit seems to be 3 ns to 5 ns. This value refers to the time the optical photon interacts with the SiPM. The actual distribution will be larger.

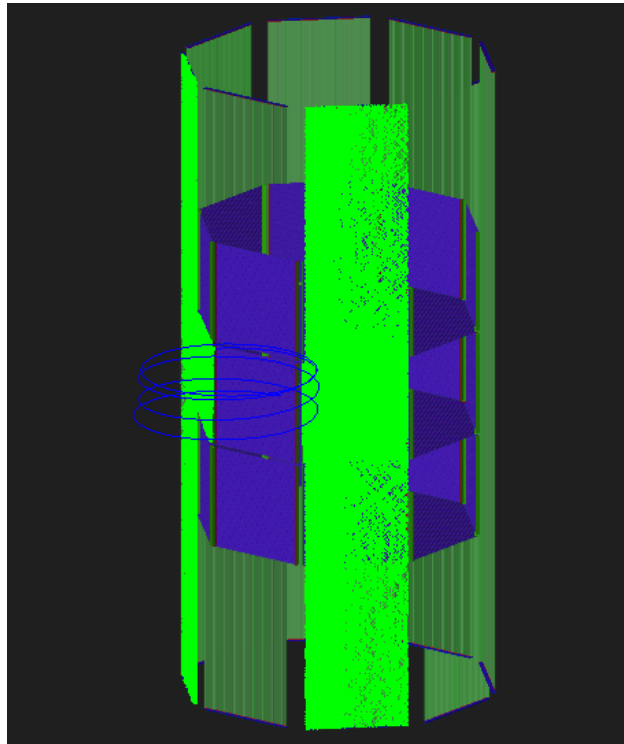


**Fig. 4.9:** An example of a GEANT4 simulated event. In green the optical photons reflecting inside the fiber ribbons; in blue the trajectory of the positron. Keeping the same color scheme, the longitudinal SciFi is green while the transverse one is blue.

### MuEDM geometry

Simulating the full geometry of our detector, including both the inner layer of transverse fibers and the outer layer of longitudinal fibers, and incorporating the effects of the magnetic field, leads to more complex events. An example is shown in Fig. 4.9. In this scenario, a single particle can pass through multiple layers, undergoing scattering and losing energy. The spatial information provided by both layers, as shown in Fig. 4.10, demonstrates that the positions of the hits on the transverse plane are relatively stable, due to the low material budget. On the contrary, the inner layer provides information about the longitudinal movement of the particle. The integration of timing information for the transverse fibers results in the plot shown in Fig. 4.11. This plot includes horizontal lines that represent the separation between different barrels. The relationship between transverse position and time provides additional information, although it can be more difficult to interpret. The resulting plots are shown in Fig. 4.12.

#### 4.2.4 Conclusions on the 2022 proposal

The tracker technology and geometry illustrated are a preliminary design, but already meet the requirements of positron tracking, i.e. millimeter and nanosecond resolutions. The interplay of a transverse SciFi detector and a silicon-based longitudinal detector seems to be a desirable choice. Working under this assumption, we envision the possibility of removing the longitudinal outer SciFi, which would be redundant, further reducing multiple scattering. On a practical level, this system requires finding a way of reading the transverse fibers from the central region of the experiment. This is non-trivial and possible improvements on this design were studied, the most

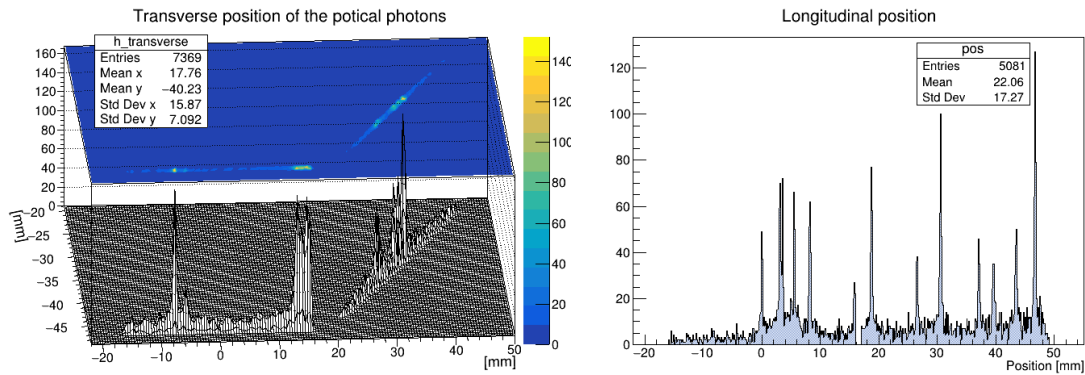


**Fig. 4.10:** Looking at the position for the photons arriving at the readout for both SciFi layers.

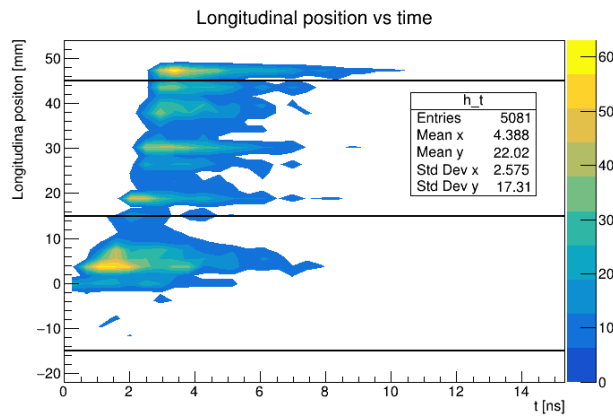


**Fig. 4.11:** Looking at the relationship between time and longitudinal position for the inner layer makes it possible to see if the particle is spiraling up or down.

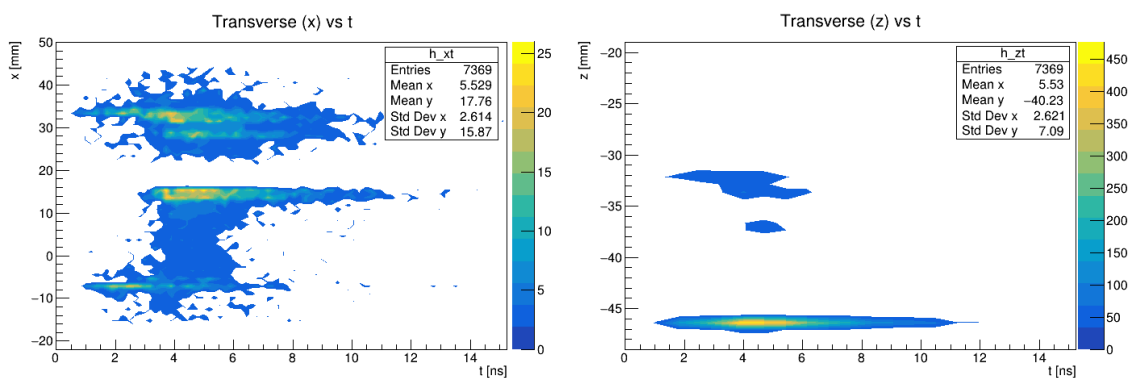


**Fig. 4.12:** The information from the joint use of transverse position and time, given by the outer layer, is more complex but essential (and a unique feature of this detector) in understanding the particle trajectory.

promising being the Cylindrical Helical Tracker (CHeT), discussed in the next section.

### 4.3 CHeT

The first step in further developing and prototyping the geometry chosen in the previous paragraph is to understand the requirements for this sub-detector and how the prospected resolutions compare to these. This scintillating fiber tracker will be used for position tracking and in particular is going to be complemented by silicon strips. The crucial information this system needs to provide is the longitudinal position of the particle with a good resolution:  $\delta\ell \lesssim 1 \text{ mm}$ .

#### 4.3.1 Resolutions of crossed fibers ribbons

Let's consider a ribbon  $3 \text{ cm} \times 15 \text{ cm}$  of squared fibers  $250 \mu\text{m}$  running vertically. Assuming a 'perfect' readout, the resolution across the ribbon is given simply by the fibers' width while the resolution along the ribbon is extracted by reading the fibers on both sides. This second resolution is often quite worse than the previous. For practical purposes we will here assume  $\delta_x = 1 \text{ mm}$ ;  $\delta_y = 10 \text{ mm}$ . Rotating the ribbon by an angle  $\theta$  changes the projection of the resolutions on the  $\hat{x}$ ,  $\hat{y}$  axes and for this reason crossing two ribbons can improve the resolutions on the position of a crossing particle. When reading the ribbon on both sides the resolutions, as a function of  $\theta$ , are given by the smaller between the projection of the two intrinsic resolutions.

$$\begin{cases} dx = \min(\delta_x \sec \theta; \delta_y \csc \theta) \\ dy = \min(\delta_x \csc \theta; \delta_y \sec \theta) \end{cases} \quad (4.1)$$

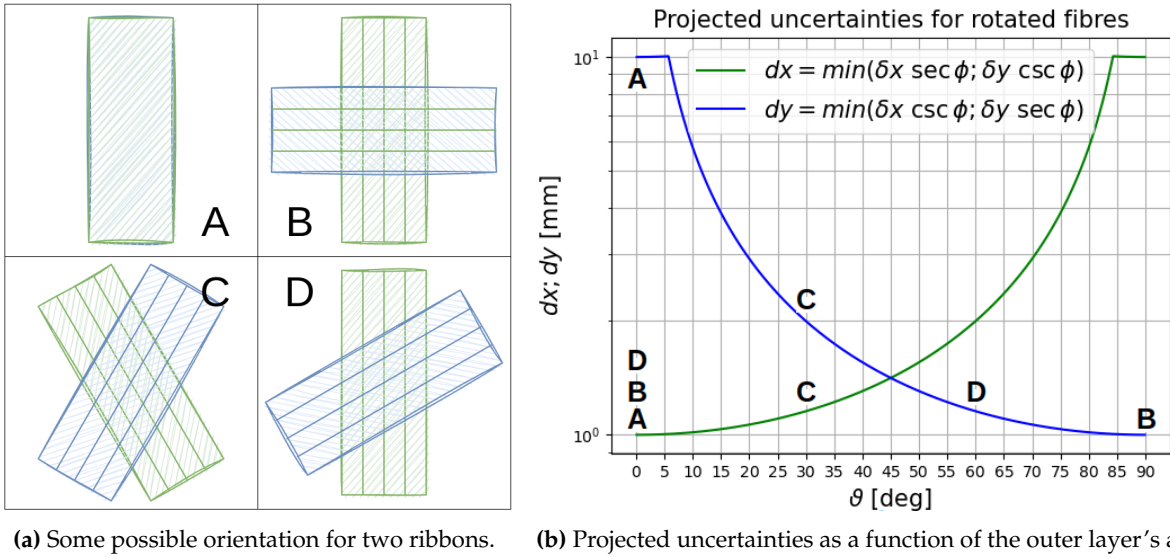
The relation between resolutions and the tilt angle is shown in fig. 4.13b.

#### 4.3.2 Angle choices for the layers

When considering two layers the angles must be chosen to improve the overall resolution, which in practice means minimizing the uncertainty only on one axes per ribbon. Let's consider the different layouts in 4.13a and how they translate to resolutions in 4.13b. Clearly having the two ribbons at 90 deg along the axes is the best option but if we want to avoid having the readout on the plane of the muon orbit we need to consider less steep angles for the single ribbons. Options C and D are the possible solutions and, looking at the resolutions, D is actually the configuration minimizing the resolutions on both axes.

#### 4.3.3 Cylindrical geometry

At this point is important to notice an additional constraint, given by the cylindrical geometry. If, instead of having planar ribbons, the fibers are woven into two concentric cylinders one needs to avoid having multiple crossings. If two fibers cross multiple times, when both are scintillating the position of the impinging particle is ill-defined. There is a 'real' crossing point but also additional *ghosts* hits. If we consider a two-layer system the requirement of having only one crossing point (i.d. no ghosts) translates to having a difference in the number of turns  $\lesssim 1$ . In a cylindrical geometry the relation between the angle of the fibers and the number of turns completed,



**(a)** Some possible orientation for two ribbons. **(b)** Projected uncertainties as a function of the outer layer's angle

**Fig. 4.13:** Relation between the direction of the fibers and the projection along the  $\hat{x}$ ;  $\hat{y}$  axes of the resolutions. The intrinsic resolutions are here assumed  $\delta_x = 1 \text{ mm}$ ;  $\delta_y = 10 \text{ mm}$ . In (a) Some specific orientations of two overlapping ribbons are shown and indicated in (b).

shown in Fig. 4.14a, is determined by the dimensions of the cylinder itself. At this point, we can plot the resolutions as a function of the angle of one of the layers keeping the angle of the second layer such as  $\Delta T = 1$ . The results are in Fig. 4.15a while Fig. 4.15b shows the difference in the angle of the two layers. We will consider two concentric cylinders, the outer layer being the one with a shallower angle: this is intended to reduce the effect of multiple scattering on the longitudinal position. Given its details, this detector has been named **Cylindrical Helical Tracker (CHeT)**.

Building the layers with infinite precision on the angle is clearly not feasible for this reason we can use the plots in Fig. 4.16, where the angles have been rounded to multiples of 5 deg. Additional attention we can have is to consider the length of the scintillating fibers: if the fibers are too long the light collection at the ends is decreased by the absorption. The length of the fibers in both layers is shown as a function of the outer angle in Fig. 4.16c. Clearly, this is the extreme case: depending on the intrinsic resolutions of the fibers, shallower angles and  $\Delta T < 1$  could be chosen, simplifying the construction.

The concepts here introduced are true for the system envisioned, but the specific values obtained depend on the specific dimensions of the cylinder as well as the intrinsic resolutions of a ribbon of fibers. For the plots shown, we considered a cylinder of  $r = 3.1 \text{ cm}$  and  $h = 20 \text{ cm}$ , reasonable sizes for the task at hand, and the intrinsic resolutions are here assumed  $\delta_x = 1 \text{ mm}$ ;  $\delta_y = 10 \text{ mm}$ .

#### 4.3.4 GEANT4 simulation

The first hurdle in the Geant4 simulation for this sub-detector is the definition of the geometry. While the inside structure of the fibers and the readout are the same as discussed previously (see Sec. 4.2.3), the fiber shape is now less straightforward.

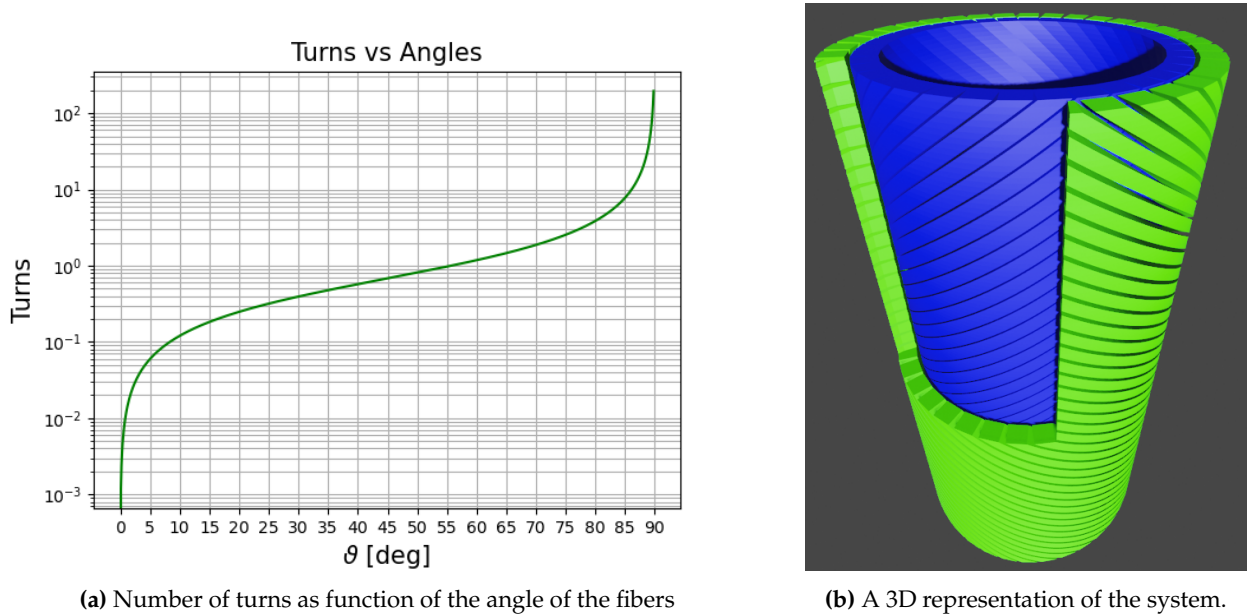


**Fig. 4.14:** In a planar configuration, the angle at which the fibers run translates directly to the angle at which the ribbon is oriented. In a cylindrical geometry, a fiber running at a given angle will complete a different number of turns depending on the dimensions of the cylinder. in (b) a 3D view with two layers in opposite directions. To make it easier to read the fibers are wider than in reality.

**G4TessellatedSolid** The shape is the result of wrapping a squared fiber around a cylinder resulting in a ‘squared helix’. After some consideration there are two ways of defying this geometry:

- Taking bool difference of two G4TwistedBox<sup>5</sup>. This is a simple solution but comes with some limitations: the shape of the fiber cannot be changed to circular and the twisted box cannot be twisted more than 90 deg, so a stack of clones is needed;
- Defying the geometry using G4TessellatedSolid<sup>6</sup>, which means creating it by hand triangulating the shape. This is a more cumbersome solution but it allows for more flexibility.

I decided to implement the latter to keep the possibility of simulating the detector with circular fibers. The core part of the code for generating the G4TessellatedSolid fibers, although perhaps not of particular interest, is in appendix ??.

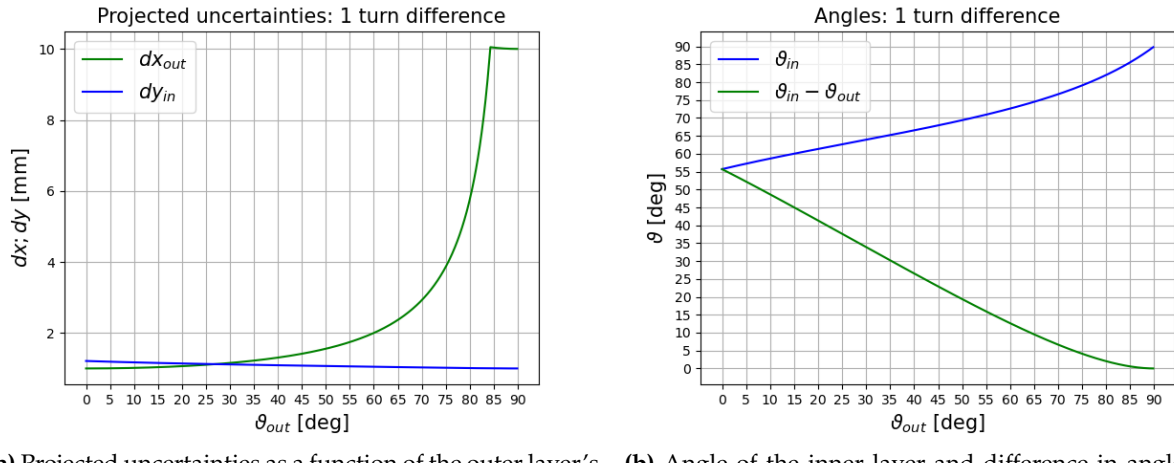
The resulting simulation, after having implemented everything so far described, is shown in Fig. 4.17, and is quite flexible: the dimensions of the CHeT, as well as the angles of the two layers and the fiber thickness, are parameters to be used when creating the CHeT geometry.

### 4.3.5 From $\gamma$ s to waveforms

The simulation in GEANT4 ends with the recording of the optical photons entering the SiPM SensitiveDetectors. The physical processes going from the impinging photons to the analog signal are quite complex and simulating them would require a lot of effort (and CPU time). To get a feeling of the type of signals we can expect from the simulation we can create a simple script *faking* the readout. The required steps are:

<sup>5</sup>The documentation can be found here: G4TwistedBox

<sup>6</sup>The documentation can be found here: G4TessellatedSolid



(a) Projected uncertainties as a function of the outer layer's angle (b) Angle of the inner layer and difference in angle as a function of the angle of the outer layer

**Fig. 4.15:** The results when considering two layers in a cylindrical geometry keeping the requirement  $\Delta T = 1$ : 4.15a shows the projected uncertainties; 4.15b shows the angle of the inner layer.

- *PDF*: probability of a photon converting. This is a binomial distribution and is SiPM dependent: reasonable values  $p_{PDF} \in [0.3, 0.5]$
- *Response*: per photon converted, add a 'waveform' at the photon time. The shape  $w(t)$  is SiPM/electronics dependent but some assumptions can be made.
- *Dead time*: when a pixel generates a signal, any additional photon coming within a  $t_D$  is lost.
- *Dark noise*: add a probability of spurious photons converting. This is a Poissonian process that gives  $n_{dark}$  photons distributed flat in the readout time.

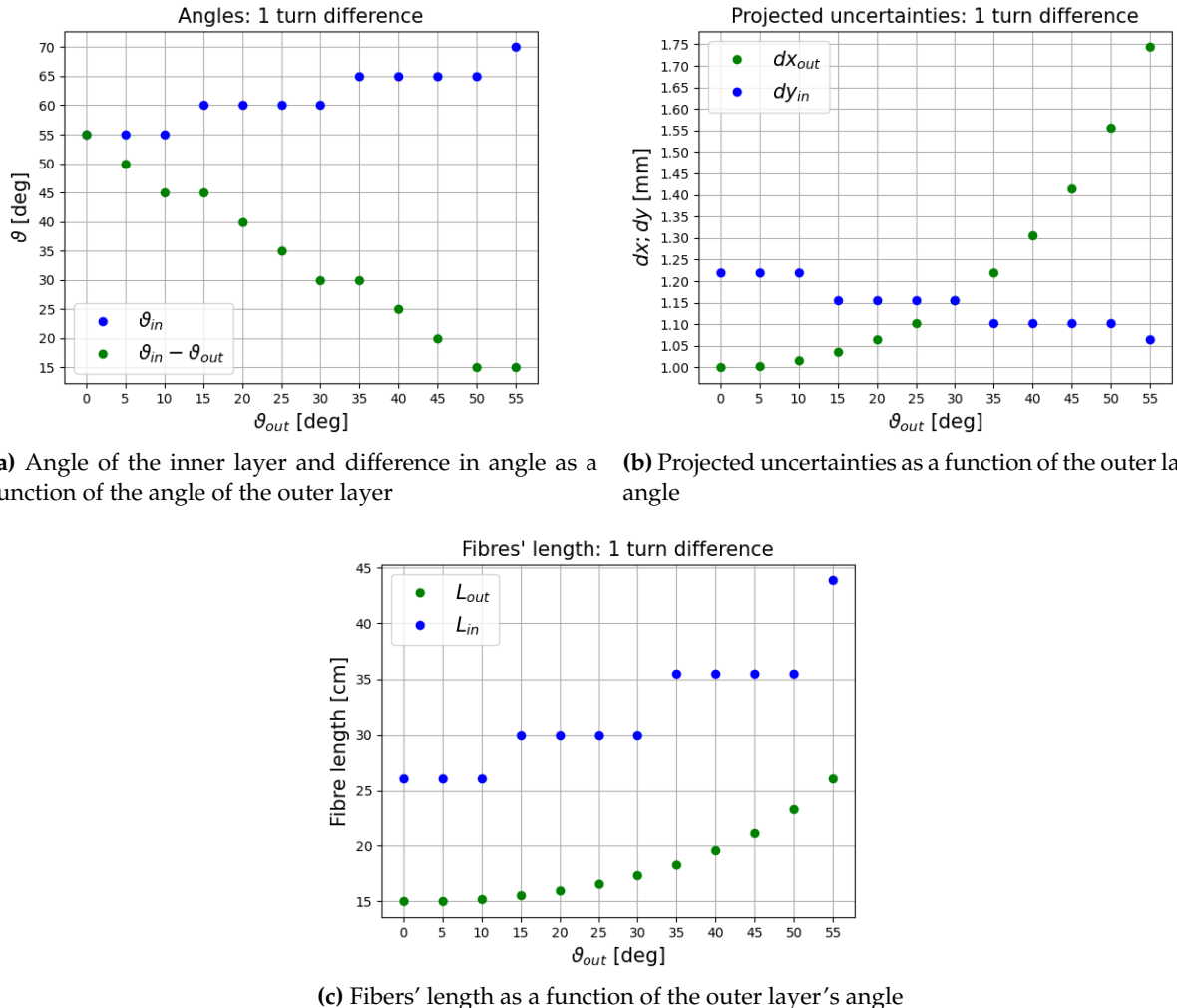
$$W(t) = \sum_{i=0}^{n_\gamma} w(t_i | \Delta t > t_D) \cdot p_{PDF} + \sum_{i=0}^{n_{dark}} w(t_{flat}) \quad (4.2)$$

Once we obtain  $W(t)$  we can apply a threshold  $w_{th}$  and turn the signal from analog to digital. If the  $w_{th}$  is crossed, we record a *hit*. In the geometry under consideration, a single particle crossing two fibers might generate 4 *hits*, assuming reading the fibers at both ends. On top of this, the particle might generate scintillation in the neighbor fibers or some cross-talk might be present. The general idea is to collect the signals from the fiber in each layer creating a 'layer'-*hit* (a *l-hit*). This could then be combined to make a 'cylinder'-*hit* (a *c-hit*). Mapping groups of hits in 1/c-hits is not trivial and takes as parameters the dimensions of the cylinder and the SiPM numbers (or their position).

### 4.3.6 Tracking

The details of the tracking procedure for the experiment are heavily dependent on the details of the detectors, which are not yet set in stone. The main option for a detector such as CHeT are

- To combine the *hits* from the two layers in *c-hits*. This would result in smaller uncertainties in *xyz* but requires delicate handling of the correlation between the variables plus reduces the number of available hits. This would also cut the number of hits in half
- To consider the *hits* separately still in *xyz*
- To perform a transformation for the *hits* in a more 'natural' coordinate system:  $xyz \rightarrow r\varphi z$



**(a)** Angle of the inner layer and difference in angle as a function of the angle of the outer layer

**(b)** Projected uncertainties as a function of the outer layer's angle

**(c)** Fibers' length as a function of the outer layer's angle

**Fig. 4.16:** Key parameters as a function of the outer layer's angle keeping 1 turn difference between the two layers and rounding the angles to multiples of 5 deg.

**GENFIT** The tracking code could be developed from scratch or based on a pre-existing working code. Given the size of the collaboration and the task, the second solution seems more adequate. In this regard, a good option would be to rely on a code developed for general track fitting in particle physics is GENFIT<sup>7</sup>. The development of the tracking procedure for the CHeT detector had to be put to a halt. This section is kept here just as food for thought for future development.

**Ghost hits** Although requiring  $\Delta T \leq 1$  made so the same couple of fibers cannot cross multiple times, there is still a risk of ill-defined hits. If the particle hits the detector in two distinct places this will create a hit on 4 fibers. If the timing resolution is not sufficient, this generates 4 possible interaction points. This situation is shown in Fig. 4.18b, where the stars indicate the real hit locations. The existence of the other crossing point forces us to implement the double-end readout scheme. The resolution along the fiber will be enough to solve the redundancy of the ghost hits.

<sup>7</sup>GENFIT: <https://github.com/GenFit/GenFit>

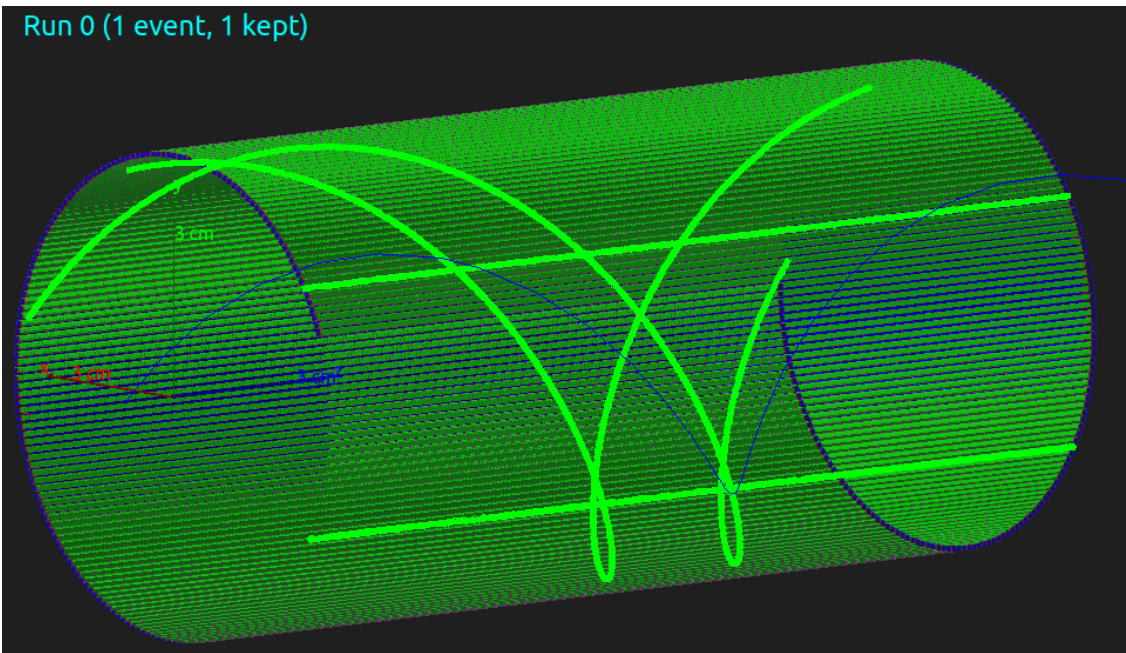
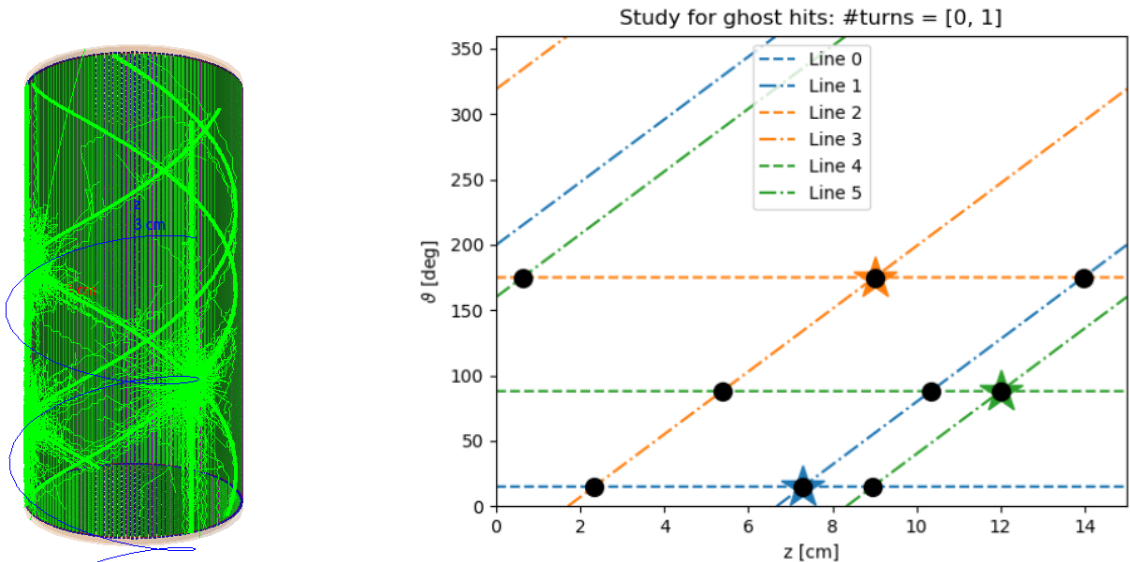


**Fig. 4.17:** GEANT4 simulation of the CHeT. The size of the fibers was increased to enhance the readability of the figure. While the structure may not be crystal clear, the fibers illuminated by the optical photons assist in guiding the eye along the two layers. In blue the particle traversing the detector.



**(a)** GEANT4 simulation of the CHeT. An event to highlight the challenge of ghosts.

**(b)** Fibers from different ‘real’ hits can still generate *ghosts*. Marked with the star the ‘real hits’ and with dots every crossing.

**Fig. 4.18:** The  $\Delta T \leq 1$  requirement prevents fibers from crossing multiple times, but there is a risk of ambiguous hits. If a particle hits the detector in multiple places, with inadequate timing resolution, multiple potential interaction points arise, as illustrated in Fig. 4.18b, with stars denoting real hits. To address this, we will implement a double-end readout scheme, with sufficient resolution to resolve ghost hits.

## 4.4 A study of radial geometry

The development of the Pixel detector, supposed to be a counterpart to the CHeT, unfortunately, had some delay. This means that, during the first phase, the Pixel detector will not be available and the scintillating fibers need to be repurposed to be the only positron tracking detector. The designs discussed up until now do not collect enough hits to be the sole tracker, hence requiring going back to the drawing board.

To rapidly study possible geometries, we opted for quick GEANT4 simulations, in which the ribbons of fibers are approximated by solid scintillator volumes with no scintillation properties. This allows us to take into consideration the energy loss and multiple scattering the positron undergoes, saving the CPU time required to run an optical simulation, tracking each optical photon bouncing in the scintillator.

### 4.4.1 Possible geometries

After a few iterations, the option of having a radial solution with crossed ribbons was discarded. Although crossed fibers improve the  $\hat{\gamma}$  resolution, as discussed in Sec. 4.3.2, it also increases the space required for the tracker at both ends, making the mechanics more complicated and adding material to the particle trajectory in non-interesting regions.

The most promising solutions seem to be:

- A purely radial geometry, with ribbons of fibers running longitudinally alternated to shorter ribbons of fibers running radially, delivering the good resolution on  $\hat{\gamma}$
- A radial geometry of vertical fibers (with fewer ribbons) complemented by an internal barrel for the same reason, analogous to the inner part of the detector discussed in Sec. 4.2.

## 4.5 Conclusions

This chapter describes the designs and simulations of the positron tracker. As of right now, some requirements for such a system are still ‘blurry’. Understanding the different aspects of the muEDM search generates requirements for the subsystem which are updated and, in turn, change the whole design of the experiment. The design included in the proposal nicely satisfied the requirements but presented some challenges in the readout, particularly for the inner barrel of the transverse layer. The ‘updated’ CHeT design overcame the readout challenge at the cost of introducing a challenge due to the possible ambiguity of the hits (ghosts). Given the delay foreseen on the Pixel side, the requirements for the fiber sub-system changed. This prompted additional studies to develop different geometries that would be autonomous and self-sufficient in the positron tracking (at least for Phase I).

# Bibliography on muEDM positron tracker

- [1] A. Stoykov, R. Scheuermann, and K. Sedlak. "A time resolution study with a plastic scintillator read out by a Geiger-mode Avalanche Photodiode". In: *Nuclear Instruments and Methods in Physics Research A* 695 (Dec. 2012), pp. 202–205. DOI: 10.1016/j.nima.2011.11.011. arXiv: 1107.2545 [physics.ins-det]. URL: <https://ui.adsabs.harvard.edu/abs/2012NIMPA.695..202S>.
- [2] Stefan Ritt, Roberto Dinapoli, and Ueli Hartmann. "Application of the DRS chip for fast waveform digitizing". In: *Nuclear Instruments and Methods in Physics Research A* 623.1 (Nov. 2010), pp. 486–488. DOI: 10.1016/j.nima.2010.03.045. URL: <https://ui.adsabs.harvard.edu/abs/2010NIMPA.623..486R>.
- [3] L. Galli et al. "Operation and performance of the trigger system of the MEG experiment". In: *Journal of Instrumentation* 9.4, P04022 (Apr. 2014), P04022. DOI: 10.1088/1748-0221/9/04/P04022. URL: <https://ui.adsabs.harvard.edu/abs/2014JInst...9P04022G>.

## **Part II**

### **MEG II**

## Chapter 5

# MEG II and the Cockcroft–Walton

This Chapter is dedicated to an in-depth description of the MEG II search and apparatus. After the description of the different subdetectors and their functionality a description of the beamlines will follow. MEG II is served by the main muon beamline, part of the PSI beamlines described in the Introduction Chapter, and a secondary proton beamline equipped with its own Cockcroft–Walton. This machine has different uses in the collaboration, which will be here discussed, and its functioning has been one of my main tasks. For this reason, some additional details will be here included. Most of the information on MEG II can be found in the two recent papers: detector [1] and 2021 data-analysis [2].

### 5.1 MEG II

The MEG II experiments aims at improving the limit set by its predecessor:  $BR(\mu^+ \rightarrow e^+\gamma) < 4.2 \times 10^{-13}$  [3] down to  $\sim 6 \times 10^{-14}$ . The signature of this process is a back-to-back pair of  $\gamma$  and  $e^+$ , with  $E_\gamma = E_{e^+} = 53.2$  MeV. The main background is the accidental coincidence of high momentum positrons from Michel decay  $\mu^+ \rightarrow e^+\nu_e\bar{\nu}_\mu$  and high energy photons from the radiative muon decay (RMD)  $\mu^+ \rightarrow e^+\nu_e\bar{\nu}_\mu\gamma$ , positron Bremsstrahlung or positron annihilation.

The experiment, which is located at PSI, is currently running and a sketch of it is shown in Fig. 5.1. In particular, the muons are delivered by the  $\pi E5$  beamline. The key aspects of the upgrade are: a thinner and more slanted target, a pixelated Timing Counter (pTC), a new Cylindrical Drift CHamber (CDCH), the addition of a Radiative Decay Counter, a finer granularity for the Liquid Xenon Calorimeter (XEC) using MPPC, new electronics and calibration methods. The kinematic variables associated with the positron are measured with the spectrometer (COntant Bending RAdius magnet (COBRA)+CDCH+pTC). The kinematic variables ( $E, t, \text{position}$ ) of the  $\gamma$ , expected to be monochromatic at 52.8 MeV, are measured with the XEC. This is a 1000  $\ell$  “c-shaped” Liquid Xe calorimeter, equipped with both PMT and SiPM.

**Coordinate system** The coordinate system used is cylindrical  $(r, \phi, z)$  with its origin located at the center of COBRA. The  $z$ -axis aligns with the COBRA axis, coinciding with the direction of the incoming muon beam. The azimuthal angle  $\phi = 0$  is positioned opposite the center of the LXe detector and corresponds to the  $x$ -axis, with the  $y$ -axis pointing upwards. Positrons follow trajectories characterized by decreasing  $\phi$  coordinates. The polar angle  $\theta$ , measured with respect

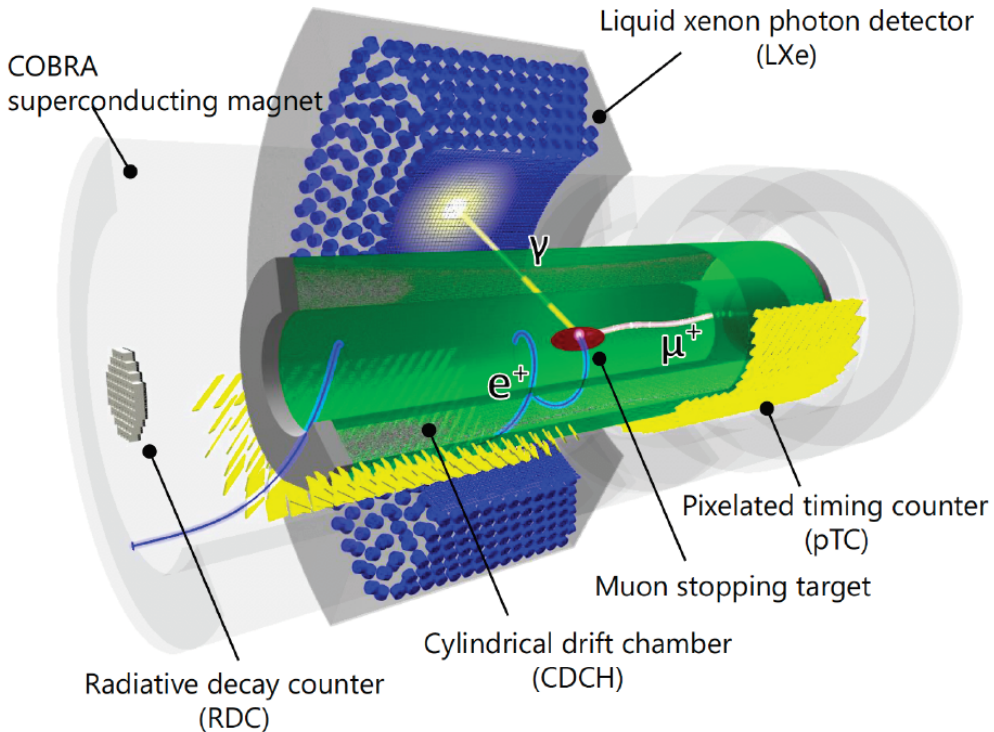


**Fig. 5.1:** Sketch of the MEG II apparatus with a  $\mu^+ \rightarrow e^+\gamma$  event.

to the  $z$ -axis, is also employed. The region where  $z < 0$  is referred to as upstream, while the region where  $z > 0$  is termed downstream. The size of the LXe fiducial volume defines the geometrical acceptance of  $\sim 11\%$ :  $\phi_\gamma \in [\frac{2}{3}\pi, \frac{4}{3}\pi]$  and  $|\cos \theta_\gamma| < 0.35$ .

**Alignment** The analysis of the relative alignment within each detector, like the extraction of the *real* position of the wires in the CDCH, and between the different detectors is key in the event reconstruction. We will not describe how these are performed but all the details can be found in [1].

## 5.2 The liquid XEnon Calorimeter

As already introduced, the kinematic variables ( $E$ ,  $t$ , position) of the  $\gamma$ , expected to be monochromatic at 52.8 MeV, are measured with the liquid XEnon Calorimeter (XEC). This is a 900 L LXe c-shaped tank and the main improvement from MEG has been the increase in the granularity of the photosensors on the inner face: from 216 5 cm round PMTs to 4092  $15 \times 15 \text{ mm}^2$  Multi-Pixel Photon Counters (MPPCs). The other faces are equipped with the same 668 PMTs as in MEG. To get the best performances from this detector, the running condition of the Xe is 165 K and 0.12 MPa. the description of the *ad hoc* cryogenic circuit will be skipped but can be found in the references. The local coordinate system is the following:  $u$  - axis along the beamline,  $v$  - vertical axis intersecting COBRA center,  $w$  - the depth in the detector.

### 5.2.1 Xe scintillation

MEG's XEC is the first large Xe detector based on scintillation. In Sec. 3.1 the working principle of scintillators was discussed but the description of liquid scintillators was postponed. Now is the time to pick up where we left off. Among the noble gases, Xe has a higher light emission wavelength, fast response, and short radiation length. On top of these qualities, its high density allows to keep the size of the detector reduced. All these aspects are the reason this element was chosen by the collaboration. However, the quality of commercial Xe is not at the level required, so a purification system was developed to guarantee transparency to the scintillation light.

Two processes can take place leading to the emission of scintillation photons at 178 nm:

- Excitation:  $\text{Xe}^* \xrightarrow{\text{Xe}} \text{Xe}_2^* \longrightarrow 2\text{Xe} + \gamma(178\text{ nm})$   
The ionizing particle creates an exciton which combines as an excimer and radiates
- Ionization:  $\text{Xe}^+ \xrightarrow{\text{Xe}} \text{Xe}_2^+ \xrightarrow{e^-} \text{Xe} + \text{Xe}^{**} \longrightarrow \text{Xe}^* + \text{heat} \longrightarrow \text{Excitation}$   
If a charged exciton is created, the charged excimer first needs to be thermalized

The fraction of excitation and ionization depends on the status of the Xe and on the ionizing particle and some deviations are possible from the processes illustrated, meaning not every exciton will lead to scintillation. We will not cover these aspects but we will name a peculiar aspect related to the ratio between the different processes. Experimentally has been proven the waveforms produced by  $\alpha$  and  $\gamma$  present different decay time:  $\tau_\alpha = (19.4 \pm 1.9)$  ns and  $\tau_\gamma = (50.9 \pm 4.0)$  ns.

**Purification** To keep a high light yield and vacuum ultra-violet (VUV) transparency, the Xe needs to be purified, removing water, oxygen, and nitrogen. The most effective way is to purify it in the liquid phase, circulating through a molecular sieve. Unfortunately, this cannot happen while taking data due to the noise introduced in the system and is done every year before the run starts. Purification in the gaseous phase is done during the whole beam time with a hot getter.

### 5.2.2 Photon detection

The MPPCs and PMTs used went through a period of R&D due to the harsh environment:

- The Xe spectrum is centered at 178 nm: vacuum ultra-violet regime
  - To ensure the light collection, the sensors are immersed at 165 K
  - A high rate is given by radiative muon decays and secondary particles from the beamline
- Still, the gains and efficiency of these sensors are continuously evolving, making it necessary to develop different calibrations to optimize the detector and specific procedures to regain efficiency lost in the in-between runs. For example, the PDE of the MPPC is recovered via the *annealing*.

**Annealing** While the value for the UVU photon detection efficiency (PDE) of the MPPS was measured to be  $0.20 \pm 0.02$ , during the commissioning run of 2017 the value measured was  $0.13 \pm 0.01$ . After a detailed investigation, the decrease was attributed to radiation damage. To recover the PDE, a process of annealing was applied to the MPPCs. The Joule heating of the MPPC served as the heat source while LED light was used to induce a current. Each MPPC was annealed  $\sim 28$  h, recovering the PDEs enough to tolerate radiation damage of the physics run for a full year. The

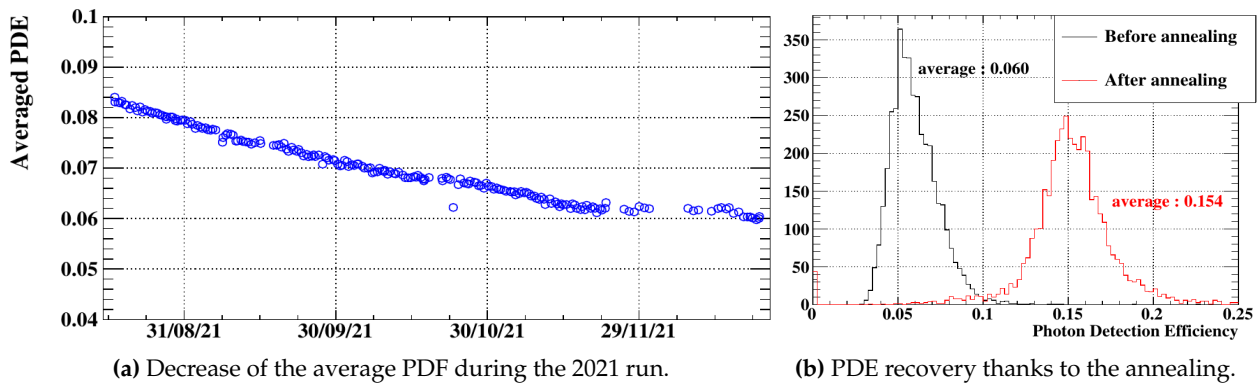


**Fig. 5.2:** The PDE of the MPPCs was found to be deteriorating due to radiation damage (a). The process of annealing carried out before every physics run, allows the recovery of the PDE (b).

decrease of PDE during 2021 and the recovery after the annealing process are shown in Fig. 5.2. This procedure has been repeated every year before the MEG II physic runs.

**PMTs' gain** The absolute gain of PMTs is evaluated by shining the sensors with a blue LED and evaluating the linear correlation between the mean and variance of the *charge* as a function of the LED intensity. At the beginning of each run, the gains are set to  $\sim 0.8 \times 10^6$  adjusting the HV. This value will then lower during the run, as shown in Fig. ??.

### 5.2.3 Calibration

As anticipated, different calibrations were developed to follow the evolution of the XEC and to tune its functionality. There are three calibrations taken 3/5 times a week plus the Charge Exchange calibration, done once a year.

**LEDs** The first of these procedures is done every day, shining the sensor with two different LED lights. This allows us to evaluate the photon detection efficiency (PDE) and Excess Charge Factor (ECF) of the MPPCs. The absolute gain of PMTs is also evaluated, with a blue LED, and extrapolating the linear correlation between the mean and variance of the *charge* as a function of the LED intensity. At the beginning of each run, the PMT's gains are set to  $\sim 0.8 \times 10^6$  adjusting the HV. Just like the MPPC PDE, this value will then lower during the run.

**$\alpha$ -particles** PDEs and QEs are evaluated by comparing the number of registered photoelectrons and the expected value, evaluated via MC knowing the positions of the  $^{241}\text{Am}$  source of  $\alpha$ -particles. The cosmic rays are the background for this calibration and are distinguished via a pulse shape discriminator. The uncertainties on the PDEs/QEs is 10%.

**$^{7}\text{Li}(p, \gamma)^{8}\text{Be}$**  The 17.6 MeV line of the  $^{7}\text{Li}(p, \gamma)^{8}\text{Be}$  reaction is also used to calibrate the XEC. This line is produced impinging a beam of 500 keV protons, produced via a Cockcroft-Walton (which will be described in a following section) on a Lithium tetraborate ( $\text{Li}_2\text{B}_4\text{O}_7$ ) target.

**CEX** The last of the calibrations is more complex and requires changing the beam from  $\mu^+$  to  $\pi$ . For this reason, it is performed only once a year. The process is the Charge EXchange reaction (CEX),  $\pi^- p \rightarrow \pi^0 n$  and  $\pi^0 \rightarrow \gamma\gamma$ , and produces flat  $\gamma$  in [54.9, 82.9] MeV. Tagging the back-to-back events it is possible to select the low end of the spectrum, which is close to the expected signature of  $\mu^+ \rightarrow e^+\gamma$  at 52.8 MeV. This calibration will be discussed in detail in Ch. 6.

### 5.2.4 Reconstruction and performance

Let's now discuss how the kinetic variables of the detected  $\gamma$  are extracted and the current understanding of the overall performance of this detector. We will outline the process for the reconstruction without going into details, which can be found in the recent paper [1].

**Position** The procedure used to find the position  $x_\gamma$  of the hit is based on the assumption the amount of light collected by each sensor is proportional to the solid angle at the interaction point. This defines a quantity to minimize, a  $\chi^2$  of the registered and expected photons, given the position of each sensor. The position resulting from the fit is then corrected to account for the directionality of the detected photon and the finite size of the EM shower.

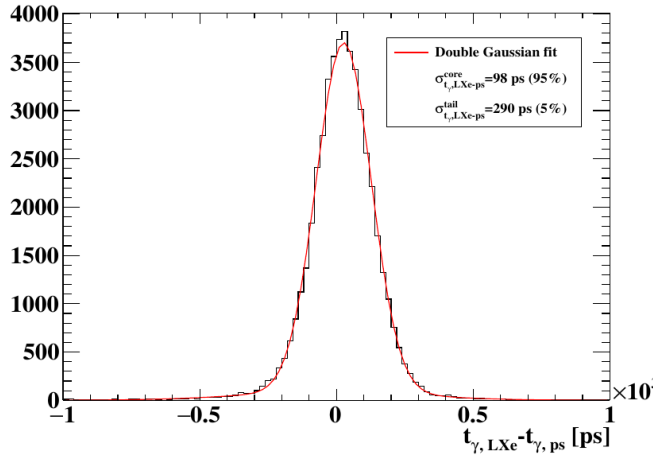
**Time** The timing  $t_\gamma$  of the first interaction of the photon is evaluated by minimizing a second  $\chi^2$  taking into consideration all the different aspects, like the travel time from the position to the sensors or the offset of each sensor. These parameters are evaluated via a dedicated calibration, the Charge EXchange reaction (CEX). The results of such a calibration are shown in Fig. 5.3a

**Energy** The last ingredient is  $E_\gamma$ , which is evaluated as the sum of the number of photoelectrons of each sensor scaled by a factor from  $N_\gamma$  to energy and corrected for a temporal and positional dependence ( $T(t)$ ,  $X(u, v, w)$ ). Again, the resolution near the signal energy is evaluated via the CEX. The results are shown in Fig. 5.3b. The energy scale has been found to be non-uniform. For this reason, a 3D correction  $C(x, y, z)$  was developed by joining the information from the CEX runs, the  ${}^7\text{Li}(p, \gamma){}^8\text{Be}$  17.6 MeV line, and the studies of the background.

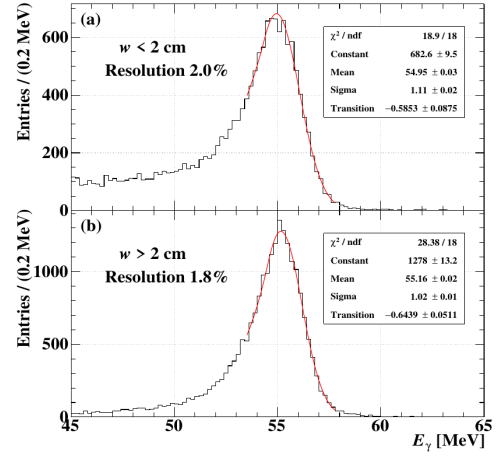
### Resolutions

From the analysis of the data collected during the CEX, energy, and timing resolutions can be evaluated near the signal region ( $E_{CEX} \sim 55$  MeV vs  $E_{MEG} \sim 52$  MeV). The resolutions are extracted by performing a fit, shown in Fig. 5.3 to a double Gaussian for the timing and Eq. 5.1 for the energy. For the energy, two regions are necessary because of a low-energy tail originating from the interaction with the detector surface. The resolutions obtained are  $\sigma_{E_\gamma}/\mu_{E_\gamma} = 2\%;$   $1.8\%$ . From design, the relative resolution was expected to be  $\sigma_{E_\gamma}/\mu_{E_\gamma} = 2\%;$   $1.7\%$  and the discrepancy is still under study. One possible explanation could be in the behavior of the Xe as a scintillator, given that a similar discrepancy was found also in MEG.

$$F = \begin{cases} A \exp\left\{-\frac{(x - \mu_{E_\gamma})^2}{2\sigma_{E_\gamma}^2}\right\} & \text{if } x > \mu_{E_\gamma} + \tau \\ A \exp\left\{-\frac{\tau(\tau/2 - x + \mu_{E_\gamma})^2}{\sigma_{E_\gamma}^2}\right\} & \text{if } x \leq \mu_{E_\gamma} + \tau \end{cases} \quad (5.1)$$



(a) Time resolution of the XEC, obtained via the time difference of XEC and *pre-shower* fitted with a double Gaussian.



(b) Energy resolution of the XEC. The function used is Eq. 5.1.

Fig. 5.3: Timing (a) and energy (b) resolutions of the XEC obtained for 55 MeV  $\gamma$ s generated via the CEX. The results are for the central region of the detector ( $u \in [-10, 10]$ cm and  $v \in [-30, -10]$ cm).

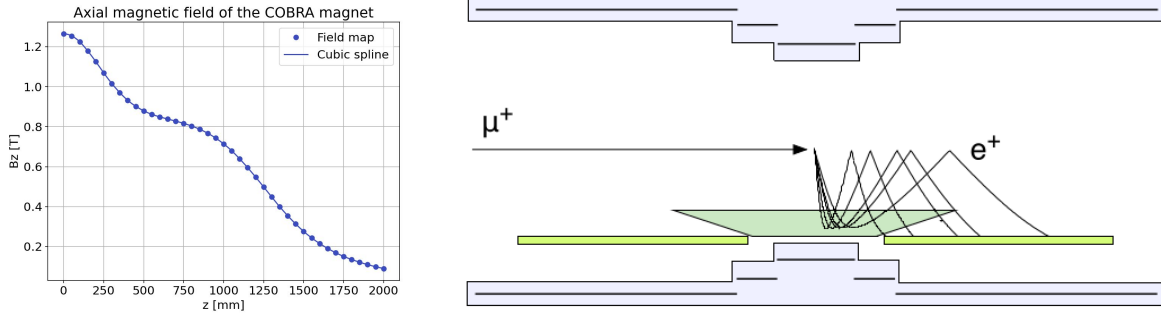


Fig. 5.4: The specific profile of the axial magnetic field of COBRA is the result of the 5 different coils. The aim is to sweep the particles at higher  $|z|$  with an independent radius.

## 5.3 Spectrometer

As already introduced, the spectrometer for the positron's kinematic variables is made of COBRA, CDCH, and pTC. We will now review their working principles and designs.

### 5.3.1 COBRA

The COnstant Bending RAdius magnet (COBRA) consists of a main superconducting magnet and two normal conducting compensation coils. The main magnet itself is made of five coils with three different radii to generate a carefully studied gradient to achieve two goals:

- Make so that a positron with a given momentum would follow a trajectory of specific radius *independently of the angle* at which the particle has been emitted
- *Quickly* sweep particles emitted at very steep angles, to reduce the pileup

The profile of the axial magnetic field obtained and the particle trajectories are shown in Fig. 5.4.

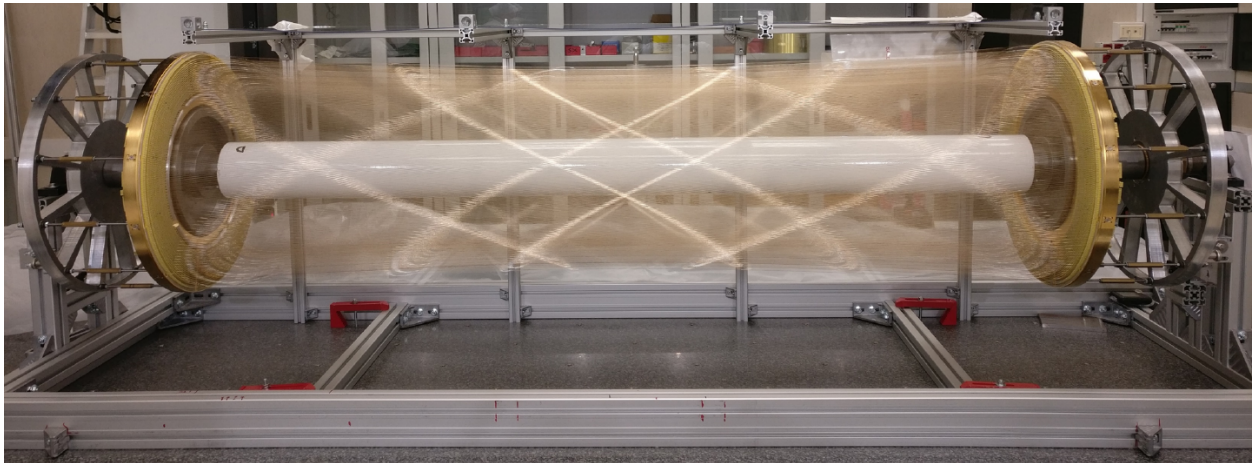


**Fig. 5.5:** CDCH with all the wires mounted. The light catching the wires highlights the stereo design of the detector.

### 5.3.2 Cylindrical Drift CHamber (CDCH)

The major difference between MEG’s drift chamber and its successor is that the CDCH is a single-volume, replacing the segmented structure. This is a  $\sim 1.9$  m long cylinder, filled with a helium-isobutane mixture and containing nine concentric layers of 192 gold-plated tungsten wires, which are the heart of this detector. While these wires collect the signals from drift electrons, cathode and guard wires ( $\sim 10\,000$  silver-plated aluminum wires) form squared drift cells ranging from 6.6 mm to 9.0 mm.

The geometry of the CDCH differs slightly from the design. For example, 10 layers were planned but 9 were installed due to time limitations. This time was invested in studies to reduce the probability of wire braking. This was mainly due to galvanic corrosion of the aluminium core, caused by air humidity penetrating through small cracks in the silver coating. The final result after mounting all the wires is shown in Fig. 5.5. The change in tracking efficiency was studied with simulation yielding a decrease of  $< 1\%$ . Many additional studies can be found in [1], like the GARFIELD++ simulations, gas mixtures analysis, and wire tensions. To prevent discharges and improve the overall stability, the original He-isobutane gas mixture (90 : 10) was also modified adding a small fraction of oxygen and isopropyl alcohol.

While the 144 HV are supplied with a commercial system, WaveDREAM boards supply the necessary low voltage for the front-end and take care of the digitalization of the waveforms collected at both ends of the wires.

**Hits** The first step in positron tracking is identifying signals (*hits*) induced by drift electrons in the waveforms of the CDCH cells. These hits are characterized by multiple pulses from different ionization clusters, stretched due to the drift time of electrons. Signal-to-noise discrimination and pileup identification are essential. Two waveform processing algorithms have been developed:

- The first algorithm entails two reductions of the noise, fixed voltage thresholds, and integration over 20 ns. First, subtraction of a coherent low-frequency noise averaged on adjacent channels (excluding the region with signal pulses). This reduces the noise levels from 23 mV to 13 mV. Then a high-frequency cut-off at 225 MHz using a discrete Fourier transform technique to eliminate incoherent high-frequency noise.

- The second method utilizes a deep-learning algorithm based on a convolutional neural network (CNN). This CNN model takes waveforms from eight neighboring cells as input and learns the patterns of coherent noise and signals, outputting the probability of the first cluster's arrival time at each sampling point. It is trained using simulated waveform data with randomly added hits and overlaid with real noise data collected without the beam.

The second method results in higher hit efficiency but also a higher fake hit rate. To optimize results, the reconstruction process is done once with hits found using the first method and once with hits from both methods combined. The final results are combined after the reconstruction is completed, favoring higher quality tracks if successful with both methods.

The arrival time differences of signals and charges collected at both ends of a wire provide rough (few cm) information about the position of the hit along the wire. Stereo wire configuration further improves the z-coordinate resolution making the track finding more robust against pileup.

Since multiple clusters often appear on one waveform, identifying the first cluster's time is crucial for correct drift circle reconstruction. The arrival time of the first cluster is determined from the summed waveform of both ends after adjusting their relative timing. The drift time of the first cluster is converted to DOCA using the time-distance relationship (TXY tables).

**Track** After identifying and reconstructing hits, a pattern recognition algorithm and a track-fitter algorithm (both based on Kalman filters<sup>1</sup>) are employed:

- The track finder initiates from hit pairs in outer layers with lower occupancy and generates track seeds by combining compatible pairs from different layers. Each seed is propagated through adjacent layers, checking consistency with hits and updating track parameters. Candidates with at least seven hits are formed.
- The track fitter utilizes an extension of the Kalman filter called the deterministic annealing filter (DAF) [5] and resolves left/right ambiguities. It fits individual track candidates, combining segments to form multi-turn tracks within CDCH. Tracks are propagated to the pTC and backward to the target, with a re-fitting based on updated DOCA.

During tracking, DOCA of each hit is iteratively refined. Initial DOCA values are estimated from Garfield++ simulations, but they can be biased due to low cluster density. An alternative DOCA estimate is obtained through neural network approaches, providing a more accurate estimation and improving positron kinematics by about 10%. This CNN-based method is used for final DOCA estimation during the re-fit process.

**Performance and efficiency** To evaluate the resolutions, the *double turns* are studied: when a particle traverses the CDCH in two positions, the two trajectories are fitted separately and the difference of the kinematical variables is studied. The resulting resolution is not  $\sqrt{2}$  of the core resolution because the effect of the particle interaction with matter is not the same for the two turns. The results need to be corrected with ad hoc simulations for both Signal and Michel positrons. The resulting values for the 2021 run are shown in Tab. 5.1, while the fit to the Michel spectrum is shown in Fig. 5.6.

---

<sup>1</sup>This is a recursive procedure to ‘adapt’ the result of a fit. A simple explanation and a 2D-example are in App. A [4]

Data	$\sigma_{y_{e^+}}$	$\sigma_{z_{e^+}}$	$\sigma_{\phi_{e^+}}$	$\sigma_{\theta_{e^+}}$
2021 DT	1.07	2.94	9.62	11.86
Signal DT	1.00	2.42	8.57	10.38
Michel DT	1.01	2.49	9.11	11.40
Effective	0.72	2.0	4.1	7.4

**Tab. 5.1:** Double Turn (DT) resolutions for 2021 data, Signal MC and Michel MC simulations. The MCs are used to correct the value extracted from the data and the last row gives the effective core resolutions.

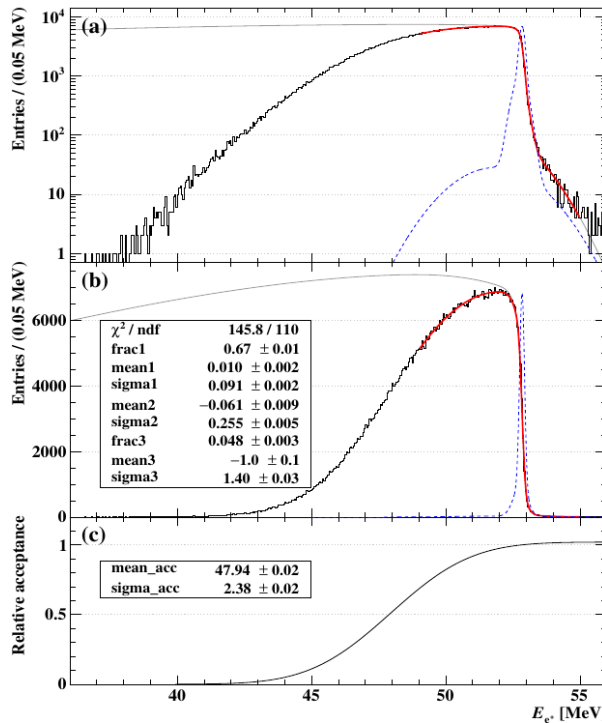


**Fig. 5.6:** Michel positron spectrum in logarithmic (a) and linear (b) scales. Black - data; Blue - 3 Gaussians to describe the resolution; Red- fit. The acceptance curve is shown in (c).

**CDCH2** The studies prompted by the wire breakage evolved in an R&D for the updated version of the CDCH. The main change was the choice of pure aluminum 50  $\mu\text{m}$  wires, almost insensitive to corrosion. One of the main challenges spawned by this choice was to develop a solid way of fixing the wires to the PCBs: the solution found was a combination of soldering and gluing. The CDCH2 will soon be completed and is expected to be delivered to PSI in spring 2024. The choice of mounting the new system will then depend on the current status and stability of the CDCH.

### 5.3.3 pixelated Timing Counter (pTC)

The time coincidence between  $e^+$  and  $\gamma$  is a crucial aspect of the experiment. The pixellated Timing Counter plays two roles: first, it is part of the trigger algorithms; second it assigns the time of the positron track, which is then propagated backward to the target plane  $t_{e^+}$ . This detector is made of two symmetric half-cylinders of scintillators between the CDCH and COBRA, as shown in Fig. 5.7. To cover the  $e^+$  acceptance corresponding to a  $\gamma$  entering the XEC, the pTC covers :  $23 \text{ cm} < |z| < 117 \text{ cm}$  and  $-166 \text{ deg} < \phi < 5 \text{ deg}$ . Each sector is made of 256 Bicron BC422<sup>®</sup> plastic scintillators read on opposite sides by arrays of 6 AdvanSiD 3  $\times$  3 mm SiPM, as shown in Fig. 5.8. The tiles are wrapped in 35  $\mu\text{m}$  polymeric reflector and 30  $\mu\text{m}$  Tedlar<sup>®</sup>.

The size and location of the tiles were optimized with ad hoc simulations: two different sizes ( $120 \times 40 / 50 \times 5 \text{ mm}^3$ ) are placed in a  $16 \times 16$  matrix in the  $z\phi$  plane and tilted by 45 deg to be orthogonal to the positron trajectories. This configuration was chosen to maximize the multiplicity for signal-like positrons limiting the material budget. The mean multiplicity from MC is  $\langle N_{\text{hit}} \rangle \sim 9$  and the obtained resolution  $\sigma_{t_{e^+},pTC} \sim 40 \text{ ps}$ . To intercalibrate the timing offsets of the system, most tiles are lit with a synchronous light pulse via optical fibers.

**Performance** The single-counter time resolutions were measured to be  $\sigma_{t_{e^+},pTC}(N_{\text{hit}} = 1) \sim 80 - 120 \text{ ps}$  for counters with heights of 40 mm and 50 mm. These resolutions correlate with light yield, influenced by scintillator aging, SiPM detachment, and radiation damage. Multi-hit time resolution is assessed via the "even-odd" method, improving average resolution to  $\sigma_{t_{e^+},pTC} = 43 \text{ ps}$  by combining results from different hit groups. Efficiency of pTC was studied with MC simulation, yielding a total detection efficiency of  $\epsilon_{e^+,pTC} = (91 \pm 2)\%$ , considering factors like geometric acceptance and scattering effects on endcaps.

An important aspect of this detector is the angle at which the tiles are tilted. This improves the overall reconstruction of  $e^+$ , which are the signature particles of the  $\mu^+ \rightarrow e^+\gamma$ . In Ch. 7 we will see that for the X17 search,  $e^-e^+$  pairs need to be reconstructed. For this search, this aspect of the pTC will generate an asymmetry in the reconstruction of the two particles.

## 5.4 Trigger and DAQ

Although the trigger and DAQ for MEG II were developed on top of the previous knowledge, the number of additional channels ( $\times 4$ ) was quite the challenge. Here we will illustrate some of the key features while the details can be found in [6]. The solution adopted was to merge the two branches in the WaveDAQ system. Between 2015 and 2020 the system was tested, expanded, and

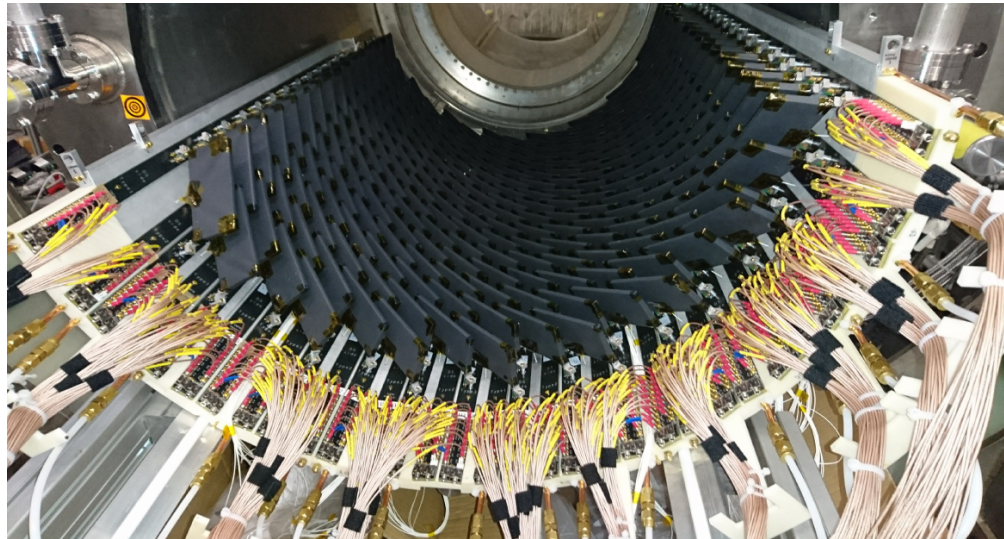


**Fig. 5.7:** Picture of the timing counter tiles.

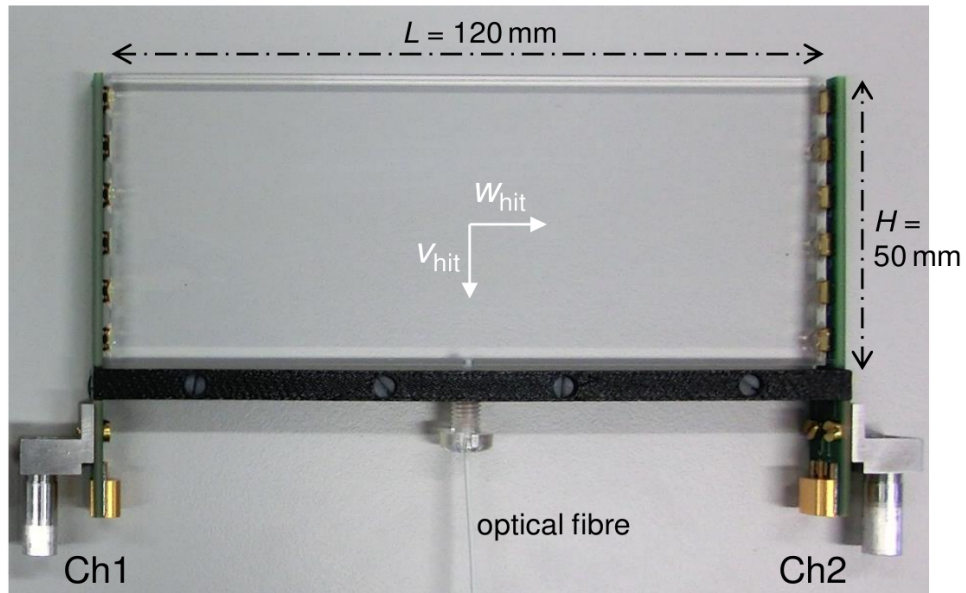


**Fig. 5.8:** A pTC tile:  $120 \times 40/50 \times 5 \text{ mm}^3$  of BC422<sup>®</sup> read by arrays of 6 AdvanSiD  $3 \times 3 \text{ mm}$  SiPM.

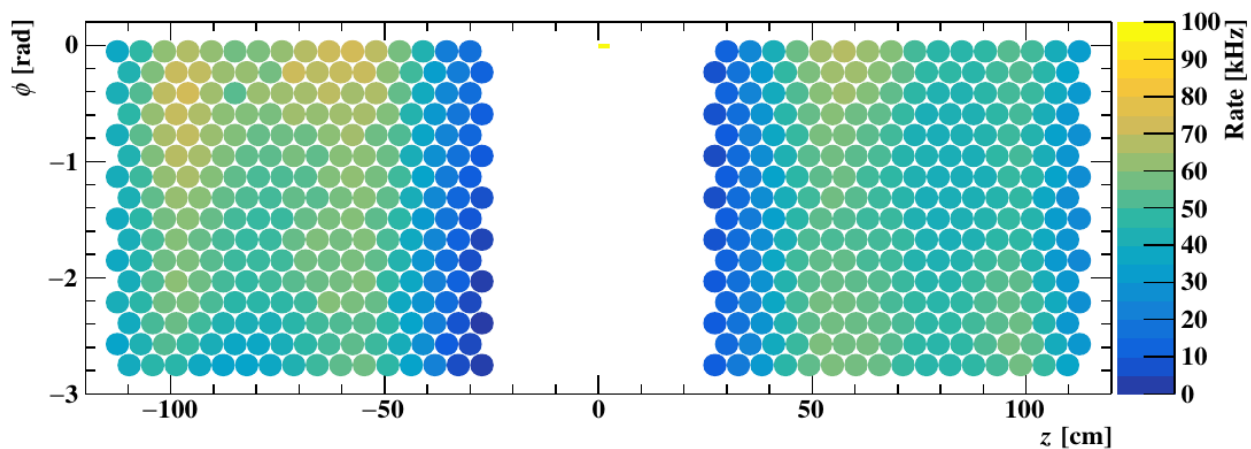


**Fig. 5.9:** Hit rates map of the pTC at  $R_\mu = 5 \times 10^7 \mu/\text{s}$  during the 2022 run. Each circle indicates a counter.

was completed in 2021. It was then ready for the DAQ campaign of May 2021, with 35 crates with up to 16 WaveDREAM modules.

### 5.4.1 WaveDAQ

The WaveDREAM is a 16-channel data acquisition platform utilizing two DRS4 chips for digitizing analog signals at speeds up to 5.0 GSPS. Input channels have a programmable gain stage (0.25–100) with an 800 MHz analog bandwidth, providing bias voltage for SiPMs. Detected events trigger external ADC readout, and data is sent to a Data Concentrator Board (DCB) over Ethernet. Trigger decisions are made by FPGA Trigger Concentrator Boards within  $\sim 600$  ns. The DAQ operates in *push-mode*: trigger signals prompt boards to prepare data for DCBs, delivered to the DAQ server via Ethernet. However, there is a potential packet loss, leading to incomplete event reception and DAQ inefficiency.

The typical trigger rate during physics runs ranges from 10 to 30 Hz. Each waveform is  $\sim 1.5$  kB, necessitating a 10 Gbit/s connection between WaveDAQ and the DAQ server. To manage the data rate, a private network, is used independently of the laboratory network. A multi-threaded software involves four independent processing steps: Collector, Builder, Worker, and Data Handler. Each step can be parallelised as needed; in total, we use 32 threads.

### 5.4.2 Data reduction

A full MEG II event is as large as 16 MB, but this can be reduced without deteriorating the experiment's performance by applying data reduction schemes tailored to each detector.

The methods implemented at the data handler stage are:

- Waveform re-binning: Merge the waveform bins in groups of  $2^n$  ( $n = 1, 2, 3, 4, 5$ ).
- Region of interest (ROI): Slice the waveform in a window around the trigger time.
- Zero suppression: Discard waveforms without pulses.

For the LXe detector, re-binning is widely used. The pTC detector is highly segmented with a very good signal-to-noise separation, making zero suppression very powerful. The size of pTC events is negligible since only a small fraction of pTC counters is hit. The same approach cannot be used for the CDCH because the signal-to-noise separation is not at the same level, so all waveforms are written to disk and re-binned by a factor of ten. The overall event size reduction is a factor  $\approx 10$ .

### 5.4.3 Performances

The infrastructure guarantees over 99% efficiency for trigger rates up to 35 Hz, corresponding to an 8 Gbit/s traffic rate on the private network. However, some inefficiency is observed above this threshold. For detector calibration runs requiring only a subsample of signals, the system can run at the current maximum rate of about 52 Hz. This is crucial to minimize detector calibration time and increase the sample of physics data.

### 5.4.4 Triggers

The WaveDAQ system supports up to 64 independent trigger lines, each with its prescaling factor. Trigger lines are identified by a number, serving as a priority order when multiple conditions are

matched. The remaining triggers are dedicated to collecting detector-specific calibration data.

**MEG trigger** The  $\mu^+ \rightarrow e^+\gamma$  trigger requires the simultaneous presence of three conditions: gamma-ray energy above a threshold, time coincidence within a programmable window, and direction match compatible with a two-body muon decay at rest. Three triggers, each with relaxed conditions, are recorded during physics runs. The offline-reconstructed observables are then used to evaluate online selection efficiency. The  $\mu^+ \rightarrow e^+\gamma$  trigger efficiency is approximately  $(80 \pm 1)\%$  at a muon rate of  $3 \times 10^7 s^{-1}$ . Improvements since 2022 include an enhanced gamma-ray conversion time algorithm and improved LXe detector calibration, with further investigations planned for direction match efficiency.

**Triggers for calibrations** A comprehensive set of calibration methods, each with dedicated trigger logic, is deployed, and signals are collected by the auxiliary crate. The most challenging calibration is for the LXe detector (see Sec. 5.2). Approximately 10 trigger lines are dedicated to LXe calibration, involving energy scale calibration with triggered  $\gamma$  rays of known energies (from 9 to 130 MeV). The pTC is calibrated daily using a laser-based system, with a dedicated trigger line providing synchronization.

## 5.5 Beam and target

The beamlines at PSI were described in 1.5. The beamline delivering  $\mu^+$  to MEG II, in particular, is the  $\pi E5$  line, shown in Fig. 5.10. The design, tuning, and deep understanding of this line play a key role in the success of the MEG experiment. Here we will describe the beamline, outline the key elements, and the related simulations. We will then describe the MEG II target, with some detail on the way to take into account its deformations during the analysis.

### 5.5.1 $\pi E5$

This beam-line has actually two possible configurations: this will allow the area to be shared between MEG II and Mu3e. As already illustrated, the surface muons delivered by this beamline are produced for the decay of the pions generated as secondary beams from the HIPA proton beam. On top of muons, pions, and positrons also are transported by the beamline. We will briefly describe the elements of  $\pi E5$  (COBRA has been already described).

- AHSW41 dipole: Captures the pions and muons in the backward direction and defines the momentum acceptance of the beamline.
- Straight section: Quadrupoles (QSF4\*), sextupoles (HSC4\*) and three slits (FS41–42–43) shape the beam. FS41 In particular is used to reduce the beam intensity and momentum spread.
- AST41 dipole: This element is used to define in which channel the beam is sent. "Z" channel for MEG II and "U" channel for (the upcoming) Mu3e.
- Separator: The beam arrives in a Wien filter via Triplet I and a quadrupole triplet. Te aim is to separate the muons from pions and positrons.
- Triplet II at a collimator: This pair focuses the beam and cuts the tails.
- BTS: This Beam Transport Solenoid contains a 300  $\mu\text{m}$  thick Mylar<sup>®</sup> moderator.

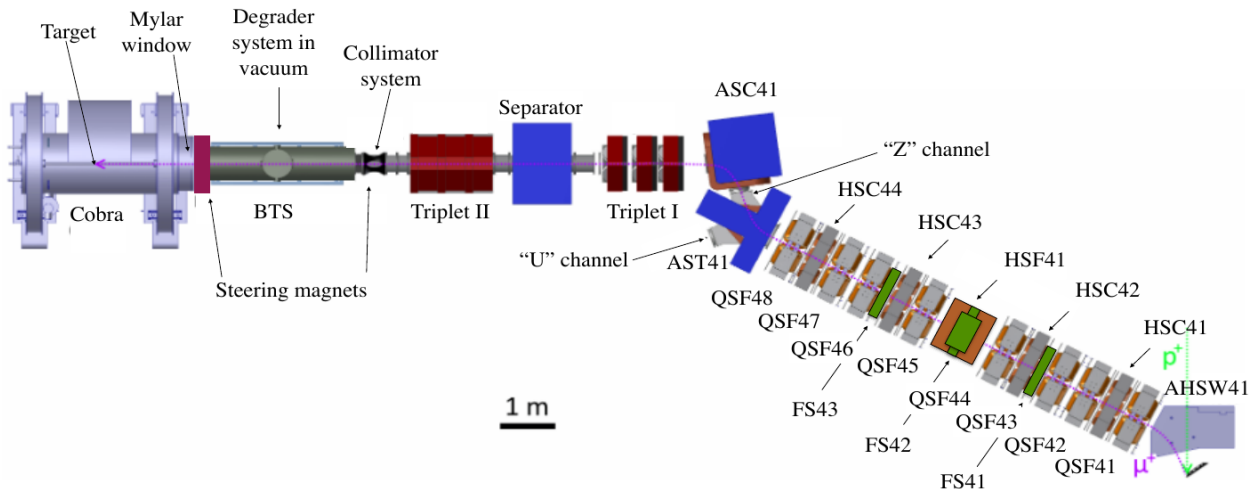


**Fig. 5.10:** Detail sketch of the  $\pi E5$  beamline at PSI.

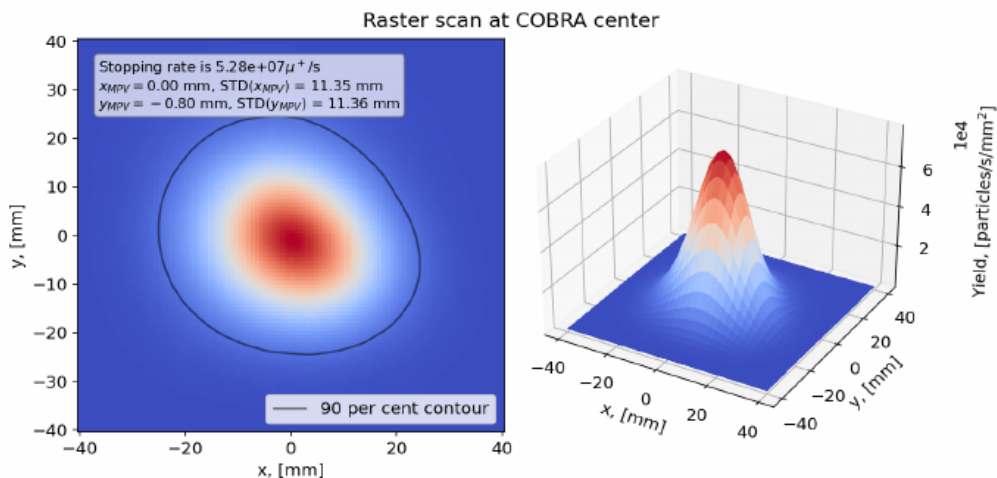


**Fig. 5.11:** Beam profile at COBRA center for a stopped muon rate of  $R_\mu = 5.3 \times 10^7 \mu/\text{s}$  at  $I_p = 2.2 \text{ mA}$ .

- A 190  $\mu\text{m}$  Mylar® window separates the beampipe from the He atmosphere in COBRA.
- COBRA: The design choice for this element was previously illustrated (5.3.1). The behavior of the beam inside this element is quite tricky to simulate consistently.

Although not one of my tasks, I helped during some of the beam tuning done during these last years. Aside from the beginning of the run, these elements are tuned also when there is a major change in the main proton beam, often related to the overall current of incoming particles. Another tune is done at the end of the year to change the beam from  $\mu^+$  to  $\pi$ , necessary for the CEX.

**Beam profile** In Fig. 5.11 is shown a typical beam profile at COBRA center: The beam is in  $x_b = (0.0 \pm 0.5) \text{ mm}$ ,  $y_b = (-0.8 \pm 0.5) \text{ mm}$  with standard deviations  $\sigma_x = (11.35 \pm 0.50) \text{ mm}$  and  $\sigma_y = (11.36 \pm 0.50) \text{ mm}$ . This beam was measured with slits such as the stopped muon rate was  $R_\mu = 5.3 \times 10^7 \mu/\text{s}$  at the primary proton beam current  $I_p = 2.2 \text{ mA}$ . Similar profiles were achieved in the range  $R_\mu = (2 \div 5) \times 10^7 \mu/\text{s}$ . The measurements on the stopped muon rate are evaluated using the stopping efficiency extracted by simulations (89%) and are affected by a 5% uncertainty due to the variations of the proton beam position on Target E.

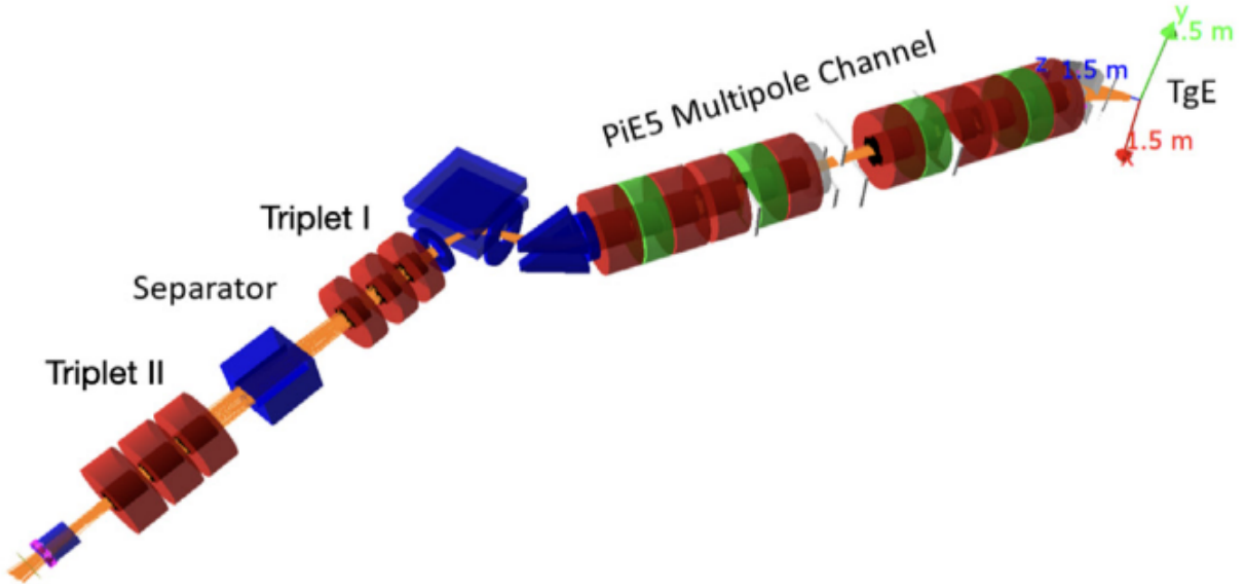


**Fig. 5.12:** G4BEAMLINE simulation of few tracks (orange lines) in the  $\pi E5$  beamline. It's possible to recognize the elements discussed previously and showed in Fig 5.10.

### 5.5.2 Simulations

As introduced in the previous section, the understanding of the beam behavior is a key aspect of the experiment. The beamline itself was developed using TRANSPORT, a beam optics simulation program. The model was later implemented in G4BEAMLINE<sup>2</sup>. The reason to have a physics-based simulation on top of the optics simulation is quite obvious: optics programs cannot simulate interaction with materials and all the physical processes taking place in a beamline.

**G4BEAMLINE** Being based on GEANT4, this program is a flexible and extensible framework for implementing complex simulations of particle interactions, including electromagnetic and hadronic processes, decay processes, and tracking in magnetic fields. Just like GEANT4, the simulation is run particle by particle and *step-based*. This means that at every interaction physical models are used to update the particle state and generate necessary secondary particles. The major extensions in G4BEAMLINE are predefined beamline elements, beam generators, and some optic tools to study the performance of the beamline. An example of particle tracking in this program is shown in Fig. 5.12. In the last years this simulation has been updated and developed by Giovanni Dal Maso to extract the best possible understanding of the stopped muon rate  $R_\mu$ .

**MAD-X** During 2022/2023 Luca Biasia, a Master student in Pisa, developed a MAD-X<sup>3</sup> simulation to describe the  $\pi E5$  line and cross-validate the results obtained using G4BEAMLINE and to start the transition from TRANSPORT to MAD-X. My contribution to this simulation was only partial: I provided Luca with some working MAD-X examples, developed while attending the JUAS, and some initial help for him to start playing with this simulation framework. After this initial ‘starting kit’, Giovanni Dal Maso was the one overseeing the development while I only followed the updates and gave feedback or suggestions.

<sup>2</sup>G4BEAMLINE is a simulation program for particle physics based on GEANT4 and can be found [here](#).

<sup>3</sup>MAD-X is a general-purpose tool for charged-particle optics design and can be found [here](#).

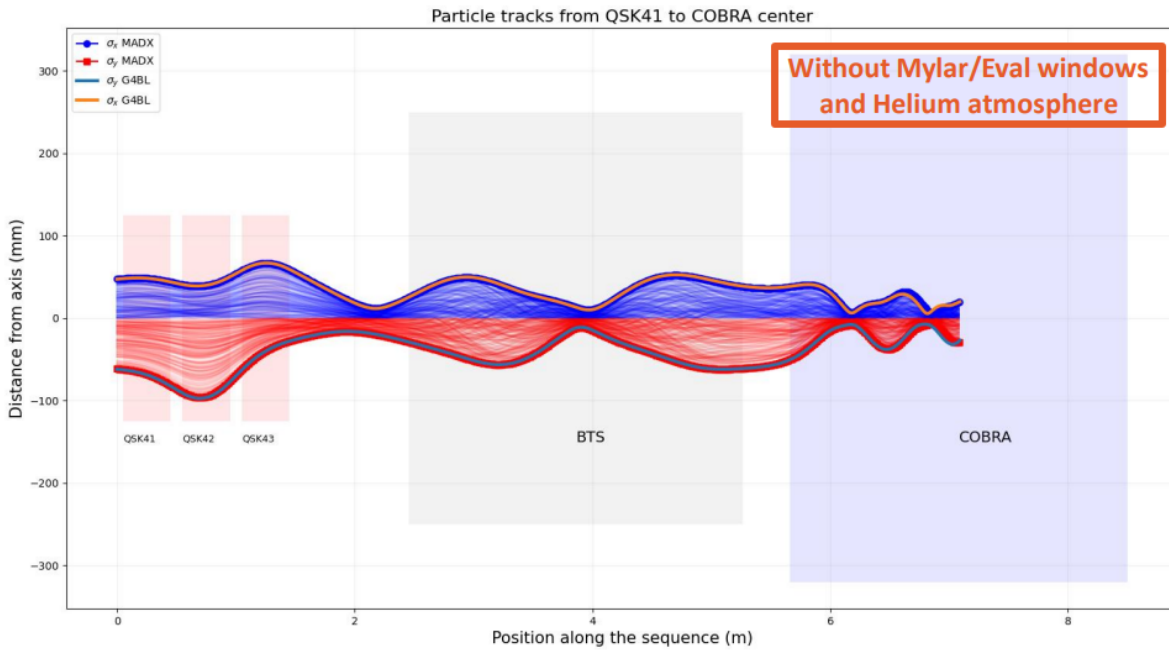


**Fig. 5.13:** Comparison of the results from the G4BEAMLINE and MAD-X simulations for  $\pi E5$ . While the agreement is very good for most of the beamline, there is some difference inside COBRA. This is due to the difficulty in describing the highly ‘non-standard’ magnet. Given MAD-X has no particle interaction, the comparison is fair only when removing all materials from the beamline in the G4BEAMLINE simulation.

After a comparison with data and G4BEAMLINE some discrepancies arose and, after many iterations, they were associated with the description of the fringing fields of the components in MAD-X. The solution adopted was to slice the field maps in thin layers and define many thin ‘MAD-X elements’. A comparison of the results from QSK41 to COBRA center is shown in Fig. 5.13. During the beam tuning in June 2023, this simulation was crosschecked: after measuring the beam spot at COBRA center the currents of the magnets were chosen with MAD-X to obtain a different beam shape. The measurement was consistent with the resulting simulation. This was a great achievement and, moving forward, this tool is going to play a key role during the beam tuning.

### 5.5.3 MEG II target

The aim of the target is to stop  $\mu^+$  at COBRA center while minimizing the interaction of the secondary particles produced. The knowledge of the position of the target and planarity are key components in evaluating the systematic errors on the reconstructed vertex position. After in-depth studies, the BC400 scintillating plastic was selected as the material for the target. The shape is a ellipse of  $270\text{ mm} \times 66\text{ mm}$  and  $170\text{ }\mu\text{m}$  thick, with a maximum variation of  $20\text{ }\mu\text{m}$ . The target is inclined such as the normal of its surface creates a  $(75.0 \pm 0.1)^\circ$  angle with the beam.

**Deformation and pictures** In order to identify the  $\mu^+ \rightarrow e^+\gamma$  process, it is necessary to measure the angles  $(\phi_e, \theta_e)$  at the target, back-propagating the reconstructed tracks. The resolution on these variables is  $\sim 7\text{ mrad}$ , but a simple displacement of  $500\text{ }\mu\text{m}$  of the target propagates as systematics of  $\geq 4\text{ mrad}$  on  $\phi_e$ . For this reason, the collaboration developed three different ways of keeping these systematics under control:

- A yearly optical survey to measure the position inside COBRA.

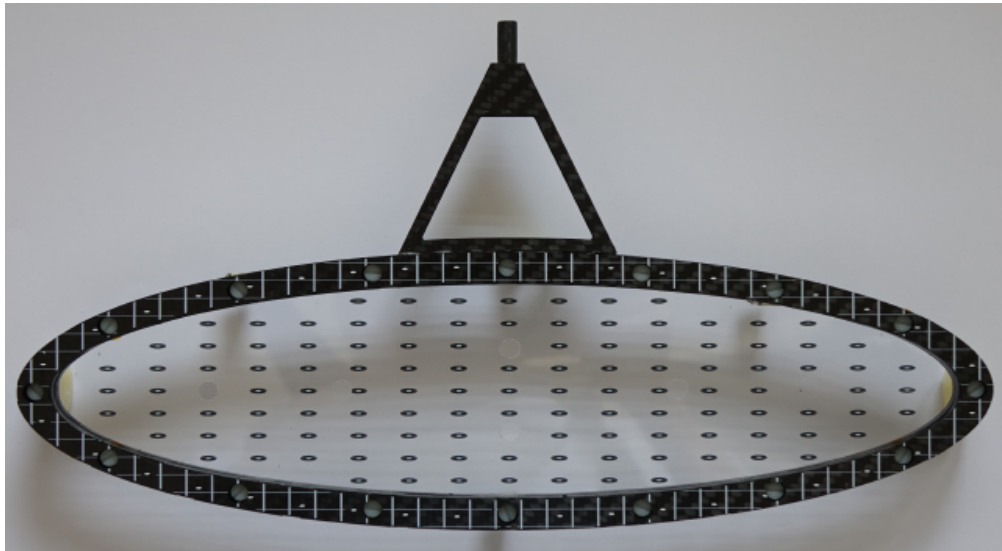


**Fig. 5.14:** Picture of the BC400 target. Clearly visible is the dot pattern on both the target and carbon fiber frame. Six holes, admittedly less visible, are located on the axes of the ellipse.

- Fiducial holes in the target: This allows to study the position of the target reconstructing the position of the vertices for many events, but it requires months of data.
- Photogrammetric survey of a dot pattern on the target itself.

While the first two were used already in MEG, the third was developed for the upgraded MEG II. A picture of the target is in Fig. 5.14, where the dot pattern is clearly visible. Two different CMOS cameras are used to take pictures of the target and two different methods are then employed to study the sequence of pictures. The position of the center of the target is described in the MEG II coordinate system, while the deformation is accounted for differently by the two methods:

- In the first method,  $\chi^2$  is evaluated between the measured and expected dot positions. The expected positions depend on the position of the target, the deformation (parametrized with Zernike<sup>4</sup> polynomials), and the optical parameters of the system.
- The second method minimizes the  $\chi^2$  for the observed and measured 2D positions of the dots on the camera plane. Clearly, the optical projection on this plane is the cardinal element.

These two methods have been proven to be compatible within 100  $\mu\text{m}$ .

## 5.6 Sensitivity

When collecting the information from all the different subdetectors the picture looks something like shown in Fig. 5.15. The confidence interval is extracted on the variables that have good discriminating power wrt the background:  $E_{e^+}$ ,  $E_\gamma$ , the relative angle  $\Phi_{e^+\gamma}$ , the relative time  $t_{e^+\gamma}$ , plus two variables relative to the RDC ( $t_{e^+,RDC} - t_{\gamma,XEC}$  and  $E_{e^+,RDC}$ ). The likelihood analysis will be here skipped but a similar analysis will be outlined for the X17 search in Ch. 7. The analysis region is defined as ( $E_{e^+} \in [48, 58]\text{MeV}$ ;  $t_{e^+\gamma} \in [-500, 500]\text{ps}$ ). The probability density functions (PDFs) for the background are constructed looking at the *sidebands*, while for the signal the expected distributions are convolved with the extracted resolutions. The sensitivity obtained reflects the

<sup>4</sup>Zernike polynomials are a set of orthogonal functions commonly used in optics and image analysis (see [Wikipedia](#)).

resolutions, efficiency, and the live time of data-taking. This information is shown in Fig. 5.16. The most recent analysis was published in 2023, setting the new upper-limit at  $3.1 \times 10^{-17}$  [2].

## 5.7 Cockcroft–Walton

In addition to the muon beamline, MEG II has a Cockcroft–Walton proton accelerator. After the description of the machine, we will highlight the use of this accelerator by the collaboration (calibrations of the XEC and exotic searches) and the recent maintenance. One of my main tasks during this Ph.D. has been the usage of this machine, so I was quite fortunate to be able to shadow the expert during the maintenance.

### 5.7.1 Description of the machine

The accelerator is a single-stage in-line singletron produced by HVEM. This machine is a compact Cockcroft–Walton with a terminal voltage of  $0.1 \div 1.0$  MV and a proton current up to 100 mA.

**Source** The RF ion source is a bottle of gas that is excited by an RF oscillator. The electrons in the gas are excited and, because of the collisions with the neutral gas particles, cause ionization. The plasma produced is confined with an axial magnetic field and serves as the source of positive ions, which are extracted by applying a DC electric field. A schematic of the working principle of the RF ion source is shown in Fig. 5.17

**CW-Circuit** The high-voltage multiplier and rectifier stack, together with the RF driver and HV control and stabilizing system, is one of the core sections of the machine. It is located in the main pressure tank, while the RF resonance coils are in a separate SF<sub>6</sub> filled tank and the RF driver in a separate cabinet. This gas is often used as a gaseous dielectric medium because of its high dielectric strength, the result of the gas's high electronegativity<sup>5</sup> and density. In the case of an arc, SF<sub>6</sub> can break down in different ways but most of the decomposition products tend to quickly re-form SF<sub>6</sub>, a process termed *self-healing*. Arcing or corona can also produce disulfur decafluoride (S<sub>2</sub>F<sub>10</sub>), a highly toxic gas, which is the reason extra care is needed when opening such a system. This stack is a parallel-fed CW power supply that consists of a series of high voltage rectifiers and capacitive coupling *corona* rings. The power is fed via an RF driver capacitive coupled. A sketch of the inner structure of a rectifier assembly (*ass'y*) is shown in Fig. 5.18c while in Fig. 5.25b is clearly visible the way the ass'ys are mounted.

**Driver** The driver, as the name suggests, is the circuit that feeds the voltage/power to the whole system. In between the driver and the CW stack of rectifiers' ass'ys a resonant circuit is used to amplify the output of the driver. The power is fed to this resonant circuit in phase with the oscillating current. Keeping the frequency at resonance, the driver controls the terminal voltage adjusting the pulse width. A block diagram of the driver is shown in Fig. 5.19

---

<sup>5</sup>Electronegativity is a measure of the attraction of an atom for bonding electrons in molecules compared to that of other atoms: large values indicate a stronger attraction and it increases from left to right across the periodic table.

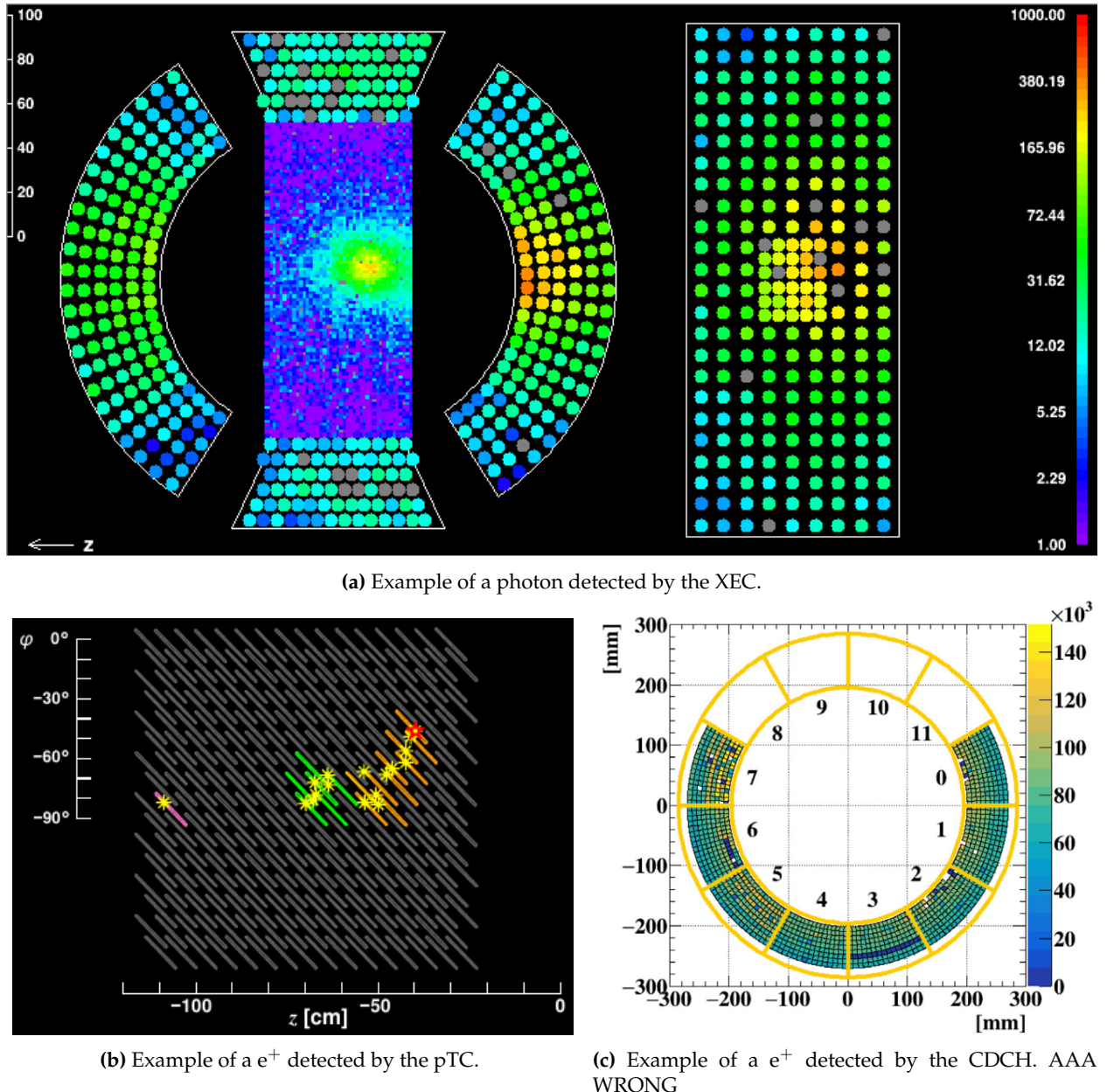


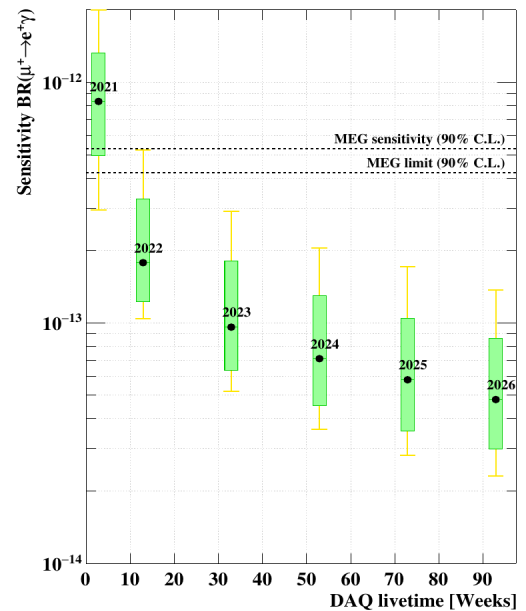
**Fig. 5.15:** Once all the MEG II detectors are combined, the usual data-taking looks something like this. These are just examples taken from different events.



Resolutions	Foreseen	Achieved
$E_{e^+}$ (keV)	100	89
$\phi_{e^+}, \theta_{e^+}$ (mrad)	3.7/6.7	4.1/7.4
$y_{e^+}, z_{e^+}$ (mm)	0.7/1.6	0.7/2.0
$E_\gamma (\%)$ ( $w < 2$ cm)/( $w > 2$ cm)	1.7/1.7	2.0/1.8
$u_\gamma, v_\gamma, w_\gamma$ , (mm)	2.4/2.4/5.0	2.5/2.5/5.0
$t_{e^+\gamma}$ (ps)	70	78
Efficiency (%)		
$\varepsilon_\gamma$	69	62
$\varepsilon_{e^+}$	65	67
$\varepsilon_{\text{TRG}}$	$\approx 99$	80

(a) Obtained and expected resolutions at  $R_\mu = 3 \times 10^7 \mu/\text{s}$ . A 5 ÷ 7% deterioration of the positron efficiency was found at  $R_\mu = 3 \times 10^7 \mu/\text{s}$ .

**Fig. 5.16:** The sensitivity reached by MEG II has a strong dependence on the DAQ livetime, as shown in (b), and the resolution/efficiency obtained, shown in (a).



(b) Expected sensitivity as a function of the DAQ livetime.

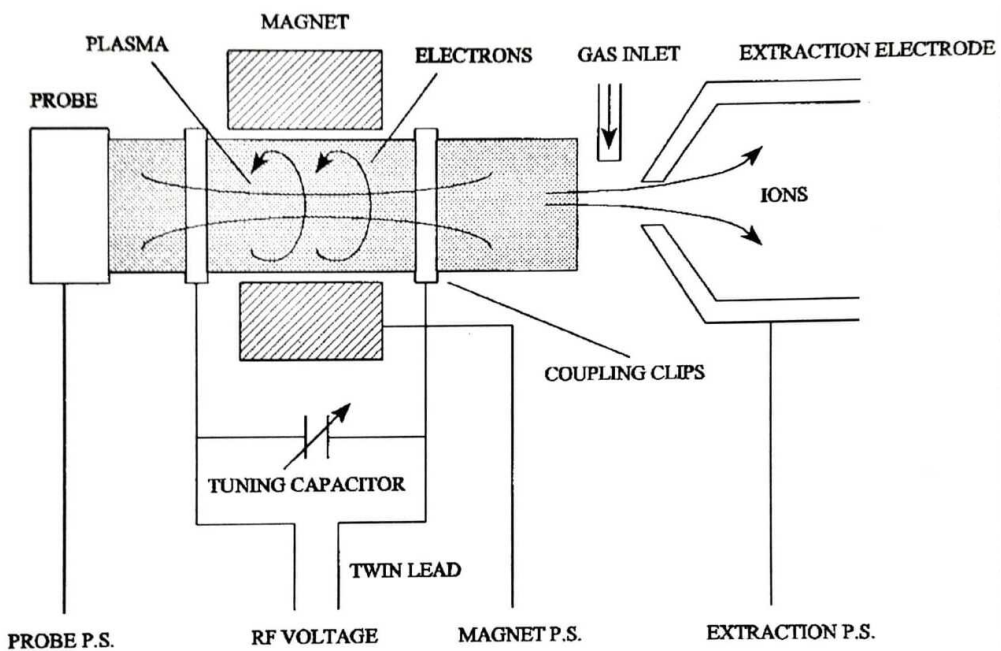


**Fig. 5.17:** Sketch of the ion source of the CW.

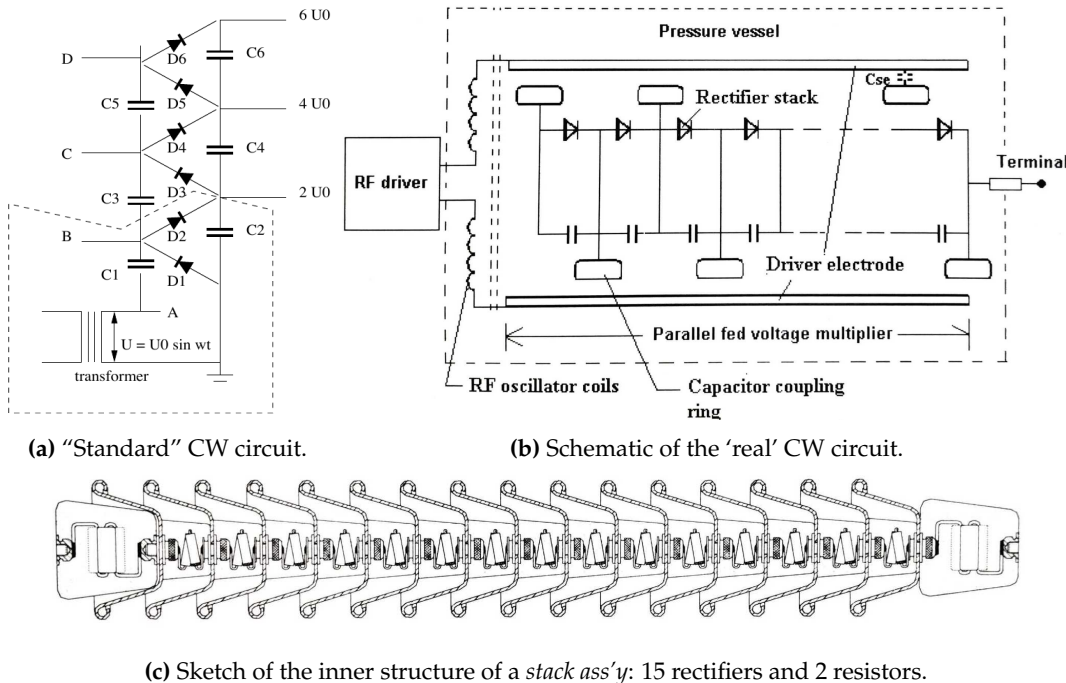


**Fig. 5.18:** The first schematic (a) is presented just for reference, given the usual depiction of a CW circuit. The second (b) shows the CW circuit and the capacitive coupling to the RF driver while the third (c) shows the internal structure of a rectifier stack (*stack ass'y*).

**Start-frequency** The system can operate only at resonance and this frequency  $f_{res}$  is defined by the coil and dynodes. During star-up, the system starts at  $f_{start}$  higher than the resonance and then lowers it until the resonance is found. A parasitic frequency  $f_{par}$ , with  $f_{par} > f_{res}$ , is also present. At this frequency, the driver oscillates at a higher frequency, and no power is transferred to the terminal. To avoid the higher frequency, a tuning is needed so that  $f_{par} > f_{start} > f_{res}$ .

**Q-factor** In the RF resonance circuit high amounts of 'blind power' can be present (up to 1 MW). The quality factor (Q-factor) of the RF resonance circuit is the ratio of blind to dissipated power. E.g. for a blind power of 1 MW and a Q-factor of 1000 the transformer coil dissipates 1 kW of heat. If this factor is not high enough the dissipated power is too high and will prevent the driver from operating correctly. The Q-factor is measured using a function generator and looking at the relative phase and amplitude of voltage in two points of the accelerator's RF resonance circuit. A sketch of the measurement is shown in Fig. 5.20a. The system is at resonance when there is no relative phase between  $V_1$  and  $V_2$ , and the value of  $V_1/V_2$  is used to evaluate the Q-factor:

$$Q = Z_{coil}/R_{loss} = 2\pi f_{req} I_{coil} (V_1/V_2 - 1)/R_l \approx 43.9 \times f_{res} [\text{kHz}] \times (V_1/V_2 - 1) \quad (5.2)$$

## 5.7.2 Usage

This machine is used 3 times a week, together with a  ${}^7\text{Li}$  target (Lithium tetraborate ( $\text{Li}_2\text{B}_4\text{O}_7$ )), to produce the 17.6 MeV line from the  ${}^7\text{Li}(p,\gamma){}^8\text{Be}$  process to calibrate the XEC. For this process, the required energy is  $E_p = 500$  keV. This process was already outlined in Sec. 5.2.3. On top of taking

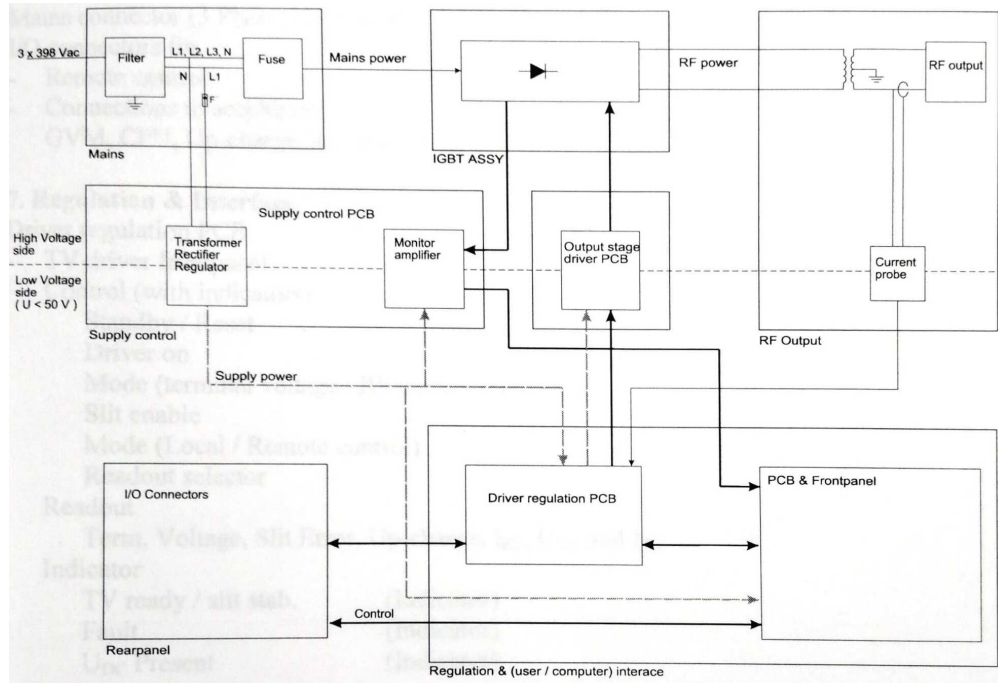


Fig. 5.19: Block diagram of the driver

care of this calibration<sup>6</sup> I ironed out the procedure and reworked the documentation to aid other members of the collaboration.

**X17** The protons coming from the CW have been mainly used for the calibration of the XEC detector, but also to perform a parasitic measurement: the search for the X17 anomaly. This search, done in 2021-2023, will be extensively discussed in Ch. 7 but we wanted to underline here the key role that the CW machine has played in this parasitic search for exotic physics. For this search, we used the machine up to  $E_p = 1080$  keV (Higher than the nominal maximum voltage).

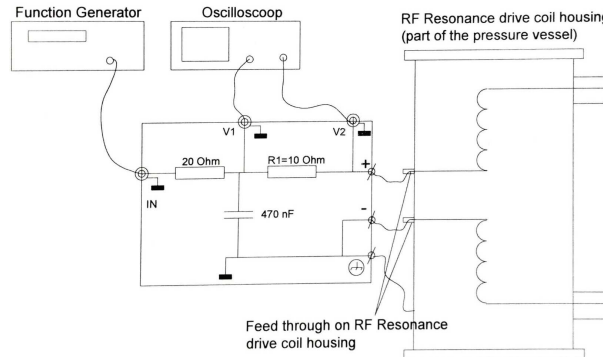
### 5.7.3 CW issues and maintenance

By the end of 2020, the CW started having some minor problems: the machine was running fine but the time required to switch it on kept growing longer. While the whole procedure would normally take  $\sim 15$  min the time required exceeded the hour. We also noticed the machine was getting unstable when running near the maximum voltage at 1 MV. Following this behavior, an intense exchange with the HVEE company started and we performed many different tests on both the software and hardware sides.

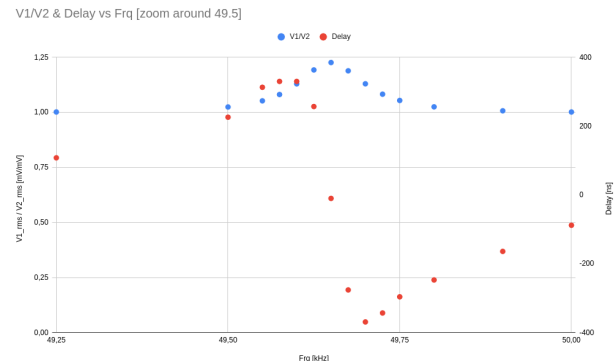
**Hot Fix** We measured the Q-factor of the machine using Eq. 5.2, shown in Fig. 5.20b. The value found was a factor  $\sim 2k$  lower than expected and the position of the resonance frequency was shifted from the design value. For more information on the functioning of the machine and the Q-factor see Sec. 5.7.1. We adjusted the frequency at which the machine starts when turning ON. This solved the delay problem but didn't recover the maximum voltage.

The machine was now starting quickly but working in a stable configuration only up to half of the

<sup>6</sup>This 3 times a week task was shared between me and other 2 people.



(a) Sketch of the circuit to measure the Q-factor.

(b) Example of measurement of the Q-factor: in red the delay while in blue the fraction  $V_1/V_2$ .

**Fig. 5.20:** The Q-factor is the ratio of blind to dissipated power. Via this number is possible to evaluate the energy dissipated as heat running the machine. If it is too low the machine cannot operate correctly.

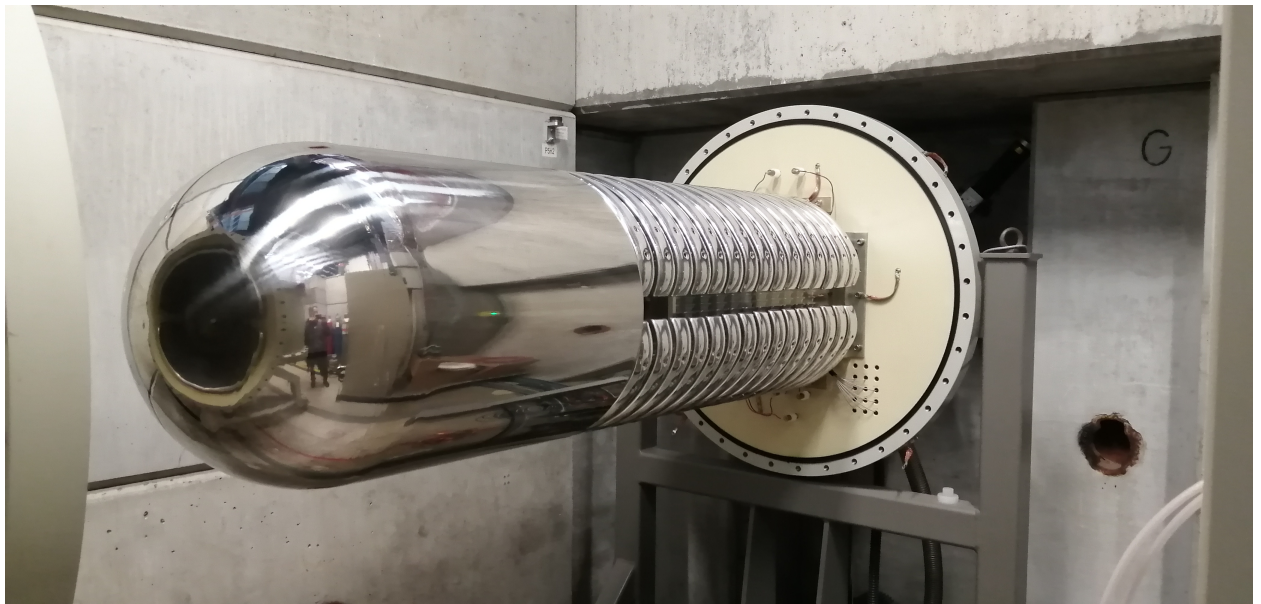


**Fig. 5.21:** View of the CW after the extraction from the external volume. This volume contains SF<sub>6</sub> which is used as a gaseous dielectric medium and needs to be evacuated before the extraction.

nominal maximum voltage. As explained in the previous paragraph this was not a problem for the  $^7\text{Li}(p,\gamma)^8\text{Be}$  calibrations but was a worrying sign on the health of the machine, and it would have prevented the CEX. At this point, an expert from HVEE was sent to inspect the machine.

**Maintenance** After running some checks, opening the CW was deemed necessary and, for this reason, we removed the SF<sub>6</sub> contained in the main tank. After the extraction of the CW, we inspected and measured all the elements, removing also some of the *corona rings* for easier inspection. We found signs of arcing on one of the *rectifier ass'y*. After the substitution of this element<sup>7</sup>, the machine was closed again, filled with SF<sub>6</sub>, and tested again. This whole process is shown in the pictures in Fig. 5.25. Unfortunately, the faulty behavior persisted and we noticed sparks in

<sup>7</sup>The rectifier ass'y are stacks of alternated diodes and aluminum capacitors capped by two resistors. We could re-use the capacitors, after careful cleaning, while resistors and diodes were too badly damaged. The process of refurbishing is shown in Fig. 5.26

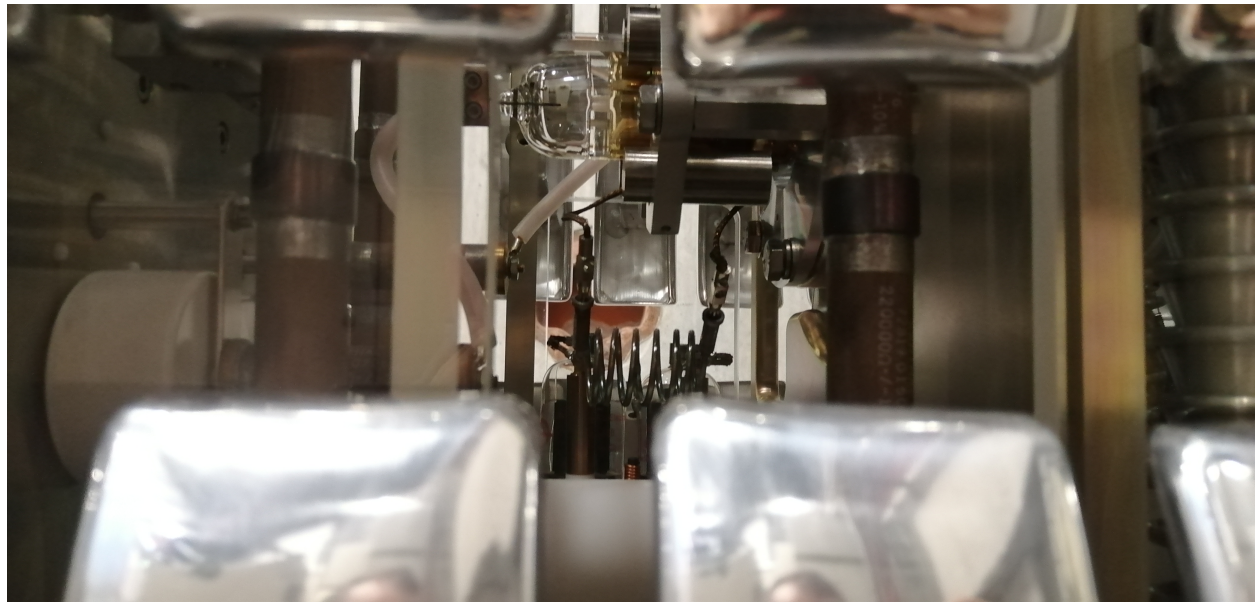


**Fig. 5.22:** View of the source of the CW machine.

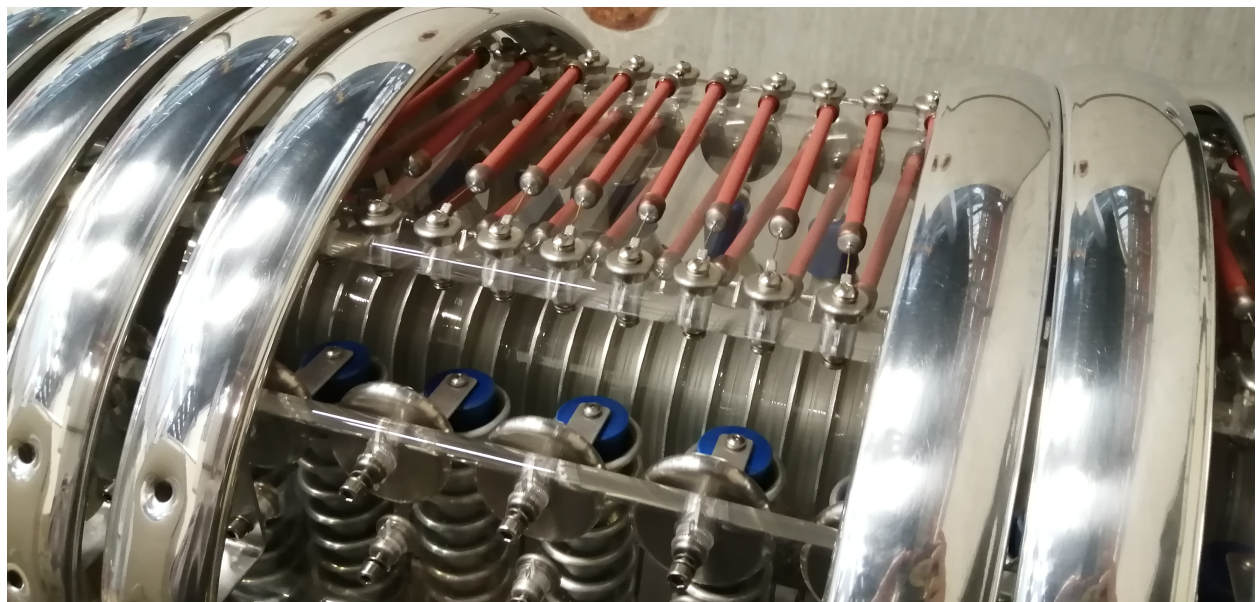


**Fig. 5.23:** Top view of the CW after the removal of a few *corona rings*. Here we can see all the elements of a CW circuit: red - the resistors on top; metallic rings on the central tube - the capacitors; blue and metallic cups - the resistance and capacitors of the rectifiers, which run vertically.

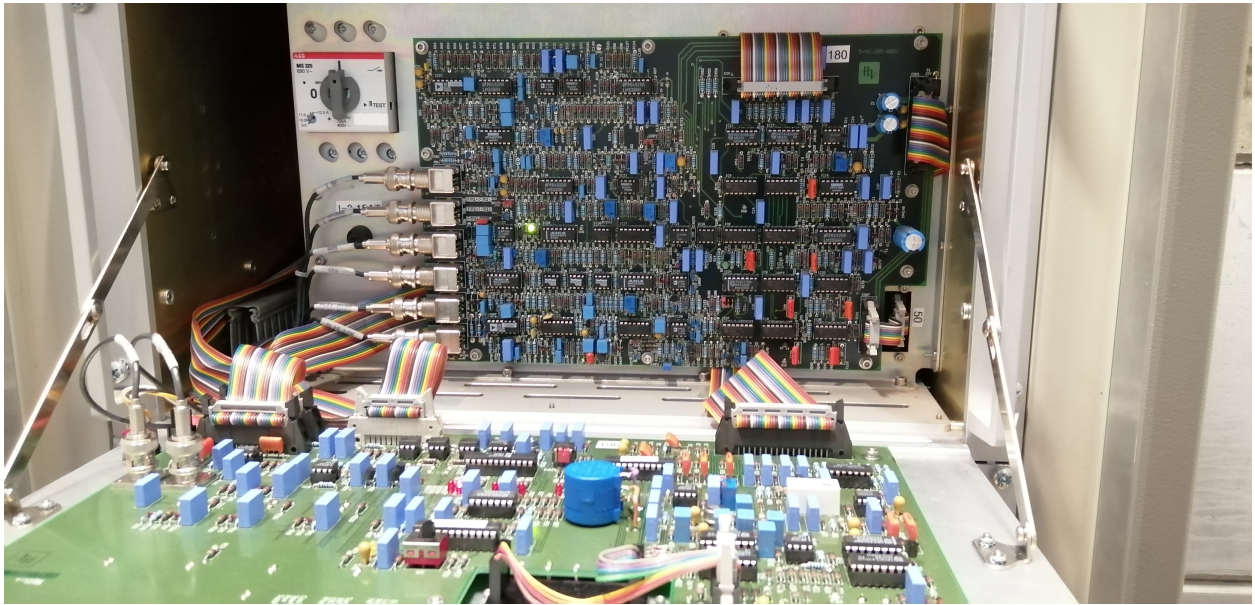
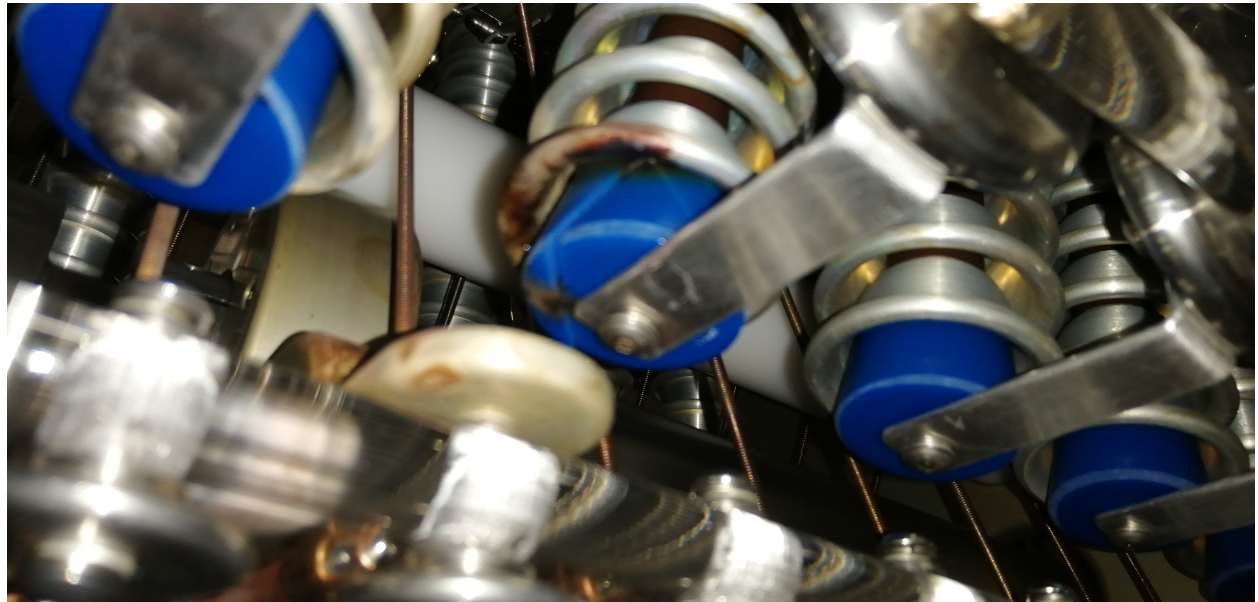


**Fig. 5.24:** Picture of the control panel for the CW machine.

the main volume. After re-opening we found burning marks on the rectifier ass'y next to the exchanged one. We then realized that both were damaged but the first was functioning as a 'bridge', preventing the second from being completely destroyed. After the substitution of the second and the tuning of the machine, we finally recovered its full functionality: quick switching ON and stable operation in the full range of voltages. 5.26.

## 5.8 Conclusions

In this (very dense) chapter we went through the description of two key elements of the work I have done during these three years: the MEG II apparatus and the Cockcroft–Walton. While I took no part in the design of either, in these years I spent a lot of time 'hands-on' on many subsystems of the MEG II apparatus: calibrations, tuning, and fixes of various types. On the other side, the CW functioning has been one of my main tasks. The unfortunate hiccup with it gave me the additional unforeseen opportunity to assist the HVEE technician in testing and fixing the machine, which was an extremely interesting and instructive experience.



(a) Discovery of the burning marks on two rectifiers. The reflectivity was a challenge in taking the picture.



(b) Extraction of the broken rectifiers.



(c) Broken rectifier ass'y after the extraction: clearly visible is the burned blue resistor at the top.

**Fig. 5.25:** After close inspection we found burning marks on two rectifiers' ass'y (5.25a). These were removed (5.25b) and carefully inspected (5.25c). The only salvageable part of the rectifiers were the aluminum capacitors, which we cleaned from burning residuals, while all diodes and resistors had to be exchanged.



(a) Picture of the burning marks on the end resistors of the rectifier ass'y.



(b) Assembly of one of the new stack: black - resistors; brown - diodes; metallic - aluminum capacitors.



(c) One of the finished new rectifiers.

**Fig. 5.26:** The rectifiers are made of three elements: diodes; aluminum capacitors; resistors (5.26a). Only the capacitors were salvageable: we re-assembled the rectifiers with new diodes and resistors (5.26b; 5.26c).

# Bibliography on MEG II

- [1] MEG II Collaboration et al. *Operation and performance of MEG II detector*. 2024. arXiv: 2310.11902 [physics.ins-det].
- [2] MEG II collaboration et al. *A search for  $\mu^+ \rightarrow e^+ \gamma$  with the first dataset of the MEG II experiment*. 2024. arXiv: 2310.12614 [hep-ex].
- [3] A.M. Baldini et al. “Search for the lepton flavour violating decay  $\mu^+ \rightarrow e^+ \gamma$  with the full dataset of the MEG experiment”. In: *Eur. Phys. J. C* 76.8 (2016), p. 434. DOI: 10.1140/epjc/s10052-016-4271-x. arXiv: 1605.05081 [hep-ex].
- [4] Bastiano Vitali. “In situ monitoring of the stopped muon flux at Mu2e”. MA thesis. Pisa U., 2020. DOI: 10.2172/1764143.
- [5] R. Frühwirth and A. Strandlie. “Track fitting with ambiguities and noise: A study of elastic tracking and nonlinear filters”. In: *Computer Physics Communications* 120.2 (1999), pp. 197–214. ISSN: 0010-4655. DOI: [https://doi.org/10.1016/S0010-4655\(99\)00231-3](https://doi.org/10.1016/S0010-4655(99)00231-3). URL: <https://www.sciencedirect.com/science/article/pii/S0010465599002313>.
- [6] L. Galli et al. “Operation and performance of the trigger system of the MEG experiment”. In: *Journal of Instrumentation* 9.4, P04022 (Apr. 2014), P04022. DOI: 10.1088/1748-0221/9/04/P04022. URL: <https://ui.adsabs.harvard.edu/abs/2014JInst...9P04022G>.

# Chapter 6

## Liquid Hydrogen target

In this chapter the Charge EXchange reaction, a calibration for the liquid XEnon Calorimeter, will be discussed and an in-depth description of the associated Liquid Hydrogen Target is given. Data taking, analysis, performances, and the different modifications will be also discussed. This target was designed in 2020 to overcome some limitations of the previous and in the last two years went through some heavy re-development. This calibration is cardinal for the correct functioning of the key subdetector of the MEG II experiment. This item was one of the main tasks in my involvement in this experiment and it absorbed a sizable portion of my time and effort.

### 6.1 Charge EXchange reaction

As already discussed, the  $\mu \rightarrow e\gamma$  process searched by MEG leads to a monochromatic photon at 53.2 MeV. We saw in Sec. 5.7 the XEC calibration which is performed three times a week. Unfortunately, while the frequent calibrations are great for the time dependencies, the photon produced by the Li is at lower energy than the signal. To calibrate the calorimeter near the signal region, the Charge EXchange reaction is exploited. The Charge EXchange (CEX) process  $\pi^- p \rightarrow \pi^0 n$ ;  $\pi^0 \rightarrow \gamma\gamma$  produces  $\gamma$  with a flat distribution in the interval [54.9, 82.9] MeV. Extremal values are reached for photons emitted back to back. Thus, a signal-like photon can be tagged by detecting a high-energy photon in the opposite direction. The tagging is performed with a BGO detector which can be positioned (steps of 30 cm in  $\hat{z}$  and 16 deg in  $\hat{\phi}$ ) opposite to specific patches of the XEC. The requirement  $\Delta E/E < 1\%$  translates to  $\Delta\theta_{\gamma\gamma} < 5^\circ$ . A sketch of the CEX measurements, a picture of the BGO detector, and its moving structure is shown in Fig. 6.1.

### 6.2 BGO

The BGO crystal already mentioned, and shown in Fig. 6.1b, is an auxiliary detector that plays a key role in two subjects of this thesis. BGO refers to  $\text{Bi}_4\text{Ge}_3\text{O}_{12}$ , a compound with a cubic crystal structure and often used as a scintillator. Given the high  $Z$  ( $Z_{\text{Bi}} = 83$ ) and high density, this material is a very good  $\gamma$  absorber (properties are listed in Tab. 6.1). This detector is, in particular, a matrix 4x4 of 4 cm  $\times$  4 cm crystals and mounted on a structure (see Fig. 6.1c) that allows it to translate and rotate around COBRA. This detector plays the key role in the back-to-back event tagging but it was also used during the X17 search, subject of Ch. 7. Key aspects of this detector

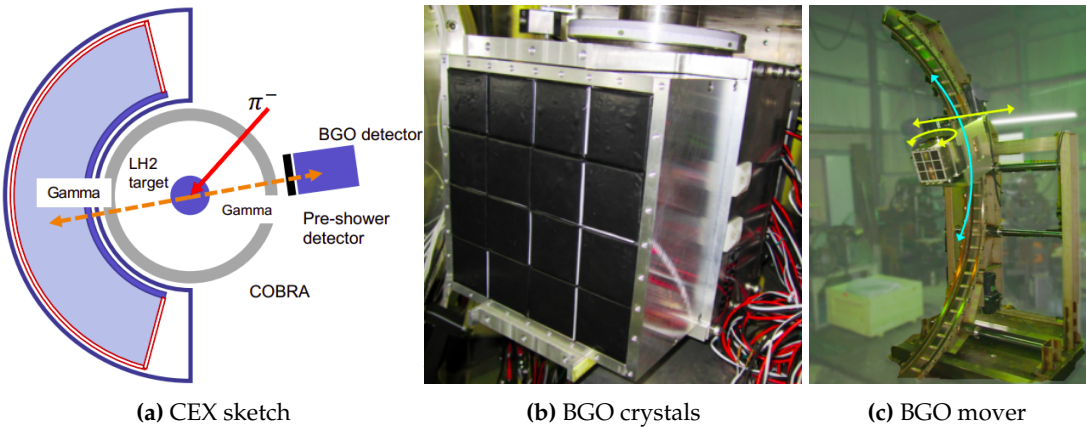


**Fig. 6.1:** Diagram of the CEX measurement, with the back-to-back photons configuration to define the XEC patch via the BGO positioning (6.1a) Picture of the BGO detector (6.1b) Picture of the BGO mover (6.1c).

**Tab. 6.1:** Properties of the Material

Quantity	Value	Unit
Density	7.130	g/cm <sup>3</sup>
Radiation Length $X_0$	1.118	cm
Molière Radius $r_0$	2.259	cm
Max. Emission Wavelength	480	nm
Lower Wavelength Cutoff	320	nm
Light Yield	8-10	photons/keV $\gamma$

are the calibration and inter-calibrations of the different crystals, discussed in App. B<sup>1</sup>.

### 6.3 LH2 target

The details of the circuit and the operation changed on a yearly basis but it's worth discussing the overall working principle before seeing the evolution of this system. Liquid Hydrogen was chosen to provide the protons needed for the CEX reaction. The incoming 70.6 MeV/c  $\pi^-$  are stopped in a cylindrical cell (60 mm diameter, 70 mm length) of 0.5 mm stainless steel containing liquid Hydrogen. This corresponds to  $\sim 90\%$  stopping efficiency. The hydrogen has to be kept liquid ( $T < 20.39$  K at 1 atm) and in the center of the COBRA magnet, requiring a cryogenic infrastructure to be inserted for 2 m. The target consists of four sub-systems:

- A “closed volume” hydrogen circuit, in which a over-pressurized 100 l buffer is connected to the target cell
- A copper rod (2 m in length and 2 cm in diameter): supported and cooled at one end with liquid helium flowing in a copper coil; holding the target cell at the other.
- Vacuum Insulation for the whole system
- A slow-control based on an SCS2000<sup>2</sup> for: temperatures, pressures, and He flux

<sup>1</sup>I worked on this item with David Stäger, a student from ETH, who collected these informations in his thesis [1]

<sup>2</sup>More info can be found here [MIDAS](#) and here [SCS](#) and [MSCB](#).

**Working principle** Let's now outline the working principle of this system. The first step is to pressurize with a Helium bottle a Helium dewar. When the liquid helium starts flowing in the copper coil, the copper rod is cooled on one side. After thermalizing the whole copper rod, the cell temperature slowly follows, reaching the same temperature. Once the temperature is low enough for the Hydrogen to condensate, this process in the cell reduces the Hydrogen pressure, sucking additional gas from the buffer.

**The circuit** The buffer volume for the gaseous hydrogen, as well as all the infrastructure and services, are kept outside the magnet. The circuit for the 2021 version is shown in Fig. 6.2 and, to increase the readability, the different sub-circuits are color-coded. Similar sketches are available for the 2022 and 2023 versions, here not shown for simplicity. The color coding is kept consistent:

- Blue - Hydrogen is filled into the buffer from a cylinder, which gets then removed. The buffer itself is connected to the cell, the exhausting line, a vacuum pump, piezoresistive pressure transmitters and a Nitrogen bottle
- Red - The liquid He flux is obtained by pressurizing a Dewar with an He bottle. The He passes around the Cu rod and through a heater before entering the He recovery line
- Green - Insulation vacuum system
- Yellow - A nitrogen bottle is used for purging the hydrogen when emptying the buffer and kept connected for safety

### 6.3.1 Operation and control

The operation of the target itself is partially manual and partially controlled through a LabVIEW program which, for example, controls the read-out of the various sensors and the flux of the incoming He. A module SCS2000 allows to read the various sensors. There are two key indicators used to monitor the liquefaction process and stability of the system:

- Temperature sensors: resistors (later replaced by Lakeshore® silicon diodes sensors) have been put in thermal contact with the Cu rod at both ends (two per side for redundancy). The readings of these elements allow us to monitor the cooling at the Cu coil and the cell.
- Hydrogen pressure: at room temperature, the hydrogen is set to 1.5 bar over-pressure. When the liquefaction starts the overall pressure is reduced and can be linked to the amount of liquid Hydrogen in the cell.

The procedures to operate the system were developed, discussed with the safety committee, and adapted to the different upgrades. We will not discuss them here.

## 6.4 2021

I started my Ph.D. in November 2020 and I joined the activities after a year, in October 2021, directly for the tests before the data-taking period. The status of the LH2 Target and the preliminary results of the 2021 CEX were presented at the 15th Pisa Meeting on Advanced Detectors [2].

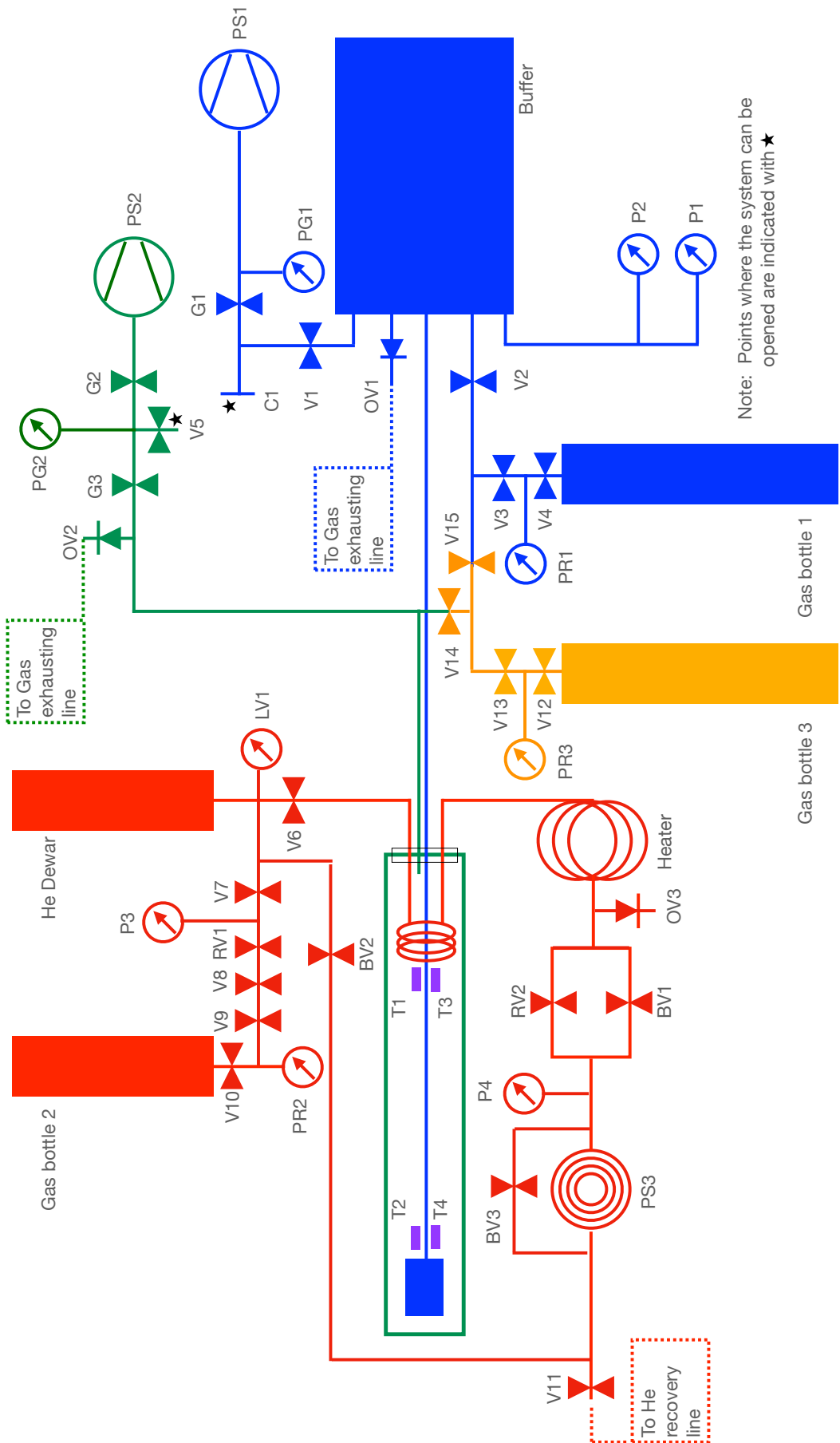


**Fig. 6.2:** Circuit of the LH<sub>2</sub> target. To increase the readability of the scheme of the circuit, the different sub-circuits are color-coded:  
 Blue - Hydrogen; Red - Liquid Helium; Green - Insulation vacuum; Yellow - A nitrogen bottle to flush the system.



**(a)** The target in the testing area, before the craning. **(b)** Target after the insertion in COBRA

**Fig. 6.3:** Pictures of the Liquid Hydrogen target outside  $\pi E5$  and after the insertion in COBRA.

#### 6.4.1 Data taking

The installation process required craning the target in the  $\pi E5$  area, on top of a rail system, aligning and inserting the target inside COBRA. Pictures of the installation are in Fig. 6.3. The data taking lasted roughly two weeks, during which CR runs and XEC calibrations were run while the target was cooling and liquefying. As soon as the level was sufficient the pion beam would be used for CEX data taking for a specific patch of the XEC. When the dewar needed to be exchanged, the data taking would be stopped and CR/calibrations would restart, waiting for the target to be sufficiently full to restart. In figure 6.16a is shown the history of the Hydrogen and Helium pressure at the dewar, where the red line marks when the beam was on. Interesting features are:

- The decreasing parts of the blue plot are the liquefaction period: the Hydrogen pressure drops because of the phase change
- During liquefaction, some spikes can be seen: these are instances in which the system became unstable and liquefaction was lost
- The speed of cooling and liquefaction is always the same, a result of hardware

CEX data could be collected when the target was ‘full enough’: below 2.1 bar, meaning 50% full. In the two weeks, this translates to efficiency of  $D_{2021} \approx 0.5$ . The efficiency for 2021 was lower than expected and the necessary statistic was not reached for every patch (Fig. 6.15a).

#### 6.4.2 Data analysis

While the broad idea of the XEC calibrations was already outlined in Sec. 5.2, it is perhaps worth now describing how the analysis of the data from the Carge EXchange reaction allows extracting not only the timing and energy resolution but also the energy parameters of the detector.

**Timing** The time resolution is evaluated by taking the difference in time between the detector and the pre-shower counter (see Fig. 6.4), correcting for the time of flight (TOF).

$$\Delta t = t_\gamma - t_{ps} - t_{TOF} \quad (6.1)$$

$$\sigma_{\Delta t} = \sigma_{t_\gamma} \oplus \sigma_{t_{ps}} \oplus \sigma_{t_{TOF}} \quad (6.2)$$

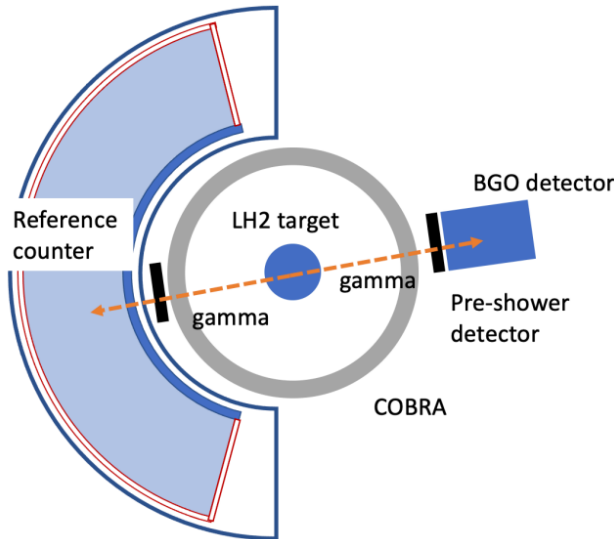


**Fig. 6.4:** The XEC time resolution is evaluated with the help of auxiliary detectors

The contribution coming from the pre-shower counter, being it comprised of scintillators, was measured and found to be  $\sigma_{ps} = (28.2 \pm 0.2)$  ns. The main contribution to  $\sigma_{t_{TOF}}$  comes from the resolution in the position of the vertex  $\sigma_{vertex}$ . This can be evaluated as

$$\sigma_{t_{vertex}} = \sigma_{vertex} \oplus \sigma_{ref} \oplus \sigma_{ps}$$

Due to the reduce statistics, the result was  $\sigma_{vertex} = (70 \pm 6)$  ps. Adding the measured  $\sigma_{\Delta t} = (99.5 \pm 0.5)$  ps (see Fig. 6.5a), we have all the elements to extract the intrinsic resolution of the detector. The timing resolution found is energy-dependent as well as position-dependent; for the interesting range  $50 \text{ MeV} < E_\gamma < 58 \text{ MeV}$  and with minimal cut, the result was  $\sigma_{t_\gamma} = (65 \pm 6)$  ps.

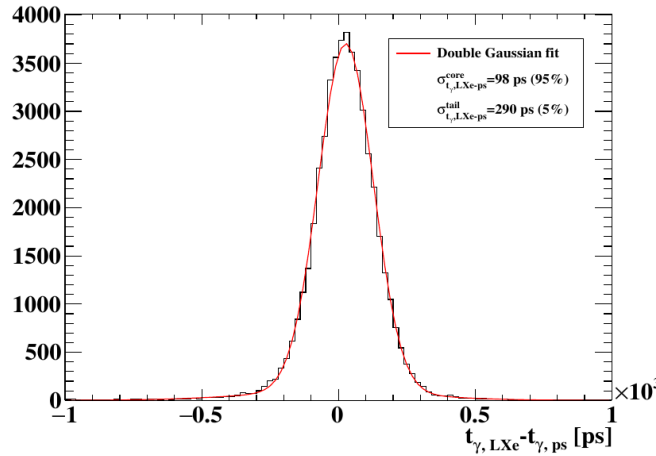
**Energy** The data collected during the CEX have been used for two purposes: as one of the points in the evaluation of the resolution in the energy of the detector (see Fig. 6.5b) and to evaluate the absolute scaling of the energy measured. This second point is related to the known energy of the  $\gamma\gamma$  pair if emitted back to back: 55 MeV. The CEX measurement allows also us to study the non-uniformity of the XEC detector. In Fig. 6.6 (taken from Sec. 5.2.4), this non-uniformity is shown along the different axes.

## 6.5 2022

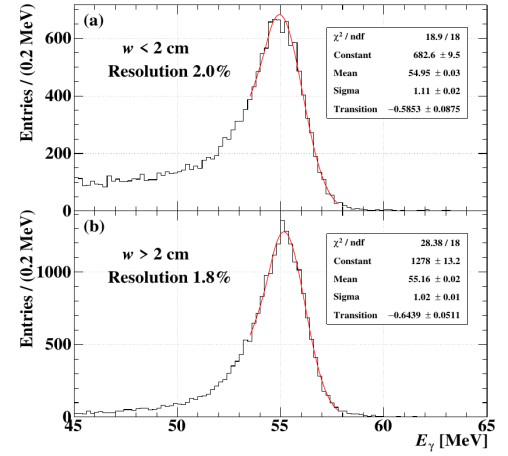
After (the only partial success of) the 2021 CEX data-taking, major upgrades were needed. We modified key aspects of the target and managed to test it before moving it to the experimental area. This step was not possible in 2021 because of safety regulations around the usage of Hydrogen.

### 6.5.1 Upgrades

**He circuit** The liquid helium circuit of the 2021 version had a design flow, namely the ‘output’ from the target was not under vacuum. This was solved by adding a section to the back side of the target, similar in design to the ‘inlet’: a beam pipe part on which an evacuated pipe was



(a) Time resolution of the XEC, obtained via the time difference of XEC and *pre-shower* fitted with a double Gaussian.



(b) Energy resolution of the XEC. The function used is Eq. 5.1.

**Fig. 6.5:** Timing (a) and energy (b) resolutions of the XEC obtained for 55 MeV  $\gamma$ s generated via the CEX. The results are for the central region of the detector ( $u \in [-10, 10]\text{cm}$  and  $v \in [-30, -10]\text{cm}$ ).

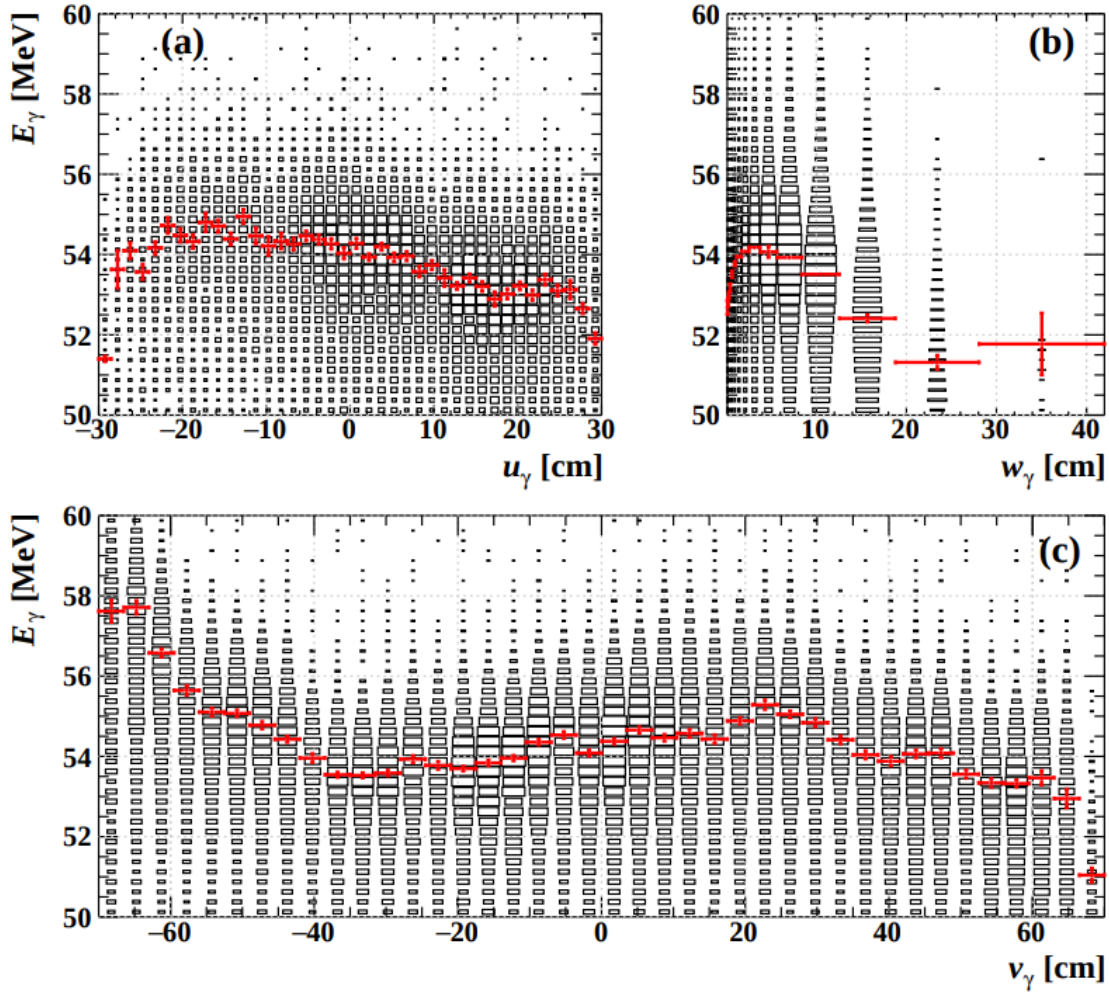


**Fig. 6.6:** Position dependence of the reconstructed 55 MeV  $\gamma$  from  $\pi^0 \rightarrow \gamma\gamma$ .

soldered such that the nozzle of the transfer line could be connected. A picture of the outlet part is in Fig. 6.9.

**Cell** Another problem of the previous design was the fact that the thermal contact between the cold copper rod and the cell was through a thick wall of stainless steel. The material is a requirement for the safe use of hydrogen, but the thickness of the back wall of the cell was excessive. The result was that, even with a very cold copper rod, this thermal contact was not enough to contrast the heat load of the cell itself. The upgraded version has a few differences from the previous one:

- The base of the cell has a thinner wall in correspondence to the copper rod, to improve the thermal contact. The thickness was chosen to be AAA mm.
- This part is brazed to a threaded copper cylinder, this allows the cell to be mounted and dismounted if needed. Another advantage is that, if the thermal connection is achieved, the surface for heat exchange is increased.

A sketch of the design and a picture of the resulting cell are in Fig. 6.7

**Shielding** To improve the stability of the system and the thermal load due to the radiation of the vacuum pipe to the cold system, two types of shielding were introduced:

- A copper sheet was bent to create an intermediate cylinder between the main copper rod and the vacuum pipe. The reason is to have this shield to an intermediate temperature and reduce the thermal radiation of the system.
- Multi-layer insulation<sup>3</sup> on the helium line, the main copper rod, and the hydrogen line. This insulation is made of alternated layers of thin metal and plastic ‘nets’ to create concentric layers at different temperatures.

Pictures of the target after adding these shieldings are in Fig. 6.9.

**Sensors** The PT100 sensors used in 2021 were not suited for very low-temperature readings but were used due to time constraints. For this reason in 2022, we added two additional sensors<sup>4</sup> from Lakeshore®. These new sensors have been screwed on the copper rod with a ring of Indium to improve the thermal connection. A picture of a mounting test of such a sensor and the additional relative feedthrough are in Fig. 6.8.

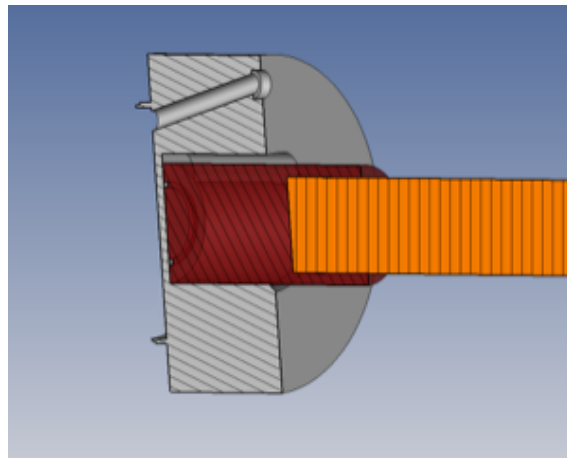
### 6.5.2 Data taking

The 2022 data taking was similar in structure to the previous: roughly two weeks of CR and CEX runs alternated given the status of the target. CEX data were collected when the target was considered ‘full enough’: below 2.1 bar, meaning 50% full. In the two weeks, this translates to efficiency of  $D_{2021} \approx 0.6$ . The hydrogen and helium pressure during data-taking is shown in Fig. 6.16b. The efficiency for 2022 was higher than the previous year and was enough to collect the necessary statistics for every patch (Fig. 6.15b). The analysis of the data collected during 2022 is still ongoing.

---

<sup>3</sup>This type of insulation is standard in cryogenic infrastructure, for example, it is used in liquid helium dewars.

<sup>4</sup>For additional info visit the [Lakeshore®](#) website.



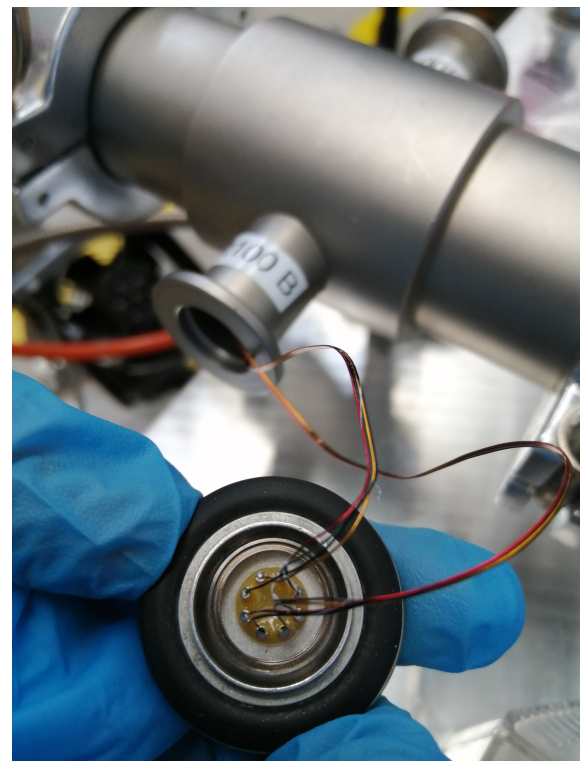
(a) Design of the new cell.



(b) Picture of the parts before brazing.

**Fig. 6.7:** A new cell was designed to be faster in the cooling/liquefaction and mountable.

(a) A test of the mounting procedure.



(b) Additional feedthrough were soldered.

**Fig. 6.8:** Pictures taken while mounting the Lakeshore® sensors.



(a) Multi-layer superinsulation was added.



(b) A vacuumed outlet was designed.



(c) Shielding was added around the whole structure.

**Fig. 6.9:** Picture of the improved heat shielding of the system. The multi-layer super insulation was added to the Cu rod (a) the outlet was designed to be under vacuum and with a nozzle of a transferring line for He (b) and the copper shielding of the whole target can be seen in (c).

## 6.6 2023

Although the 2022 CEX campaign was much more successful than the previous one, the limitations of the second iteration dictated a hectic schedule during data taking. The (somewhat risky) modification of the liquid hydrogen cup turned out to be a good improvement but there was still room for refinement. Mainly, we wanted to reduce the time/amount of liquid Helium needed to reach the liquid hydrogen status. For this reason, we went back to the drawing board. The starting idea of the design used in 2021 and 2022 was to assess the feasibility of using a long Cu rod to transport the heat with the final aim of installing a 'cold head' as a cooling mechanism. This system was proven good enough for the calibrations needed but eventually, the re-design of the system was deemed unnecessary. Once the plan of installing a cryopump was no longer on the table, we opted to adapt the current design free from the constraint of having such a long system.

### 6.6.1 Upgrade

**He circuit** The first item was to try reducing the time needed to cool the system down. In this direction, the only change on the Helium circuit was to install a new cooling coil. This was built in a similar fashion but longer (120 mm instead of 60 mm) increasing the thermal conduction between liquid helium and the main copper parts. A sketch of the new copper coil is shown in Fig. ???. On top of this change to the He circuit, we replaced the copper rod with a shorter copper cylinder, threaded on both sides, to reduce the thermal load of the system. This meant the position of the cooling coil was moved further inside COBRA, requiring longer in/out helium lines.

**Cell** Learning from the modifications done in 2022, a new Cell was produced (see Fig. ??):

- This was built with the copper connection so that it could be screwed on the copper rod
- The thermal connection with the copper was improved by making the wall thinner ( $-999\text{ mm}$  instead of  $-999\text{ mm}$ ) and having a larger copper surface, covering most of the wall (see Fig. ??)

**Shielding** The shielding also went through few changes:

- Multi-layer insulation was added to the in/out helium lines, to prevent the liquid helium from evaporating before reaching the cooling coil.
- A copper shielding was added around the cooling section
- Multi-layer insulation was added to the cell itself to improve the stability of the system

**Sensors** As already discussed, the slow control of the system is based on an SCS2000. Just like in 2022, unfortunately, we did not manage to have the Lakeshore® read by this module, meaning they were not recorded on the MIDAS page of the experiment.

In total, we had four Lakeshore® sensors:

- Two sensors were placed on the inlet and outlet of the helium line, near the cooler.
- Two were used to follow the temperature of the cell
  - one at the end of the Cu rod, to ensure the cooler-rod thermal connection
  - one on the cell, to ensure the rod-cell thermal connection

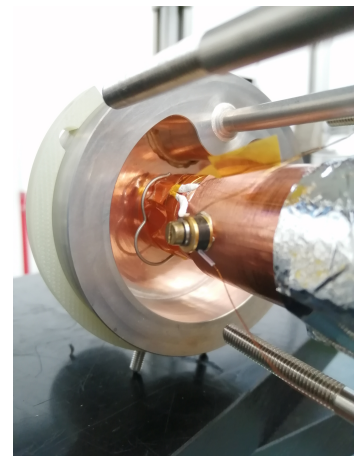
The sensors are shown in Fig. 6.10.

### 6.6.2 Tests

A few hiccups with the production and delivery of the parts forced us into a hectic schedule to ensure the proper testing of this renovated system. The main challenges were linked to a mistake in the production of the cooler, which led to unwanted thermal connections and the reproducibility of the proper thermal connection when screwing the different parts together. The first problem was solved by adjusting the assembly procedure. The second point was solved, with a bit of trial and error, using thermal grease and indium. In Fig. 6.12 the results of one of the successful liquefaction. In the plot, the azure line represents how full the cell is. The reason for the multiple drops is that the test was to reduce the Helium flux while keeping the liquid Hydrogen.

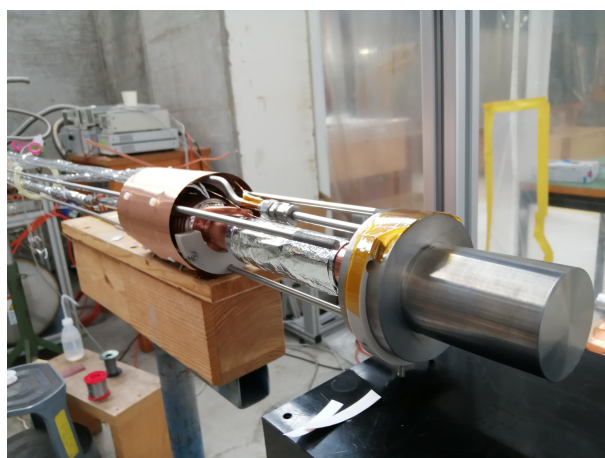


(a) The sensor have been placed on the He lines with a Cu 'clamp'.



(b) An additional sensor on the cell to ensure the thermal contact.

**Fig. 6.10:** To study the behaviour and stability of the system, additional Lakeshore® sensors were placed on the inlet/outlet He lines (a) and both on the CU rod and the cell (b). The additional sensor on the copper part of the cell, although not easy to place, allowed us to ensure the thermal connection.



(a) Picture of the 'compact' LH<sub>2</sub>.



(b) Super-insulation added on the cell.

**Fig. 6.11:** The 'compact' version of the LH<sub>2</sub> target is shown in (a), with the Cu shield on the cooler, the new vetroneite parts and the super-insulation on the different sections. An additional layer of super-insulation was placed on the cell itself (b) to reduce the heat-lode due to radiation of the vacuum pipe.

## LIQUEFACTION COMPACT 23/11/23 (250 liter dewer)

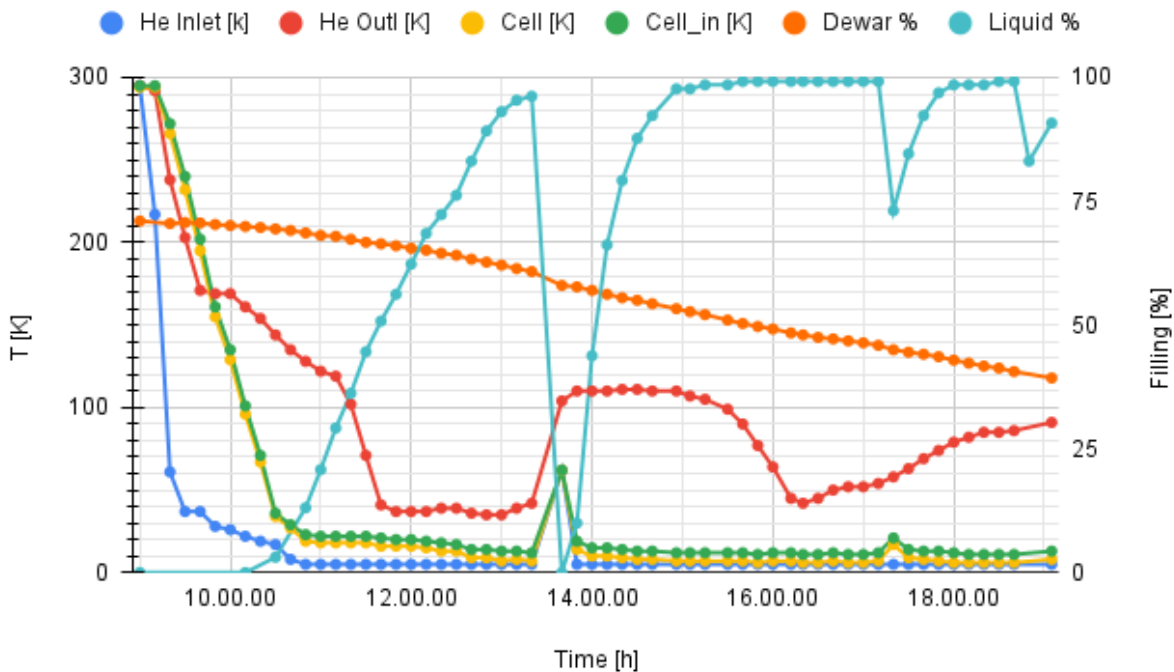


**Fig. 6.12:** This plot illustrates the outcome of a successful liquefaction process. The azure line depicts the fill level of the cell. The repeated drops in the line signify that the test aimed to decrease the Helium flux while maintaining the presence of liquid Hydrogen.

### 6.6.3 Data taking

The last test outside the experimental area was performed on the 13th Oct. 2023 and the target was installed on the 14th. The warped shape of the insertion system forced us to insert the target lower than the beam height. After managing a sufficient alignment in x and z, the target was lifted to center it vertically (y). The alignment, shown in Fig. 6.13 was performed by observing the tip of the target via the UCI camera (this item was discussed in Sec. 5.5.3) The main points of this data taking were the following:

- The cell was full (>90%) during data taking. This was unfortunately not the case in 2021 and 2022, during which we collected data when the level was >50%
  - > Higher trigger rate ( $30 \rightarrow 45\text{Hz}$ ) and better quality events, improvement of  $> \times 1.5$
- A shorter dead time after the dewar exchange: 30 mins for cooling and 2h for liquefaction
  - > Higher duty-cycle  $15 \rightarrow 20\text{h}/24\text{h}$ , an improvement of  $\times 1.3$
- We used a 250L dewar every 24h
  - > Cheaper than last year and simpler to organize

Compared to the previous years, more data were collected in a shorter period (Fig. 6.15c), marking a success for this iteration of the LH<sub>2</sub> target. At the same time, the usage of Liquid Helium, although still elevated, was much lower than in 2022. In Fig. 6.14 the comparison between the dewar usage in 2022 and 2023 (this info was lost for 2021). The analysis of the data collected is still ongoing.

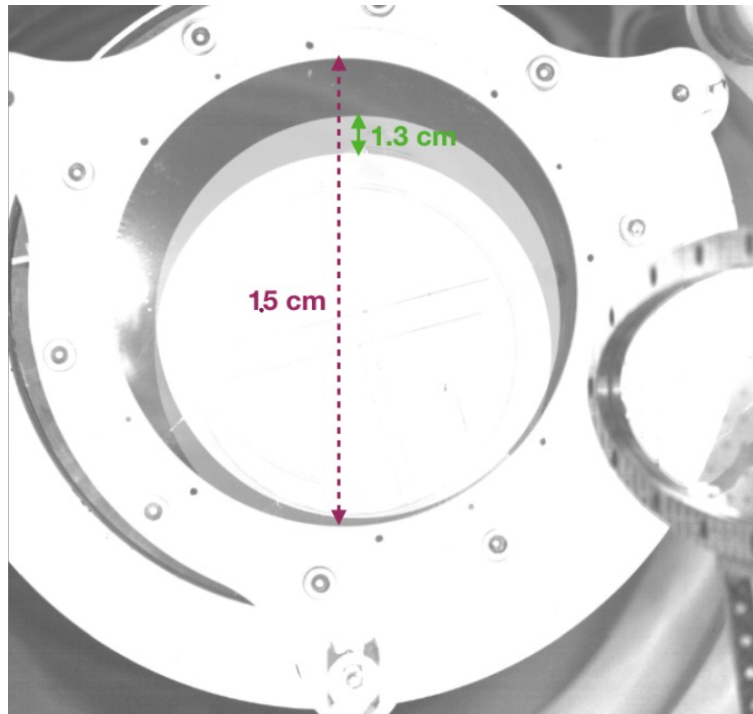


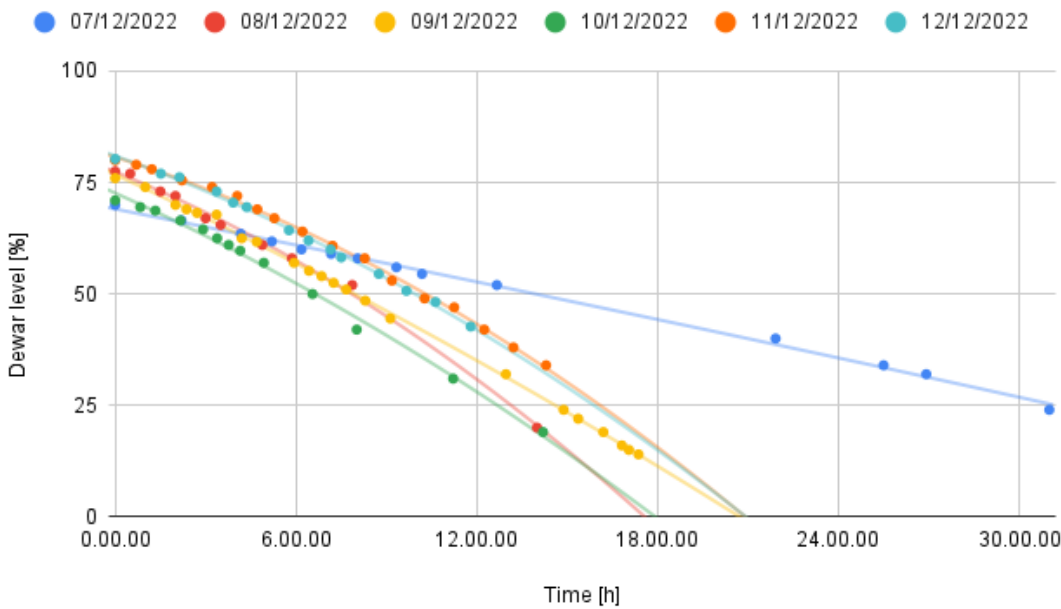
**Fig. 6.13:** After inserting the target in COBRA, it was centered (as much as possible). In red a known distance for reference, in green the displacement needed to center it. NB: the UCI pictures are upside-down.

## 6.7 Conclusions

After a recap of the task at hand, the history of the Hydrogen Target design was highlighted. As just illustrated, the duty cycle, the stability, and the level of the target improved significantly during these three years:  $D_{2021,50\%} \approx 0.55 \rightarrow D_{2022,50\%} \approx 0.6 \rightarrow D_{2023,90\%} > 0.8$ . Although minor adjustments are still planned, this will probably stay as the final design.

The development of this system has been my first (and only) real immersion in the vast subject of cryogenics. Many things were quite new to me, from the materials' thermal properties to the inner structure of a Helium dewar and from the working principle of low-temperature sensors to the CAD design of peek/vetronite parts required for structural stability and thermal insulation. Although being still far from any shade of *expertise*, this has been quite an eye-opening endeavor.

### Dewar usage during CEX 2022: 450L dewars



### Dewar usage during 2023 CEX: 250L dewars

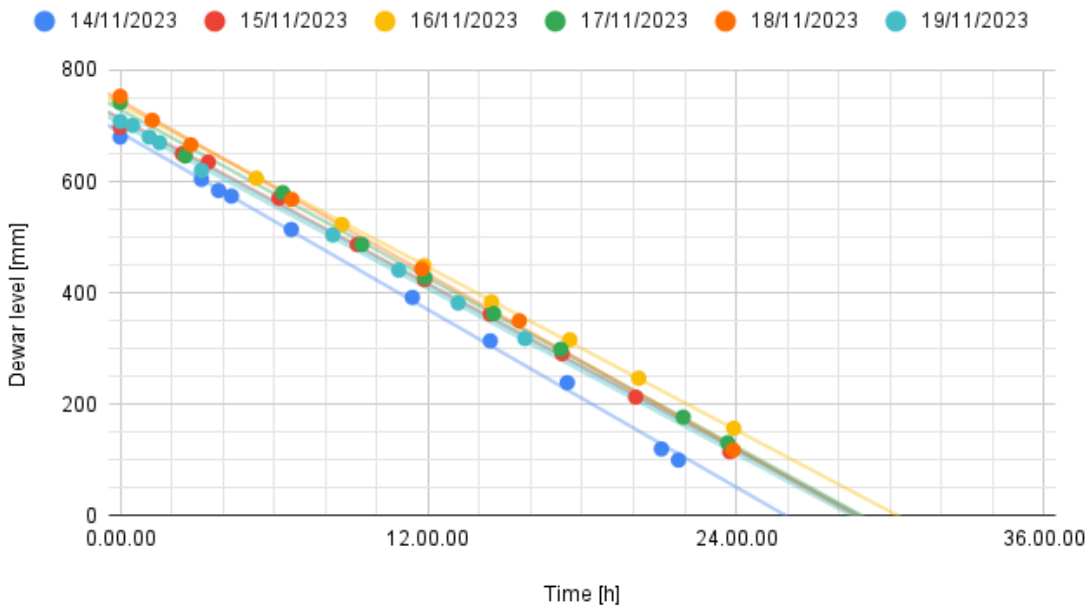


**Fig. 6.14:** Comparison of the dewar usage in 2022 and 2023. While the general trend during 2023 has been much better than in 2022, a spurious day of data-taking in 2022 was particularly efficient. The reason is unfortunately no clear and the condition hard to reproduce.

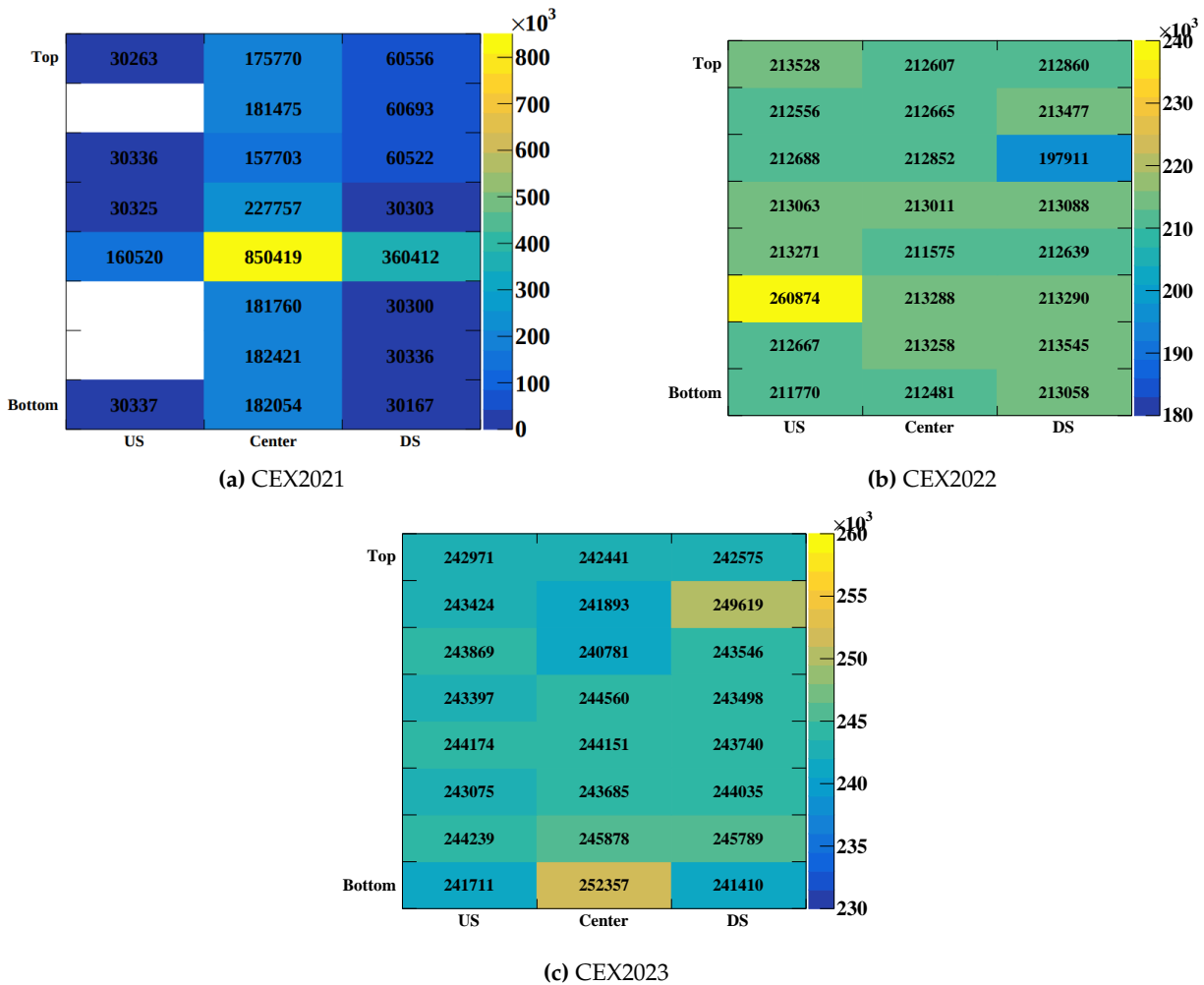
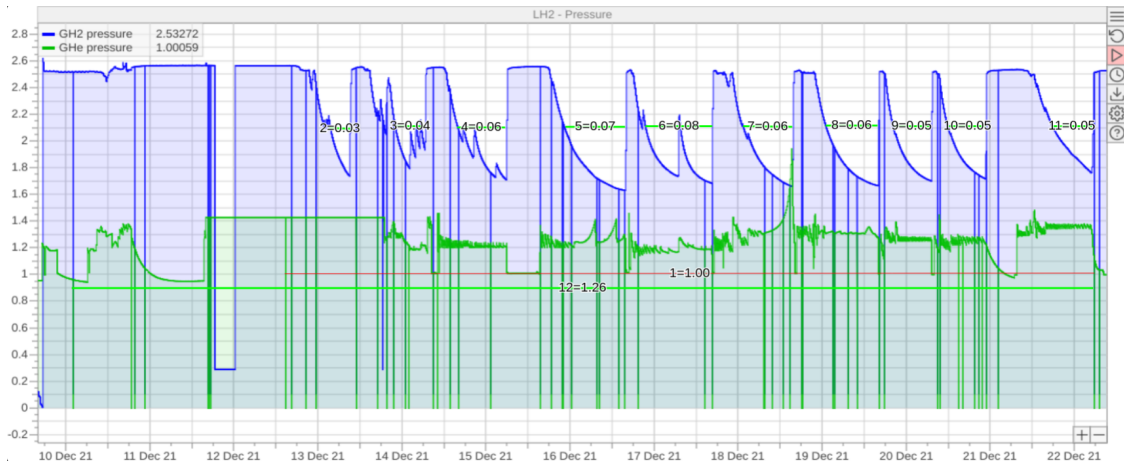


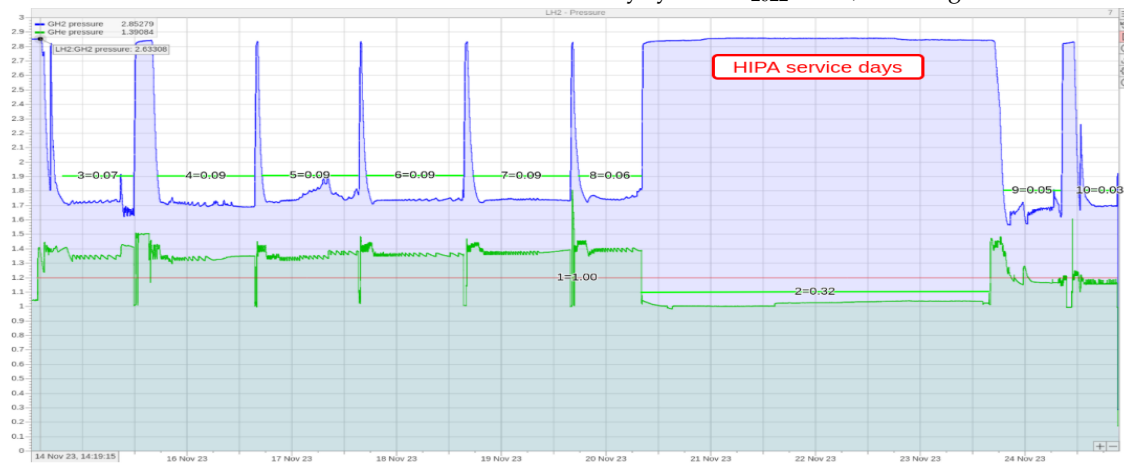
**Fig. 6.15:** Number of triggered events during Charge EXchange data taking in 2021 2022 and 2023. Notice the lack of events in 3 patches in 2021 due to the low dutycycle of the LH2 target. For 2022 and 2023, the required statistics was collected and exceeded.



(a) CEX 2021: beam below 2.1 bar. This translates to a duty cycle of  $D_{2021} \approx 0.5$ , with target level  $> 50\%$ . The low efficiency prevented the collection of the necessary statistics for every patch.



(b) CEX 2022: beam below 2.1 bar. This translates to a duty cycle of  $D_{2022} \approx 0.6$ , with target level  $> 50\%$ .



(c) CEX 2023: beam below 1.9 bar. This translates to a duty cycle of  $D_{2023} > 0.8$ , with target level  $> 90\%$ .

**Fig. 6.16:** Measured hydrogen pressure in the target and helium pressure in the dewar used for cooling during the different CEX data takings. The beam was ON (red line) when the target was considered ‘full enough’. This value changed as a consequence of the different upgrades of the target and was evaluated by measuring the XEC trigger rate.

# Bibliography on LH<sub>2</sub>

- [1] D. Stäger. "Scintillation Detector Research for Experiments Probing Beyond Standard Model Physics". PhD thesis. Swiss Federal Institute of Technology (ETH), 2023.
- [2] B. Vitali et al. "A liquid hydrogen target to fully characterize the new MEG II liquid xenon calorimeter". In: *Nucl. Instrum. Meth. A* 1049 (2023), p. 168020. DOI: 10.1016/j.nima.2023.168020.

# Chapter 7

## Search for X17

After the recent publications from the ATOMKI collaboration, the so-called X17 anomaly piqued the interest of the community. The flexibility of the MEG II apparatus allows for a variety of exotic searches and the collaboration deemed of interest searching for this anomaly in an uncorrelated way. The chapter starts with a recap of the previous searches and then moves to the description of this search in MEG II: setup used, simulations developed, data acquisition, and data analysis.

### 7.1 ATOMKI and the X17 ‘anomaly’

In recent years, the nuclear reaction  ${}^7\text{Li}(\text{p}, \text{e}^-, \text{e}^+) {}^8\text{Be}$  peaked the physics community’s interest. The reason is, in 2016 the Atomki laboratory reported an excess in the angular distribution of the pairs  $\text{e}^- \text{e}^+$  coming from the Internal Pair Creation (IPC) [1]. The significance found was  $\approx 7\sigma$  and similar results were later obtained. The current hypothesis is the creation of a  $17 \text{ MeV}/c^2$  boson (hence the name), associated with the interaction of dark and ordinary matter. A good review of the status for the searches of this anomaly is in [2].

#### 7.1.1 The process

The proton on Lithium reaction shows two distinct resonances [3], as illustrated in Fig. 7.1. The first is at a proton energy of  $E_p = 441 \text{ keV}$ , leading to a  $17.64 \text{ MeV}$  excited state. The second, for  $E_p = 1030 \text{ keV}$ , rising to the  $18.15 \text{ MeV}$  state. The energy state levels are shown in Fig. 7.2. Both excited Beryllium states can emit a photon, which can later convert into a  $\text{e}^- \text{e}^+$  External Pair Conversion (EPC), or a directly a  $\text{e}^- \text{e}^+$  pair ( $BR \approx 3.9 \times 10^{-3}$ ), hence an Internal Pair Conversion (IPC). In addition to the ground level, both can also decay in the first excited level, at  $E = 3.03 \text{ MeV}$ . The relative fraction of these processes is shown in 7.2b and details on the energy levels can be found in [4]. In total, we have four possible transitions from the  $17.64 \text{ MeV}$ <sup>1</sup> and four from  $18.15 \text{ MeV}$ <sup>2</sup>. On the practical side, we can talk of IPC15, EPC15, IPC18, and EPC18.

---

<sup>1</sup>EPC(17.64), EPC(14.61), IPC(17.64), IPC(14.61)

<sup>2</sup>EPC(18.15), EPC(15.12), IPC(18.15), IPC(15.12)

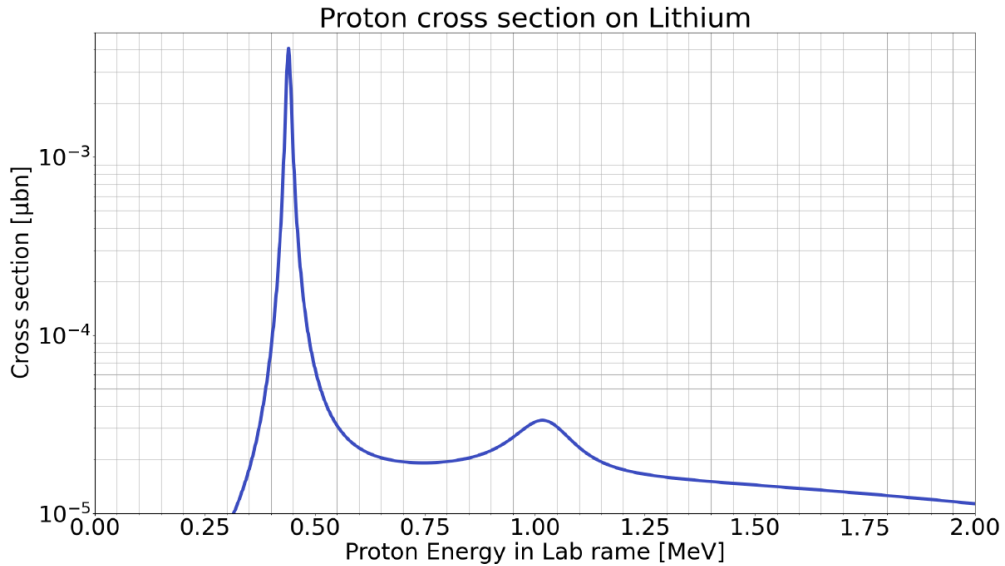
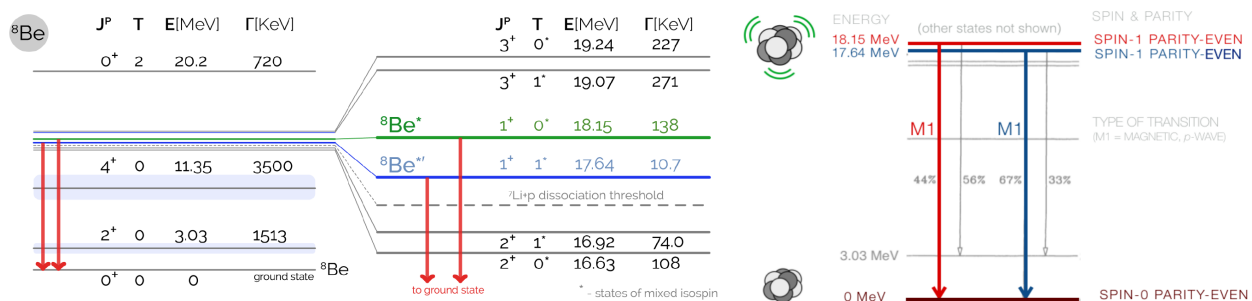


**Fig. 7.1:** Shape of the cross-section as a function of the proton energy [3] with two resonances.



**(a)** The first resonance occurs at a proton energy of  $E_p = 441 \text{ keV}$ , leading to a  $17.64 \text{ MeV}$  excited state, while the second resonance, observed at  $E_p = 1030 \text{ keV}$ , results in the  $18.15 \text{ MeV}$  state.

**(b)** Additionally to the ground level, both states can decay to the first excited level at  $E = 3.03 \text{ MeV}$ .

**Fig. 7.2:** The proton-Lithium reaction exhibits two distinct resonances, shown in Fig. 7.1 [3] and different transitions [4]. The relative fractions of these processes are illustrated in Fig. 7.2b.

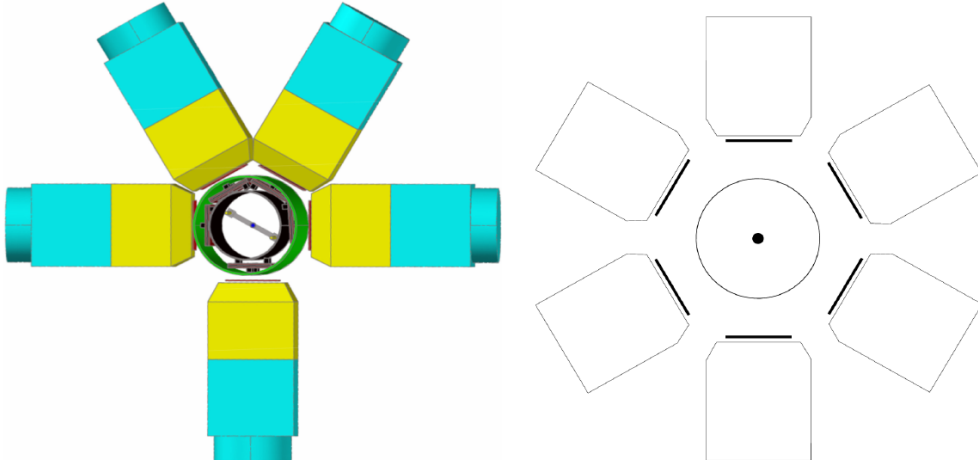


**Fig. 7.3:** The planar geometry is the one chosen in all searches to date. In both versions, the energy is measured with plastic scintillators while the position is measured with a multi-wire proportional chamber, later upgraded to double-sided silicon strip detectors.

### 7.1.2 The results

What the ATOMKI collaboration found was an excess at  $\sim 140$  deg in the IPC. The initial result yielded an invariant mass of  $M = 16.70 \pm 0.51$  MeV [5], later refined to  $M = 16.94 \pm 0.12 \pm 0.20$  MeV [2]. These results were confirmed studying the  ${}^3\text{H}(\text{p}, \gamma){}^4\text{He}$  and  ${}^{11}\text{B}(\text{p}, \gamma){}^{12}\text{C}$ .

After these results, Zhang and Miller [6][7][8] improved the reaction model to predict the cross sections. Unfortunately, this model could not explain the excess.

The latest entry was the preliminary result by the University of Sciences in Hanoi [9]. Unfortunately, all these studies have the same limitation: the measurements were done with a planar configuration, on the plane perpendicular to the proton beam, as shown in Fig. 7.3. A study with wider acceptance is required [2], and this was what sparked the MEG II interest.

## 7.2 X17 in MEG II

After reading with great interest the papers from ATOMKI, the MEG collaboration started evaluating if repeating this measurement was achievable with the MEG II apparatus. In 2022 the first data collection was performed but the time constraints, required to keep the main focus of the experiment on  $\mu \rightarrow \gamma e$ , meant not all the necessary preparatory studies could be performed. The details of this first data-taking will be skipped and we will move directly to the second campaign, performed in 2023. To be underlined is that this first campaign was cardinal in the rapid development of the tools required for the rest of the search: MC simulation, triggers, and analysis. Through the analysis of the data collected in 2023 some upgrades are ongoing and more data will be collected in 2024.

### 7.2.1 Magnetic field choice

The first step is to identify the magnetic field required. The geometry of the MEG II detector, in junction with the magnetic field, defines the acceptance of the produced particles. Given the nature of the COBRA magnet, the parameter here is the scaling of the magnetic field. Thorough



**Fig. 7.4:** Construction of the carbon fiber vacuum chamber and picture of the copper arm used to hold the targets and of the internal structure of the chamber.

simulations were run to optimize the scaling factor, finding the best compromise between the efficiency for signal and background reconstruction to be  $B_{X17} = 0.15 \times B_{MEG}$ . This value can be roughly estimated considering that a scale factor of 1 is optimized for positrons of 53 MeV while the pair produced by the X17 decay should be roughly at 8 MeV ( $8/53 \approx 0.15$ ). In reality, the hypothetical X17 would be produced with a boost, placing the energy of the pair particles in the range [5.9, 12.2] MeV. In 2022 and 2023 data were collected at 15% 16% and 17% and the optimal value was found to be the first. This translates to an energy acceptance [ $\sim 7.5, \sim 10.8$ ] MeV.

### 7.2.2 Target

The setup for the target has been optimized with dedicated studies [10]. The final design is quite straightforward: a carbon fiber vacuum chamber mounted at the tip of the insertion system of the CW bellows system; a mounting system, made of copper, holds different types of targets at 45 deg. The bellows system is the one used for XEC weekly calibrations and will be not discussed.

**Vacuum and mechanical structure** The thickness ( $400\text{ }\mu\text{m}$ ) and diameter (13 cm) of the carbon fiber vacuum chamber have been optimized via dedicated simulations for both integral structure and particle interaction. After receiving the carbon fiber, the chamber was glued to an aluminum flange and end-cap, with three stainless steel rods and three acrylic rings to reinforce the structure, and tested for vacuum. This setup is shown in Fig. 7.4. The mechanics of holding the target itself is also shown and it is made of copper. The reason for using this material is to improve the dissipation of the heat generated by the beam on the target. This, unfortunately, means a good percentage of the transition leading to a photon (meaning not an IPC) will generate an external pair (EPC) when the photon interacts with the copper. This contribution is bigger at lower angles, meaning IPC are the one dominating the region of interest. To reduce the contribution from EPC, the copper ring holding the target was later made thinner.

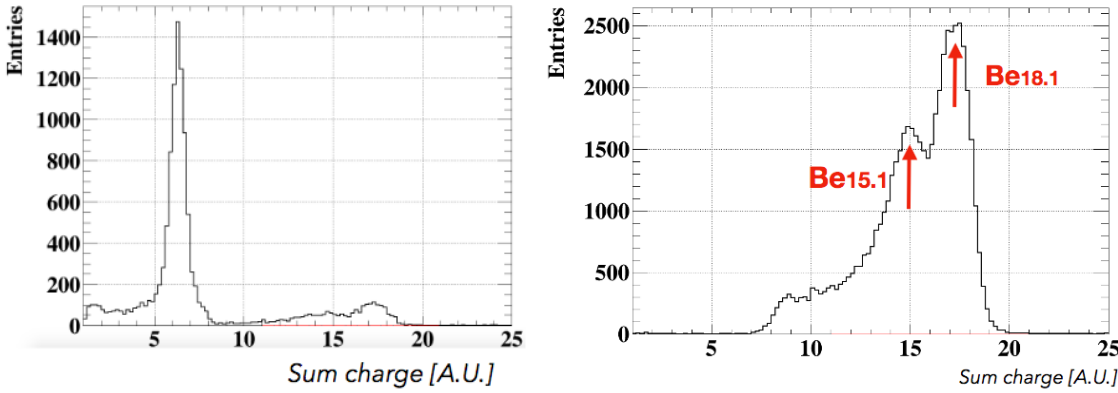


**Fig. 7.5:** BGO spectrum for  $E_p = 500$  keV with LiF target (left) and for  $E_p = 1080$  keV LIPON target (right).

**Lithium targets** The interesting process requires Lithium atoms but Lithium targets tend to be unstable. Among the options studied, LiF and  $\text{Li}_{3.6}\text{PO}_{3.4}\text{N}_{0.6}$ <sup>3</sup> were the most promising, both on Cu substrate. LiF targets were produced by INFN Legnaro while LiPON targets were produced at PSI. Looking back we now know that the spattering process behind the production of the LiPON targets resulted in a poorly characterized end-product (more on this in a following section). Some data were acquired using the LiF target, but the Fluorine has resonances  $^{17}\text{F}(\text{p}, \alpha\gamma)^{16}\text{O}$  at 6.13 MeV, 6.92 MeV, and 7.12 MeV with a cross-section much higher than the one of the Lithium []. This meant that the events of interest were hidden by the F resonance. For this reason, the collaboration opted for LiPON. Some spectra taken with the BGO for both targets are in Fig. 7.5.

### 7.2.3 MC simulations

To develop a complete simulation, the obvious decision was to implement the details in the pre-existing MEG II simulation. This is GEM, based on GEANT4, which returns the detector responses to the physics event. After that, the *bartender* converts the simulation into realistic waveforms, to be analyzed with the standard MEG II hit reconstructions. The track-finding algorithms and trigger strategies can be then tested on realistic events. The core aspects of the simulation are:

- The 15 MeV line is simulated with 3 MeV width, while the 18.1 MeV is monochromatic
- The excited beryllium is at rest
- Isotropical decay in the rest frame of the X17 ( $M = 16.7 \text{ MeV}/c^2$ )

While IPC and X17 can be easily generated, EPC are more challenging because the particle generated is the  $\gamma$  which then converts. The aim for the MC statistics is to produce:  $2 \times 10^5$  X17,  $10^6$  IPC18,  $10^6$  IPC15, and  $10^9$   $\gamma$  to generate EPC. In the following, the MC data will be the one produced in July 2023.

**IPC** IPC events at 18 MeV and 15 MeV are simulated in the following steps: Proton energy loss follows a Gaussian distribution, with mean and standard deviation determined from GEANT4 simulations; the interaction depth of the proton is generated based on the randomly obtained energy loss; the IPC spectrum is generated using the Zhang-Miller cross-section, which includes non-resonant proton direct capture; the transition energies are generated separately. Zhang-Miller

<sup>3</sup>The fraction of the different atoms depends on the production process, which in this instance was *sputtering*. These were the values measured for the target produced at PSI.

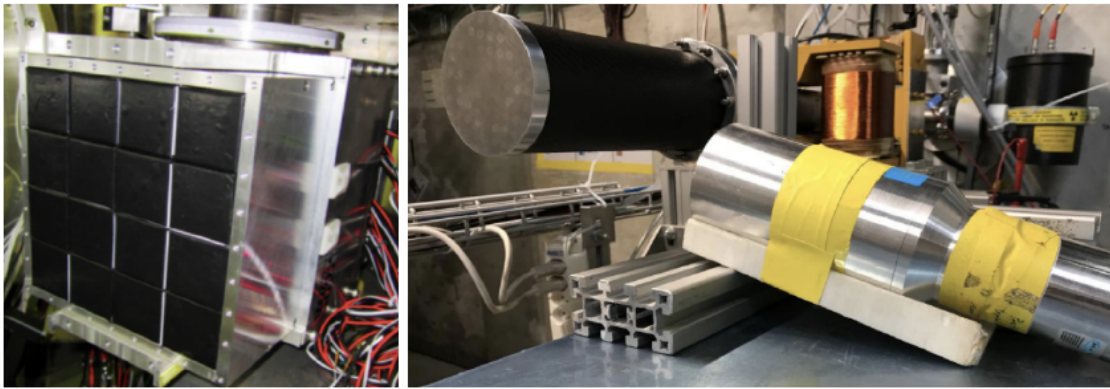


**Fig. 7.6:** Pictures of the auxiliary detectors: BGO, on the left, and Brillance, on the right.

model, originally for the 18.15 MeV transition, is also applied to the 15.12 MeV transition, introducing additional uncertainty. The cross-section parameters are determined using old photon data and may benefit from updated measurements.

#### 7.2.4 Data acquisition(s)

We went through different data-taking periods. The first was at the end of 2022 and lasted 3 weeks while the second was in Feb. 2023 and lasted 4 weeks. During the first period, we collected data used to develop the MC simulations, event reconstruction, and optimize the trigger. At this stage, the understanding was only partial but we deemed it sufficient to collect useful data as an intermediate step. The second period was the main data acquisition. A short data-taking in May 2023 followed to collect some photon spectra with the XEC. Additional studies were performed in Nov. 2023 and Feb. 2024. These last two will be discussed later.

**Setup** Although this search is done with the MEG II apparatus, some minor changes should be underlined. The X17 data were collected while the MEG II acquisition was not ongoing. This means it was in parallel with the maintenance of the XEC, which was undergoing annealing to recover MPPC PDE. For this reason, we relied on two auxiliary detectors, shown in Fig. 7.6: the BGO and an additional 3-inch Lanthanum Bromide crystal ( $\text{LaBr}_3$  ‘Brillance’), both read by PMTs. We also took data with the BGO in different positions to study the asymmetry of the spectra.

**Beam tuning** The beam tuning was performed by substituting the end cap of the proton beam line with a transparent cap with a quartz crystal. The proton beam produces visible photons hitting the crystal so the beam position can be observed. Normally this operation would be done while the upstream side of COBRA is not closed, allowing the installation of a webcam that gives instant feedback on the beam position. This was not the case so we were forced to use the camera installed inside COBRA for MEG II target monitoring. This camera has some settings for *gain* and *aperture* but is controlled using a script in *ssh* and to view the picture first is necessary to move them locally, making the whole procedure somewhat cumbersome. Key aspects of the tuning:

- Energy: This parameter is controlled by the *Terminal Voltage* of the CW.
- Position: This parameter is controlled by the three dipoles of the CW beamline. The change of the position for different values of the dipoles at 500 keV is shown in Fig. 7.7.

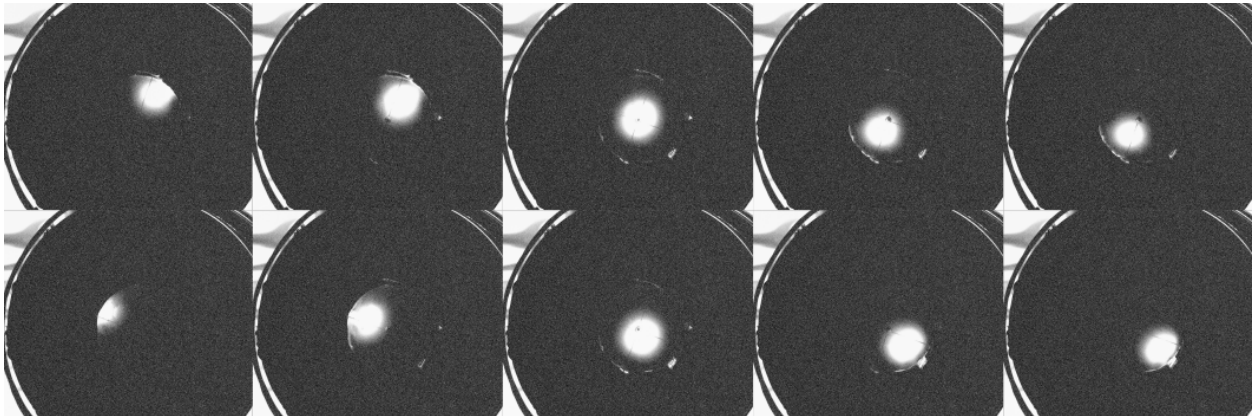


**Fig. 7.7:** Position of the proton beam at 500 keV when changing the current in the dipoles (the vertical dipole V and only one of the two horizontal dipoles H). In the first row, H is changing and the beam moves diagonally. In the second row, V moves the beam on the perpendicular diagonal.

- Focus: This parameter is controlled by the *Extraction Voltage* of the CW. Fig. 7.8 shows how the beam spot changes as a function of this parameter.

After a careful scan, working points at different energies were chosen: the most relevant are the ones for 500 keV and 1080 keV. It is of interest to notice that 1080 keV is the balance between what was previously discussed and the limitations of the CW machine: a higher ( $\sim 1100$  keV) energy would be a better choice but the nominal upper limit of the machine is 1 MeV, meaning having it running stably at 1080 keV is already an achievement. To the best of our knowledge, the beam at COBRA center during data-taking was  $(x, y) = 2, -2$  mm;  $(\sigma_x, \sigma_y) = 2, 2$  mm.

After the first tuning, these parameters were used for the different data-takings. In Sec. 7.5 we will see why this beam-tuning had a fundamental flaw, linked to the presence of  $H_2^+$ .

**Trigger and Rates** The X17 trigger developed requires 18 hits on both CDCH ends<sup>4</sup> and at least one hit in the pTC. At the same time, BGO, Brilliance, pTC single, CDHC Track, and pedestal trigger were acquired, with a prescale factor. A comparison between the trigger rate in data and MC has been made for a proton current of  $6\mu\text{A}$ . At this current, X17 trigger rate is about 30 Hz on data. Based on measured gamma rates on BGO (60 kHz), trigger efficiencies estimated from simulation (0.039% and 6.5% for EPC and IPC respectively), and the IPC BR (0.0032), the background rates can be estimated. It is found that expected trigger rates are 23 Hz and 12 Hz for EPC and IPC respectively, for a total rate of about 35 Hz, in fair agreement with the measured 30 Hz at  $6\mu\text{A}$ .

### 7.3 Data analysis

My contribution to the data analysis was only partial so I will not go into much detail. Even so, at least a broad overview of the analysis status at the time of writing is in order. Most of the studies on event reconstruction and quality cuts were performed by Hicham Benmansour, while the Likelihood analysis was developed by Giovanni Dal Maso [11]. I contributed in different aspects but mainly during the development of the Likelihood analysis and BGO analysis.

<sup>4</sup>Unfortunately, at trigger level we cannot match the same wire on both sides

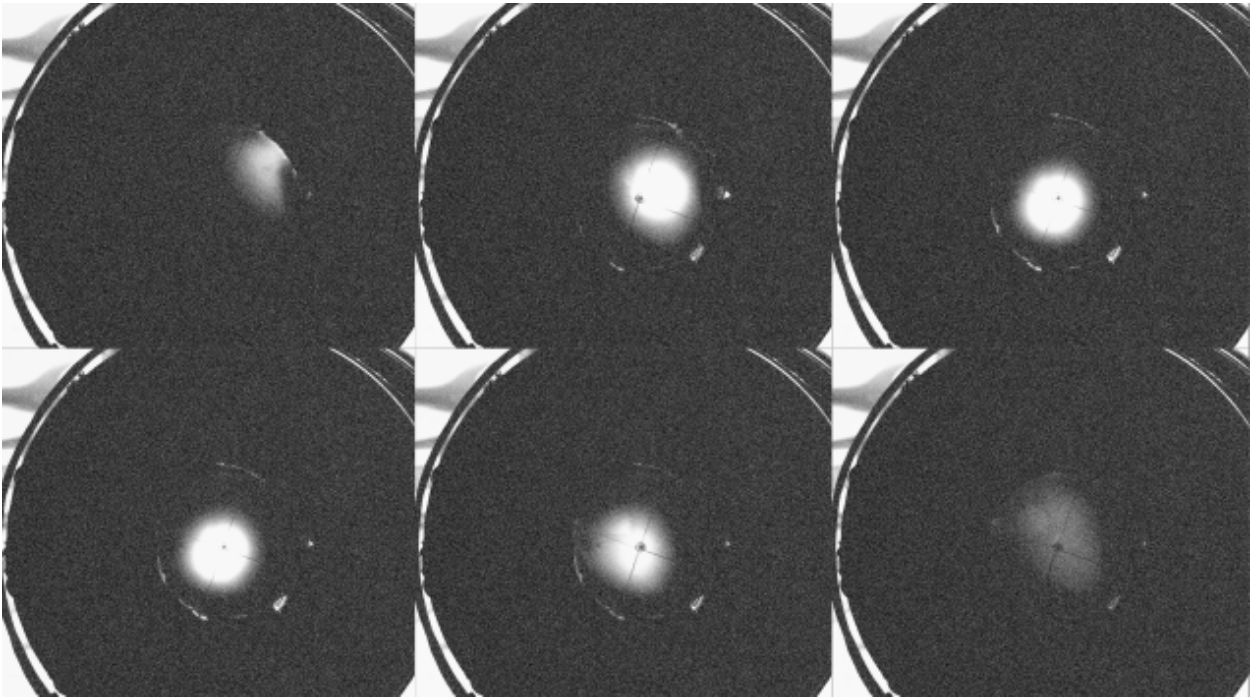


**Fig. 7.8:** Focus of the proton beam at 500 keV when changing the *extraction voltage* of the CW: values in the range  $6 \div 15$  keV. Is clearly visible for extreme values the beam barely reaches the crystal.

### 7.3.1 Pair reconstruction

The first step for this search is to correlate particles and create  $e^-e^+$  pairs. This is not a given in an experiment that was developed for a different task, namely reconstructing  $e^-$  and  $\gamma$ . The idea was, of course, to adapt the existing reconstruction code to the new aim.

**B inversion** As well known, particles of opposite charge behave symmetrically in the same B field. This means the  $e^-$  reconstruction in  $\mathbf{B} = B\hat{z}$  is equivalent to reconstructing a  $e^+$  in  $\mathbf{B} = -B\hat{z}$ . This is a simple change to apply to the reconstruction code but holds only in the assumption the two particles behave in the same way while interacting with the different parts of the experiment.

**Track selection** A series of quality selections is applied to single tracks. The purpose is to reject tracks that are reconstructed with the incorrect sign. These tracks, called *fake*, are often short or have low hit density and are often close to COBRA center at  $z = 0$ . Fig. 7.9 shows the requirements for the number and quality of hits while Fig. 7.10 shows the effectiveness of the final selection in reducing the fake pairs to a more simple selection in X17 data ( $E_{sum}$  side-band region, as defined in 7.3.5). The requirements are:

- successful propagation of the track to the beam axis;
- at least 10 good hits (ngoodhits) on track;
- if  $11 \leq \text{ngoodhits} \leq 16$ , track hit density should be  $> 1.1$  hits/cm;
- $|z_{vertex} - z_{beamspot}| < 2.5$  cm,  $z_{vertex}$  being the z coordinate of the point of closest approach to the beamline and  $z_{beamspot}$  the best estimate of the z coordinate of the beam spot on target;
- time order in the hits  $T_{0,\text{lasthit}} > T_{0,\text{firshit}}$ ;
- $(z_{lasthit} - z_{firshit}) \times z_{firshit} > 0$ , to ensure the track goes away from the target;

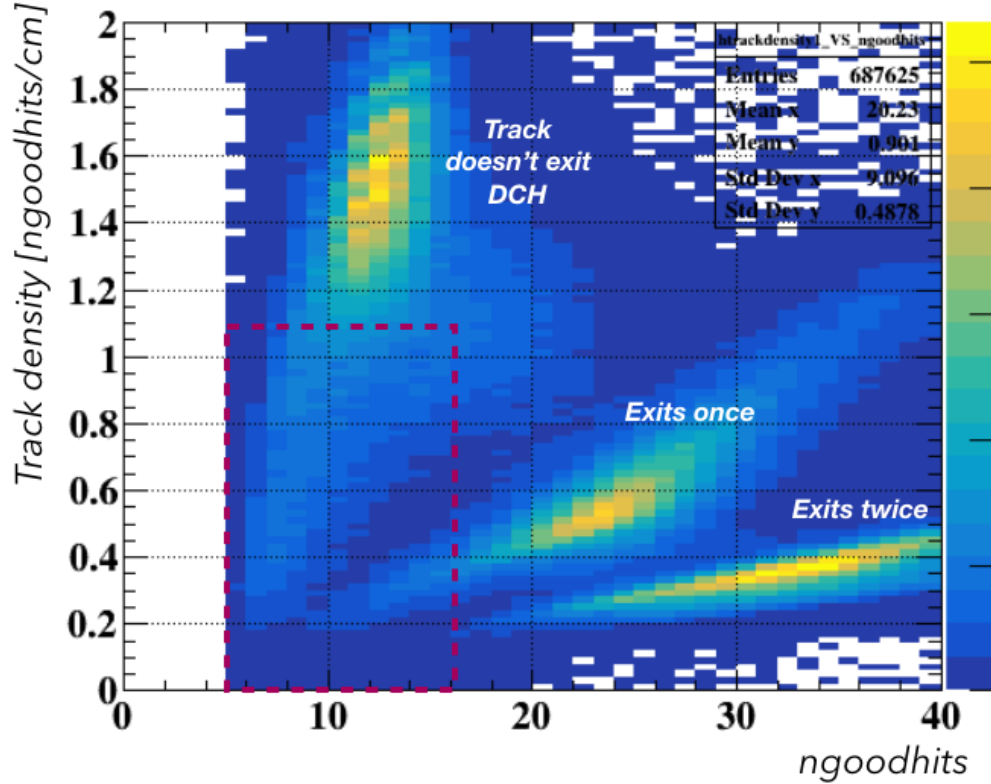


**Fig. 7.9:** Track density vs ngoodhits. Three types of tracks can be observed with increasing ngoodhits and decreasing density, tracks not exiting the chamber, tracks exiting it once and tracks exiting twice. The poorest quality tracks, in the red dashed rectangle, are rejected.

- distance 1<sup>st</sup> hit to vertex smaller than 35 cm, to ensure the first turn is not missed;
- half-turn tracks (tracks which never exit the chamber) should have a hit density > 0.8 hits/cm and a track score > 20, track score being defined as ngoodhits + 10 × track hit density;
- $|z_{firsthit}| > 2.5$  cm;
- no hits with opposite  $z_{hit}$ ;
- each half-turn should have a standard deviation for the consecutive hits distance below 0.9 cm (to ensure most hits are included in the track fit);
- $|z_{mean}| > 2.0$  cm,  $z_{mean}$  being the average of  $z_{hit}$  for all good hits (to ensure the track is far enough from the target);
- $z_{mean} \times (\theta - 90^\circ) < 0$ .

**Pair selections** For events where at least one positron track and at least one electron track pass the previous selection, pair selection criteria are applied:

- the e<sup>-</sup>/e<sup>+</sup> tracks should have no hits in common, to ensure no track is reconstructed with the wrong sign-
- the distance between the vertices of both tracks should be  $\leq 3$  cm.

**Track and pair efficiencies** When considering the whole reconstruction, the efficiency for the different types of events is summarized in Table 7.1 and Fig. 7.11 shows the total efficiency on X17 events (trigger, acceptance, and reconstruction efficiency) as a function of the angle of the reconstructed X17 momentum direction to the beam axis.

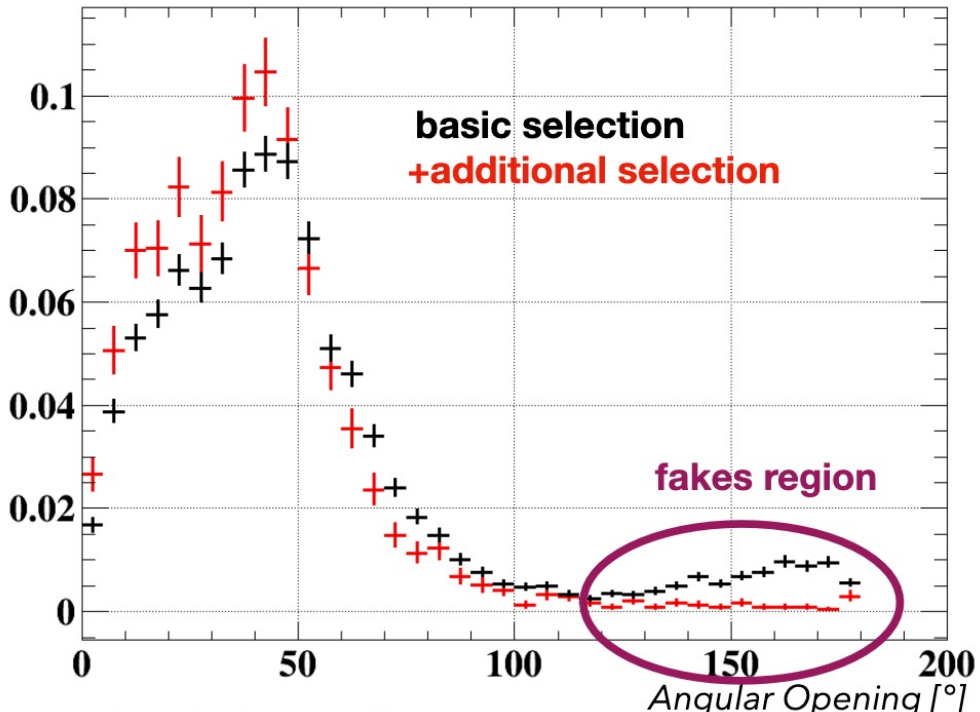


**Fig. 7.10:**  $E_{sum}$  distributions for the X17 data ( $E_{sum}$  sideband region, as defined in 7.3.5) before (black dots) and after (red dots) the cuts specific for removing fake pairs, described in the text.

	signal	IPC 18 MeV	IPC 15 MeV	EPC 18 MeV	EPC 15 MeV	data
trigger selection	14%	4.5%	3.9%	0.032%	0.027%	100%
positron track selection (wrt trg)	38%	37%	33%	27%	21%	8%
pair selection (wrt trg)	9%	8%	5%	5%	0.4%	1.4%

**Tab. 7.1:** Efficiency of the different reconstructions.

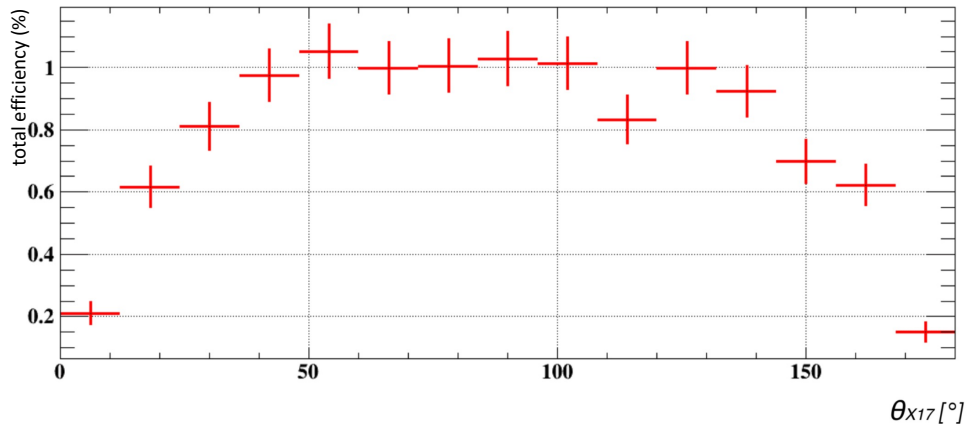


**Fig. 7.11:** Total efficiency on X17 events (trigger, acceptance, and reconstruction efficiency) as a function of the angle of the reconstructed X17 momentum direction to the beam axis.

### 7.3.2 Angular corrections

Due to multiple scattering in the air between the target and CDCH, some tracks are reconstructed far ( $\sim$ cm) from the true vertex, this can be improved by studying the correlation between the reconstructed vertex position and the reconstructed momentum direction. Fig. 7.12a and 7.12b show the correlation between the residuals of the polar and azimuthal angle, as a function the residuals on the x, y, z coordinates, on MC. A strong correlation can be observed (and linearly correct) in the residuals of the polar angle vs the residuals of the z coordinate, as well as in the residual of the azimuthal angle vs the residuals of the x coordinate. The true value of x and z can be approximated to be zero. Fig. 7.13 and 7.14 show the effect of the correction in the opening angle and invariant mass resolutions for IPC18 and X17 MC events.

### 7.3.3 Vertexing

To improve the  $E_{sum}$  and  $\theta_{rel}$  resolution, a vertex fit has been introduced using the positron and electron state vertex at the z-axis POCA and the beam spot information. The procedure is:

- all tracks are fitted separately to the z axis POCA
- the best positron and electron tracks are selected
- the common vertex is searched with a beam spot constraint using the tool RAVE (Reconstruction in Abstract Versatile Environments), supported in GENFIT [12][13]. The beam spot constraint is defined as (x,y,z) coordinates plus the invariant matrix with  $\sigma = 3$  mm.

Fig. 7.15 shows the comparison in the opening angle resolution for IPC18 and X17 MC with and without vertexing, obtaining a 25% improvement in the core resolution of a double Gaussian.

### 7.3.4 Beam spot

Fig. 7.16 shows the distributions of the reconstructed vertex at the target for positrons and electrons, on X17 data. It can be noted that the vertices are off-center by 7 mm and the positron and electron vertices distributions are shifted versus one another. On MC, IPC vertices are correctly reconstructed (within 1 mm) while EPC vertices are reconstructed with a systematic shift toward negative y (most likely from the gamma anisotropy and a bias from the trigger) and there is a shift between positrons and electrons. The beam spot position on data has been determined according to the following procedure: the x coordinate was extracted from an IPC-enriched data sample at a low opening angle; the y coordinate was determined by fitting the data y distribution to the MC distribution where a 60%-40% proportion has been assumed for EPC/IPC. The fit is shown in Fig. 7.17. The values obtained are  $(x, y) = -2, -3$  mm;  $\sigma_x = \sigma_y = 3$  mm.

### 7.3.5 Blinding strategy

A blinded signal region has been defined according to the following conditions:  $E_{sum} \in [16 \text{ MeV}, 20 \text{ MeV}]$  and  $\theta_{rel} \in [115^\circ, 160^\circ]$ . Fig. 7.18 shows, in the  $E_{sum}$  vs  $\theta_{rel}$  plane, the blinded signal region together with the relative angle sideband ( $16 \text{ MeV} < E_{sum} < 20 \text{ MeV}$  and  $0^\circ < \theta_{rel} < 115^\circ$ ) and the  $E_{sum}$  sideband ( $14 \text{ MeV} < E_{sum} < 16 \text{ MeV}$  and  $0^\circ < \theta_{rel} < 180^\circ$ ).

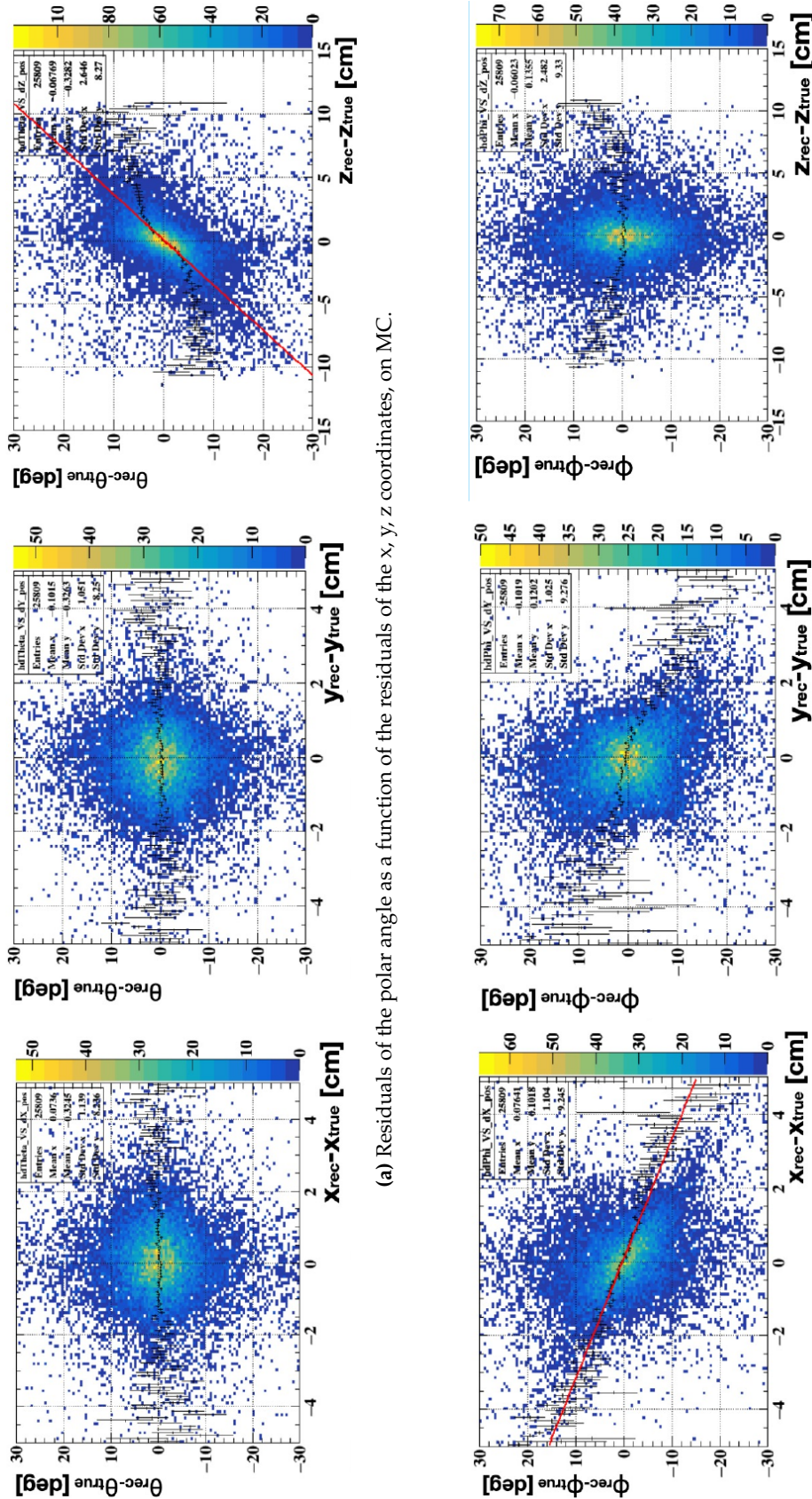


**Fig. 7.12:** The correlation of vertex displacement and momentum direction are modeled and corrected.  
 (a) Residuals of the polar angle as a function of the  $x, y, z$  coordinates, on MC.  
 (b) Residuals of the azimuthal angle as a function of the residuals of the  $x, y, z$  coordinates, on MC.

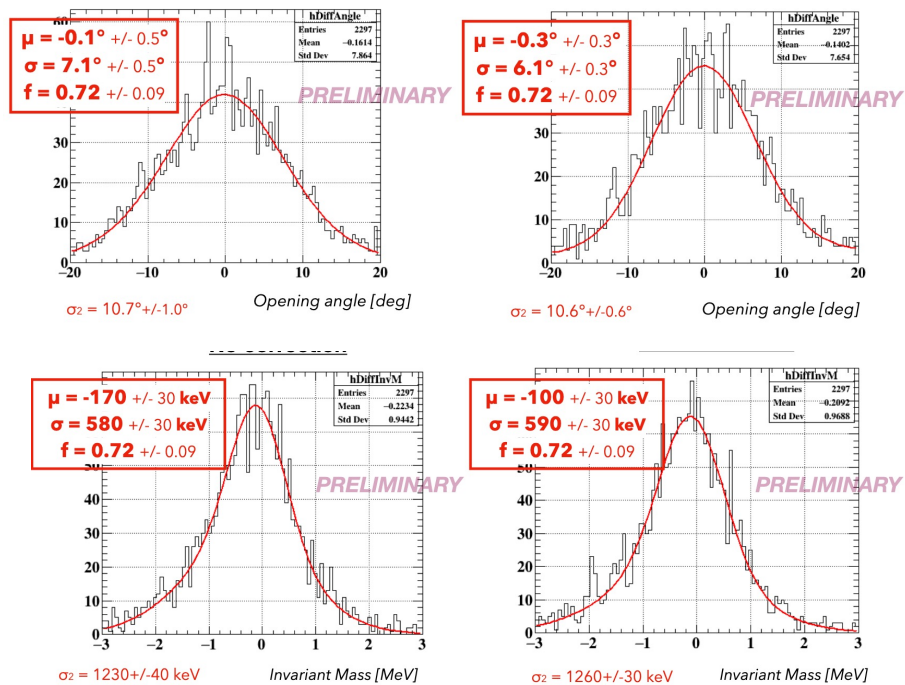
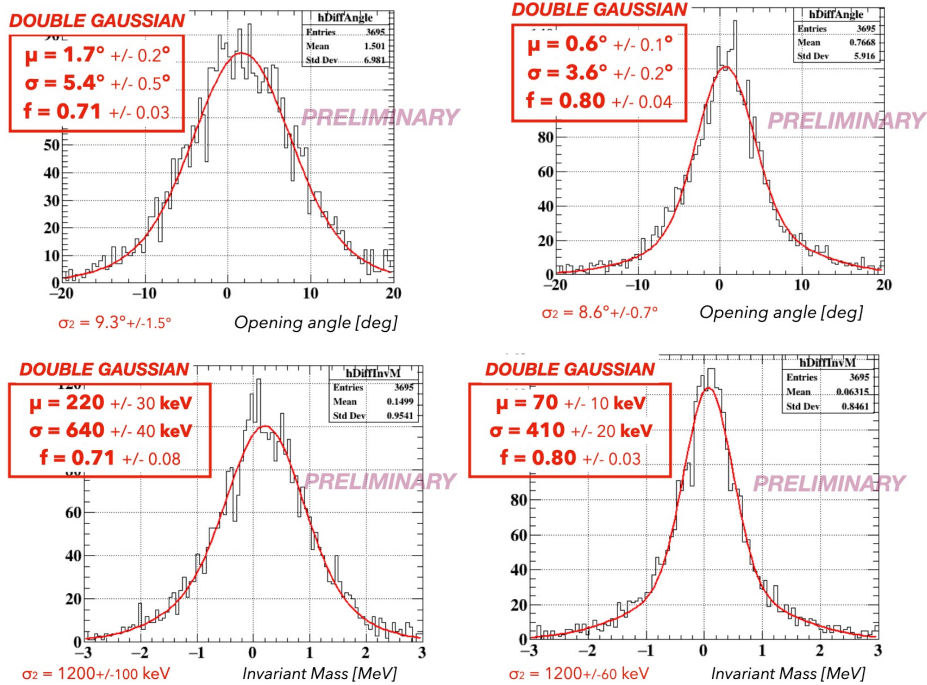


**Fig. 7.14:** Opening angle resolution (upper plots) and invariant mass resolution (lower plots) for MC X17 events, fitted to a double Gaussian. On the left there is the distribution obtained without the angle correction, on the right the one with the angle correction.

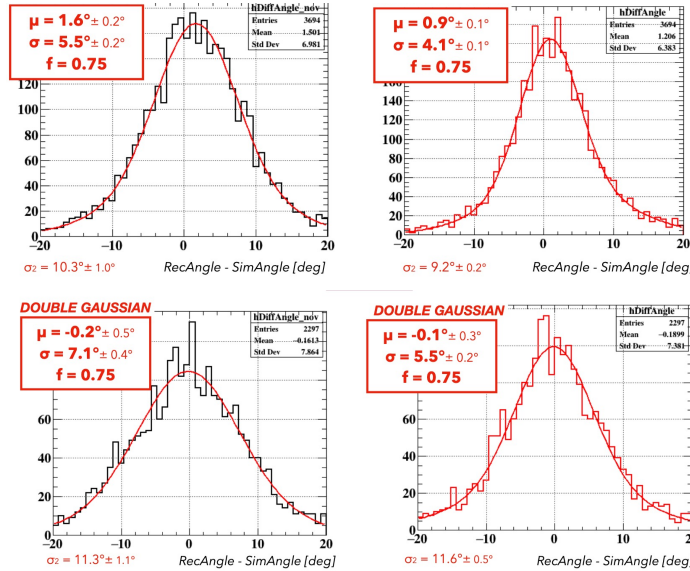


**Fig. 7.15:** Opening angle resolution for IPC18 (upper plots) and X17 (lower plots) MC, fitted to a double Gaussian. On the left, the distribution obtained without vertexing, and on the right the one with vertexing.

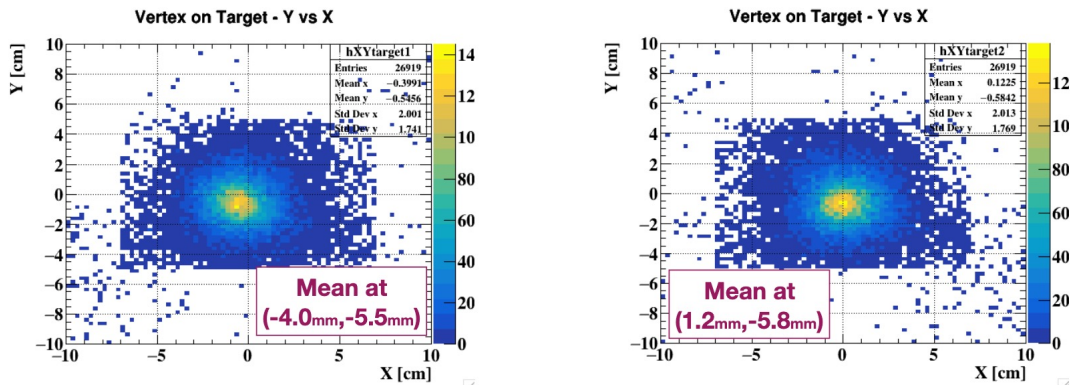


**Fig. 7.16:** Distribution of the reconstructed vertex position positrons (left) and electrons (right) on X17 data.

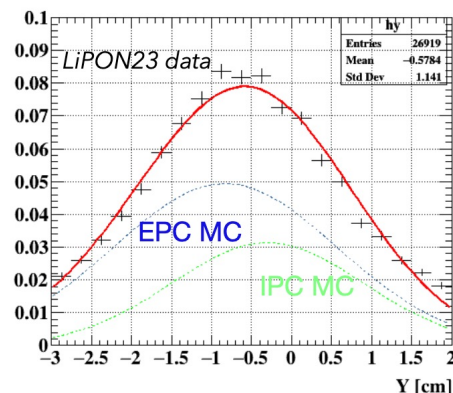


**Fig. 7.17:** Y vertex distribution fitted to the MC: a 60%-40% proportion has been assumed for EPC/IPC.

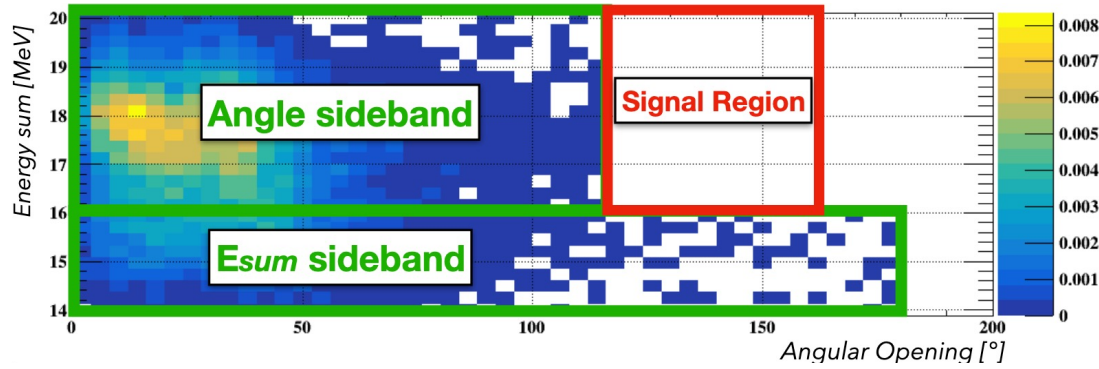


Fig. 7.18: Blinded signal region and sidebands in the  $E_{sum}$  vs  $\theta_{rel}$  plane.

### 7.3.6 Likelihood analysis

Although the Feldman-Cousin approach is well-established in particle physics research, this was our first hands-on experience. After studying the relevant papers [14][15] and the internal notes of the collaboration, we decided to first develop a mock-up<sup>5</sup> to understand the framework necessary for a Feldman Cousin approach to data analysis. The full-blown X17 analysis will be performed with the code already written for the MEG II analysis. This code was developed and improved upon over many years and was both more robust and flexible. Although I followed the whole procedure, the finalization of the mock-up and the transition to the MEG II code was done by Giovanni Dal Maso. The broad idea is to extract the Probability Density Functions (PDF) parametrizing the spectra generated in GEM and benchmarked with the side-bends. This approach relies on the statistics of the MC production, which is unfortunately limited. An alternative method would be to implement background PDFs as histogram templates, as in the Beeston-Barlow [16]. All the missing details can be found in the PhD thesis of Giovanni Dal Maso [11].

**Likelihood** The likelihood is defined by five populations: X17, IPC15, IPC18, EPC15, and EPC18. Given the flexibility of the framework, the analysis can be 1D, in *invariant mass/ relative angle* or 2D, adding the *energy sum* and can be binned or un-binned. The likelihood is shown in Eq. 7.2, in which  $\mathbf{x}_j$  are the kinematic variables of the  $i$ -th event. The parameters are the mass of the X17 and the expected number of pairs per population, with the sum distributed as Poisson. The additional exponent  $\mathcal{N}_i$  is needed for the binned version.

$$\mathcal{L} = (\mathbf{x} | \hat{\mathcal{N}}_S, \hat{\mathcal{N}}_{EPC15}, \hat{\mathcal{N}}_{EPC18}, \hat{\mathcal{N}}_{IPC15}, \hat{\mathcal{N}}_{IPC18}, \hat{m}) \quad (7.1)$$

$$= \frac{\hat{\mathcal{N}}^{\hat{\mathcal{N}}} e^{-\hat{\mathcal{N}}}}{\hat{\mathcal{N}}!} \prod_{i=1}^m \left( \sum_{j=0}^4 \frac{\hat{\mathcal{N}}_j}{\hat{\mathcal{N}}} \text{pdf}_j(\mathbf{x}_j) \right)^{(\mathcal{N}_i)} \quad (7.2)$$

The likelihood function incorporates systematic effects by introducing nuisance parameters, which are distributed with a Gaussian penalty term centered around their expected values, as in Eq. 7.3. These parameters account for uncertainties, particularly in the shape of probability density functions (PDFs) of certain events, primarily due to limited Monte Carlo statistics. Additionally, when analyzing mono-dimensional invariant mass or relative angle, the distribution of energy sum is

<sup>5</sup>The full description of the code will be here skipped but it can be found in the following git repository [🔗](#)

fitted separately to estimate the number of pairs in each population. This information is then integrated into the likelihood analysis through a Poisson penalty term for each type of background event. This adds a penalty to the likelihood like in Eq. 7.4.

$$\mathcal{L}_{syst} = \mathcal{L} \prod_{k=1}^N \frac{1}{\sqrt{2\pi\sigma_k}} e^{-\frac{(\theta_k - \hat{\theta}_k)^2}{2\sigma_k^2}} \quad (7.3)$$

$$\mathcal{L}_{const} = \mathcal{L} \prod_{j=1}^4 \frac{\hat{\mathcal{N}}_j^{\hat{\mathcal{N}}_j} e^{-\hat{\mathcal{N}}_j}}{\hat{\mathcal{N}}_j!} \quad (7.4)$$

The Feldman-Cousins construction involves defining a parameter space grid, typically for parameters of interest like branching ratio and X17 mass. The likelihood ratio (Eq. 7.5, in which  $\hat{\cdot}$  marks the best value for the  $k$ -th parameter, fixed in  $\theta_{k,0}$  on the FC grid) is computed for each point in this grid using toy Monte Carlo experiments (ToyMC). Each experiment involves sampling from distributions accounting for systematics and background populations, followed by computing the likelihood ratio for the data compared to the generated samples. Confidence levels are determined based on the fraction of toy experiments with a lower likelihood ratio than the data, with 90% confidence belts commonly considered. The uncertainty on the CL depends on the number of ToyMC per toy experiment and can be evaluated as:

$$\begin{aligned} \sigma_{CL} &= \sqrt{\frac{\hat{CL}(1 - \hat{CL})}{N_{ToyMC}}} \\ \lambda_{LR} &= -2 \left[ \ln(\mathcal{L}(\hat{\theta}, \theta_{k,0})) - \ln(\mathcal{L}(\hat{\theta})) \right] \end{aligned} \quad (7.5)$$

The significance of a signal is evaluated by comparing the likelihood ratio of the data to that of null experiments. Computational demands may require approximations, such as estimating p-values based on asymptotic distributions. The likelihood function is optimized using the MINUIT algorithm [17][18], allowing for extended analysis over higher-dimensional parameter spaces and binned likelihood analysis. The framework offers flexibility in selecting PDFs from a database.

**PDFs** The PDFs are parametrized based on the limited MC production done in July 2023. The yields of each population can be evaluated by comparing measured and expected BGO rates. The resulting populations are in Tab. 7.2. The PDFs utilized to model the EPC spectra are crucial for accurately representing the signal region, especially given the limited EPC MC statistics. The choice, in Eq. 7.6 and Eq. 7.7, was an asymmetric Gaussian distribution for  $E_{sum}$  and a Gaussian with asymmetric asymptotes. An example of binned likelihood fit on ToyMC is in Fig. 7.19

$$\text{pdf}_{EPC}(E_{sum}) = \begin{cases} \mathcal{G}(E_{sum} | \mu_E, \sigma_{E,L}), & \text{if } E_{sum} < \mu_E \\ \mathcal{G}(E_{sum} | \mu_E, \sigma_{E,R}), & \text{if } E_{sum} \geq \mu_E \end{cases} \quad (7.6)$$

$$\text{pdf}_{EPC}(\theta_{rel}) = \begin{cases} \exp\left(-\frac{1}{2} \frac{(\theta_{rel} - \mu_\theta)^2}{\sigma_\theta^2 + \alpha_L^2 (\theta_{rel} - \mu_\theta)^2}\right), & \text{if } \theta_{rel} < \mu_\theta \\ \exp\left(-\frac{1}{2} \frac{(\theta_{rel} - \mu_\theta)^2}{2\sigma_\theta^2 + \alpha_R^2 (\theta_{rel} - \mu_\theta)^2}\right), & \text{if } \theta_{rel} \geq \mu_\theta \end{cases} \quad (7.7)$$

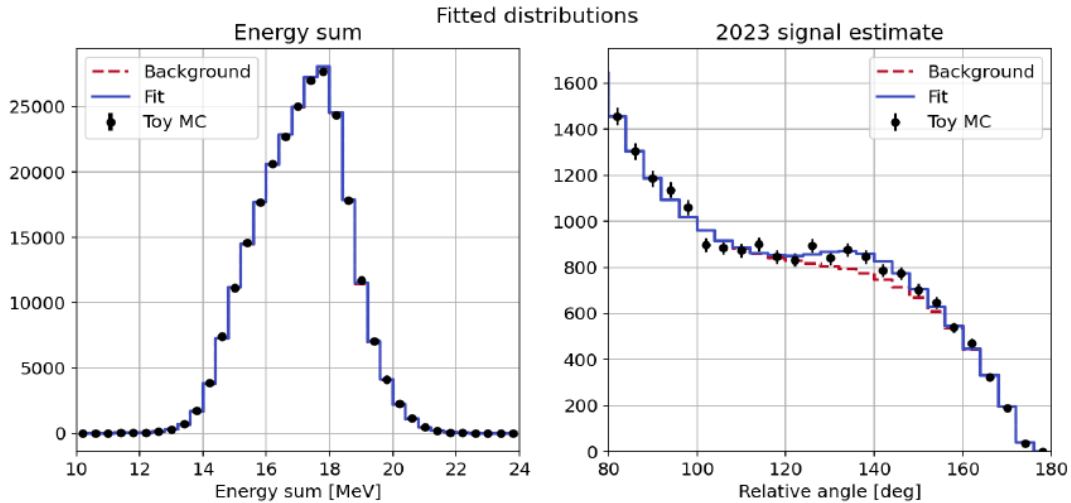


**Fig. 7.19:** The binned likelihood fit of a ToyMC sample. It uses 2-dimensional PDFs for  $E_{sum}$  and  $\theta_{rel}$ , presenting ToyMC data (black), the best fit (blue), and summed background PDFs (red).

A ranking of systematic effects was devised, leading to four potential sets of systematics for the final fit, essential to ensure the sensitivity of the analysis:

- A** : Only the systematics not related to the shape of the EPC PDFs, e.g. signal normalization;
- B** : A plus the  $\alpha_R$  parameters of both EPC 15 and EPC 18;
- C** : B plus the  $\sigma_\theta$  parameters of both EPC 15 and EPC 18;
- D** : C plus the  $E_{sum}$  parameters of both EPC 15 and EPC 18.

**Tab. 7.2:** Population sizes for different categories

	X17	EPC 15	IPC 15	EPC 18	IPC 18
Population size	450	$3.75 \times 10^4$	$2.75 \times 10^4$	$1.35 \times 10^5$	$5 \times 10^4$

**Tests** Many tests are ongoing, like comparing estimators from unbinned and binned likelihood analyses on 500 ToyMC samples, with the second being  $>50$  times faster. The different ‘options’ are also tested, revealing option **D** consistently yields a signal compatible with zero. The parametrization for Esum EPC PDFs, dictated by the limited MC production, seems to tend to an overpopulation in background yield. The current strategy also lacks consideration for possible correlations between energy sum and relative angle and more tests are needed with final MC production.

**CL estimate** The distribution of  $\lambda_{LR}$  is computed on a  $15 \times 15$  grid between 0 and 900 average X17 events and between  $15 \text{ MeV}/c^2$  and  $18.15 \text{ MeV}/c^2$  X17 mass. For each point in the grid, the ToyMC generation and fitting was performed for 1 h. This delivered an inhomogeneous number of ToyMCs produced per point on the grid as the convergence time depends on the strength of the signal. Each point in the grid has a generated statistics ranging between  $\sim 130$  and  $\sim 350$  ToyMCs. To compute the CLs, the likelihood on the data sample, which is in this case a reference ToyMC sample, is profiled in the grid points and the  $\lambda_{LR}$  is computed. For each grid point, the  $\lambda_{LR}$  is ranked giving the local CLs. The procedure is then repeated 100 times by resampling the dataset and computing the profile likelihood for each iteration for different values of the average X17 yield. The median of the upper and lower limits and of the best-fit estimates are studied as a

function of the average X17 yield. Such estimates depend on the template used, resulting in a bias on the best fit and on the quoted limits. The bias is visible, leading to a median yield of 400 X17 events for a scenario where the true value is 450. The corresponding plots are in Fig. 7.20.

**Improvements** Due to the current (and anticipated) limited Monte Carlo statistics, an alternative likelihood approach has been developed. In their work, the authors in [16] formulated a binned likelihood for template fits, accounting for the impact of low MC statistics. This likelihood combines terms for the observed data ( $\mathcal{L}_{data}$ ) and the template distributions ( $\mathcal{L}_{nuisance}$ ), treating each bin's population as following a Poisson distribution around its true value:

$$\mathcal{L} = \mathcal{L}_{data} + \mathcal{L}_{nuisance} = \sum_{i=1}^n D_i \log(f_i) - f_i + \sum_i^n \sum_j^m a_{ij} \log(A_{ij}) - A_{ij} \quad (7.8)$$

where  $n$  is the number of bins,  $m$  the number of populations,  $D_i$  the population in the data i-th data bin,  $f_i$  the estimated population in the i-th bin,  $a_{ji}$  the observed statistics in the j-th MC sample in bin i, and  $A_{ij}$  is the estimator of  $a_{ji}$ . This approach introduces one nuisance parameter  $A_{ij}$  per bin per population, which is used to estimate  $f_i$  defining the *population strength*  $p_j$

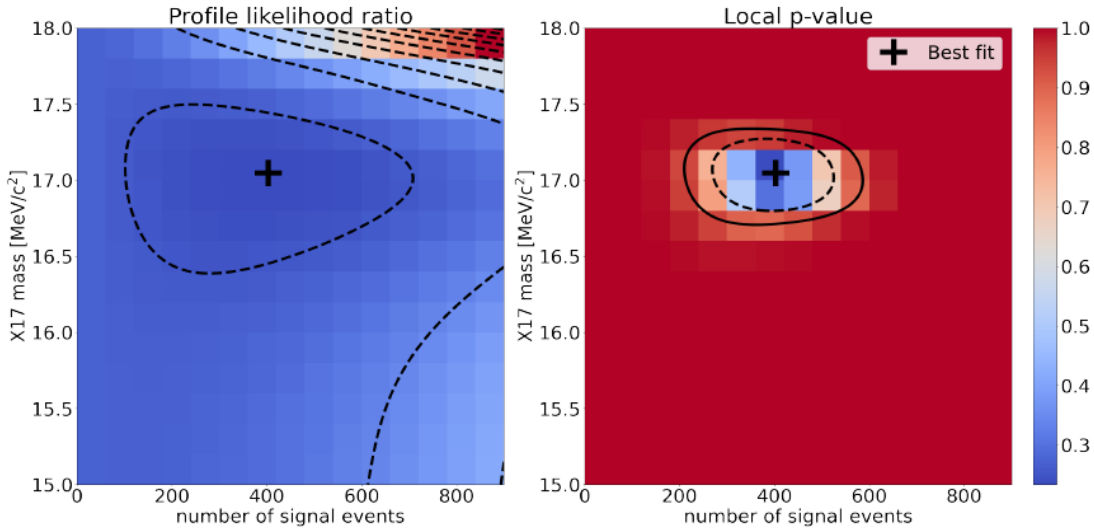
$$f_i = \sum_{j=1}^m \frac{\hat{\mathcal{N}}_{data,j}}{\hat{\mathcal{N}}_{MC,j}} A_{ij} = \sum_{j=1}^m p_j A_{ij} \quad (7.9)$$

The maximum of the likelihood is found by solving  $\partial_{p_j} \mathcal{L} = 0$  and  $\partial_{A_{ji}} \mathcal{L} = 0$  analytically or via a minimizer, like MIGRAD. We will skip the details but this approach would allow us to correct for limited statistics and possible correlations between variables. This likelihood is currently still under study, with possible changes to implement the analytical (and faster) minimization.

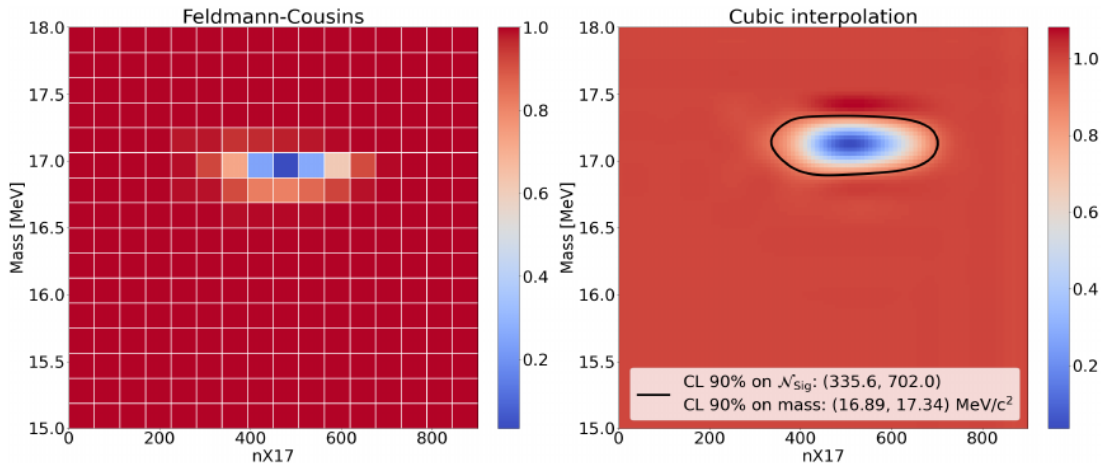
### 7.3.7 Asymmetry and normalization

Important aspects to be considered during this search are the different asymmetries expected for the photons resulting from the interaction and the fact that our analysis will require a normalization measurement to keep track of the proton beam intensity. For the first task, the obvious choice would have been the XEC but this had two drawbacks: the detector itself is quite limited in extension along the beam direction and it was not always available due to the annealing process described in Sec. 5.2. The solution was to use the BGO, described in Sec. 6.2, and crosscheck the results via a dedicated data set collected with the XEC. For the normalization, the idea was to install a small NaI crystal below COBRA and use the combined information from this detector, the BGO, and the various measurements of the CW proton current.

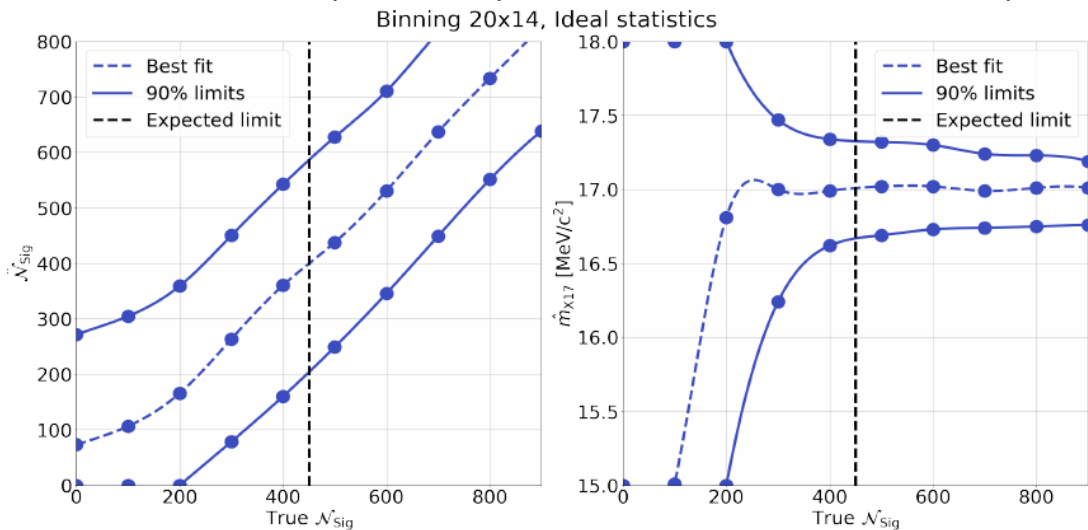
**CW stability** The CW is usually used for short periods during CEX calibrations and it is not possible to remote access it. On top of it, the only way of measuring the delivered beam current is to momentarily close the beam-shutter, which behaves as a Faraday cup. We tried keeping track of the beam intensity during the datataking to cross check this information with the auxiliary detector employed for normalization. The idea is to have a way of determining, if a drop in rate is observed, if the CW beam had issues or the target. A history of the beam current is in Fig. 7.21



(a) The profile likelihood (left) and the local p-value (right) estimated with Wilks' theorem, for 500 X17, are shown. The solid/dashed black lines shows the 90%/68% p-value levels.



(b) FC construction in the ideal statistics scenario for 500 X17. On the right, a cubic spline interpolation is shown. The solid black line shows the 90% CL belt. By reducing the statistics of the EPC templates by a factor 10, the limits on the X17 yield increase by 14%, and the limits on the X17 mass increase by 11%



(c) Median 90% CLs and best fits expected as a function of the true X17 yield in the ideal statistics scenarios. The limits are shown both in the estimated X17 yield (left) and mass (right).

**Fig. 7.20:** Example of the profile likelihood ratio (a) and of the full FC construction (b) for 500 X17 events in an ideal case. In (c) the median 90% CLs and best fits expected as a function of the true X17 yield.

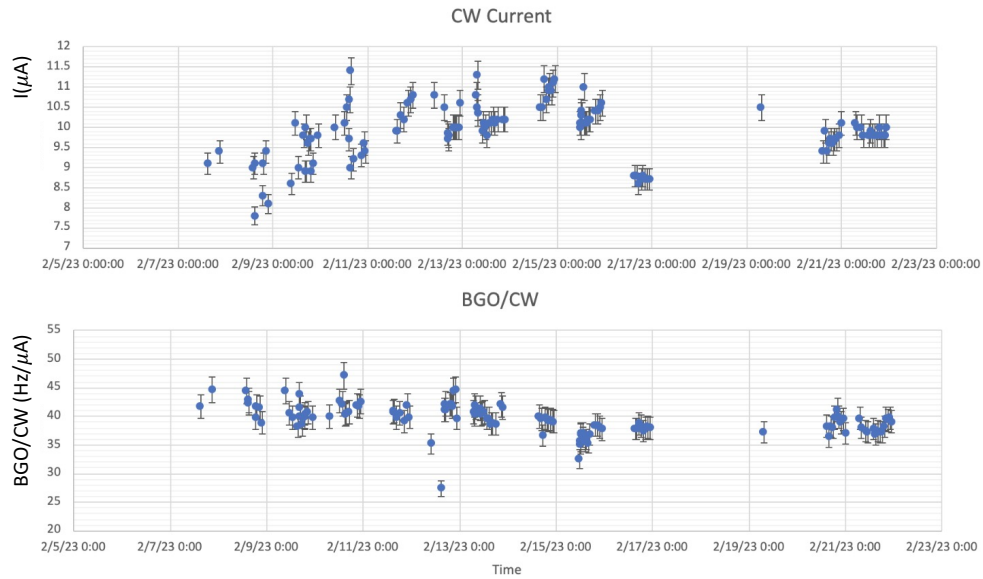


**Fig. 7.21:** History of the CW beam current during X17 data-taking in 2023. In the second plot, the CW current is used to normalize the BGO rate, which is a way to evaluate the stability of the target itself.

**BGO spectra** Here we will not discuss the BGO calibration, which is described in App. B. The first test was to see if the rotation of the target holder of 90 deg would affect the  $\gamma$  spectra. This could be the case because of the different position of the copper ring holding the target. The BGO spectra in the ‘X17’ and the ‘rotated’ position are shown in Fig. 7.22 and no substantial difference was found. From the width of the 17.6 MeV, which is very narrow ( $\Gamma = 11$  keV), we can extract the BGO energy resolution to be  $\sigma_{BGO} \approx 3.1\%$ . When comparing two subsequent 500 keV and 1080 keV datasets, we found the two peaks closer than the expected 500 keV. In practice, the 18.15 MeV is at a lower energy and this discrepancy cannot be justified by the precision of the calibration. The spectra are shown in Fig. 7.23. No definitive hypothesis was made on this behavior. The two lines of thought were: either the line generated is not the 18.1 MeV resonance or there is some detail missing in the detector setup. This point will be discussed later in this chapter after the analysis done on the targets and on the CW beam.

**Xenon Calorimeter** In May 23 data with XEC calorimeter as a gamma detector were taken to study the photon spectra, with a 500 nm thin Lipon photon target. Fig. 7.24 shows the photon spectrum taken at different proton energies. As already noticed in the BGO, the two Be(17.6) and Be(18.1) lines don’t appear to be separated. Another puzzling feature is the relative height of the 15 and 18 MeV peaks. Looking at the cross-section in Fig. 7.1, one would expect the relative height of the resonance to vary differently.

## 7.4 Target studies

To further understand the results of the preliminary analysis, and to cross-check different hypotheses, a few of the targets were studied by experts at PSI and from Sapienza University of Rome. These targets were studied with SAM and EDX measurements and the results, of which an example is shown in Fig. 7.26, were in line: the targets were found to be poorly characterized,

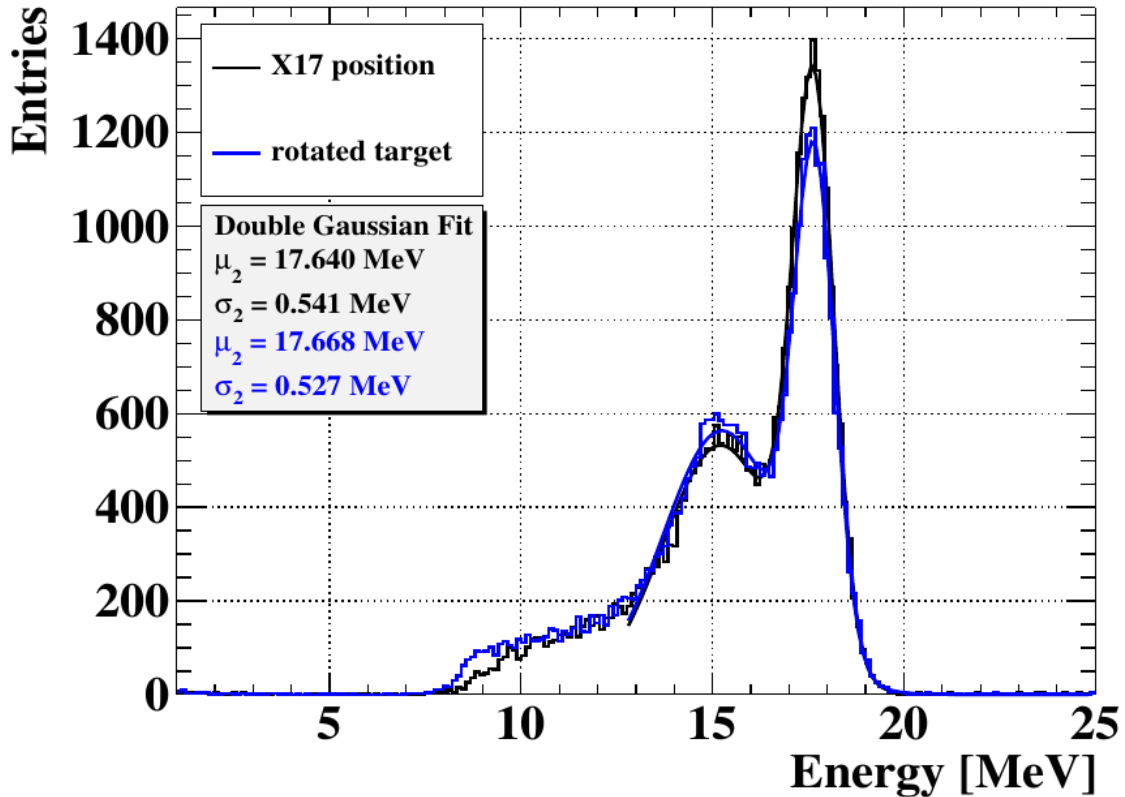


Fig. 7.22: BGO spectra at  $E_p = 500 \text{ MeV}$  for a normal and rotated target. The two spectra are compatible.

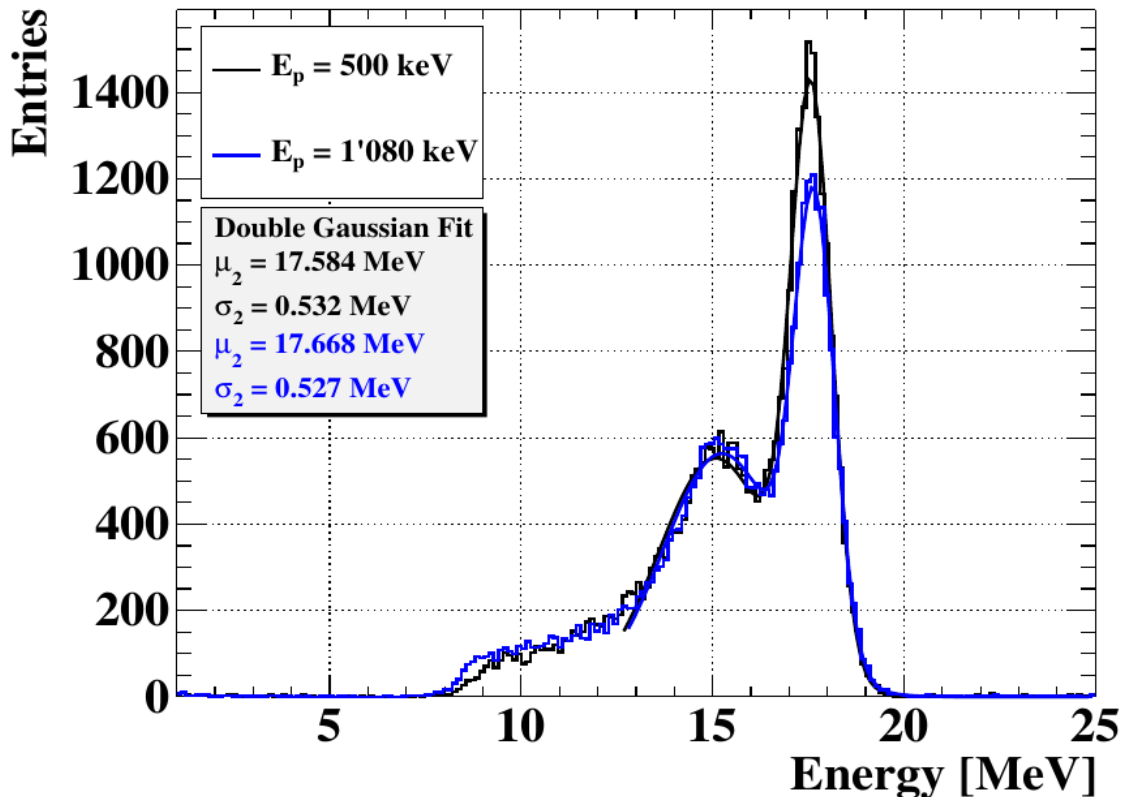
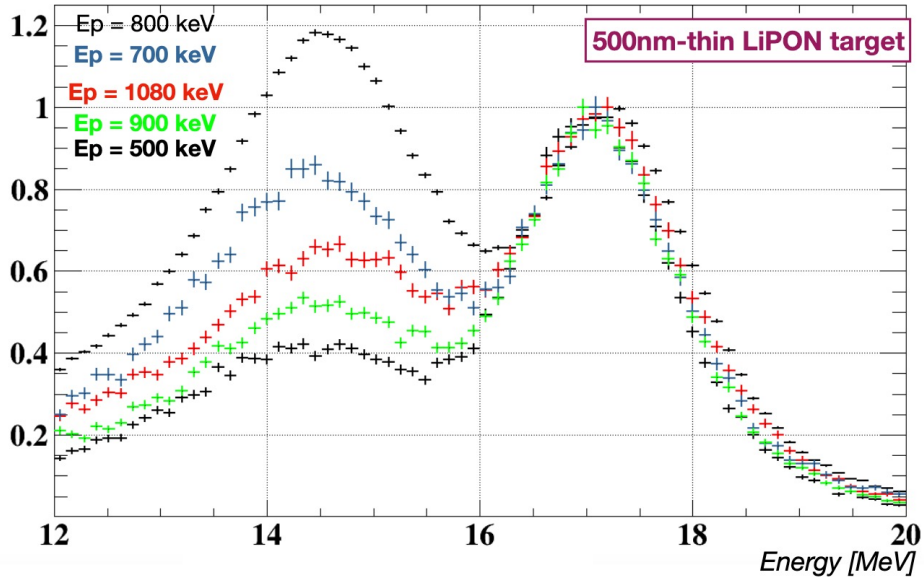


Fig. 7.23: BGO spectra taken at  $E_p = 500 \text{ MeV}$  (Black), and  $E_p = 1080 \text{ MeV}$  (Blue) on LIPON. The second spectrum should be peaked at  $18.15 \text{ MeV}$  (+500 keV) but is not. The  $17.6 \text{ MeV}$  line seems to be prevalent.



**Fig. 7.24:** Photon spectrum measured by XEC detector in May 2023 at different proton energies with a 500 nm thick Lipon target.

with thicker than expected and uneven deposit. After the analysis done on the target used in Feb. during the data-taking, we asked some colleagues from PSI to produce a different LiPON target. The requirement was a target ‘as big as possible’ and with a thickness of 500 nm. The way the machine works made it so that the maximum dimension of the target was a diameter of 1 cm. Given the setup developed for the target was for bigger substrates we had to improvise ways to hold this new target in position. We first tried to hold it between two folded aluminum foils. This system was not satisfactory so we moved to a Cu foil with two parallel cuts to create a ‘pocket’. A picture of the two setups is in Fig. 7.26 while a picture of the target is in Fig. 7.27.

#### 7.4.1 Al and Cu Data-taking

The data taken with the two different supports (Al and Cu) are confronted in Fig. 7.28 for both 500 keV and 1080 keV protons: for the lower energy we see no difference, the only line excited is the expected resonance at  $E_p = 440$  keV; for the higher energy a new line appears for the Al. This line demonstrates the energy of the incoming beam to be 1 MeV. Looking at the sample with the Cu support at the two energies we would expect a shift of 500 keV in the peak position. As in the previous data-taking, the shift found is much smaller (see Fig. 7.29). Performing a fit with two Gaussians in the expected positions we can evaluate the rough estimate of the two components. The result is a small percentage of the 18.1 MeV, around  $\sim 6\%$ . The results of these tests highlighted two things: the energy of the CW machine is reliable; the old target seems to not be the (only) cause of the reduced shift in energy at 1080 keV.

## 7.5 Beam studies: Jan 2024

After the analysis of the different targets and the small data-taking at the end of 2023, we realized the problem may lay in the proton beam produced by the CW. The option of the beam not being

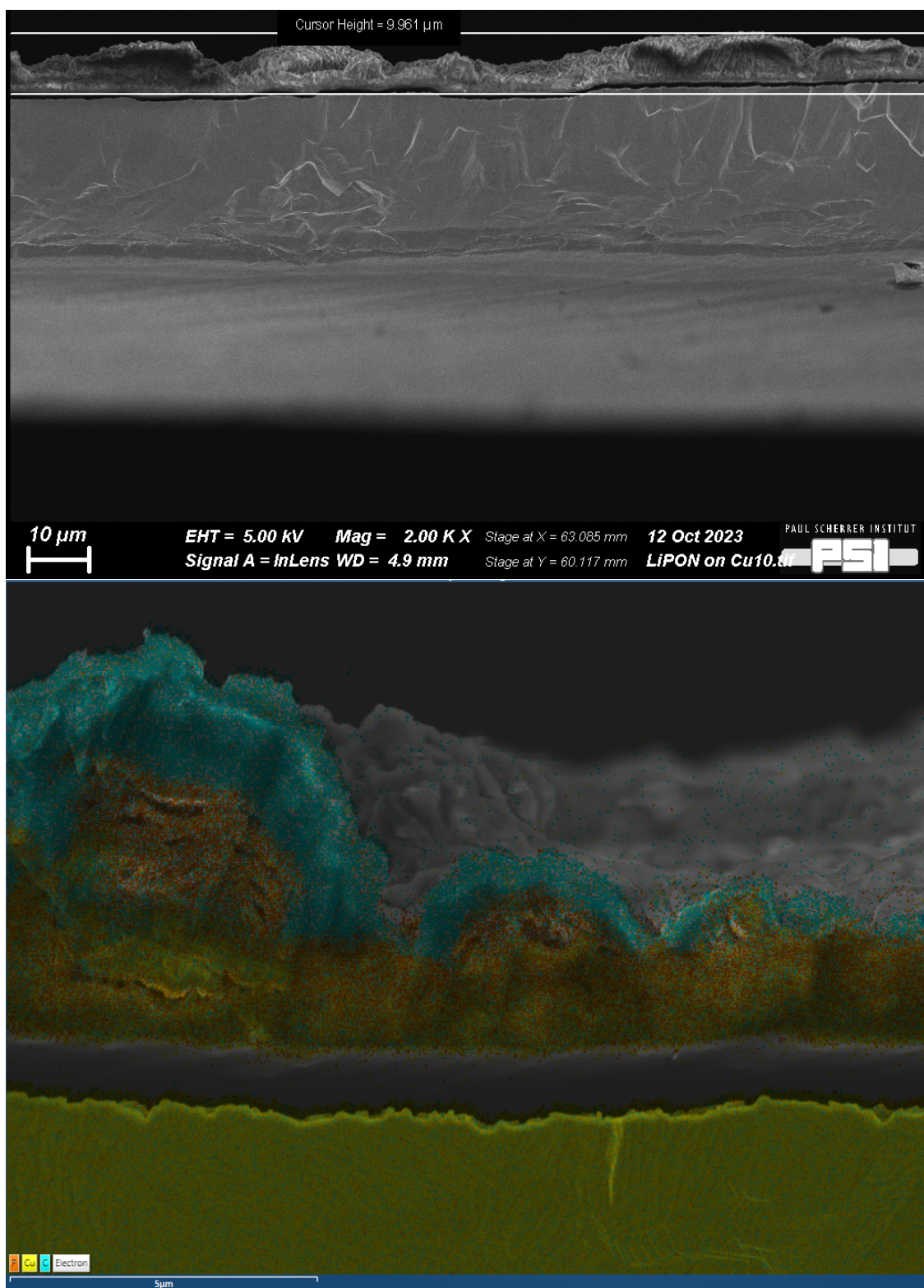


**Fig. 7.25:** SEM and EDX measurement of the  $\text{Li}_3\text{PO}_4\text{N}_2$  deposit on the Cu substrate. For this particular target, the LiPON deposit was supposed to be 2  $\mu\text{m}$ . In the top picture, the LiPON rests on the copper substrate. In the bottom picture, the colors highlight the different atoms: Cu-yellow, P-orange, C-cyan. The presence of carbon is linked to the oxidation of the material, creating  $\text{LiPO}_4$ . The lamination between LiPON and Cu was attributed to the cutting procedure for the analysis.



**Fig. 7.26:** Two different ways to hold the small LiPON sample given to us by the PSI colleagues. We first tried to hold it in place with folded aluminum foils. We later realized this was not the optimal solution given the spectrum produced by protons on Al. We then moved to a cleaner Cu setup.

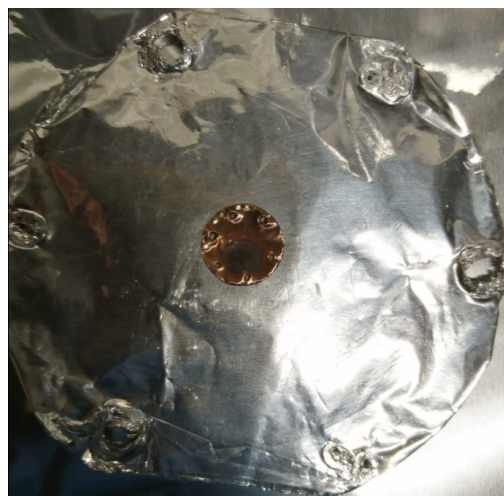


**Fig. 7.27:** Here is a picture of the target itself after two days of data-taking at 5 and 10  $\mu\text{A}$ . The dark spot marks the position on which the beam was impinging.

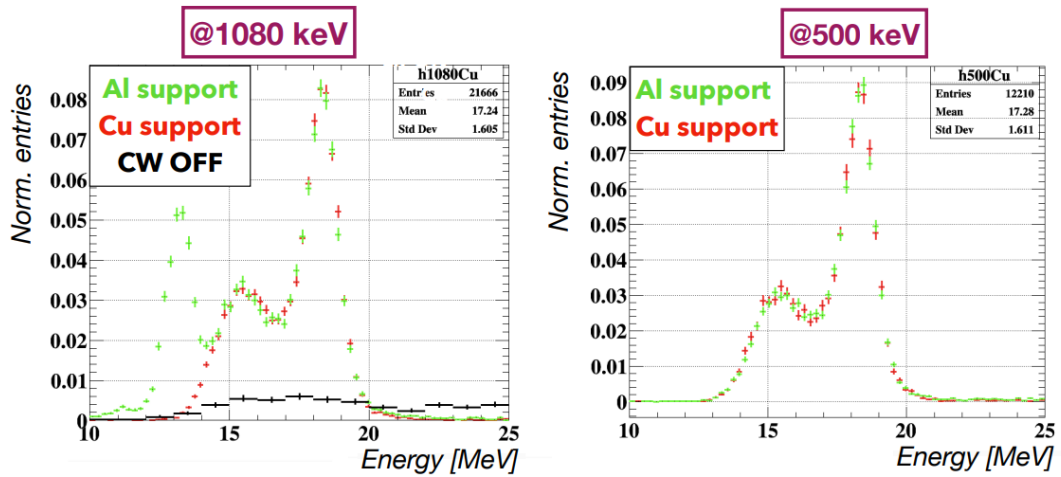


**Fig. 7.28:** The data from two supports (Al and Cu) were compared for 500 keV and 1080 keV protons. At the lower energy, no difference was observed; only the expected resonance at  $E_p = 440$  keV was detected. However, at the higher energy, a new line appeared for Al, indicating the energy of the incoming beam.

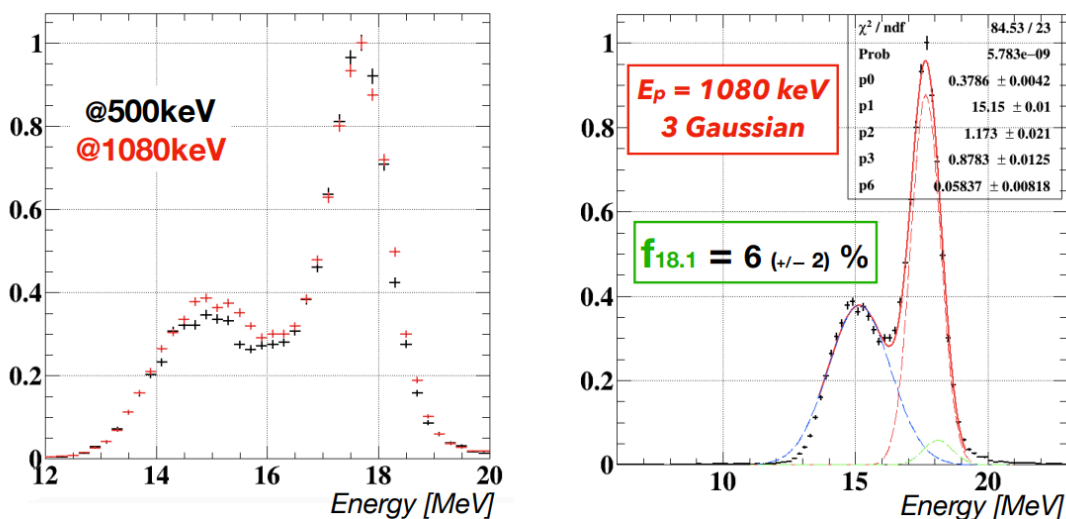


**Fig. 7.29:** Examining the sample with Cu support at both energies, we anticipated a peak position shift of 500 keV. However, the observed shift was significantly smaller. By fitting two Gaussians at expected positions, we estimated the two components to be approximately  $\sim 6\%$  of the 18.1 MeV.

COBRA	Collimator	Faraday Cup / Beam shutter
OFF	no	0.736
OFF	yes	0.518
0.15 T	no	0.748
0.15 T	yes	0.530

**Tab. 7.3:** Summary of the measurements on the CW beam

at the expected energy was already discarded, for example by the peak measured at 11 MeV using aluminum to hold the target. The point was that, while producing mainly  $H_1^+$ , the machine produces also  $H_2^+$  and  $H_3^+$ . The relative fraction of the different species is roughly 0.7 : 0.25 : 0.05, meaning the fraction of  $H_2$  is non-negligible. Having this specie the same 1 MeV energy as the protons, when interacting with the target could split, creating 500 keV protons. These particles would interact with the Lithium in the much higher resonance, generating the measured 17.6 MeV line.

### 7.5.1 Collimator and beam studies

After mounting the quartz crystal, used already for the beam-tuning in Sec. 7.2.4, as close as possible to the CW source ( $\approx 2$  m) it was possible to see the position of the two beam spots. Assuming the brighter one was the one generated by the protons, it was possible to mount a temporary copper collimator to stop the second component of the beam. The beam blocker normally functions also as beam current measurement. This system is not designed for that and the occasion was taken to install a Faraday cup and compare the two measurements. By measuring the current with both devices, with and without a collimator, and at different COBRA magnetic fields, it is possible to evaluate the fraction of  $H_1^+$  and  $H_2^+$  reaching the target. The results are shown in Tab. 7.3 and indicate  $\sim 70\%$  of the beam is  $H_1^+$ . An example of the plot used for such a study is in Fig. 7.30.

Unfortunately, we experienced a problem similar to what was described in Sec. 5.7.1. The machine started sparking at  $V > 800$  V, meaning that these studies could not be conducted at 1080 keV and no further data taking was possible in Feb. 2024. The fault seems to be the condition of the SF<sub>6</sub> in the machine but further investigation is ongoing and new SF<sub>6</sub> is on the way to PSI.

## 7.6 Results and conclusions

This chapter was dedicated to the X17 search with the MEG II apparatus. After a summary of the anomaly under study we saw how the search is ongoing in MEG II, with details on the analysis. Unfortunately, the data of 2023, while still of interest, are dominated by the 17.6 MeV line instead of the 18.1 MeV due to the target and/or  $H_2^+$  CW beam component. I had an active role in all preparations and data-taking and played a marginal role in the analysis, particularly in the development of the likelihood analysis framework and the BGO calibration procedure.

Regarding the data-taking campaign of 2023, the MC simulation accuracy is under investigation in sidebands, with ongoing MC production. We plan to address the limited MC statistics, due to resource constraints, implementing the Beeston-Barlow likelihood, discussed in Sec. 7.3.6. The

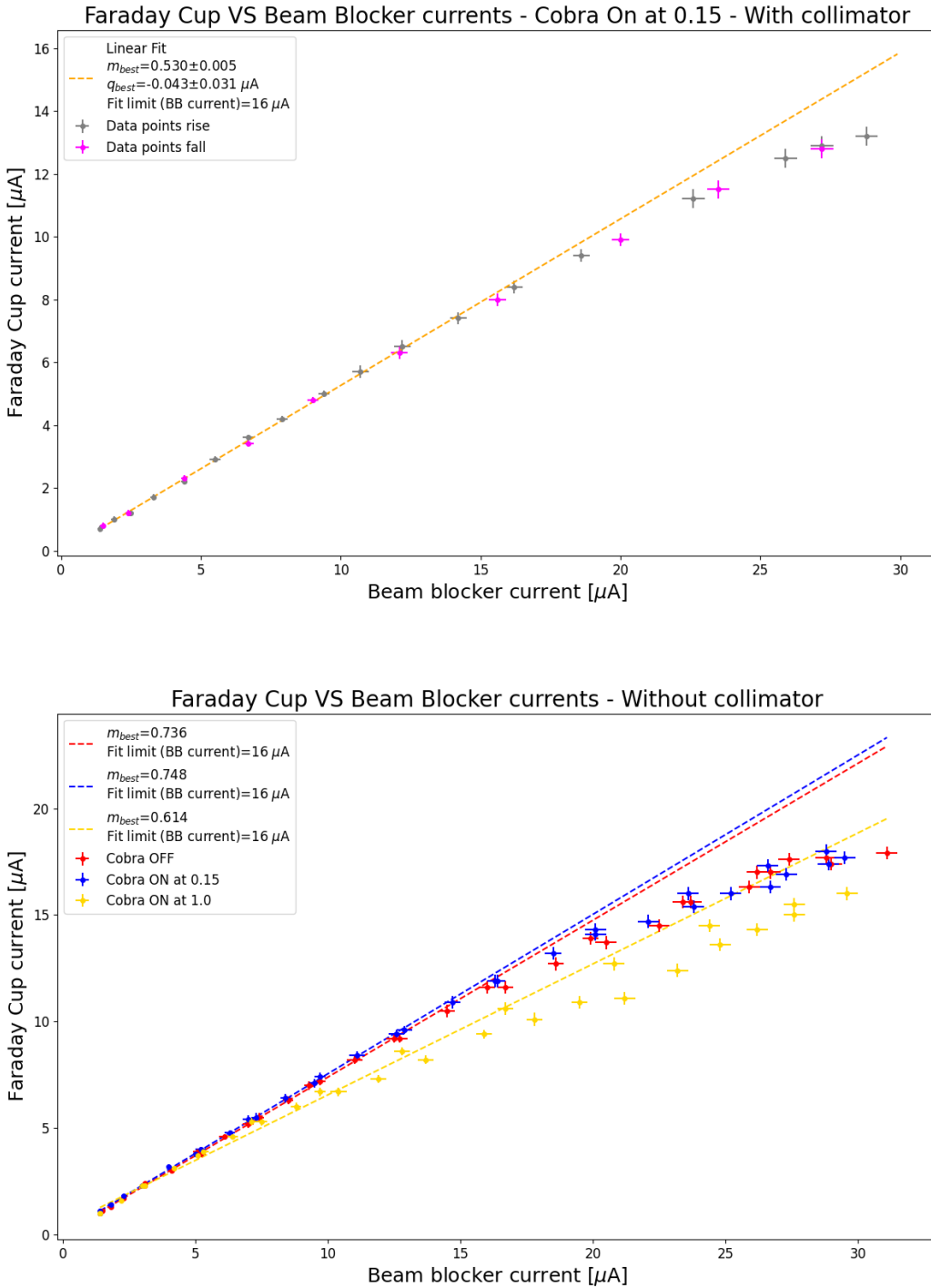


**Fig. 7.30:** Example of the data taken in Feb. 2023 to study the CW beam. The top picture shows the dependence of the current measured with the Faraday Cup with collimator as a function of the Beam Blocker current with COBRA at 15%. The bottom plot shows the same plot with no collimator but with different magnetic fields.

expected sensitivity on the 2023 data is 272(4) X17 events, compared to 450 by ATOMKI. The estimated significance of an anomaly akin to ATOMKI's measurements is  $3.36\sigma$ ; a  $4.27\sigma$  significance could be reached with a tenfold increase in EPC MC statistics.

The collaboration plans to have another data-taking focusing on the 18.1 MeV line changing the target, as discussed in Sec. 7.4, and removing the  $\text{H}_2^+$  from the CW beam, as discussed in Sec. 7.5. These two improvements should give a sample that is purer and with a higher expected sensitivity.

# Bibliography on X17

- [1] A. J. Krasznahorkay et al. "New experimental results for the 17 MeV particle created in  $^8Be$ ". In: *EPJ Web Conf.* 137 (2017). Ed. by Y. Foka, N. Brambilla, and V. Kovalenko, p. 08010. DOI: 10.1051/epjconf/201713708010.
- [2] Daniele S.M. Alves et al. "Shedding light on X17: community report". In: *The European Physical Journal C* 83.3 (Mar. 2023), p. 230. ISSN: 1434-6052. DOI: 10.1140/epjc/s10052-023-11271-x. URL: <https://doi.org/10.1140/epjc/s10052-023-11271-x>.
- [3] D. Zahnow et al. "The S(E) factor of  $^7Li(p, \gamma)^8Be$  and consequences for S(E) extrapolation in  $^7Be(p, \gamma_0)^8B$ ". In: *Zeitschrift für Physik A Hadrons and Nuclei* 351.2 (June 1995), pp. 229–236. ISSN: 0939-7922. DOI: 10.1007/BF01289534. URL: <https://doi.org/10.1007/BF01289534>.
- [4] D.R. Tilley et al. "Energy levels of light nuclei A=8,9,10". In: *Nuclear Physics A* 745.3 (2004), pp. 155–362. ISSN: 0375-9474. DOI: <https://doi.org/10.1016/j.nuclphysa.2004.09.059>. URL: <https://www.sciencedirect.com/science/article/pii/S0375947404010267>.
- [5] A. J. Krasznahorkay et al. "Observation of Anomalous Internal Pair Creation in  $^8Be$ ". In: *Acta Phys. Polon. Supp.* 8.3 (2015). Ed. by Marek Gozdz, p. 597. DOI: 10.5506/APhysPolBSupp.8.597.
- [6] Xilin Zhang and Gerald A. Miller. "Can nuclear physics explain the anomaly observed in the internal pair production in the Beryllium-8 nucleus?" In: *Physics Letters B* 773 (2017), pp. 159–165. ISSN: 0370-2693. DOI: <https://doi.org/10.1016/j.physletb.2017.08.013>. URL: <https://www.sciencedirect.com/science/article/pii/S0370269317306342>.
- [7] Xilin Zhang and Gerald A. Miller. "Can a protophobic vector boson explain the ATOMKI anomaly?" In: *Phys. Lett. B* 813 (2021), p. 136061. DOI: 10.1016/j.physletb.2021.136061. arXiv: 2008.11288 [hep-ph].
- [8] Xilin Zhang and Gerald A. Miller. "Can a protophobic vector boson explain the ATOMKI anomaly?" In: *Physics Letters B* 813 (2021), p. 136061. ISSN: 0370-2693. DOI: <https://doi.org/10.1016/j.physletb.2021.136061>. URL: <https://www.sciencedirect.com/science/article/pii/S0370269321000010>.
- [9] Tran The Anh. "Confirmation the  $^8Be$  anomaly with a different spectrometer". 52nd International Symposium on Multiparticle Dynamics (ISMD 2023).
- [10] M. Meucci. "Search for the X(17) particle in the  $^7Li(p, e^+e^-)^8Be$  reaction with the MEG II detector". PhD thesis. Sapienza University of Rome, 2022. URL: <https://hdl.handle.net/11573/1638985>.
- [11] G. Dal Maso. "TITLE". PhD thesis. Swiss Federal Institute of Technology (ETH), 2024.

- [12] Wolfgang Waltenberger, Winfried Mitaroff, and Fabian Moser. "RAVE—a Detector-independent vertex reconstruction toolkit". In: *Nuclear Instruments and Methods in Physics Research Section A: Accelerators, Spectrometers, Detectors and Associated Equipment* 581.1 (2007). VCI 2007, pp. 549–552. ISSN: 0168-9002. DOI: <https://doi.org/10.1016/j.nima.2007.08.048>. URL: <https://www.sciencedirect.com/science/article/pii/S0168900207017196>.
- [13] C. Hoppner et al. "A Novel Generic Framework for Track Fitting in Complex Detector Systems". In: *Nucl. Instrum. Meth. A* 620 (2010), pp. 518–525. DOI: [10.1016/j.nima.2010.03.136](https://doi.org/10.1016/j.nima.2010.03.136). arXiv: 0911.1008 [hep-ex].
- [14] Gary J. Feldman and Robert D. Cousins. "Unified approach to the classical statistical analysis of small signals". In: *Physical Review D* 57.7 (Apr. 1998), pp. 3873–3889. DOI: [10.1103/physrevd.57.3873](https://doi.org/10.1103/physrevd.57.3873). URL: <https://doi.org/10.1103%2Fphysrevd.57.3873>.
- [15] Till Moritz Karbach. *Feldman-Cousins Confidence Levels - Toy MC Method*. 2011. arXiv: 1109.0714 [physics.data-an].
- [16] Roger J. Barlow and Christine Beeston. "Fitting using finite Monte Carlo samples". In: *Comput. Phys. Commun.* 77 (1993), pp. 219–228. DOI: [10.1016/0010-4655\(93\)90005-W](https://doi.org/10.1016/0010-4655(93)90005-W).
- [17] F. James and M. Roos. "Minuit: A System for Function Minimization and Analysis of the Parameter Errors and Correlations". In: *Comput. Phys. Commun.* 10 (1975), pp. 343–367. DOI: [10.1016/0010-4655\(75\)90039-9](https://doi.org/10.1016/0010-4655(75)90039-9).
- [18] F. James. "MINUIT Function Minimization and Error Analysis: Reference Manual Version 94.1". In: (1994).

# Appendix A

## Kalman filter

This Appendix is to illustrate the working principle of a Kalman filter, showing a simple linear problem in 2D. This is taken, with minor adjustments, from my Master Thesis: *In situ monitoring of the stopped muon flux at Mu2e*. Although during my PhD I did not implement any Kalman filter, this concept is central in MEG II analysis as well as the muEDM upcoming track fitting and in modern particle physics at large.

### A.1 The problem

Once the pattern recognition algorithms have been executed, a preliminary but rough estimate of the track parameters  $\vec{\eta}$  is available. At this point, there are still numerous effects that should be accounted for when trying to optimize track reconstruction. Some of these effects are obvious, like, for example, the non-uniformity of the magnetic field, while others are less so. An example of the latter is the fact that a hit might have an intrinsic symmetry in a specific detector.

Mathematically, a track can be parameterized using a running variable and a vector of parameters. To make an example, quite often in particle physics, the particles move in magnetic fields, following a helicoidal trajectory. In this case the vector  $\vec{\eta}$  with the helix parameters and the position along the beam axis  $z$  can be used:  $F(\vec{\eta}; z)$ . The fitting procedure then determines the best estimate of the vector  $\vec{\eta}$  and the corresponding covariance matrix  $V$ . The task gets substantially more complicated if the parameters vector depends on the running variable  $\vec{\eta}(z)$ . This is the case when the traveling particle can lose energy, interact with some material along its path, or when the magnetic field is not uniform. These are common conditions and the effect in terms of variation of the track parameters values can be substantial. Fig. A.1 shows one possible simple example [1]. Now the procedure of finding the ‘optimal’ track parameters suddenly implies also that we need to define the position where we want to determine those parameters. It is often the case we are interested in determining the value of  $\vec{\eta}$  at the target because this is where the physical process takes place.

### A.2 The solution

The Kalman filter is a well-established algorithm in the standard formalism employed for track fitting developed to account for mechanisms like interactions with the detector material and mag-

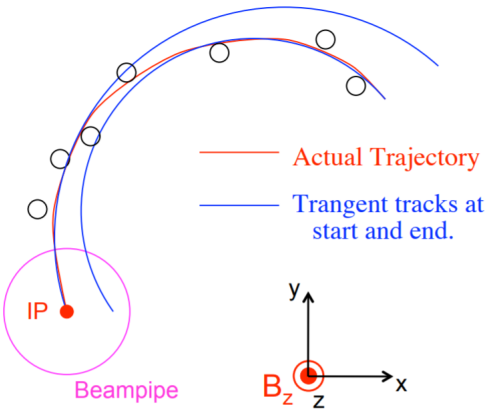


**Fig. A.1:** Pictorial view of the trajectory of a particle traveling along a circular path which has variable parameters [1]. The two blue circles represent the tangent circles at the beginning and at the end of the track segment: both circles are separately valid approximations of the particle trajectory in specific regions but they are not the best estimates of the entire trajectory.

netic field distortions that can affect the particle trajectory [2][3]. Most of today's implementations are based on the BaBar filter and adaptations of [4][3]. In the typical track fitting procedure, the pattern recognition algorithms employed to find a first estimate of the track are followed by a simplified Kalman filter. This version does not account for all the effects yet, like the interaction with the detector material, but improves the accuracy of track parameters reconstruction. If more effects need to be accounted for, a second and more complete Kalman filter can be executed to introduce the missing residual effects. There are two important general aspects of this iterative algorithm we should briefly mention:

- With  $N$  points and  $n$  parameters the algorithm does not require to compute the inverse of  $N \times N$  matrices<sup>1</sup> and simply uses multiplications of  $n \times n$  matrices (easy to program and fast to run). If the problem is linearized the algorithm does not even require the inverse of the  $n \times n$  matrix;
- Executing the algorithm in both directions of the trajectory once, storing the values of  $\vec{\eta}$  and  $V$  after considering each point, allows us to determine the estimates with optimal uncertainties in any position.

The full implementation is extremely complicated and its thorough description is beyond the scope of this Thesis. Nonetheless, it is still useful to describe the basic principle through the discussion of a simplified problem, as a 2D linear fit. This will be done in Sec. A.4.

### A.3 Implementation

The Kalman filter equations, linearized in  $\eta$ , are reported in Eq.A.1 with no proof, which is available in [5]. In these equations,  $\eta$  (dropping the vector symbol to avoid a too-heavy notation) and  $V$  are the current estimates of the vector and the covariance matrix, while the primed versions are the new estimates after a new hit is added. The measurement is indicated as  $d_m$ , with uncertainties  $\sigma$ , and  $d(\eta)$  is the measurement as predicted by the track parameters. Finally,  $D_i$  represents the derivatives with respect to one of the track parameters. To iterate, the key feature to be noticed is

<sup>1</sup>This is the case when introducing multiple scattering in a general fitting procedure: the position of a hit changes because of the interaction in another position creating a correlation between hits, summarized in a  $N \times N$  matrix.

that no matrix inversion of the order of  $N \times N$  is needed in this calculation, which reduces the load in terms of required computational resources.

$$\begin{aligned} D_i &= \frac{\partial d_m}{\partial \eta_i} \\ V' &= V - \frac{V D D^T V}{\sigma^2 + D^T V D} \\ \eta' &= \eta + V' D \frac{d_m - d(\eta)}{\sigma^2} \end{aligned} \quad (\text{A.1})$$

## A.4 Example: a 2D linear fit

Track fitting and Kalman filtering are complex procedures and we have reported the description of the simpler 2D linear problem (Fig. A.2) in the following to better explain them. More detailed documentation is available in [1] [5]. In the following, we can assume to have a particle moving along a straight line and a number of tracking stations positioned at the relative distance  $L$  among them which measure the vertical coordinate. The tracking stations measure the  $y_i$  positions, all with the same uncertainty  $\sigma$ , and our goal is to estimate the parameters of the line at a point IP placed externally to the volume occupied by the detectors. The equation of the trajectory is reported in eq. A.2, the vector of parameters and the covariance matrix are reported in eq. A.3

$$y = mx + b \quad (\text{A.2})$$

$$\eta = \begin{bmatrix} m \\ b \end{bmatrix}, \quad V = \begin{bmatrix} V_{mm} & V_{mb} \\ V_{bm} & V_{bb} \end{bmatrix} \quad (\text{A.3})$$

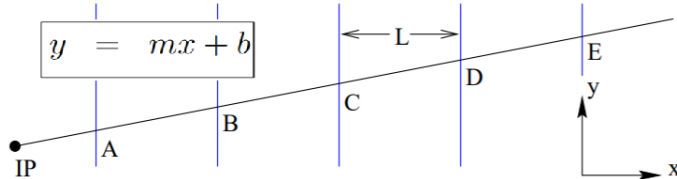


**Fig. A.2:** Pictorial view of a 2D trajectory of a particle moving along a straight line and interacting with a number of equally spaced tracking stations [1]. The stations measure the  $y$  positions and the goal is to determine the track parameters at some Initial Point (IP). The  $x$  origin is positioned on the last station while the  $y$  origin is not relevant for this exercise.

**Initialization** The first step is to provide a *seed* for the procedure. This is normally done with a pattern recognition algorithm which determines an initial estimate of the parameters, while  $V$  is assumed diagonal and with large values.

$$\eta = \begin{bmatrix} m_0 \\ b_0 \end{bmatrix}, \quad V = \begin{bmatrix} V_{mm,0} & 0 \\ 0 & V_{bb,0} \end{bmatrix}$$

**First hit** The procedure continues by adding point E and is simply necessary to apply the equations A.1, (the explicit calculation can be found in [1]):

$$V^{(1)} \approx \begin{bmatrix} V_{mm,0} & 0 \\ 0 & \sigma^2 \end{bmatrix}$$

$$\eta^{(1)} = \begin{bmatrix} m_0 \\ b_0 \end{bmatrix} + \begin{bmatrix} V_{mm,0} & 0 \\ 0 & \sigma^2 \end{bmatrix} \begin{bmatrix} 0 \\ 1 \end{bmatrix} \frac{y_E - b_0}{\sigma^2} = \begin{bmatrix} m_0 \\ y_E \end{bmatrix}$$

It is pretty straightforward to understand that employing just one hit provides information only on the track impact parameter, while there is no information on the trajectory slope.

**Transport** At this point the track is transported from E to D and, to do this, it is helpful to define a new coordinate system located on the second measurement plane. In this system the trajectory is  $y' = m'x' + b'$  with  $y = y'$ ,  $x' = x + L$ ,  $m' = m$  and  $b' = b - mL$ . By defining  $A_{i,j} = \frac{\partial \eta'_i}{\partial \eta_j}$ , the same track can be represented in a new base:

$$\eta^{(1')} = \begin{bmatrix} m_0 \\ y_E - m_0L \end{bmatrix}$$

$$V^{(1')} = AV^{(1)}A^T = \begin{bmatrix} V_{mm,0} & -LV_{mm,0} \\ -LV_{mm,0} & \sigma^2 + L^2V_{mm,0} \end{bmatrix}$$

As expected, the uncertainty on the slope remains unchanged by this transport, while the error on the impact parameter is now increased since the extrapolation used a slope with large uncertainty.

**Second hit** Since the track is now defined in the coordinate system of the second plane, adding the point D and applying again the Kalman equations A.1 is straightforward. The derivatives take the simple form:  $D = \begin{bmatrix} 0 \\ 1 \end{bmatrix}$ . we can skip the calculations and simply report the new estimators:

$$V^{(2)} \approx \begin{bmatrix} \frac{2\sigma^2}{L^2} & -\frac{\sigma^2}{L} \\ -\frac{\sigma^2}{L} & \sigma^2 \end{bmatrix}$$

$$\eta^{(2)} = \begin{bmatrix} m_0 \\ y_E - m_0L \end{bmatrix} + V^{(2)} \begin{bmatrix} 0 \\ 1 \end{bmatrix} \frac{y_D - (y_E - m_0L)}{\sigma^2} \approx \begin{bmatrix} \frac{y_E - y_D}{L} \\ y_D \end{bmatrix} \quad (\text{A.4})$$

The interesting feature is that all the assumed starting values have no impact on the estimates:  $m_0$ ,  $b_0$ ,  $V_{mm,0}$  and  $V_{bb,0}$ . The uncertainty on the impact parameter is function of solely the local information ( $\sigma$ ), while  $V_{mm}$  depends on both  $\sigma$  and  $L$ .

**Transport and third hit** In order to add a third measurement, the same two steps are needed: express the same track in the new base and then add the hit. The calculations are again detailed in [5] and we will only report the result:

$$V^{(3)} \approx \begin{bmatrix} \frac{\sigma^2}{2L^2} & -\frac{\sigma^2}{2L} \\ -\frac{\sigma^2}{2L} & \frac{5}{6}\sigma^2 \end{bmatrix}$$

$$\eta^{(3)} \approx \begin{bmatrix} \frac{y_E - y_C}{2L} \\ \frac{2y_D - y_E + 5y_C}{6} \end{bmatrix}$$

It is interesting to notice that once the third point has been added, the diagonal elements of the covariance matrix are reduced with respect to the case with only two points.

**Finishing** Once the procedure has been iterated to reach point A, the estimators of the trajectory use all the available information and are valid in a neighborhood region of A. To extrapolate to the track IP, the procedure is the same as before, describing the trajectory in the coordinate system set in the IP.

### A.4.1 Adding multiple scattering

How does the problem of track fitting change if the detectors are not ideal planes but consist of a thin scattering volume? The initialization and the inclusion of the first hit do not change. The uncertainty due to multiple scattering on the first hit is negligible because of the starting covariance matrix. In this simple model, the scattering is *local* and contributes only to the slope error and not the off-diagonal terms and the intercept, but as the track is extrapolated away from the surface it contributes to these terms as well.

If the surface introduces a factor  $\delta$  in the error of the slope, the matrix in eq A.4 the vector remains the same while the matrix becomes

$$V^{(2)} \approx \begin{bmatrix} \frac{2\sigma^2}{L^2} + \delta^2 & -\frac{\sigma^2}{L} \\ -\frac{\sigma^2}{L} & \sigma^2 \end{bmatrix}$$

From this point on the presence of  $\delta$  can change substantially the results because at the next iteration, it will enter in both  $V'$  and  $\eta'$ . In [5] the calculations are extensively developed up to the third point (point C) with the specific example  $\delta^2 L^2 = \sigma^2$  to keep the passages easy to follow.

## Bibliography

- [1] Robert K. Kutschke. "Kalman Filters: As Told by a Physicist to Physicists". In: *Mu2e-doc-557-v2* (June 2009).
- [2] Pierre Billoir. "Track fitting with multiple scattering: A new method". In: *Nuclear Instruments and Methods in Physics Research* 225.2 (1984), pp. 352–366. ISSN: 0167-5087. DOI: [https://doi.org/10.1016/0167-5087\(84\)90274-6](https://doi.org/10.1016/0167-5087(84)90274-6). URL: <http://www.sciencedirect.com/science/article/pii/0167508784902746>.
- [3] R. Frühwirth. "Application of Kalman filtering to track and vertex fitting". In: *Nucl. Instrum. Meth. A* 262 (1987), pp. 444–450. DOI: 10.1016/0168-9002(87)90887-4.
- [4] D. N. Brown , E. A. Charles , D. A. Roberts. "The BaBar Track Fitting Algorithm". In: () .
- [5] Robert K. Kutschke. "Example of a Kalman filter n a straight line". In: (Mar. 1998). URL: [https://home.fnal.gov/~kutschke/Tracking/kalman\\_simple.pdf](https://home.fnal.gov/~kutschke/Tracking/kalman_simple.pdf).

## Appendix B

# BGO Calibrations

The BGO is an auxiliary detector of the MEG II apparatus. It is usually used during the CEX calibration, as discussed in Ch. 6, but it was also part of the X17 data-taking discussed in Ch 7. Here we will see how the calibration (and inter-calibration) is tackled. I worked on this item with a master student from ETH, David Stäger, who compiled all the information in his thesis [1].

Calibrating a calorimeter involves establishing a relationship between the observed waveforms in the PMT readout channels and the energy of incoming photons. In the case of calibrating the BGO, we assume the energy deposited by the photon ( $E_\gamma$ ) is directly proportional to the observed PMT charge ( $I_j$ ) in each channel, considering that the energy can be distributed across multiple crystals (Eq. B.1). The calibration factors ( $f_j$ ) for each channel are determined from real data. However, since many detector processes are energy-dependent, the BGO response may not be strictly linear, especially away from the calibration point. To address this, calibration is done close to the 18.15 MeV transition of excited  ${}^8\text{Be}$ , which is crucial for the X17 measurement. Hence, calibration is performed using the 17.64 MeV transition of  ${}^8\text{Be}$ , excited by protons with a kinetic energy of 500 keV. Various collected datasets are available for calibration purposes, as listed in Tab. B.1.

$$E_\gamma = \sum_{j=0}^{15} I_j \cdot f_j \quad (\text{B.1})$$

Date	Runs	$E_p$ [keV]	$I_{CW}$ [ $\mu\text{A}$ ]
29.01.2023	482350 - 482425	500	2
30.01.2023	482539 - 482628	500	2
31.01.2023	482784 - 482828	500	3
28.02.2023	510122 - 510171	500	6

**Tab. B.1:** Collected datasets for the BGO calibration.

### B.1 Calibration factors

To calibrate the detector, we determine calibration factors  $f_j$  for each of the 16 channels using photons emitted in the  $\text{Li} + p \rightarrow \text{Be} + \gamma$  reaction at  $E_p = 500$  keV. Since the reaction yields a continuous spectrum, due to the width of the 15.6 MeV line, we adjust the observed spectrum by

shifting peaks to expected energies in a step procedure:

1st We introduce a scale factor  $K_{scale}$  to relate the charge  $I_j$  to the energy

$$E'_j = K_{scale} \cdot I_j$$

2nd We ensure uniform channel response by scaling each channel's spectrum by a factor  $a_j$ , determined by shifting peaks to 17.64 MeV.

$$E''_j = K_{scale} a_j \cdot I_j$$

3rd We sum energy contributions of all channels, considering only events where the highest charge is in central crystals. We introduce  $K_{leak}$  to shift the rightmost peak to 17.64 MeV, accounting for energy leakage between crystals. The reconstructed energy deposit is:

$$E_\gamma = \sum_{j=0}^{15} K_{scale} \cdot K_{leak} \cdot a_j \cdot I_j$$

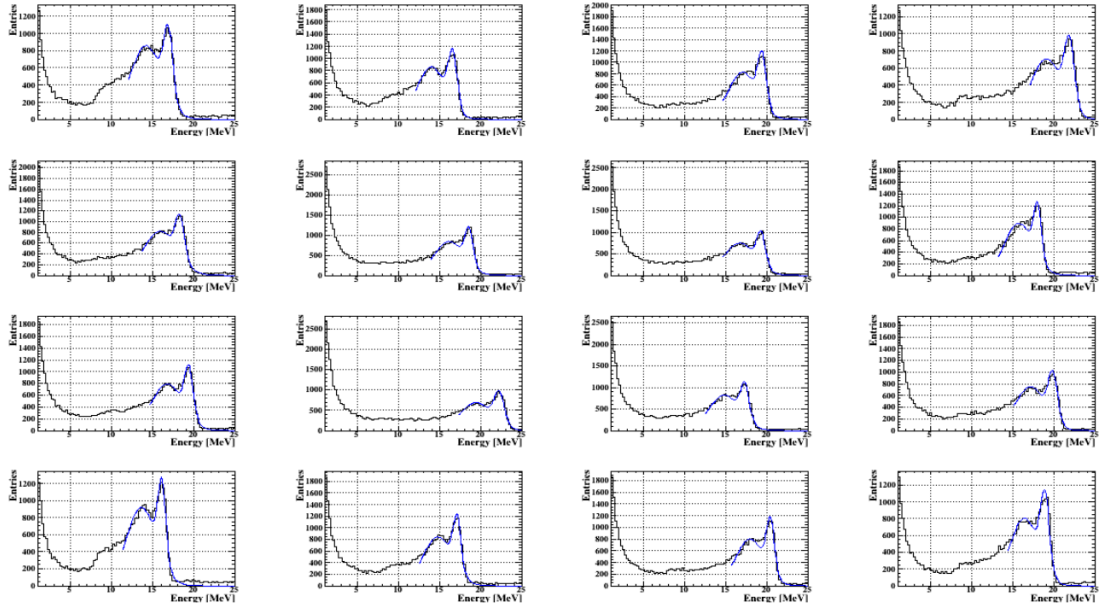
The steps are highlighted in Fig. B.1 and Fig. B.2. For convenience, we split calibration factors into  $f_j = K_{scale} \cdot K_{leak} \cdot a_j = K_{scale} \cdot c_j$ , where  $c_j$  is determined from data after selecting a  $K_{scale}$ .

### B.1.1 Sample size

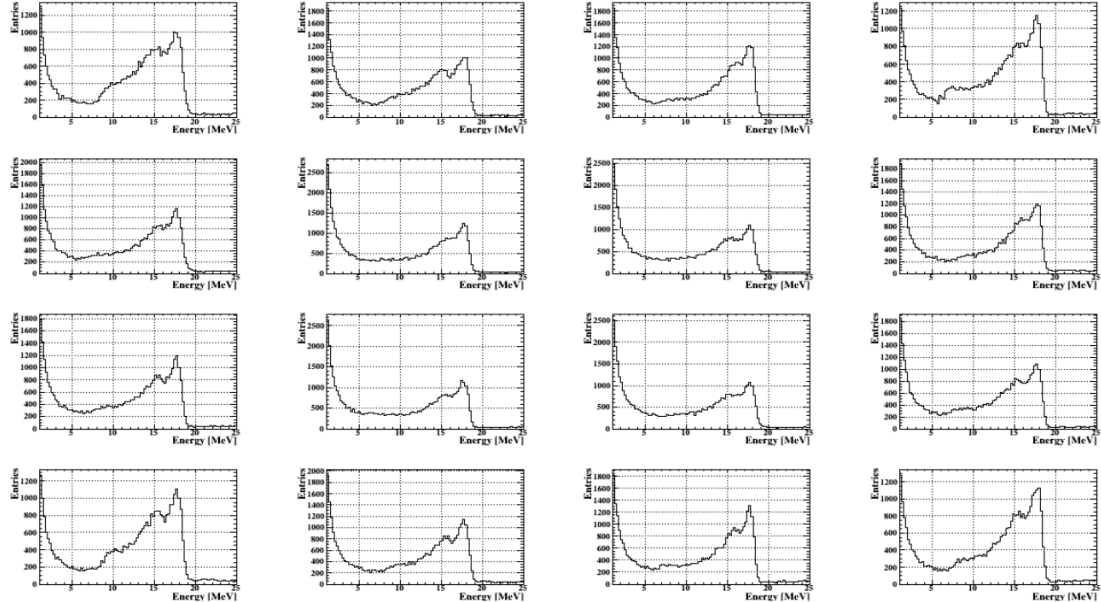
To examine the sensitivity of calibration factors to sample size, we utilized a dataset of 90 runs collected on January 30, 2023, just before a month-long period of X17 data collection with no further calibration runs. Initially, we determined calibration factors using the described procedure for the entire 90-run dataset. To assess variation with sample size, we created 500 sub-samples of N runs each, randomly selected from the full set. For each subsample (with 50 and 30 runs, respectively), we computed the product of calibration factors  $K_{leak} \cdot a_j$  and evaluated the mean and standard deviation. The results, tabulated in Tab. B.2 for N = 30 and N = 50, indicate the extent of variation in calibration factors with smaller sample sizes. Notably, the mean calibration factor obtained from the 500 subsamples aligns with that from the full dataset. Across tested sample sizes, the standard deviation of the product  $K_{leak} \cdot a_j$  remained below 0.5%.

Channel	0	1	2	3	4	5	6	7
$c_j = K_{leak} \cdot a_j$	1.0106	1.0300	0.8793	0.7798	0.9311	0.9198	0.8845	0.9489
$\sigma_B$ (N = 30)	0.0016	0.0019	0.0016	0.0013	0.0015	0.0012	0.0010	0.0016
$\sigma_B$ (N = 50)	0.0010	0.0013	0.0011	0.0009	0.0010	0.0010	0.0007	0.0012
Channel	8	9	10	11	12	13	14	15
$c_j = K_{leak} \cdot a_j$	0.8799	0.7670	0.9858	0.8590	1.0593	0.9971	0.8357	0.9026
$\sigma_B$ (N = 30)	0.0013	0.0010	0.0015	0.0015	0.0018	0.0014	0.0011	0.0020
$\sigma_B$ (N = 50)	0.0009	0.0007	0.0010	0.0010	0.0011	0.0010	0.0007	0.0012

**Tab. B.2:** Calibration factors and standard deviations for different sample sizes.

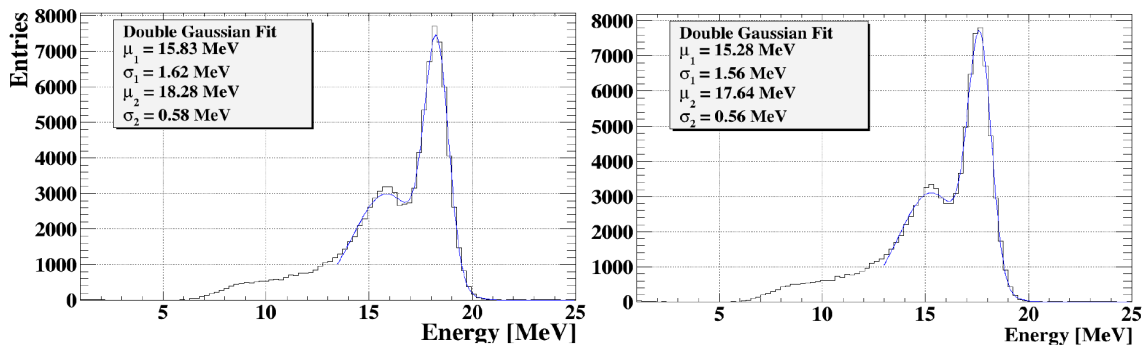


(a) The single channels are fitted with a doublegauss to find the peak.



(b) Intercalibration factors  $a_j$  are applied to alligne the peaks.

**Fig. B.1:** We start by fitting the single channel (multiplied by  $K_{scale}$ ) to align them.



(a) The spectrum is the sum of the aligned channels. (b) The spectrum needs to be corrected with  $K_{leak}$ .

**Fig. B.2:** The aligned channels sum is the BGO spectrum it is corrected for the leak between crystals.

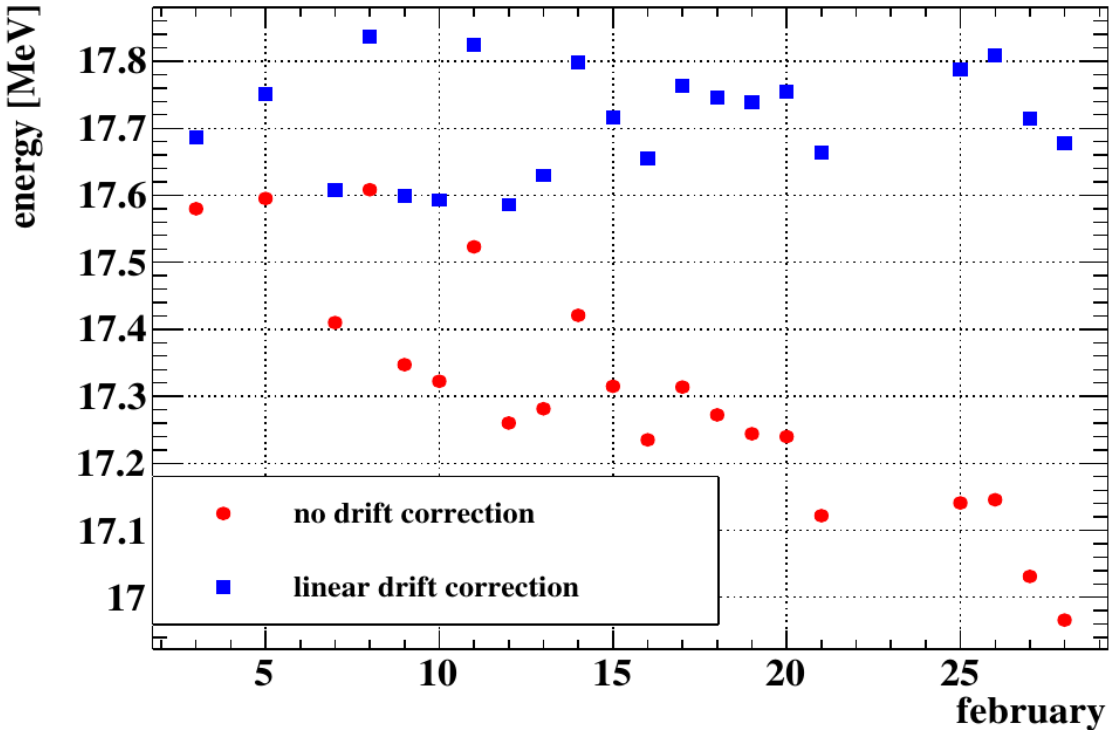


Fig. B.3: History of the 17.6 MeV line with and without linear correction for the drift found in Fig. B.4b.

## B.2 Stability

An interesting point is the time stability of the calibration. For this purpose, data were taken on three days: 29-30-31.01.2023. The variation, shown in Fig. B.4a, is found to be very dependent on the channel. This is not a problem because calibration runs were taken every day to follow the evolution of the detectors. When looking at the variation over a longer time, beginning-end of the data-taking, we find a systematic drift, shown in Fig. B.4b. The drift might be explained by a slow drop in the PMT voltage supply and can be compensated by assuming a linear dependence with time. The difference of the peak position before and after linear correction is shown in Fig. B.3.

## Bibliography

- [1] D. Stäger. "Scintillation Detector Research for Experiments Probing Beyond Standard Model Physics". PhD thesis. Swiss Federal Institute of Technology (ETH), 2023.

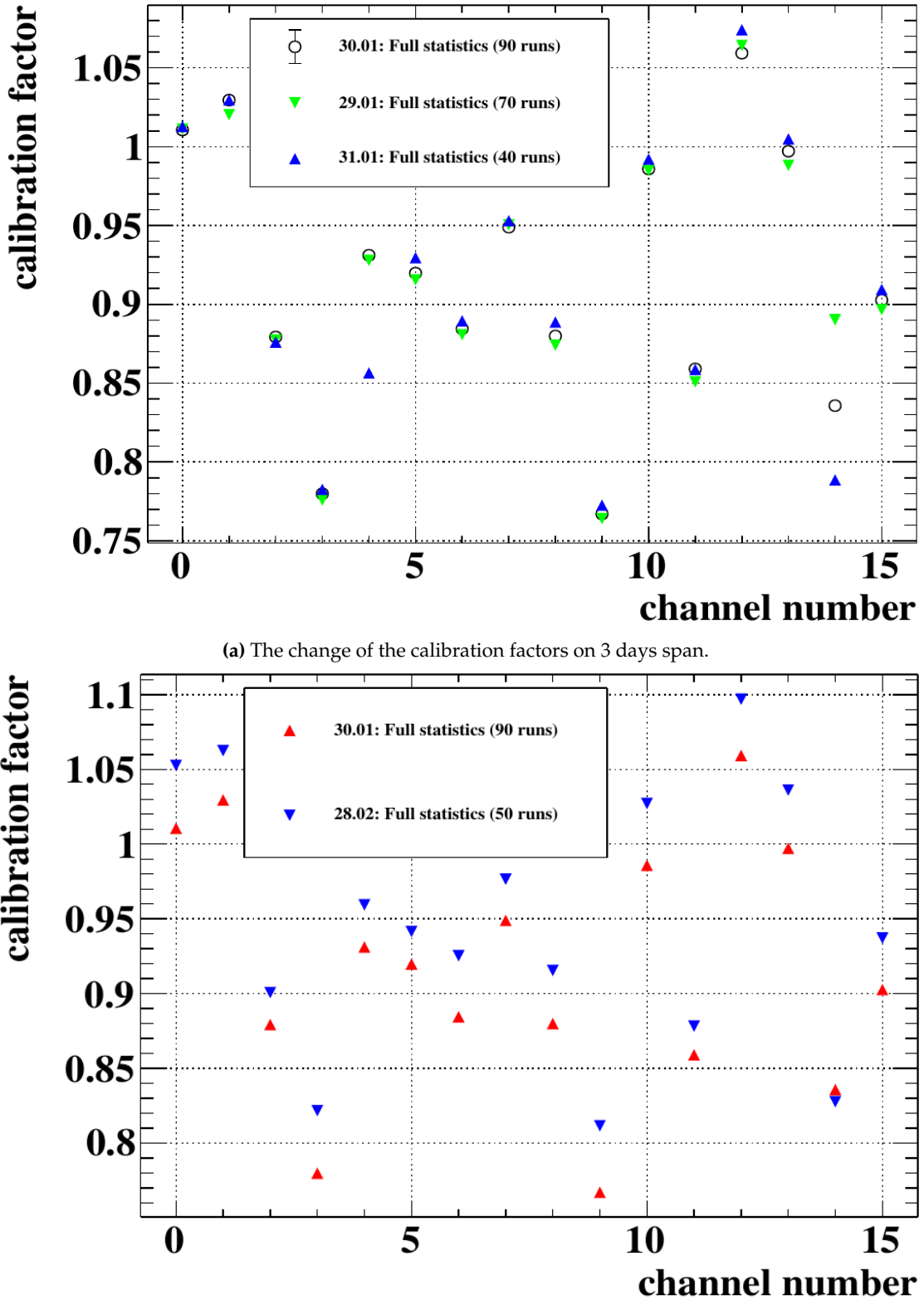


**Fig. B.4:** Time stability of the calibration factors: (a) 3 days, (b) start and finish of the data-taking.